



UNIVERSIDADE FEDERAL DE SANTA CATARINA
CENTRO TECNOLÓGICO DE JOINVILLE
PROGRAMA DE PÓS-GRADUAÇÃO EM ENGENHARIA E CIÊNCIAS MECÂNICAS

Anselmo Thiesen Junior

**Selection of processing parameters for the laser directed energy deposition process
applied to additive manufacturing: a methodological proposal**

Joinville

2021

Anselmo Thiesen Junior

**Selection of processing parameters for the laser directed energy deposition process
applied to additive manufacturing: a methodological proposal**

Dissertação submetida ao Programa de Pós-Graduação em Engenharia e Ciências Mecânicas da Universidade Federal de Santa Catarina para a obtenção do título de mestre em Engenharia e Ciências Mecânicas.

Orientador: Claudimir A. Carminatti, Dr. Eng.

Coorientador: Jhonattan Gutjahr, Me. Eng.

Joinville

2021

Ficha de identificação da obra elaborada pelo autor,
através do Programa de Geração Automática da Biblioteca Universitária da UFSC.

Thiesen Junior, Anselmo

Selection of processing parameters for the laser directed energy deposition process applied to additive manufacturing : a methodological proposal / Anselmo Thiesen Junior ; orientador, Claudimir Antonio Carminatti, coorientador, Jhonattan Gutjahr, 2021.

180 p.

Dissertação (mestrado) - Universidade Federal de Santa Catarina, Campus Joinville, Programa de Pós-Graduação em Engenharia e Ciências Mecânicas, Joinville, 2021.

Inclui referências.

1. Engenharia e Ciências Mecânicas. 2. Manufatura aditiva. 3. L-DED. 4. Metodologia. 5. Parâmetros de processamento. I. Carminatti, Claudimir Antonio. II. Gutjahr, Jhonattan. III. Universidade Federal de Santa Catarina. Programa de Pós-Graduação em Engenharia e Ciências Mecânicas. IV. Título.

Anselmo Thiesen Junior

**Selection of Processing Parameters for the Laser Directed Energy Deposition process
applied to Additive Manufacturing: A methodological proposal**

O presente trabalho em nível de mestrado foi avaliado e aprovado por banca examinadora
composta pelos seguintes membros:

Prof. Reginaldo Teixeira Coelho, Dr.
Universidade de São Paulo

Prof. Leandro João da Silva, Dr.
Universidade Federal de Uberlândia

Prof. Adriano Fagali de Souza, Dr.
Universidade Federal de Santa Catarina

Prof. Alexandre Mikowski, Dr.
Universidade Federal de Santa Catarina

Certificamos que esta é a **versão original e final** do trabalho de conclusão que foi julgado
adequado para obtenção do título de mestre em Engenharia e Ciências Mecânicas.

Prof. Rafael de Carmargo Catapan, Dr.
Coordenador do PósECM

Prof. Claudimir Antonio Carminatti, Dr. Eng.
Orientador

Jhonattan Gutjahr, Me. Eng
Coorientador

Joinville, 2021.

A minha família, meus amigos e a todos aqueles que me apoiaram.

AGRADECIMENTOS

Agradeço aos meus pais que sempre me ensinaram que a busca pelo conhecimento é sempre o caminho mais sólido para obter o sucesso em todas as áreas da vida.

Aos professores que despertaram em mim o pensamento crítico e a visão científica do mundo, isso é algo fascinante que me mudou para sempre como ser humano. Em especial aos meus orientadores Carminatti e Gutjahr por guiar meu caminho nesta trajetória.

À Carine, minha companheira, por estar sempre presente nos momentos difíceis me fornecendo todo o suporte possível, me incentivando, sendo meu alicerce e acreditando em mim muitas vezes mais do que eu mesmo acreditava.

Aos meus amigos de trabalho por todos os ensinamentos, discussões, críticas construtivas e contribuições neste trabalho.

Ao Instituto Senai de Inovação em Sistemas de Manufatura e Processamento a Laser por todo o suporte que tornou este trabalho possível.

*The good thing about science is that it's true
whether or not you believe in it.*

Neil deGrasse Tyson

RESUMO

A manufatura aditiva metálica através do processo de deposição de energia direcionada a laser (L-DED) é uma tecnologia que vem ganhando espaço frente aos processos de manufatura tradicionais. Uma dentre as principais vantagens dessa tecnologia é a possibilidade de utilização de diversas ligas metálicas e não metálicas, visto a viabilidade de utilização do material de adição no formato de arame e pó metálico, aumentando consideravelmente a gama de ligas disponíveis no mercado. Diferentes ligas requerem diferentes condições de processamento, de modo a se obter os requisitos de qualidade e performance desejados. Este fato aliado ao elevado número de variáveis presente no processo L-DED faz com que a seleção dos parâmetros de processamento se torne um desafio. Muitos autores desenvolveram metodologias para seleção de parâmetros de processamento baseando-se nas características de cordões simples. Entretanto, poucos estenderam seus estudos à modelagem das características de camadas. Deste modo, se faz necessária uma metodologia de obtenção de parâmetros estruturada. Esta dissertação propõe um método de seleção de parâmetros aplicado a manufatura aditiva, utilizando a tecnologia L-DED. Considerando a discrepância de diversos autores na forma de se medir monocamadas, assim como na definição das características mais relevantes, um método padronizado de medição de camadas foi proposto. Uma função desejabilidade foi definida para cada característica de camada, de modo que posteriormente essas funções pudessem ser unidas a fim de possibilitar a comparação de camadas de maneira quantitativa, avaliando a relação entre os parâmetros de processamento e as características finais obtidas. Na última etapa, os resultados obtidos foram aplicados ao conceito de multicamadas presente na manufatura aditiva. Corpos de prova para ensaio mecânico de tração e ensaio mecânico de impacto foram fabricados utilizando o parâmetro de processamento selecionado a fim de correlacionar os resultados obtidos com suas propriedades mecânicas e características microestruturais. Também foram avaliadas as características de microdureza Vickers, porosidade e microestrutura de corpos de prova depositados. Os resultados médios obtidos foram de cerca de 173 HV de microdureza Vickers, 301 MPa de tensão de escoamento para as amostras termicamente tratadas e 381 MPa para as amostras sem tratamento térmico, 594 MPa de tensão máxima admissível, 50% de alongamento, 172 J na melhor condição de energia absorvida em ensaio charpy e densidade de 99,86%. A metodologia proposta se mostrou eficiente em modelar o comportamento do processo, em padronizar o processo de medição das características

geométricas de camadas simples e selecionar parâmetros de processamento com base nas características geométricas desejadas.

Palavras-chave: Manufatura aditiva. L-DED. Otimização de parâmetros de processamento. Regressão múltipla. Propriedades mecânicas.

RESUMO EXPANDIDO

Introdução

A manufatura aditiva consiste no processo de união de materiais de modo a fabricar objetos a partir de um modelo 3D. Para isto, um material de adição é depositado camada a camada, sendo assim oposto aos processos de manufatura subtrativos tradicionais. Essa tecnologia possibilita a obtenção de componentes de geometria complexa, com ganhos de performance otimizados, antes inviáveis através dos métodos de processamento existentes.

Um grande número de técnicas e nomenclaturas de manufatura aditiva está disponível hoje no mercado, que se diferem basicamente na forma em que as camadas se consolidam, no mecanismo do processo e nos materiais que são utilizados. Se tratando de manufatura aditiva de materiais metálicos pode-se dividir basicamente em dois grandes grupos: fusão em leito de pó (Powder Bed Fusion - PBF) e deposição de energia direcionada a laser (Laser Directed Energy Deposition – L-DED). A grande diferença entre ambas é que na fusão em leito de pó, o pó metálico está previamente depositado em um leito, e a medida em que as camadas são fundidas o leito é baixado e uma nova camada de pó é distribuída para que a próxima camada possa ser fundida pelo feixe laser, enquanto que na tecnologia L-DED um bocal expõe o pó metálico coaxialmente com um feixe laser sobre um substrato. Enquanto a tecnologia PBF possibilita a obtenção de geometrias mais complexas e com maior riqueza de detalhes, ao custo de menores taxas de deposição e componentes de menores dimensões; a deposição de energia direcionada possibilita a fabricação de componentes maiores e com maiores taxas de deposição, ao custo de maiores limitações quanto a resolução e geometria.

L-DED envolve interações complicadas entre feixe de laser, feixe de pó, substrato, e peça produzida. Os gradientes de temperatura envolvidos no processo são muito elevados, gerando elevados níveis de tensão residual, o que o torna mais susceptível a defeitos como trincas e poros (tanto gerados por gás enclausurado quanto por falta de fusão). Uma abordagem interessante no estudo da processabilidade de novas ligas por L-DED é comparar com a soldabilidade destas ligas.¹ Desta forma, é esperado que ligas de boa soldabilidade também sejam mais facilmente processáveis por L-DED. Considerando a complexidade do processo em questão, aliado ao grande número de variáveis, é razoável que estudos iniciais

¹ Soldabilidade é a capacidade de uma liga em produzir soldas livres de defeitos.

sejam desenvolvidos com ligas de melhor soldabilidade, avançando posteriormente para ligas mais complexas.

Muitos autores desenvolveram estudos para gerar mapas de processo baseados nas características de cordões simples, o que acaba sendo pouco representativo nas características de componentes. Há então um desafio em elaborar uma metodologia mais representativa, que aborde também questões relacionadas às características de camadas simples e multicamadas.

Essa dissertação tem por foco a elaboração de uma metodologia para seleção de parâmetros de processamento que possibilitem sua correlação com características desejadas, gerando adicionalmente um estudo das propriedades mecânicas (tensão de escoamento, tensão máxima admissível, módulo de elasticidade, microdureza Vickers, resistência ao impacto) e microestruturais obtidas utilizando o parâmetro selecionado.

Objetivos

O objetivo principal desta dissertação é desenvolver e aplicar um método para seleção de parâmetros de processamento que possibilite prever as características geométricas de deposições realizadas através do processo de deposição de energia direcionada a laser, selecionando um parâmetro otimizado com base em critérios geométricos pré-estabelecidos. Após selecionado o parâmetro otimizado, avaliar suas propriedades mecânicas e microestruturais.

Quatro objetivos específicos foram estipulados com o intuito de atingir o objetivo principal:

- a) Definir quais são as principais características geométricas das camadas simples e como medi-las.
- b) Desenvolver uma metodologia para seleção de parâmetros de processamento (potência do laser, velocidade de escaneamento, vazão mássica, *hatch spacing*) da tecnologia de deposição de energia direcionada a laser.
- c) Verificar a funcionalidade do método proposto através da deposição de corpos de prova utilizando o parâmetro selecionado usando aço inoxidável AISI 316L como metal de adição.
- d) Realizar as caracterizações mecânicas (ensaio mecânico de tração, ensaio mecânico de impacto, microdureza Vickers) e microestruturais (microscopia óptica), verificando a presença de descontinuidades.

Metodologia

A metodologia básica se divide em cinco estágios: exploratório, modelagem, otimização, camadas múltiplas e caracterização. A primeira etapa, chamada de etapa preliminar, está contida dentro do estágio exploratório. Nesta etapa são levantadas as informações mais importantes a respeito da liga e das condições de trabalho. Baseado nessas informações, algumas decisões são tomadas, como material e dimensões dos substratos, a necessidade ou não de pré-aquecimento, a escolha do gás de proteção e a definição de alguns problemas críticos que podem vir a ser observados. Se necessário, alguns testes podem ser conduzidos de modo a auxiliar na tomada destas decisões e no conhecimento da liga e/ou equipamento a ser utilizado.

O estágio exploratório tem por objetivo indicar aproximadamente quais são as regiões onde as janelas de processamento do material em estudo estão situadas. Para que isso seja possível, os ensaios são conduzidos com grandes variações dos parâmetros de processamento, de modo que englobe o maior número possível de respostas. Nesta etapa o estudo se dá na forma de cordões simples, de modo a agilizar o procedimento de realização de experimentos. A avaliação dos cordões também se dá de maneira simplificada, sem avaliação de seção transversal, de modo a tornar o processo mais acelerado.

No estágio de modelagem, são depositadas camadas simples, e as regiões próximas da janela de processamento (com uma leve extrapolação para as bordas, de modo que não se exclua boas regiões intermediárias) são avaliadas mais a fundo. Nessa fase o valor da vazão mássica é fixado e passa-se a variar a distância entre cordões. Avalia-se as seções transversais das camadas depositadas e os dados de cada camada são gravados juntamente com os parâmetros de processamento relativos a ela.

No estágio de otimização são geradas as superfícies de resposta através de regressão múltipla, correlacionando a variação de parâmetros com as variações de características. Utilizando critérios de desejabilidade são estipulados os requisitos necessários. Estes requisitos são comparados com as superfícies de resposta obtidas na regressão e o parâmetro otimizado é então obtido. Uma camada de verificação é depositada para comparar as características reais com as previstas através do modelo.

Após obtido e verificado o parâmetro otimizado, inicia-se o estágio de camadas múltiplas. Alguns ensaios podem ser necessários de modo a se obter melhora nas características da camada otimizada através de sensíveis modificações nos parâmetros de processamento. A análise da necessidade e de quais testes serão realizados estão a cargo do usuário. Após realizada esta etapa, os ensaios de camadas múltiplas se iniciam de fato. O

objetivo é estipular a melhor taxa de sobreposição de camadas analisando a relação entre produtividade e presença de descontinuidades (principalmente poros e falta de fusão).

Por fim são depositados os corpos de prova de acordo com as necessidades de caracterização de cada caso. Neste trabalho, foram depositados 38 corpos de prova onde 22 foram submetidos a caracterizações mecânicas (9 para ensaio mecânico de tração e 9 para ensaio mecânico de impacto), microestruturais e de presença de descontinuidades (4). Os corpos de prova remanescentes serão ensaiados em estudos posteriores.

Resultados e Discussões

O grupo de características geométricas selecionado para representar as camadas simples foi considerado eficiente na execução de sua função. As ilustrações desenvolvidas para exemplificar o modo correto de medir monocamadas minimizam a chance de erro no processo de medição, e irão auxiliar o processo de aprendizado na utilização do método por novos usuários.

O método proposto foi capaz de modelar as tendências de características das monocamadas de acordo com a variação dos parâmetros de processamento, podendo prever suas características geométricas. Houve maior dificuldade em modelar o comportamento do parâmetro “hatch spacing”². Maiores estudos podem ser desenvolvidos a respeito da modelagem deste parâmetro de modo a melhorar a funcionalidade do método. Nas etapas posteriores, o método se mostrou eficiente quanto a estender a aplicação para camadas múltiplas voltado a fabricação de componentes por manufatura aditiva via L-DED.

A caracterização das amostras obtidas exibiu resultados consistentes na grande maioria dos ensaios (com exceção da propriedade “módulo de elasticidade”). Isso pode ser observado através da similaridade nas curvas obtidas através do ensaio mecânico de tração e o baixo desvio padrão dos resultados obtidos. Adicionalmente, o comportamento mecânico observado foi predominantemente dúctil e com resistência consideravelmente superior aos requisitos mínimos da mesma liga processada por forjamento.

Considerações Finais

De modo geral, a metodologia proposta neste trabalho está apta a auxiliar o usuário na seleção de parâmetros de processamento aplicados a manufatura aditiva através da tecnologia L-DED, provendo componentes de comportamento mecânico consistente.

² “A distância lateral entre dois passes subsequentes do cabeçote de deposição quando depositando uma camada” [11].

Palavras-chave: Manufatura aditiva. L-DED. Otimização de parâmetros de processamento. Regressão múltipla. Propriedades mecânicas.

ABSTRACT

The Laser Directed Energy Deposition (L-DED) technology is an additive manufacturing process that allows producing metal parts through the melting of metallic powder using a laser beam as a source of heat. One of the highest challenges when processing new alloys or new powder configurations using L-DED is to link the processing parameters to the characteristics of the layers. It happens because this technology has many processing variables and the interactions between them are very complex to predict. Many authors use simple or full factorial design to understand the behavior of an alloy, which may be fast but probably not the best representative model in most scenarios. This study proposes a method based on multiple regression analysis to obtain processing parameters for L-DED based on the geometrical needs of the user. The regressions use full factorial designs as inputs and exhibit a continuous behavior of the process. The structure is split into five stages, Exploratory, Modeling, Optimization, Multilayer, and Characterization. The experiments are conducted initially with single beads and simple analysis. After the first stage, the second and refined stage of experiments is more complete, with single layers and cross-section analysis. The cross-section characteristics feed a database generating surfaces of response. Using desirability criteria to quantify the needs of the user, an optimized layer is obtained, with its processing parameter related. In the Multilayer Stage, some little adjustment may be done and the overlayer is defined. AISI 316L powder was used to apply the methodology and the model proposed was able to predict most of the characteristics. Considering all the outputs analyzed, the most discrepant was dilution. It was concluded that it was due to the hatch spacing variation. Dilution has a complex and non-linear variation when varying hatch spacing, and it was the major difficulty in the regression setting. The characterization of the samples exhibited results with low standard deviation. It may be seen by the similarity of the tensile curves and the low standard deviation of all the results. That achievement increases the credibility of the method, once the characterization showed a predictable behavior of the parts obtained. The mechanical behavior observed was predominantly ductile and higher than minimal wrought material requirements. It can be concluded that the proposed method generated processing parameters able to generate parts with trustworthy mechanical behavior and higher mechanical properties when compared to wrought components.

Keywords: Additive manufacturing. L-DED. Processing parameters optimization. Regression analysis. Mechanical properties.

LIST OF FIGURES

Figure 1 – Timeline of the evolution of Additive Manufacturing technology.	26
Figure 2 – Comparison of various Metal Additive Manufacturing processes.....	27
Figure 3 – Beam waist and diffraction angle.....	31
Figure 4 – Single bead dimensions and characteristics.	34
Figure 5 – Bead cross-sections with wettability angle.	35
Figure 6 – Overlapping model.....	36
Figure 7 – Layer orientation with 90 degrees variation between layers.....	36
Figure 8 – Schematic of (a) lack of fusion (interlayer porosity) and (b) keyholing porosity (intralayer porosity).	37
Figure 9 – Possible types of porosity.	38
Figure 10 – Processing map for Ti-6Al-4V alloy on the same substrate in terms of P vs. F/V representation.....	40
Figure 11 – Processing window.	40
Figure 12 – Processing window for different materials.	43
Figure 13 – Particle morphology for each atomization process.	45
Figure 14 – Gas (a) and plasma (b) atomization processes.	46
Figure 15 – Presence of a pore inside a metallic particle.	47
Figure 16 – Relation between tensile stress and elongation of commercial stainless steel compared to low alloy steels.	48
Figure 17 – 300 series stainless steel.....	51
Figure 18 – Fusion zone microstructure of a fully austenitic (a) and an austenitic-ferritic (b) solidification after an arc-based welding process.....	52
Figure 19 – Solidification map.	54
Figure 20 – Suutala diagram.....	55
Figure 21 – Pseudobinary section of the Fe-Cr-Ni system at 70% iron.....	55
Figure 22 – Schaeffler diagram.	56
Figure 23 – Processing window of 316L for different AM techniques.....	57
Figure 24 – Processing window of 316L for different AM techniques.....	57
Figure 25 – Mean bead width in the top and bottom layers.	59
Figure 26 – Microstructure according to layers (a), cellular structure with arrows showing solidification borders (b), dendritic structure (c).....	60
Figure 27 – Cross-section of the repaired area for 0,5 mm joint (a), 1 mm (b), and 2 mm (c).....	61

Figure 28 – Microhardness distribution according to the distance from the surface. Samples “A” are related to powder 1 and samples “B” are related to powder 2.	62
Figure 29 – Comparison between simulated and experimental melt pool.	63
Figure 30 – Indentations in regular materials and processed by AM.	64
Figure 31 – Methodology flowchart.	69
Figure 32 – Problems observed on single beads: (a) high convexity, (b) irregularity, (c) cracks, (d) detachment, and (e) surface porosity.	73
Figure 33 – Height measure of a single bead using a height caliper gauge.	74
Figure 34 – Tabular map (left) and the related subtitle (right).	75
Figure 35 – Representative scheme of dilution in a single layer.	78
Figure 36 – Representative scheme of layer height measurement.	78
Figure 37 – Representative scheme of height-variation.	79
Figure 38 – Representative scheme of layer slope.	79
Figure 39 – Histograms of outputs.	82
Figure 40 – Figure (a) represents maximization desirability, (b) represents minimization desirability, and (c) represents target desirability. Both of them show high, low, and standard sensitivity.	84
Figure 41 – Flowchart of the applied method.	87
Figure 42 – Equivalent circular diameter of metallic powder exposed by number (left) and volume (right).	88
Figure 43 – Circularity of the metallic powder.	89
Figure 44 – FESEM morphology analysis, 500x (left) and 1000x (right) magnification.	90
Figure 45 – Optical microscopy of powder cross-section for pores evaluating, 50x (left) and 100x (right) magnification.	90
Figure 46 – RPM Innovations 535 with 25° nozzle.	92
Figure 47 – Exploratory Stage deposition.	94
Figure 48 – Substrate positioning setup.	94
Figure 49 – Substrate heating control.	96
Figure 50 – Thermal camera inspection to assure temperature homogeneity in the Modeling Stage.	96
Figure 51 – Sample nomenclature for build 1 (left), build 2 (center), and build 3 (right).	99
Figure 52 – Sample nomenclature.	99
Figure 53 – Buildings of samples. Build 1 (a), build 2 (b), and magnification on the surface of an impact absorption sample from build 1 (c).	100

Figure 54 – Laser power calibration procedure.....	101
Figure 55 – Difference between the cross-section of a single bead with powder and laser spot misaligned (left) and aligned (right).....	102
Figure 56 – Feedrate calibration arrangement (left) and resultant straight (right).....	103
Figure 57 – Single-beads categorization.	105
Figure 58 – Application of the Suutala Diagram.....	105
Figure 59 – Cross-sections of single layers.....	107
Figure 60 – Histograms of cross-section measurements.	108
Figure 61 – Cross-section of deposition with high layer slope and decreasing dilution due to low hatch spacing (the deposition starts from the left).....	108
Figure 62 – Regression analysis for dilution.....	110
Figure 63 – Regression analysis for height.	110
Figure 64 – Regression analysis for waviness.....	111
Figure 65 – Regression analysis for capture efficiency.....	112
Figure 66 – Regression analysis for capture layer slope.	112
Figure 67 – Desirability distributions.....	114
Figure 68 – Verification of the predicted single-layer (a) and the blocks using 5% (b), 10% (c), 15% (d), 20% (e), and 25% (f) of overlayer.	116
Figure 69 – Damaged lens (a) and samples with soot (b).	117
Figure 70 – Verification single-layer with very widely spaced beads.	119
Figure 71 – Hatch spacing refinement.....	119
Figure 72 – Verification block for 20% (a) and 25% (b) overlayer.	121
Figure 73 – Porosity of the heat-treated sample using a 50x magnification mosaic.....	122
Figure 74 – The orange rectangle represents the area used to perform the porosity analysis.	122
Figure 75 – Pores and voids size distribution.....	123
Figure 76 – Porosity observed for (a) single-built (not heat-treated) and (b) nine-built samples at three different regions (bottom, middle, and top).....	124
Figure 77 – Microhardness profile.	125
Figure 78 – Schaeffler Diagram (left) and a pseudobinary diagram for 70% iron (right) analysis using the metallic powder composition.	126
Figure 79 – Microstructure of as-built sample (200x magnification).	127
Figure 80 – Microstructure of as-built sample (200x magnification).	128
Figure 81 – Microstructure of as-built sample (100x magnification).	129
Figure 82 – Microstructure of as-built sample (500x magnification).	129

Figure 83 – Microstructure mosaic of the heat-treated sample (50x magnification).	130
Figure 84 – Specimen 2 dimensions (left) according to ASTM E8 and after machined (right).	131
Figure 85 – Results of tension tests from vertical heat-treated (a), horizontal heat-treated (b), and vertical as-built (c) samples.	133
Figure 86 – Vertical HT sample T1V-1 (left), vertical AB sample T2V-3 (center), and vertical AB sample T1V-3 (right) showing the shape of the fracture after the tensile test. Only the right sample exhibits brittle behavior.	134
Figure 87 – Groove position on impact absorption sample.....	135
Figure 88 – Ductile fracture of the impact absorption samples.....	136
Figure 89 – Regression analysis for the first attempt of methodology.....	137
Figure 90 – Correlation between the dilution and the sequence of deposition (a, b, and c) and between the dilution and power (d).	138

LIST OF TABLES

Table 1 – Optimal dilution range for different materials.	43
Table 2 – Processing parameters for L-DED found in the studied papers.	65
Table 3 – 316L powder chemical composition.	86
Table 4 – 316L powder characteristics obtained through Particle Insight Analysis.	89
Table 5 – 316L substrate chemical composition.	91
Table 6 – RPM Innovations 535 features.	93
Table 7 – Laser source and optical set features.	93
Table 8 – Exploratory Stage parameters.....	93
Table 9 – Specifications of the characterizations.	98
Table 10 – Desirability configuration.....	113
Table 11 – Comparison between predicted and real characteristics.....	114
Table 12 – Comparison between predicted and real characteristics of the new optimized parameter.	118
Table 13 – The characteristics of the new optimized parameter for the three layers of the additional experiment of hatch spacing adjustment.	120
Table 14 – Tension tests results.....	132
Table 15 – Impact absorption results.....	136

LIST OF CHARTS

Chart 1 – Additive manufacturing classes.....	26
Chart 2 – Alloys elements and their functions.	49
Chart 3 – Summary of approached articles.	66
Chart 4 – Main factors of Exploratory Stage.....	71
Chart 5 – Main factors of the Modeling Stage.	76

LIST OF ABBREVIATIONS AND ACRONYMS

AM	Additive Manufacturing
PBF	Powder Bed Fusion
SLM	Selective Laser Melting
OM	Optical Microscopy
L-DED	Laser Directed Energy Deposition
LMD	Laser Metal Deposition
MMC	Metal Matrix Composite
FGM	Functionally Graded Materials
CAD	Computer-Aided Design
LB	Laser Beam
EB	Electron Beam
LC	Laser Cladding
LENS	Laser Engineered Net Shaping
BPP	Beam Parameter Product
DOE	Design of Experiments
HT	Heat-treated
AB	As-built
SS	Stainless Steel
ECA	Equivalent Circular Area
ECD	Equivalent Circular Diameter

SUMMARY

1	INTRODUCTION	25
1.1	Objectives	29
1.1.1	General Objective	29
1.1.2	Specific Objectives	29
2	LITERATURE REVIEW	30
2.1	Laser	30
2.2	Laser Directed Energy Deposition.....	31
2.2.1	Process parameters for L-DED.....	32
2.2.2	Beads and layers characteristics	34
2.3	Discontinuities	37
2.4	Bead quality and parameters selection	38
2.5	Powders for L-DED.....	44
2.5.1	Atomization processes	44
2.5.2	Particle size and morphology.....	46
2.5.3	Rheology.....	47
2.5.4	Defects in metallic powder	47
2.6	316L stainless steel processing.....	48
2.6.1	Austenitic stainless steels	50
2.6.2	Weldability of austenitic stainless steel.....	51
2.6.3	Usage of predictive diagrams	54
2.7	Austenitic stainless steel processed by L-DED	56
2.7.1	Characterization of 316L parts made by L-DED.....	58
3	METHODOLOGY	68
3.1	Exploratory Stage	70
3.2	Modeling Stage.....	75
3.3	Optimization Stage	80
3.4	Multilayer Stage.....	85
3.5	Characterization Stage.....	85

4	MATERIALS AND METHODS	86
4.1	Powder characterization.....	86
4.2	Substrate characterization.....	91
4.3	Exploratory Stage	92
4.4	Modeling Stage.....	95
4.5	Optimization Stage	97
4.6	Multilayer Stage.....	98
4.7	Characterization Stage	98
4.8	Calibrations.....	101
4.8.1	Laser power	101
4.8.2	Laser and powder spots alignment	102
4.8.3	Powder feedrate	103
5	RESULTS AND DISCUSSIONS	104
5.1	Methodology.....	104
5.1.1	Exploratory Stage	104
5.1.2	Modeling Stage.....	106
5.1.3	Optimization Stage	109
5.1.4	Multilayer Stage.....	115
5.1.5	Restraining the process boundaries	116
5.2	CHARACTERIZATION.....	121
5.2.1	Porosity.....	121
5.2.2	Microhardness profile.....	124
5.2.3	Microstructure.....	126
5.2.4	Tensile testing.....	131
5.2.5	Impact testing.....	134
5.3	First attempt of methodology application (bad succeed).....	136
6	CONCLUSIONS	139
	REFERENCES	141
	APPENDIX A – Single Beads Images	148
	APPENDIX B – Processing Parameters used in Exploratory Stage	154

APPENDIX C – Single Beads Height.....	155
APPENDIX D – Single Beads Width.....	156
APPENDIX E – Modeling Stage Parameters.....	157
APPENDIX F – Single Layers top images.....	158
APPENDIX G – Single Layers cross-sections.....	160
APPENDIX H – Single Layers Measurements.....	161
APPENDIX I – Multilayer Geometry Depositions.....	164
ATTACHMENT A – Reference material certificate.....	168
ATTACHMENT B – Particle Insight Report.....	171
ATTACHMENT C – Stress Relief Heat Treatment Report.....	174
ATTACHMENT D – Solubilization Heat Treatment Report.....	175
ATTACHMENT E – Sequence for the Deposition of Specimens.....	176
ATTACHMENT F – Porosity Report.....	179

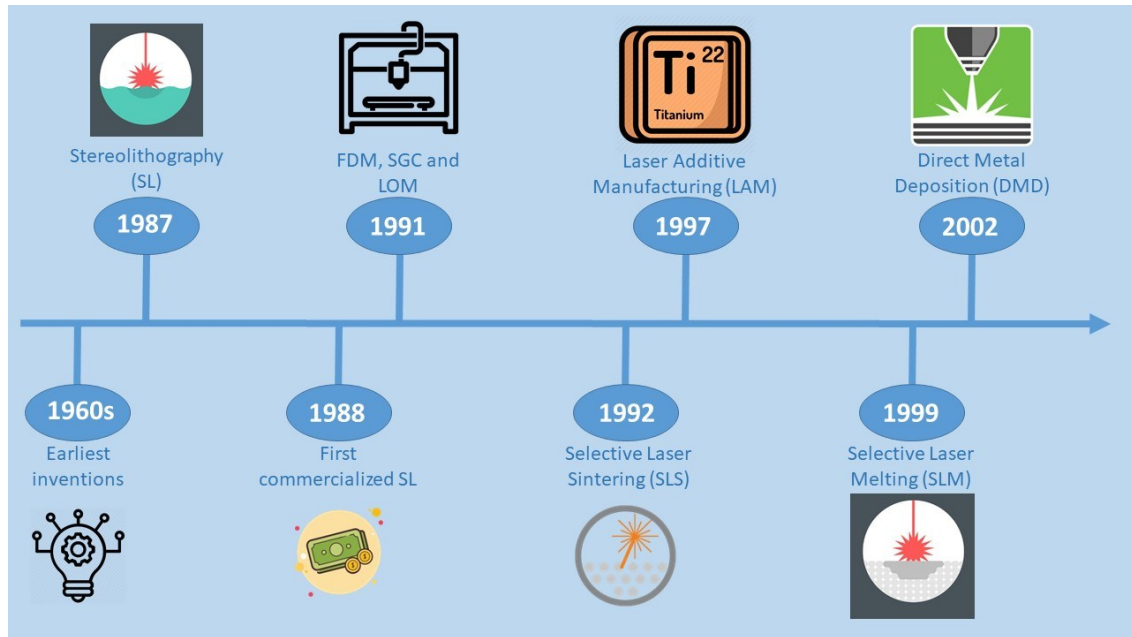
1 INTRODUCTION

Additive manufacturing (AM) is a process of joining materials to make objects from 3D model data, usually layer upon layer, as opposed to subtractive manufacturing methodologies [1]. It exhibits many advantages when compared to traditional subtractive methods and consists of produce a 3D component or part starting from a Computer Aided Design (CAD) model. The continuous model is discretized, sliced, and the part is built layer by layer [2]. This technology offers prospects to design complex geometries that can be optimized for performance gains impracticable under conventional manufacturing constraints. AM further introduces the potential to generate complex, engineered materials with composition gradients, microstructures, and properties that are impossible via traditional manufacturing techniques [3].

The first studies about AM came out around 50 years ago. However, the first commercial systems appeared just in the late 1980s. It first emerged in 1987 with stereolithography (SL), a process that solidifies thin layers of ultraviolet light-sensitive liquid polymer using a laser beam. One year later, the first SL system was commercialized. 1991 came out with three new technologies, including Fused Deposition Modeling (FDM), Solid Ground Curing (SGC), and Laminated Object Manufacturing (LOM). In 1992 DTM, now part of 3D systems, created Selective Laser Sintering (SLS), making it possible to process metallic and ceramic materials. The first titanium processing, using a high-power laser, happened in 1997 with a process called Laser Additive Manufacturing (LAM). In 1999, a partnership between Fockele & Schwarze and the Fraunhofer Institute for Laser Technology (ILT, Aachen – Germany) created one of the most relevant technologies related to AM nowadays, Selective Laser Melting (SLM). Finally, in 2002, Precision Optical Manufacturing Group began to sell its Direct Metal Deposition (DMD) machine to repair purposes [4]. The timeline representing the development of AM based on the main historic advents of the technology is exposed in Figure 1.

A large number of additive manufacturing processes are now available; they differ in the way layers are consolidated to create parts, in the process mechanism, and in the materials that can be used [5]. According to ASTM International Committee F42, additive manufacturing technologies are categorized into seven classes, as shown in Chart 1. To satisfy the demands for laser-based AM fabrication of cost-effective and end-use metallic components, two typical processes in terms of Powder Bed Fusion (PBF) and Directed Energy Deposition have been developed [6].

Figure 1 – Timeline of the evolution of Additive Manufacturing technology.



Source: Author (2019).

Chart 1 – Additive manufacturing classes.

Process	Materials	Market
Vat Photopolymerization	Photopolymers	Prototyping
Material Jetting	Polymers, Waxes	Prototyping, Casting Patterns
Binder Jetting	Polymers, Metals, Foundry Sand	Prototyping, Casting Molds, Direct Part
Material Extrusion	Polymers	Prototyping
Powder Bed Fusion	Polymers, Metals	Prototyping, Direct Part
Sheet Lamination	Paper, Metals	Prototyping, Direct Part
Directed Energy Deposition	Metals	Repair, Direct Part




















Source: Adapted from [7].

Parts produced by PBF are impressive in their capacity to elaborate structures including the thin walls, sound surface finish, fine features, and small internal channels, due to the small focused laser beam size and thin powder layer thickness [6]. Powder bed fusion generates parts by selectively fusing metallic powders with localized heat from an infrared-focused laser beam. The process is similar to stereolithography in that a thin layer is placed on a plate and a pattern is solidified on it; after which another layer is laid on top and the process is repeated until the object is built slice by slice [8]. There were significant advances over the past twenty years, including lower cost reliable industrial lasers, inexpensive high-performance computing hardware and software, and metal powder feedstock technology has

enabled it to become a state-of-the-art processing method. It has now reached a critical acceptance level, as evidenced by the rapid growth in sales of commercial systems [9]. That progress may be seen in industrial market applications, for example, medical implants, automotive, aerospace tooling, and power generation [10].

According to the ASTM F3187, the standard guide for Directed Energy Deposition (DED) of metals, DED Systems comprise multiple categories of machines using Laser Beam (LB), Electron Beam (EB), arc, or plasma energy sources [11]. The comparison between these processes is shown in Figure 2.

Figure 2 – Comparison of various Metal Additive Manufacturing Processes.

Process	Build Volume	Detail Resolution	Deposition Rate	Coupling Efficiency	Potential for Contamination
Laser Directed Energy Deposition					
Electron Beam Directed Energy Deposition					
Arc Plasma Directed Energy Deposition					
Lower					Higher
This table is intended as a general guide. Variations in individual systems and process advancements may affect the characteristics of each process.					

Source: [11].

Different countries and authors use different names for the same technology, such as Laser Metal Deposition (LMD), Directed Metal Deposition (DMD), Laser Cladding (LC), Laser Engineered Net Shaping (LENS), and Laser Directed Energy Deposition [2]. It consists of melting a metallic powder employing the thermal energy provided by a high-power laser beam. Typically, the powder is carried by inert gas and sprayed by a nozzle, with a coaxial laser beam passing through the nozzle and overlapping with the powder jet, hence generating a melted material pool on a substrate. A solid layer is obtained along the deposition track after the material solidification, and three-dimensional (3D) structures can be built by repeating the procedure over the previous layers [12]. L-DED stands out by its high productivity when compared to other laser additive manufacturing techniques, even being significantly low when

compared to arc processes. Otherwise, the main advantages of the L-DED process when compared to the arc-based processes are the higher accuracy of the final geometries [13] and the small total amount of energy introduced to the part. That way, a minimum heat-affected zone is generated and geometrical distortions caused by the successive heating and cooling cycles are reduced [14]. Another advantage is the possibility to work with Metal Matrix Composite (MMC) and Functionally Graded Materials (FGM), mixing materials during the process or changing the material in each desired layer [15, 16].

L-DED involves complicated interactions between laser beam, powder jet, substrate, and built part. The temperature changes dramatically during the deposition process, so cracks, porosities (including gas porosities and porosities caused due to incomplete fusion between deposited layers or tracks), and some other metallurgical defects easily occur. The defects usually have a dimensional range from tens to hundreds of microns and they have a strong impact on the mechanical properties of parts [17].

An approach for studying the processability of new alloys by L-DED is to compare it with the weldability of an alloy. Weldability is the capacity of an alloy to produce welds free of defects [18]. For some authors, the processability of an alloy is linked to its thermal stresses. The lower the thermal stresses generated during processing, the lower the residual stresses, and the lower the susceptibility to cracks; and, therefore, the better the processability of an alloy [19, 20]. Attallah et al. (2016) consider weldability as a processability parameter. The authors explain that AM may be described as multi-pass welding. Therefore, parts made by AM are subjected to common welding defects [21].

Considering the difficulties inherent to the L-DED process, it is reasonable to start studying an alloy with good weldability, and after that move forward with more complex alloys. A structured design of experiments is necessary to achieve the maximum potential of the building part, in terms of geometry, density, and productivity. There are many studies related to additive manufacturing using the L-DED process and stainless steel, but the majority restrict the analysis to single beads. This work aims to extend previous studies to a level where it is possible to compare results with practical applications, selecting processing parameters, building samples, and analyzing the discontinuities, in a way that it is possible to build parts predicting their mechanical behavior.

1.1 OBJECTIVES

1.1.1 General Objective

The main objective of this dissertation is to develop and apply a method for the selection of processing parameters that makes it possible to predict the geometric characteristics of depositions carried out through the L-DED process and to select an optimized parameter based on pre-established criteria. After selecting the optimized parameter, build samples using it and evaluate their mechanical and microstructural properties. Four specific objectives were stipulated to achieve the general objective, which is listed below.

1.1.2 Specific Objectives

- a) Define the most important geometric characteristics of single-layers and how to measure them.
- b) To develop a methodology for the selection of processing parameters (laser power, travel speed, federate, hatch spacing) for laser-directed energy deposition technology.
- c) Verify the functionality of the proposed method through the deposition of specimens using the selected parameter and 316L stainless steel as the filler metal.
- d) Perform mechanical (tensile test, impact absorption test, Vickers microhardness) and microstructural (optical microscopy) characterizations, checking for the presence of defects.

2 LITERATURE REVIEW

The L-DED process aims to melt filler metal (in form of powder) onto a solid substrate, using a continuous wave or pulsed laser heat source [22]. Considering that there are many laser source configurations and many laser characteristics that can directly impact the quality of the building part, the next section will introduce laser technology applied to the L-DED process.

2.1 LASER

The word “laser” is an acronym for light amplification by stimulated emission of radiation. It was first proposed by Schawlow and Townes [8]. Some important characteristics differ the lasers from regular lights. In a filament lamp, for example, the light is caused by spontaneous emission. It is radiated out in all directions and exhibits different wavelengths. In a laser, what happens is stimulated emission. Three properties define a laser:

- a) Monochromatic: all light waves have the same wavelength;
- b) Coherent: all light waves are in phase, producing a continuous laser beam;
- c) Directional: all light waves have almost the same direction.

The last property allows a laser to be guided by a long-distance and be highly focused. The power density is ten million (10^7) times higher than that on an incandescent bulb [23].

Laser are commonly classified by their media (solid-state, gas, liquid, diode) and time modes of operation (continuous-wave, pulsed-wave). Considering each media gives a different wavelength range and each time mode offers advantages and disadvantages, the selection of the best setup will depend on the process and material it will be applied [24]. For AM of metal parts, solid-state or diode continuous-wave lasers are commonly employed.

The beam quality describes how the laser beam spreads out. It spreads because the laser beam is represented by a caustic math curve, which has the narrowest part called “waist” (Figure 3). The diameter of the beam waist and the angle of divergence (angle of spread) defines the beam quality. The higher the angle of divergence and the higher the waist diameter the worse is the beam quality because it is worse to be focused [23]. According to DIN EN ISO 11145 beam quality is characterized by beam parameter product (BPP) or M^2 (diffraction factor), expressed by equations 1 and 2, respectively.

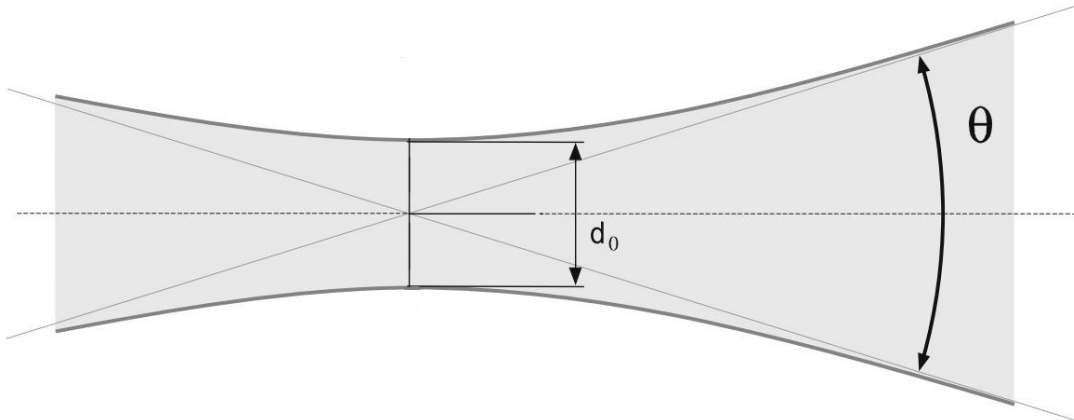
$$BPP = \frac{1}{4} d_0 \theta \quad (1)$$

$$M^2 = \text{BPP} \frac{\pi}{\lambda} \quad (2)$$

where d_0 is the beam waist, Θ is the diffraction angle and λ is the wavelength in m.

The smaller the beam parameter the higher the beam quality. For solid-state lasers, the achievable minimum is 0.3 mm·mrad. M^2 describes how much BPP deviates from the optimum, where the minimum is 1, and the closer to 1 the better quality is achieved [23].

Figure 3 – Beam waist and diffraction angle.



Source: Adapted from [23].

Knowing laser characteristics and how to classify its quality is important for a better understanding and controlling of the process linked to it, as for relating it to processing problems if necessary.

2.2 LASER DIRECTED ENERGY DEPOSITION

L-DED systems have a concentrated power source allied to a raw material flux, achieving the same spot, generally protected by an inert gas. That spot initially hits a substrate, giving birth to a melt pool. After the first layer, the material is deposited over the previous layer, building the designed part [19]. The molten pool is small when compared to arc processes, this fact, allied to the relative movement between laser and substrate, makes the solidification rate very high. The heat dissipation splits in radiation, convection, and conduction, but is mainly by conduction for the substrate, forming a strong metallurgical bond [25]. It is possible to affirm that the L-DED process has low heat input, repeated temperature

cycling, rapid heating, and rapid cooling [26]. Comparing wire and powder-based L-DED, wire provides lower resolution, higher deposition rate, and higher efficiency³ [19].

Major characteristics present in the final part are linked to thermal history. Thus, one of the biggest challenges, when working with L-DED, is to measure, monitor, control, and analyze the temperatures during the process. Grain size, phase transformation, and residual stress are directly linked to thermal history and have a direct impact on the final parts' properties, dimensional accuracy, and finishing [27].

Another important fact is that every set of equipment (L-DED machine, nozzle, laser source, powder feeder) allied to a specific set of raw material (substrate, shielding gas, powder characteristics) produces different results, even when working with the same processing parameters. Considering the previous fact, it is crucial to understand how every processing parameter works, and its impact on the final part. That is the only possible way to develop processing parameters for a specific set of equipment and alloy.

2.2.1 Process parameters for L-DED

According to ASTM 52900, process parameters are “*n-set of operating parameters and system settings used during a single build cycle*” [28]. One of the factors that make the L-DED process very complex is the high number of variables involved. To do not extend this section too much, only the most relevant ones will be described.

- a) Laser power (P): “The power of a laser is measured in Watts (and often reported in terms of nW, mW, W, etc.). This is referring to the optical power output of the laser beam, which is the continuous power output of continuous wave (CW) lasers, or the average power of a pulsed or modulated laser” [29]. As soon as the power is increased, more energy is delivered to the part, and the higher the chance of feed material has a metallurgical bond with the previous layer or substrate. However, with more energy, geometrical distortions tend to grow [22].
- b) Travel speed (v): Some authors call it “traverse rate” [30] but the correct name according to ASTM is travel speed [11]. Is the relative speed between the part and the headstock. Speed influences the amount of diluted material in the previous layer. The higher the speed the less filler metal per length, consequently, the height gets smaller. Oppositely, low speeds result in higher

³ Relation between the amount of filler metal that is used in the process with the amount that becomes a part.

height but may generate a lack of fusion. It is necessary to be careful about some factors. Very high speeds may cause a lack of fusion between layers, very slow speeds may cause high thermal input, distortions, and thermal stress. Once travel speed influences line energy (energy delivered per unit length) and amount of powder per length, it is a very important and complex processing parameter [30].

- c) Focal spot (\emptyset_f): “A location at which the beam has the most concentrated energy and the smallest cross-sectional area” [31].
- d) Spot size (\emptyset): Sometimes, if the lens necessary to achieve the desired spot size is not available, it is possible to work out of the focal spot, to achieve higher spot sizes. It may cause some problems as you move away from the focal spot, but is an option frequently used. The spot used for processing is called “spot size”, which may even be the focal spot [22].
- e) Feedrate (\dot{m}): It is the amount of powder that is delivered by the nozzle per unit of time. It is generally expressed in grams per minute [22].
- f) Carrier gas (g): “Typically inert, used to transport the powder from the deposition head to the melt pool and also in some systems to assist the transport of powder from the storage system to the deposition head” [11].
- g) Shielding gas (G): “Protective gas used to prevent or reduce atmospheric contamination” [31].
- h) Hatch spacing (D): “The lateral distance between subsequent, adjacent passes of the deposition head while depositing a layer” [11].
- i) Layer thickness (t): “Programmed distance between one layer of the deposited material and the subsequent layer” [11].
- j) Overlayer (OL): It is the percentage of the programmed thickness when compared to the single layer. Additionally, there are some combined parameters used to further explain the process behavior, which are set out below.
- k) Dilution: it can be defined as “the mass of the original substrate or previously deposited track melted, divided by the sum of the combined mass of substrate and added material melted” [22]. Its value is highly dependent on the feedrate (\dot{m}); if it is too low, it can indicate incomplete fusion or lack of metallurgical bond with the previous track; if it is too high, it can indicate excessive remelting [22].

- l) Power density (I): By definition, power density is power per unit area which is usually expressed in terms of W/cm^2 . It is calculated using output power and spot area, expressed by equation 3 [32], where “A” is the area related to spot size (\emptyset).

$$I = \frac{P}{A} \quad (3)$$

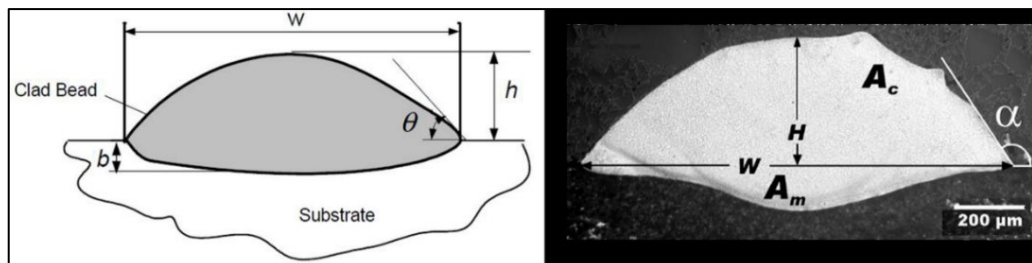
- m) Delivered energy (E): It is defined as the parameter which provides a measure of the delivered energy to the process by the laser. This energy is principally responsible for melting the substrate (or previous layer) surface and powder and can be defined by equation 4. It is expressed in terms of J/mm^2 [33].

$$E = \frac{P}{v\emptyset} \quad (4)$$

2.2.2 Beads and layers characteristics

Usually, the development of the laser processing parameters and their optimization begins with the deposition of linear tracks, commonly referred to as “single beads”. Single beads are the standard geometry often used to build complex 3D structures (whole parts). It is possible to get many different shapes of these beads by changing some variables of the process. Figure 4 (left) shows the most important dimensions/characteristics to be observed on a single bead. They are width (w), height (h), penetration (b), and wettability angle (θ). Figure 4 (right) shows both the top area (A_c) and the bottom area (A_m), which are necessary to analyze the dilution and productivity.

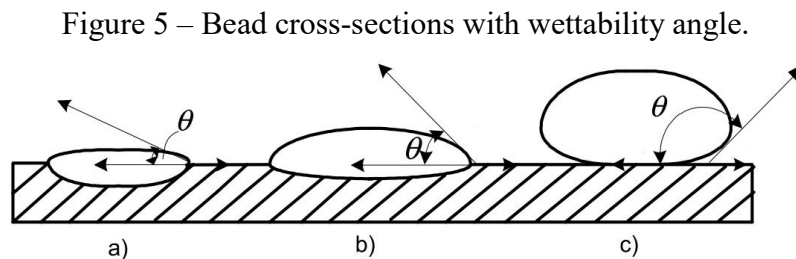
Figure 4 – Single bead dimensions and characteristics.



Source: [34] (left), [35] (right).

The most complex of these variables is the wettability angle. First of all, as seen in Figure 4, different authors consider the outside angle (α), and others consider the inside angle

(θ). Besides that, there is even a different way each author measures the angle. Some of them use a tangent line and some use dimensional relations. Anyway, the wettability angle is an important factor to be analyzed, to prevent the appearance of pores and voids. However, considering the difficulty to measure and define limits, one possible approach is to deal with them qualitatively. Additionally, one relation that is very commonly used to describe bead characteristics is the “aspect ratio” (R). It is the relation between height and width (h/w) [30] and it can be directly linked to the wettability angle as a way to analyze bead shape.

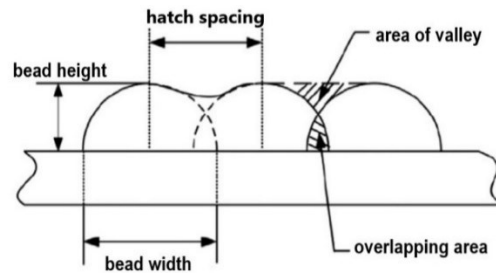


Source: Adapted from [34].

Figure 5 illustrates three situations. In the case “a” the dilution is too high, the height of the bead is low as so the wettability angle. This situation is unwanted for building parts because it will probably carry some problems like high thermal stress and geometrical distortions. It could be a good parameter for other purposes like thin cladding. Case “c”, despite the high deposition rate, has not enough dilution, which may cause a lack of metallurgical bond between layers. Additionally, the high wettability angle will probably generate pores and voids between beads. Case “b” is the ideal one, with dilution enough to cause metallurgical bond, sufficient height for good productivity, and a good wettability angle to avoid pores and voids.

The last, but not less important factor about layers is hatch spacing (D), which is associated with overlapping rate. As higher the hatch spacing, the more distant the center of one bead will be from the others, and waviness tends to be increased. On the other way, if “D” is too low, beads tend to be very tight, more energy is dispersed to the current layer, and consequently bigger is the susceptibility to voids, pores, and lack of fusion. Figure 6 is a schematic model for better understanding the impact of hatch spacing on the layer quality.

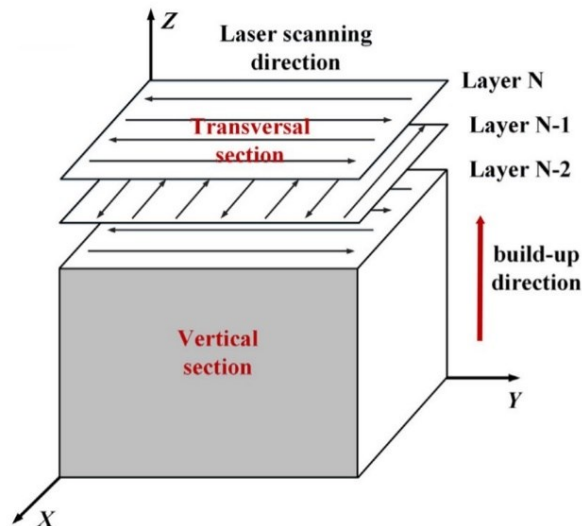
Figure 6 – Overlapping model.



Source: Adapted from [36].

Now talking about important characteristics between layers, two factors are crucial, layer thickness (setting overlayer rate) and layer orientation. Layer thickness, as previously said, is the “*programmed distance between one layer of the deposited material and the subsequent layer*”. It seems trivial but it is not so simple. First of all, it is necessary to figure out what is the height of your layer. But layer height is not necessarily (and probably will not be) the layer thickness that will be applied to the building part. If the surface of the layer is very wavy, it is possible to decrease layers thickness (for example 90% or the original thickness) to better fulfill all the voids and gaps of the surface of the previous layer. Layer orientation is the angle between the previous layer beads and the current one, as better shown in Figure 7.

Figure 7 – Layer orientation with 90 degrees variation between layers.



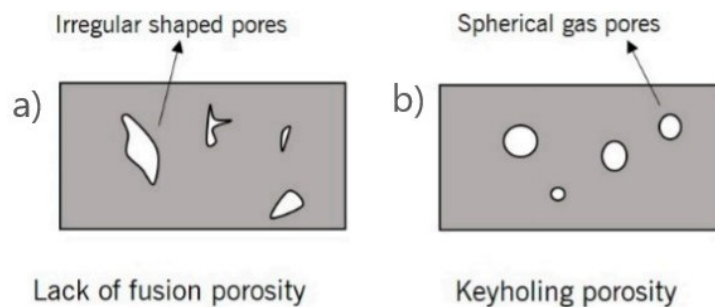
Source: Adapted from [37].

2.3 DISCONTINUITIES

According to ASTM E1316, a defect is “*one or more flaws whose aggregate size, shape, orientation, location, or properties do not meet specified acceptance criteria and are rejectable*” [38]. Standard specifications for L-DED procedures have not yet been developed. Considering that, acceptance criteria, in the form of levels of tolerable imperfections, are specified by the end-user. The most common discontinuities found in the L-DED process are described below.

- a) Lack of fusion: it is often observed when the aspect ratio of the single bead parameter is very high. One strong piece of evidence is the presence of crevices at the toes of layers. One possible way to avoid it is to decrease the relation \dot{m}/v . By doing that, it is possible to deliver more power to melt filler metal, improving the integrity of the building part and the bond between layers [30]. It is common to misunderstand the source of pores and voids present in the part. Figure 8 helps to understand the porosity’s shape.

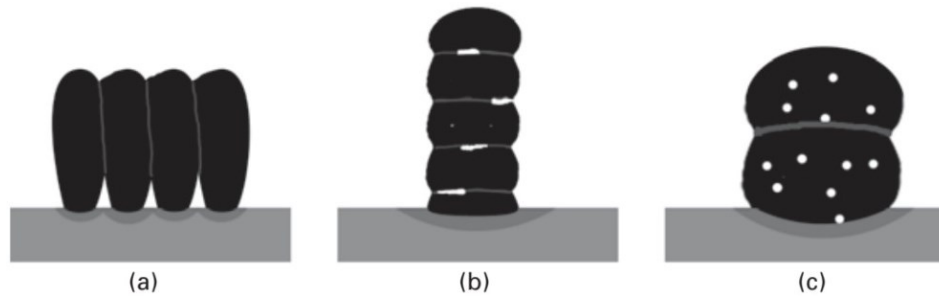
Figure 8 – Schematic of (a) lack of fusion (interlayer porosity) and (b) keyholing porosity (intralayer porosity).



Source: Adapted from [19].

- b) Porosity: Pores and void formation present in the L-DED process can be divided into three categories: inter-track, inter-layer, and intra-layer. Inter-track porosity Figure 9-a) occurs near the base of deposited tracks and is caused by high aspect ratios. Inter-layer porosity Figure 9-b) is caused by incomplete bonding between layers. Intra-layer porosity Figure 9-c) is often spherical and is located inside the bead. It may be caused by trapped gas, carrier, or protection gas; or gases vaporized from filler metal (small particles or low boiling point elements) [22].

Figure 9 – Possible types of porosity.



Source: [22].

- c) **Cracking:** One factor that is very important in crack behavior study is the chemical composition and phase distribution of the material. In austenitic stainless steel processed by L-DED for example, it was observed solidification cracks originated from a thin film rich in sulfur, phosphorous, and silicon present in interdendritic regions [39]. Additionally, the L-DED process has as one of its characteristics high thermal gradients during cooling. It generates thermal stress into the part, which may cause cracks. Preheating the substrate is one way to reduce it [30].
- d) **Residual stress and distortion:** complex residual stress fields are caused by thermal expansion and contraction due to transient thermal gradients as the material cools and heats track by track. That stress may affect tensile and fatigue properties. It also may vary along the building part, according to geometry, material composition, or just because heating related to processing time. There are some ways to minimize thermal stress like set dwell time between layers, reduce thermal input, use a pulsed laser beam, and controlling melt pool size. High thermal stress may even cause distortions, that may disable the part or be corrected in post-processing [22], [30].

2.4 BEAD QUALITY AND PARAMETERS SELECTION

One of the biggest issues found in the L-DED process is the single bead's quality evaluation. That evaluation is generally based on a qualitative analysis, which can generate different selected parameters, depending on the person who is doing the analysis, even using the same criteria. Considering the previous fact, this section aims to summarize previous

studies related to bead quality criteria and parameter selection for the L-DED process. Additionally, it aims to define standard criteria to select the parameters that will be analyzed in this study.

a) Processing Parameter DOE for 316L using Directed Energy Deposition

Sciammarella and Najafabadi [40] created evaluation criteria to analyze single beads for L-DED. It was deposited 90 single beads using stainless steel AISI 316L for feed material, constant power of 645W, and changing travel speed and feedrate. The following criteria were set:

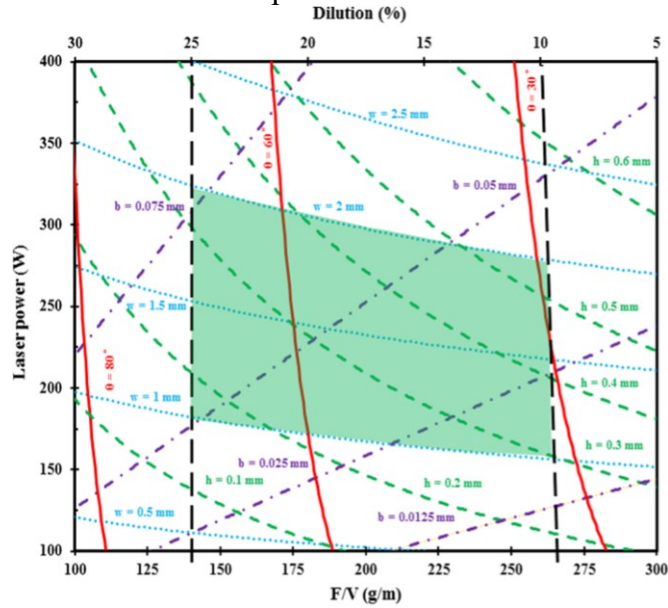
- Wettability angle not higher than 110° ;
- Vickers hardness higher than 220HV;
- Subgrains refined in the order of 2-5 μm ;
- Less than 1,1% of porosity.

After the best beads had been chosen, it was seen that they had linear mass density (\dot{m}/v) between 0,011 and 0,013 g/mm. It was also observed that the normalized equivalent energy density [41] varies between 3 and 4, which is inside the limits considered good [40].

b) An empirical-statistical model for laser cladding of Ti-6Al-4V powder on Ti-6Al-4V substrate

Nabhani et al. [42] purposes to investigate the influence of processing parameters on the geometry of single beads using Ti-6Al-4V, and develop a processing map. It is recommended by the author to keep the dilution between 5% and 10%. However, it is common that dilution decreases on the overlapping, due to refusion. Considering that, it is recommended to keep dilution between 15% and 25% on the single bead phase. The wettability angle should be between 30 and 80 degrees [42]. The map was disposed of a relation between power and \dot{m}/v (the author uses F for feedrate and V for travel speed), as shown in Figure 10, where “w” is width, “h” is height, “b” is penetration and “ Θ ” is wettability angle.

Figure 10 – Processing map for Ti-6Al-4V alloy on the same substrate in terms of P vs. F/V representation.

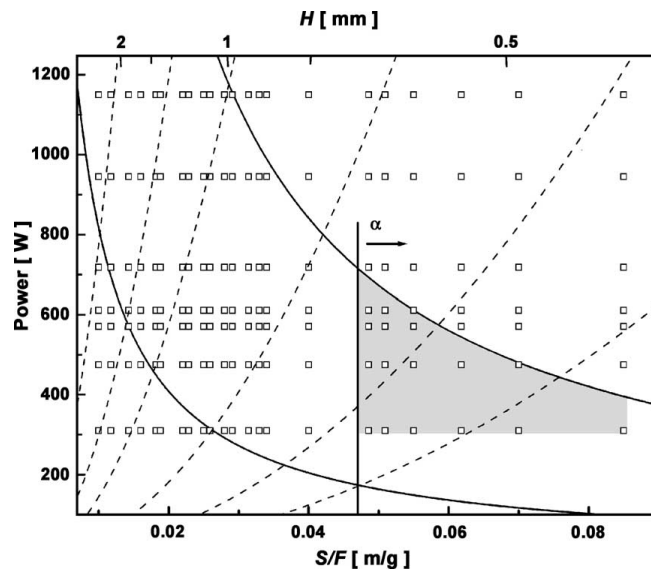


Source: [42].

c) Analysis of coaxial laser cladding processing conditions

A similar study was developed by De Oliveira et al. [43] using a Ni-Cr alloy. In this case, 25 single beads were deposited. The criteria were to keep dilution between 10% and 30%, and wettability angle higher than 100°. Figure 11 shows the processing window for P vs. v/m (F for feedrate and S for travel speed) representation. Points correspond to analyzed

Figure 11 – Processing window.



Source: [43].

single beads cross-sections. The vertical solid line determines the clad angle condition required for continuous coating; two solid hyperbolas terminate an area of allowed dilution and the grey area shows the window, where an optimal clad layer can be formed. Dashed curves are isolines with denoted values of the clad area [43].

d) Systematic evaluation of process parameter maps for laser cladding and directed energy deposition

Bax et al. [44] purposes guidelines to evaluate processing maps for Inconel 718 single beads. The parameters considered to do the evaluation were deposition rate and a geometric dimensionless factor " w^2/A_{ab} " (where "w" is the width and " A_{ab} " is the area above the substrate line). 100 single beads were deposited, varying power (800, 1200, 1600, 2000, 2400 W), travel speed (250, 500, 1000, 2000 mm/min), and feedrate (5, 10, 15, 20, 25 g/min). The laser beam profile used was a 3 mm diameter tophat. The selection criteria were dilution between 10% and 30% and dimensionless factor higher than 3,5 (author considers to be the limit to obtain a lack of porosity in overlappings higher than 50%). It has been concluded that the method is precise enough to detect statistical anomalies when correlating geometrical characteristics of the samples with combined parameters. This work focuses on the optimization of single beads and does not extend the results to single layers or building parts [44].

e) Effect of laser energy density on defects behavior of direct laser depositing 24CrNiMo alloy steel

In this study, Cao et al. [45] analyzed the influence of delivered energy (E) on dilution, porosity, and cracks, on a 24CrMoNi alloy. The values of "E" varied between 80 and 120 J/mm^2 . It was concluded that with the accumulation of the deposition layers, the thermal effect was also continuously accumulating. The dilution highly increased from 90 to 100 J/mm^2 , after that value, the increase normalizes again. The inclusion of defects was higher in the overlapping zone. It is believed that it is caused by the amount of energy at the boundaries of the heat source, which is lower than at the center, causing a lack of fusion. It was observed that the best bead had dilution of 46,2%, density of 99,25%, cracks rate of 13,2%; all of that with delivered energy of 100 J/mm^2 [45].

f) Processing window development for laser cladding of zirconium on zirconium alloy

Harooni et al. [46] used feedrate, dilution, presence of defects, and circularity to evaluate the quality of the single beads of zirconium. The circularity is calculated by the following equation:

$$Circularity = \frac{4\pi(A_c + A_m)}{perimeter^2} \quad (5)$$

where “ A_c ” is the top area and “ A_m ” is the bottom area.

The author figured out that by decreasing travel speed the geometrical symmetry was improved. The ideal parameter set found had a dilution of 50%, a circularity of 0,51, and a feedrate of 0,80 g/min [46].

In this specific case, the circularity was an important factor to be careful, due to the difficulty inherent to the processing material, and the high number of bad shapes found.

g) State of the Art in Directed Energy Deposition: from Additive Manufacturing to Materials Design

Dass and Moridi [47] made a review about L-DED that approaches, between many other characteristics inherent to the process, what is considered good for many authors. Most of them use dilution as criteria, and also suggest working between 10% and 30%. However, there are different values applied to different alloys, as shown in Table 1. Another approach, shown in

Figure 12, exhibits the processing window for different materials as a function of feedrate and linear heat input [19].

Analyzing the previous studies, it was observed that many authors used dilution as a criterion for selecting parameters. It was due to the fact that most studies were related to cladding, and not to multilayer deposition. It is not wrong, once it says a lot about the bead characteristics. Otherwise, it is necessary to be careful because the dilution of the single bead is not the same in the single-layer [42].

Another approach is the use of the wettability angle and the presence of defects. The wettability angle gives a good feeling about the possible presence of pores and voids, but it is not easy to measure it efficiently. The presence of defects (cracks and voids) has also an issue; the defects observed in the single bead will not necessarily be repeated in a building part, once the thermal cycle is different. Considering that, it is important to evaluate discontinuities, but

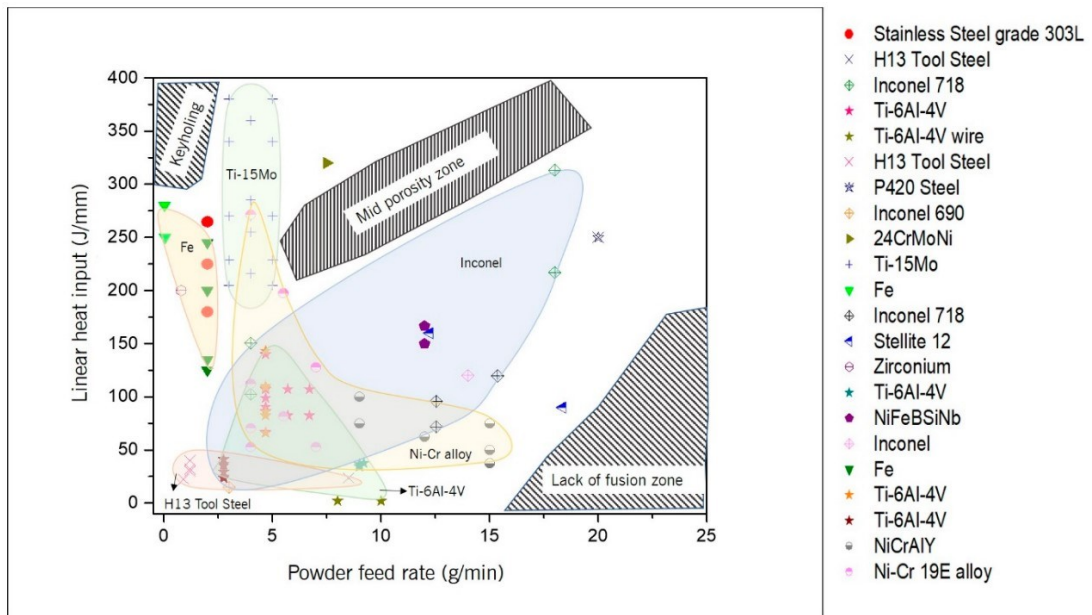
it is necessary to be careful to not exclude parameters with discontinuities in single beads, once they may be a good parameter for single layer or multiple layers.

Table 1 – Optimal dilution range for different materials.

Material System	Optimal Dilution Range or Optimal Process Parameters or Acceptable Range Values as Reported
Stainless steel grade 303L	–
H13 tool steel	Optimal, generally low dilution preferred
Inconel 718 in steel substrate	–
Ti-6Al-4V	Within 10%–30%
Ti-6Al-4V	–
H13 tool steel	–
P420 steel on low carbon steel	12%–20%; optimal is 16%
Inconel 690 on Inconel 600	Optimal
24CrMoNi alloy steel	32%
Ti-15Mo	54%–68%
Fe	10%–20%
Inconel 718 on AISI 1045 carbon steel	–
Stellite® 12 (Cr-W based alloy) on 0.2% C steel	–
Zirconium on Zr alloy	50%
Ti-6Al-4V	48%–52%
NiFeBSiNb on mild steel	Above 10%
Inconel	Optimal
Fe	–
Ti-6Al-4V	Within 10% to 30%
Ti-6Al-4V	Zero porosity data; optimal
NiCrAlY on Inconel 738 superalloy	15%–25%
Ni-Cr based alloy (commercially known as 19E alloy)	5%–30%

Source: Adapted from [19].

Figure 12 – Processing window for different materials.



Source: [19].

Fewer articles use geometrical parameters, none of them talked about surface finishing, and most of them were restricted to single beads analysis. Considering all the facts previously discussed, it was considered necessary to create a new and more complete method to analyze and select parameters for L-DED processing, extending the analysis to multiple layers.

2.5 POWDERS FOR L-DED

Besides control processing parameters, another important factor that directly impacts the quality of parts made by L-DED is the quality of the metallic powder used as raw material. The powder as raw material was largely studied in the last decades. Even so, the requirements necessary for metallic powder used for L-DED are usually different for each equipment setup, demanding higher control for particle size, shape, and chemical composition. Otherwise, the quality and repeatability of the process may be harmed [9]. The characteristics of the particulate material are highly linked to its manufacturing route, including atomization, sieving, and storing [9, 48, 49]. It is necessary then, deeply know the powder that will be used as raw material, to better control and understand the manufacturing process, allowing to prevent or correct problems and defects [48]. Once known the importance of metallic powder features, this section will describe them, and will also show the most relevant techniques to characterize them.

2.5.1 Atomization processes

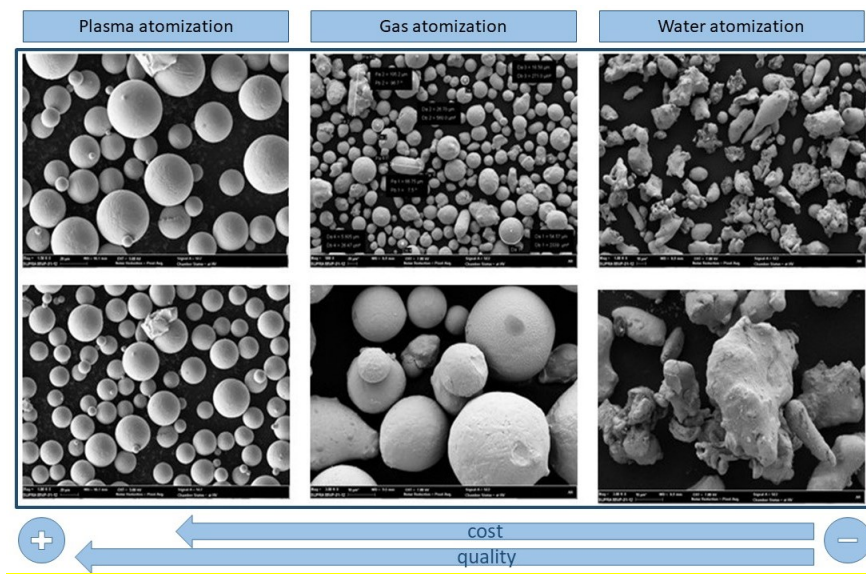
Among many techniques present in the market of producing metallic powder, atomized is the most commonly used in the L-DED process, due to its higher shape quality when compared to the other ones. Atomization processes may be split into water, gas, and plasma atomization [9, 48, 49].

The water atomization process uses water jets symmetrically positioned around a liquid metal jet to cool it down, forming the metal particles. The next step is to take these particles to dry, removing any liquid that may be present in the powder. This technique generates irregularly shaped particles, which affects the flow and packing properties. Another issue linked to water atomization is that it can't be used with alloys that are sensible to corrosion and oxidation, because of its contact with water. The previous facts make this

technique not ideal for additive manufacturing. Even so, it is often used due to its low production cost [48, 49].

The gas atomization process is similar to water atomization. The main difference is that now the metal is cooled by an inert gas jet. In that process, the control over all the variables of the process is significantly higher than in the previous one. For example, it may be used a VIM (vacuum induction melting) to melt the metal before the atomization, which decreases the presence of interstitial elements. This is the most common kind of powder used in AM [49].

Figure 13 – Particle morphology for each atomization process.

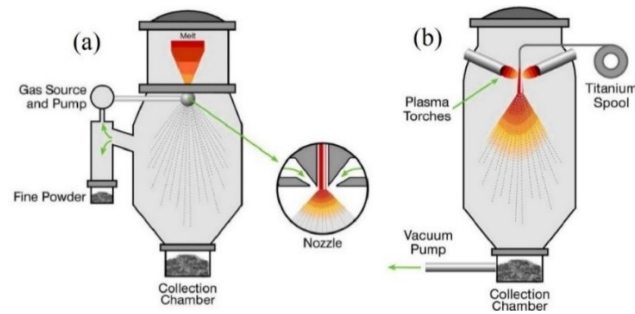


Source: Adapted from [50].

It is possible to see in Figure 13 different particle shapes for each atomization process. As soon the quality is increased the production costs increase also.

The plasma atomization process allows obtaining particles with a higher degree of spheroidicity. The powder produced is fully dense (different than water and gas atomization) and the surface contamination is significantly reduced through the vaporization of impurities. In this case, the atomizer needs to be fed with powder or wire. During this process, the material is fed in a solid-state, after that it is hit by plasma and high-pressure inert gas, making the material melt and atomize simultaneously. Figure 14 represents a scheme of gas and plasma atomization processes.

Figure 14 – Gas (a) and plasma (b) atomization processes.



Source: [51].

2.5.2 Particle size and morphology

Particle size and particle morphology are two of the main characteristics of a metallic powder for AM. Each process and equipment setup demands different particle size distribution. For example, low-size particles (around 15-50 μm) are better for selective laser melting, once this process needs higher resolution and works with lower power levels when compared to L-DED. Higher particle sizes (around 50-160 μm) are often used for L-DED, once it works with higher power levels, sufficient to fuse the particles, prioritizes productivity instead of the resolution, and low size particles may cause clogging in many L-DED headstocks. A metallic powder size is defined by its distribution, or Particle Size Distribution (PSD), which is the range of values where all of that powder is included. The PSD is a statistical analysis, made by a sample, and may be defined by its maximum, minimum particle size, and average, among other statistical parameters. The PSD is expressed by frequency distribution. There are many techniques to define PSD like optical microscopy, FEG-SEM, dynamical image analysis, laser diffraction, etc. Except for the last one, the same analysis may be used to define morphology [52–54].

Morphology is not allied to size, but just the shape of a particle. It may be done by comparing the shape of the particle with a circle, ellipse, or rectangle, or may even be done just in a qualitative way, depending on the technique applied. Another important factor is the presence of satellite particles. Satellite particles are very small particles attached to the bigger ones or dispersed on the powder. They are very common to be observed on gas atomized powders. These satellite formations decrease the quality of powders such as reduce free-flow ability and compaction, which may directly imply defects in the final part [48, 49, 55].

2.5.3 Rheology

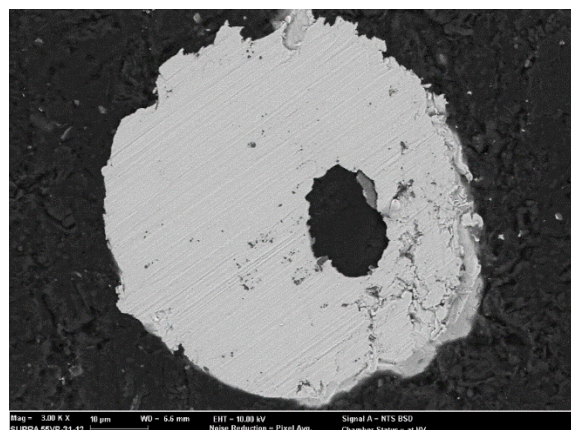
Rheology is, briefly, the science of deformation and flow. Rheological properties of a material are noted when a force is exerted on it, and as a result of which it deforms or flows. The extent to which a material deforms under a certain force depends strongly on its properties [56]. The techniques used to characterize the rheology of material have two basic approaches: static and dynamic. Considering that it is very hard to correlate static and dynamic properties, it is necessary to choose the correct characterization technique which is closer to real conditions where that material will be applied [57]. The main techniques used to analyze rheology are the Hall flowmeter, Carney flowmeter, and angle of repose.

2.5.4 Defects in metallic powder

Some defects may be observed in powders used for additive manufacturing, which may carry significant impacts on the final part. The most important of these defects are satellite particles and pores, both highly dependent on the atomization process. Satellite particles may impact the flow causing clogging and flow variations, and may even cause alteration in the interaction between particles and the laser beam [55].

On the other hand, the impact of the presence of pores inside the particles has a direct impact on the final part. They are directly carried to the part and may be distinguished by their size and shape. The pores inside the particles may be observed by embedding the powder in bakelite, sanding, and polishing, and after that making an optical microscope analysis [49], [58]. In Figure 15 it is possible to observe a pore inside a 316L metallic powder.

Figure 15 – Presence of a pore inside a metallic particle.



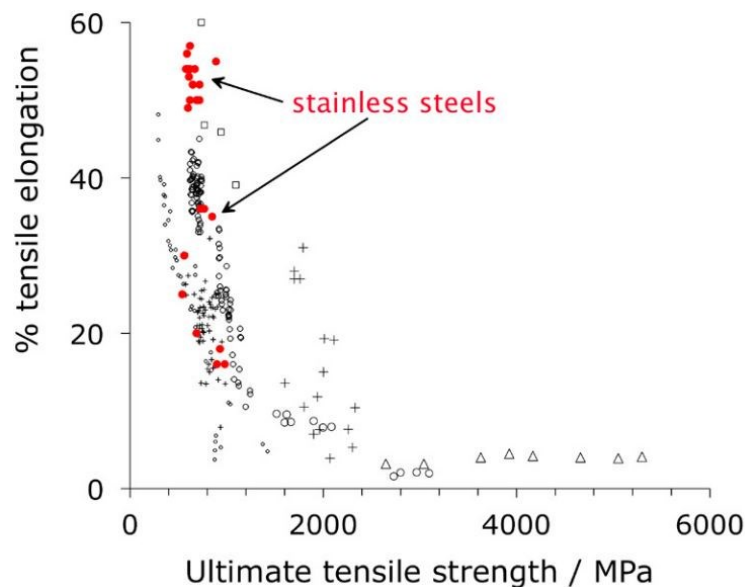
Source: Author (2019).

2.6 316L STAINLESS STEEL PROCESSING

Stainless steels are iron (Fe), carbon (C), and chromium (Cr) alloys with a minimum of 10.50% Cr. Other metallic elements also integrate these alloys, but Cr is considered the most important element because it gives stainless steels a high corrosion resistance [59]. This amount of chromium is important in forming a passive chromium oxide-rich film that protects the surface from corrosion [60]. The term "passive" means that the reaction of the metal with the surroundings, for example, an oxygen atmosphere, forms a uniform protective surface that suppresses other reactions. If the film is damaged, the chrome present in the steel reacts again to rebuild the damaged protective layer. This reaction occurs in a matter of seconds [61]. Some stainless steels are often used at elevated temperatures and in harsh environments as they resist oxidation and maintain their mechanical integrity under these conditions; the upper-temperature limit in an oxidizing atmosphere is approximately 1000 °C [62].

In general, stainless steels are alloyed by several other elements that make them resistant in various environments. These elements also modify the alloy microstructure, which in turn has a distinct influence on its mechanical and weldability properties [63]. In terms of mechanical strength and ductility, the various types of stainless steels follow the same general trend as low alloy steels, as shown in Figure 16.

Figure 16 – Relation between tensile stress and elongation of commercial stainless steel compared to low alloy steels.



Source: [61].

There are several configurations regarding the chemical composition of stainless steel. It is important to know the function of each alloying element to understand and predict the behavior of these materials through various applications and processing techniques. Chart 2 describes the functions and effects of each alloying element.

Stainless steels may be classified into five groups:

- a) Austenitic stainless steels (SS) containing 12-27% chromium and 7-25% nickel.
- b) Ferritic SS containing 12-30% chromium with a carbon content of less than 0.1%.
- c) Martensitic SS, which has a chromium content between 12 and 18% with 0.15-0.30% carbon.
- d) Austenitic ferritic (Duplex) steels containing 18-25% chromium, 3-5% nickel, and up to 3% molybdenum.

Martensitic-austenitic steels, which have 13-16% chromium, 5-6% nickel, and 1-2% molybdenum.

The 316L fits into the group of austenitic stainless steel.

Chart 2 – Alloying elements and their functions.

Carbon (C)	- Austenite former. - Added to some high-strength alloys to increase hardness and strength.
Manganese (Mn)	- Austenite former.
Silicon (Si)	- Ferrite former. - Increases corrosion resistance of austenitic steels. - It improves resistance to high temperatures and carbonization.
Chrome (Cr)	- Ferrite former. - Increases corrosion resistance. - 12% minimum for chrome passivation.
Nickel (Ni)	- Austenite former. - It gives resistance to low temperatures. - Increases corrosion resistance against not oxidant liquids. - Added in small amounts to chromium can improve mechanical properties.
Molybdenum (Mo)	- Ferrite former. - Improves resistance to high temperatures and deformation. - Increases corrosion resistance in not oxidant environments.
Copper (Cu)	- Increases corrosion resistance.
Niobium (Nb)	- Carbide former used to stabilize austenitic stainless steels against harmful chromium carbide precipitation at 480-820 ° C. - Ferrite former. - Added to some alloys that require high mechanical strength and hardness.

Titanium (Ti)	- Carbide former used to stabilize austenitic stainless steels against harmful chromium carbide precipitation at 480-820 ° C. - Ferrite former. - Added to some alloys that require high mechanical strength and hardness.
Cobalt (Co)	- It generates creep resistance at high temperatures.
Tungsten (W)	- Improves mechanical resistance to high temperatures and resistance to deformation.
Nitrogen (N)	- Strong austenite former. - Used to minimize chromium grains formed at high temperatures.

Source: [63].

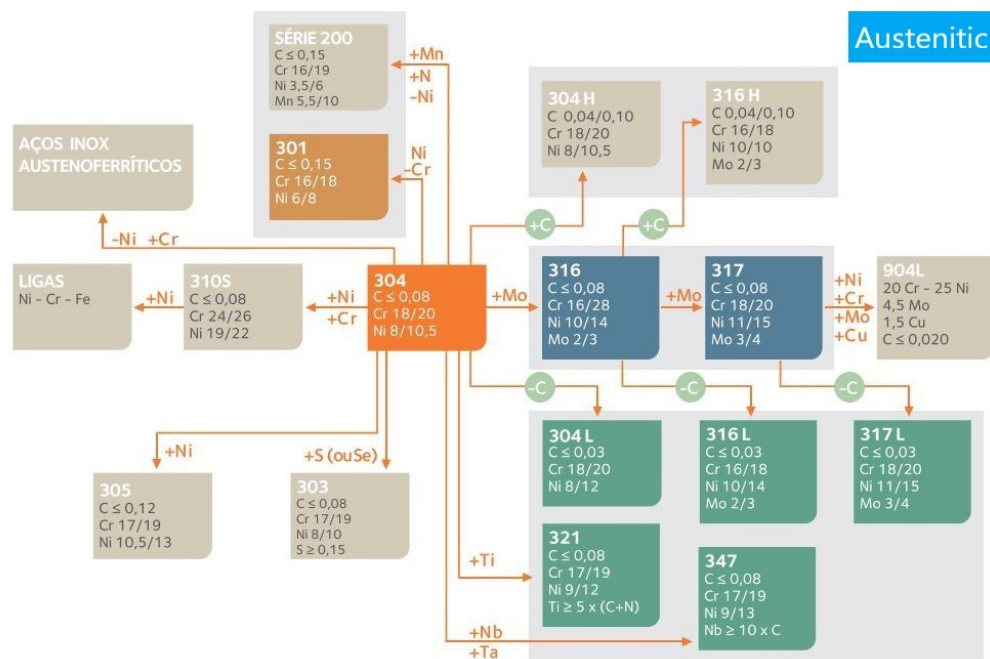
2.6.1 Austenitic stainless steels

Austenitic stainless steels are the most resistant to corrosion due to their high chromium content but also to nickel additions. Both, martensitic and ferritic stainless steel, are magnetic, whereas austenitic stainless steels are not [63]. The most common kind is called 18-8 containing about 18 wt% Cr and 8 wt% Ni. It has the smallest amount of nickel concomitant with a fully austenitic structure. They have a wide application due to their excellent resistance to corrosive environments. These characteristics are improved as nickel content is increased. as chromium content is increased, it improves resistance to intergranular corrosion [61].

The mechanical strength of austenitic stainless steel is very similar to medium carbon steel. The typical yield stress range is between 200 and 275 MPa. Stretching is around 40% and 60%. The 310 Series, which contains higher chrome and carbon contents, is suitable for higher working temperatures. The 316 class, which contains molybdenum, has better resistance in marine environments [60]. The addition of Mo (between 2% and 4%) substantially improves pitting corrosion resistance, which can be defined as local penetrations in passive films, occurring mainly in chloride solutions [61]. When working submerged, AISI 316 is recommended for waters containing up to 800 ppm chloride. If the amount is higher (or even lower but with higher temperature, or the medium has acidic characteristics), larger additions of molybdenum are needed, as is the case with 317 steel. 316 is slightly better than 304 in stress corrosion (corrosion that usually involves three factors: aggressive medium, temperature, and stress, whether applied or residual from the manufacturing process). But the advantages of 316 over 304 in this form of corrosion are very limited. Stress corrosion is known as the Achilles heel of austenitic stainless steel. A large increase in nickel content decreases the risk of stress corrosion. It is very important to note that ferritic stainless steels

are immune to this form of corrosion [59]. Corrosion along the grain boundary may be a very serious problem, especially when a high-temperature process is employed, such as welding processes, allowing precipitation of $M_{23}C_6$ in these regions. This type of corrosion is known as weld decay. To combat this effect, the amount of carbon present in steels is reduced to values below 0.03 wt%, forming the class L, such as 304L and 316L [61]. Figure 17 shows 300 series stainless steels, which includes the austenitics.

Figure 17 – 300 series stainless steel.

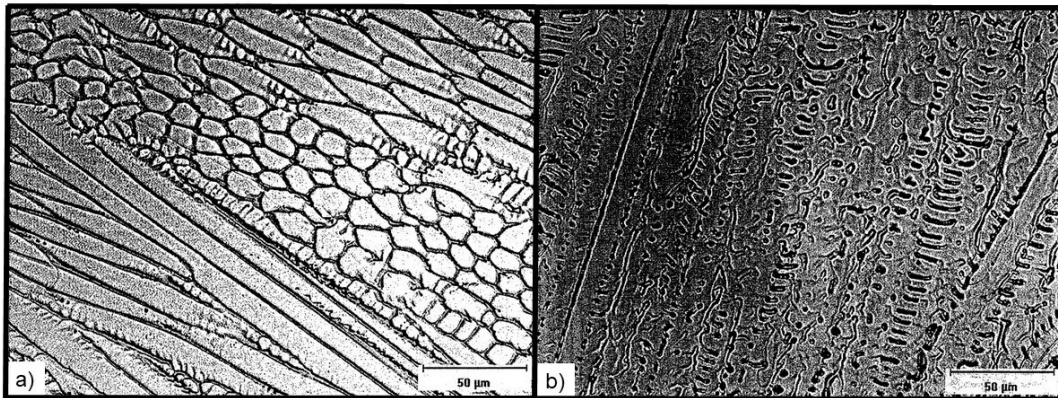


Source: [59].

2.6.2 Weldability of austenitic stainless steel

AM can be described as multipass welding. Therefore, components manufactured by additive manufacturing are subjected to common welding defects. Thus, the capacity of an alloy to be processable by AM can also be estimated from its weldability. As austenitic steels are not brittle and have low yield strength, the level of residual welding stresses is often low and the risk of cracking is much lower than in hard and brittle materials. Also during working conditions (with external stresses acting) the material as a weld deforms and relieves the internal stress. It should only be remembered that as these steels are "high alloyed", their relief only occurs at very high temperatures, and usually, when the relief is required, the material solubilization temperature is used [64]. Figure 18 shows the microstructure of a fully austenitic and an austenitic-ferritic solidification after a welding process.

Figure 18 – Fusion zone microstructure of a fully austenitic (a) and an austenitic-ferritic (b) solidification after an arc-based welding process.



Source: [18].

The main defects observed in both welding and AM processes are porosity and hot cracking. In general, austenitic steels are not susceptible to cold cracking because they dissolve hydrogen and do not harden on cooling [64].

Porosity may occur in three ways. First, as a result of chemical reactions in the melt pool, such as if a steel melt pool is improperly deoxidized, the iron oxides may react with the carbon present to release carbon monoxide (CO). Second, by the expulsion of solution gas as the weld solidifies, which happens in aluminum alloys welding, when hydrogen from moisture is absorbed into the puddle and later released. Third, by trapping protection gases at the base of turbulent fusion pools [64].

Most steels can be welded with a weld metal of similar composition to the base metal. Many high alloy steel and most non-ferrous alloys require electrodes or add metal different than the base metal because they have a higher solidification temperature range than other alloys. It makes these alloys more susceptible to solidification or hot cracking, which can be avoided by choosing special consumables that provide the addition of elements that reduce the solidification temperature range. Hot cracking is also strongly influenced by the direction of grain solidification in the weld. When opposite-sided grains grow together columnar, impurities and low melting constituents can be pushed on the solidification front to form a weak line in the center of the weld. Welds in low carbon steels that may contain high sulfur may behave this way, it implies that cracking can occur in the center of the weld. Even at normal sulfur levels, there may still be a weak line in the center of the weld that can break under welding deformations, so very deep penetration cords are usually avoided [65]. Solidification cracks can be a big problem with austenitic stainless steel. Crack susceptibility

is primarily a function of chemical composition and materials having purely austenitic solidification are more susceptible to that. Those materials that solidify in ferrite-austenite form tend to be very resistant to solidification cracks [18]. Austenitic steels, when welded with similar material (austenitic consumable) are very susceptible to hot cracking, which occurs due to the low solubility of impurities in the austenitic structure. These impurities remain in grain boundaries and have a lower melting point, creating an easily opening liquid film. Coarse-grained materials (eg castings) are those with higher susceptibility, since the area where the impurities are concentrated is smaller, and consequently, the accumulation is greater. To minimize hot cracking, solder is usually made with a consumable that is not completely austenitic but rather austenitic-ferritic, where the biphasic structure decreases the concentration of impurities and reduces the risk of cracking.

As steels that are used in special applications, one of the main problems with stainless steels, usually undetectable during welding, is related to the loss of specific corrosion resistance properties, such as heat or wear resistance properties.

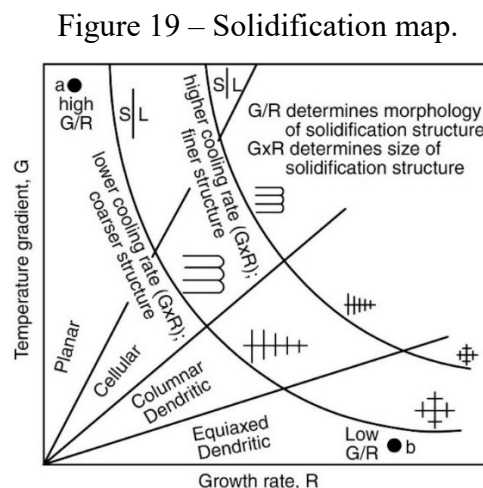
- a) Loss of corrosion resistance: As the corrosion resistance of stainless steel is related to the formation of a protective oxide film, guaranteed by a minimum chromium content, if there is any transformation that reduces the chromium content in a solid solution for a given region of the steel, this region no longer forms the protective oxide and is susceptible to corrosion. This can happen whenever some element combines with chromium, usually, carbon forming carbides, and sometimes nitrogen forming nitrides. The temperature range of chromium carbide formation, known as sensitization, is between 400 °C and 800 °C. During welding, the region that spends the most time within this range is situated a little apart from the weld. When the cooling of the welded joint is slow, there is a possibility of carbide formation, which precipitates in grain contours and steals the chromium from the steel, causing the adjacent regions to become impoverished and, when placed in aqueous media, to undergo a corrosive process, known as intergranular corrosion [18, 64, 66].
- b) Loss of wear resistance: Hadfield austenitic steels (austenitic manganese-steels) have good wear resistance due to strain-hardening and strong hardening of austenite when subjected to wear. This means that the material is normally put to work in the "soft" state, and when it is working (in wear), its surface hardens for strain over the surface, becoming increasingly resistant. The main problem in this type of material is also the formation of precipitates,

which can destabilize austenite and favor the formation of martensite, with consequent localized embrittlement and detachment during wear service. Likewise, slow cooling should be avoided for Hadfield austenitic steels [64].

- c) Loss of heat resistance: Materials that suffer a loss of heat resistance typically work in less corrosive media (gaseous and non-aqueous) and the carbon content of steel is often high to ensure creep resistance. Undoubtedly, if the carbon content of the steel is high and it still works hot, it is basically impossible to avoid carbide formation. But that does not mean that the material will suffer intergranular corrosion, as these materials also have high chromium, and even suffering from it, precipitation still leaves a lot of chrome in solution to ensure its passivity. But even so, low heat input techniques should also be employed to ensure minor changes [18, 64, 66].

2.6.3 Usage of predictive diagrams

Aiming to help on predicting the characteristics of metal components after processed, a sort of predictive diagrams was developed. The most generic of those which will be shown next is a solidification map, showing the effect of the temperature gradient (expressed in Figure 19 by “G”) and growth rate (expressed in Figure 19 by “R”) on the morphology and size of the solidification microstructure.

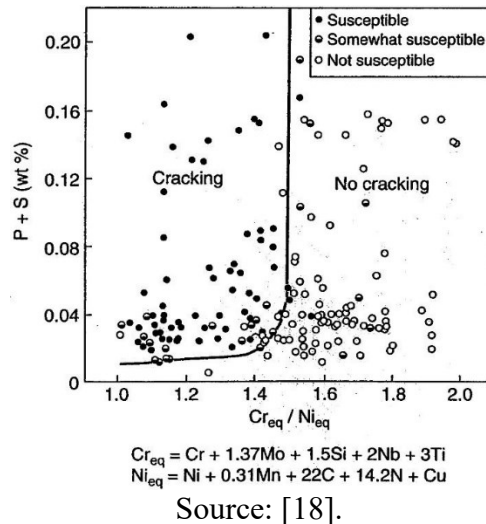


Source: [67].

Some diagrams have been developed to predict crack susceptibility based on chemical composition. One of the first, introduced in the 1980s, was developed by Kujampää

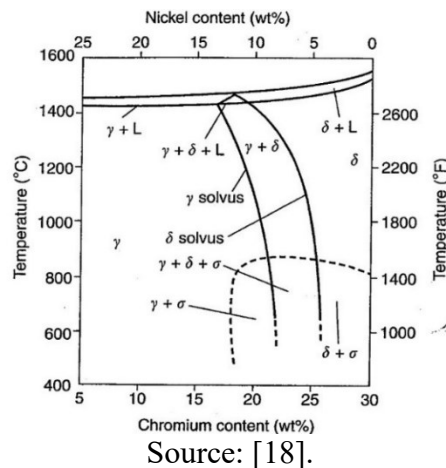
and Suutala, usually referenced by the Suutala diagram. This diagram, shown in Figure 20, was developed through the analysis of a large number of published articles, which addressed the presence of cracks in welds made of austenitic stainless steel. In this case, susceptibility to cracking is demonstrated as a function of chemical composition, P + S as a function of the relationship between chromium and nickel equivalent [18].

Figure 20 – Suutala diagram.



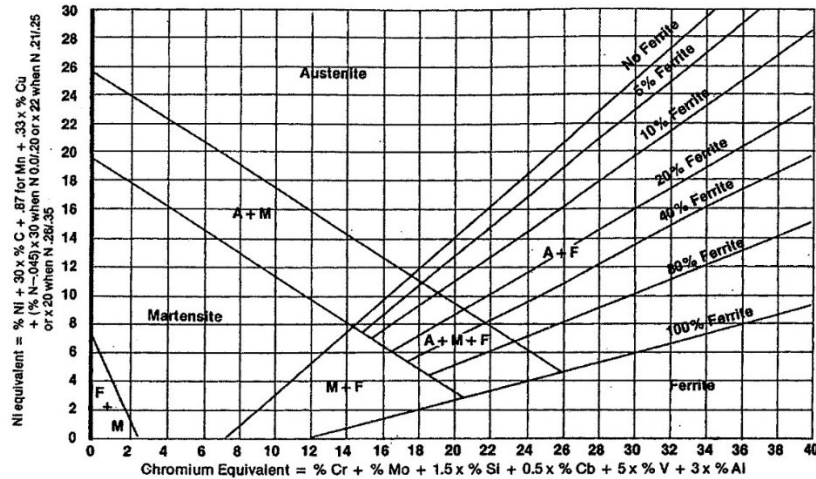
Austenitic stainless steels are formulated in such a way that they have a mostly austenitic structure. Depending on the fraction of austenitizing or ferritizing elements, the matrix can be completely austenitic or partially ferritic. The pseudobinary diagrams help to predict the fractions of the ferritic and austenitic matrix based on the chromium and nickel fraction of an alloy, disregarding other elements. Figure 21 is an example of a pseudobinary diagram for 70% iron.

Figure 21 – Pseudobinary section of the Fe-Cr-Ni system at 70% iron.



Additionally, there is the Schaeffler Diagram, exposed in Figure 22. This is the most accepted diagram for the prediction of the final microstructure of stainless. When using 316L it is commonly employed to estimate the δ -ferrite content in the final microstructure.

Figure 22 – Schaeffler diagram.



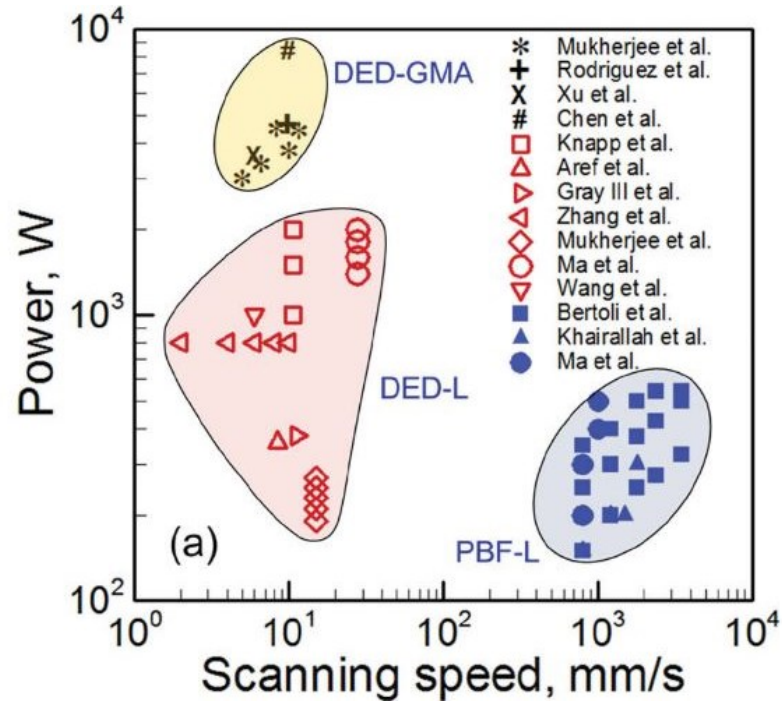
Source: [18].

2.7 AUSTENITIC STAINLESS STEEL PROCESSED BY L-DED

Initially, the L-DED deposition process can be compared with other additive manufacturing techniques, to acquire a sensitivity regarding its processing characteristic to other AM processes. For this, Mukherjee and Debroy (2019) observed the processing of austenitic AISI 316 stainless steel by L-DED, DED-GMA (direct arc deposition), and PBF techniques. These processes occur using a wide range of power (heat source), scanning speed, and feedrate, resulting in varying layer thickness. Using data from the literature, it was possible to construct a processing window comparing the techniques above.

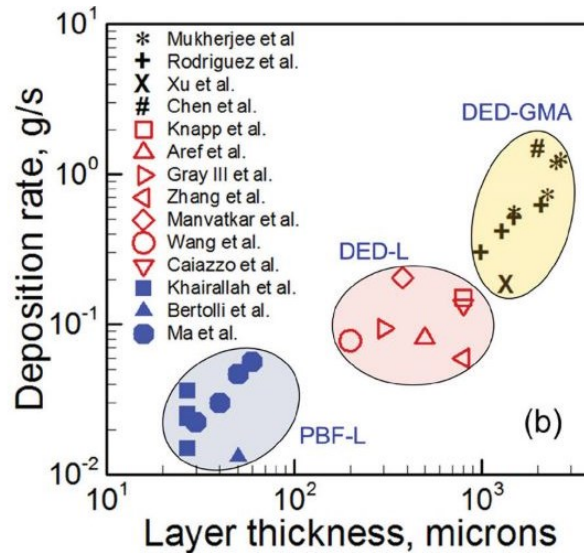
It has been observed that the arc process has 5 to 10 times more input power compared to laser processes. In contrast, the scanning speed in the PBF can be 80 to 100 times faster compared to the other two processes. About layer thickness, the PBF process is around 10 to 50 times smaller than the directed deposition processes, and in the arc processes, it is possible to obtain the highest deposition rates. Figure 23 demonstrates the processing window for the three techniques, displaying scanning speed and input power. Figure 24 compares the deposition rate and layer thickness [68].

Figure 23 – Processing window of 316L for different AM techniques.



Source: [68].

Figure 24 – Processing window of 316L for different AM techniques.



Source: [68].

The processability of the material was evaluated against the various techniques approached.⁴ As a result of the processes, it was generally observed that L-DED technology

⁴ The term processability cited herein refers to the ease of converting a filler material into a functional part having characteristics similar to those of the base material by an additive manufacturing technique.

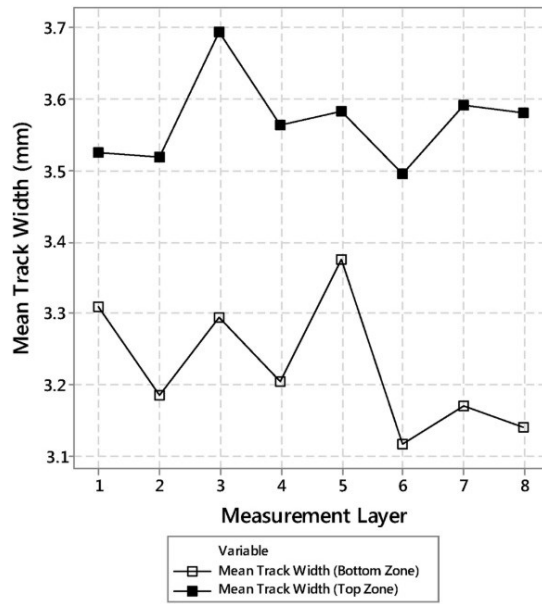
exhibits intermediate results in deposition rate, chemical composition stability, layer fusion vulnerability, and susceptibility to dimensional distortion [68].

2.7.1 Characterization of 316L parts made by L-DED

Several studies address the characterization of AISI 316L by L-DED, to understand the influence of various factors such as composition and morphology of the filler material, processing parameters, and deposition strategies on the obtained properties, as well as the presence of discontinuities. Thus, there is progress towards defining the whole strategy of building part with a prediction of the results to be obtained increasingly close to reality. Next, a series of studies related to this theme will be shown.

TAN et al. (2019) made blocks to characterize porosity, density, and microstructure through analysis by microscopy and 4-point tomography. Vickers microhardness was also done to determine the solidification mode. The uppermost layers were found to show a greater width than the lower ones, as seen in Figure 25. This is due to the different temperature gradients and cooling rates in the two process steps. The density measured on all specimens was above 99.8%. A small portion of slightly larger pores was found in the first layers (21-40 μm), along with regions of lack of fusion in the first layer. In the upper layers, a significantly larger amount of pores was observed, but they were smaller (10-21 μm). The circularity and spheroidicity observed in the pores suggest that their origin comes from enclosed gas from evaporation and incomplete fusion. To produce a layer of material using the L-DED technique, several single beads are deposited side by side, so that, part of the previous bead is overlapped on each new bead, thus causing the surface of the layer to have less waviness. Part of this overlapping layer is refluxed. The microhardness in the fused zone and the bead zone was analyzed. The remelting process makes the grain smaller in this region, as a consequence, an increase in microhardness compared to the bead zone was also observed. Through EDX it was possible to detect the presence of oxides in the remelted region, due to the natural oxide surface generated by AISI 316L in each deposition layer [69].

Figure 25 – Mean bead width in the top and bottom layers.



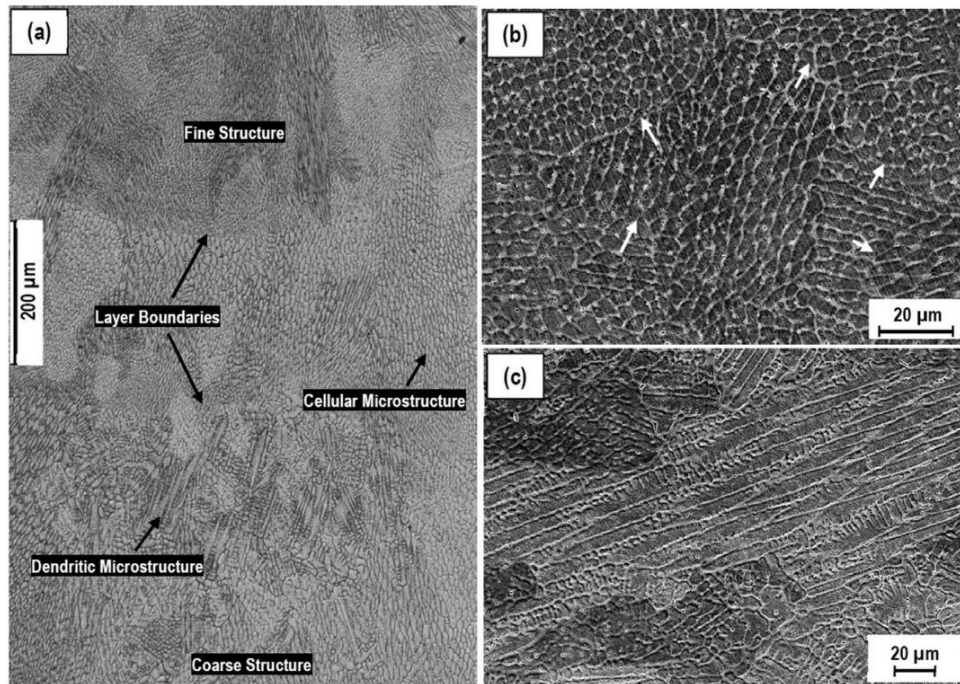
Source: [69].

An important feature of the L-DED process is the anisotropy of the parts produced, related to microstructure and mechanical properties. Due to the characteristics inherent to the process, the cooling rates that occur on the surfaces are different from those observed in the core of the produced part. Similarly, there is a difference in the layers closer to the substrate compared to the last layers produced, mainly due to different temperatures between the substrate at the beginning of the process and the temperature of the part at the end of the process. Higher cooling rates result in higher grain refining, resulting in higher hardnesses. In addition to the factors previously mentioned, manufacturing parameters such as layer orientation, part shape, complexity, size, deposition strategy, among others, also contribute strongly to the anisotropy of the produced part related to its microstructure as well as its mechanical properties.

Mukherjee (2019) studied the effect of layer orientation on the microstructure and properties of parts produced by L-DED with 316L. In the tensile test, the yield stress found by AM (352-465 MPa) was higher than forged material (310 MPa), and the specimens built in the horizontal direction (layers parallel to loading) had higher strength than those produced in the vertical position (orthogonal layers to loading). The maximum allowable stress obtained by AM (572-597 MPa) was lower than that of forged material (624 MPa). Regarding the failure mode, both specimens showed ductile behavior to fracture. However, the vertical block showed greater ductility (48 to 59% elongation) and was much closer to the forged one (55%)

than the horizontal ductility (20 to 45%). Differences in microstructure vary according to the temperature gradient and solidification rate. Figure 26 shows the microstructure evolution according to the layers. Cell structures can be observed in “b” and dendritic structures in “c”.

Figure 26 – Microstructure according to layers (a), cellular structure with arrows showing solidification borders (b), dendritic structure (c).

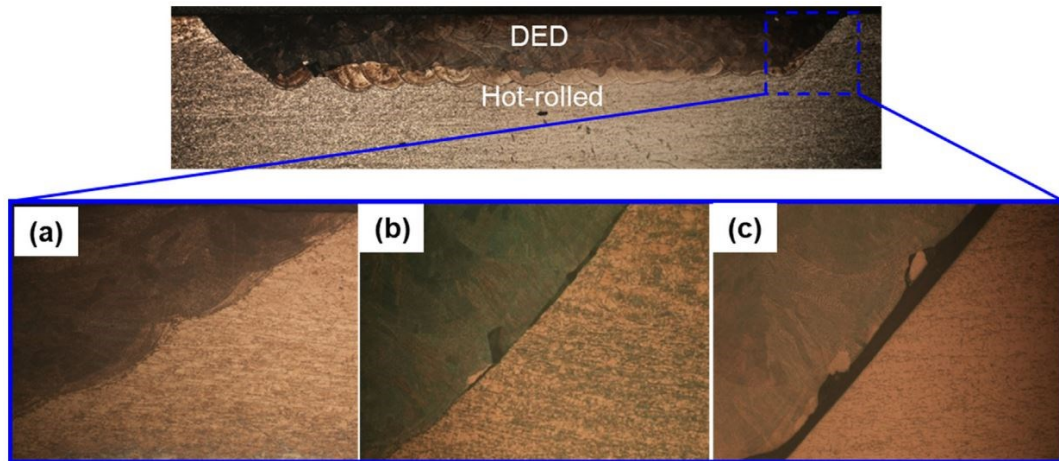


Source: [70].

Conventional repair processes such as welding and brazing can generate many pores and cracks, and a very large heat-affected zone, which is undesirable. As a breakthrough alternative in this area, a widely explored line of research is the use of the L-DED technique for repair. Oh et al. (2019) studied the repair of 316L parts originally produced by powder bed fusion, that were damaged in their use, applying the L-DED process. The hardness of the repaired area and the heat-affected zone was observed. Tensile tests were also performed, as well as the analysis of the fractured surfaces by microscopy. For comparison purposes, the repairs were performed on the substrate produced by PBF and hot-rolled steel. The repair process consists of: making a partial cut of the region to be repaired, with slanted side chamfers; perform deposition; finish with grinding. The surface preparation to be repaired was made through grooves of 0.5 mm, 1 mm, and 2 mm deep. In the 1 mm and 2 mm specimens, the fracture occurred at the interface. At interfaces with grooves of 0.5 mm no

cracks were observed, however, there were cracks at the interfaces with the substrate with grooves of 1 and 2 mm, as can be seen in Figure 27.

Figure 27 – Cross-section of the repaired area for 0,5 mm joint (a), 1 mm (b), and 2 mm (c).



Source: [71].

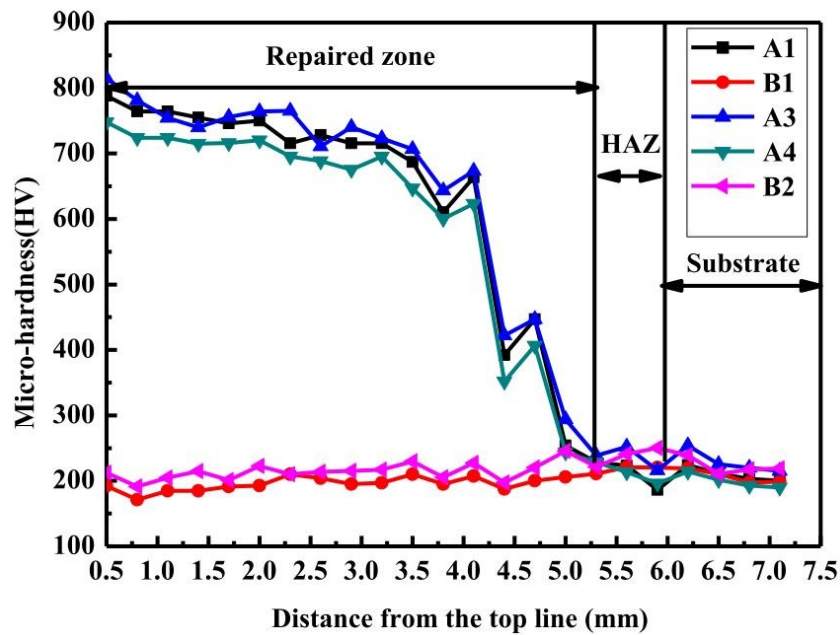
In a second study in the area of repairs, Sun et al. (2019) investigated the influence of the chemical composition of the filler metal on the microstructure and mechanical properties of L-DED repaired parts. Plates with 20 mm thickness slots were repaired using two types of powders with different chemical compositions:

Powder 1: bal Fe / 0.15C / 11.80Cr / 0.15Mn / 0.20Ni / 0.031P / 0.56Si / 0.05S (wt.%)

Powder 2: bal Fe / 0.017C / 17.05Cr / 1.20Mn / 11.28Ni / 0.019P / 0.46Si / 0.09S / 2.8Mo (wt.%)

The microstructure and mechanical characteristics were investigated by microhardness, tensile stress, flexural strength, and low-temperature impact strength tests. It was possible to perform repairs without micro defects and with a good metallurgical bond. Powder 1 had a homogeneous dendritic structure with chromium-rich martensite. Powder 2 produced a structure with cellular crystals composed of ferrite and austenite. Due to the reinforcement generated by solid solution formation, the repair performed with powder 1 had a hardness about 4 times higher than powder 2. Powder 2 showed considerably higher yield strength, maximum allowable stress, flexural strength, and impact absorption. In both static tensile and impact absorption tests, repairs with powder 2 presented ductile fracture, while powder 1 showed a mixed characteristic of ductile and brittle fracture. Figure 28 shows the different behavior of two powders when analyzing micro-hardness.

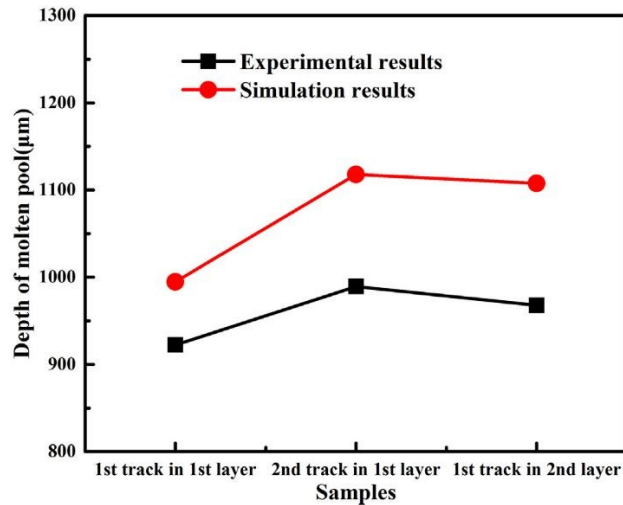
Figure 28 – Microhardness distribution according to the distance from the surface. Samples “A” are related to powder 1 and samples “B” are related to powder 2.



Source: [72].

The third study about repair takes a slightly different approach. Zhan et al. (2019) performed a repair on a 316L plate using the L-DED process. A finite element method was used to predict the thermal behavior of the molten pool during the process. The comparison between simulated and experimental melt pools is shown in Figure 29. The influence of heat generation of the second line of the first layer and the first line of the second layer on the characteristics of the first line of the first layer was also observed. Optical microscopy and SEM analysis were applied to evaluate the microstructure generated in the first line of the first layer and a Vickers microhardness test in the first layer. The heat accumulation effect was found to have a significant influence on the size and temperature of the melt pool, increasing in subsequent layers. The first bead had a good metallurgical union with the substrate. The second bead has remelted part of the first one, with good adhesion between the two of them. The cross-section of the simulated repaired area has good equivalence with the experimental results obtained, showing that the model can predict the geometry of the repaired area. The grain refining varies according to the proximity of the posterior layers, varying the thermal cycle to which it is submitted. The more refined, the higher the hardness obtained. Between the three points observed in the first bead, the one closest to the second bead had the lowest hardness.

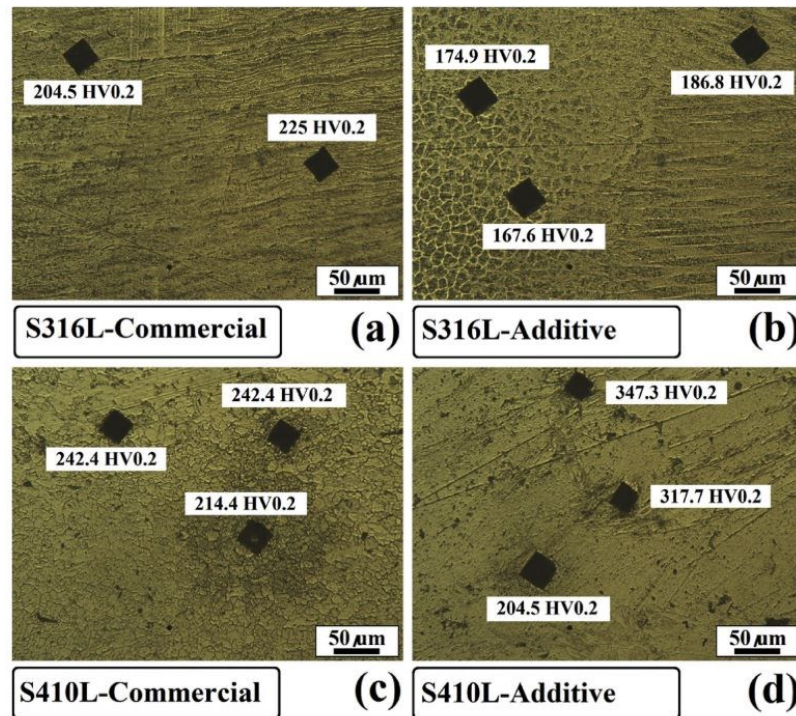
Figure 29 – Comparison between simulated and experimental melt pool.



Source: [73].

Another interesting research area is the comparison of characteristics between the same material processed by traditional manufacturing processes and AM methods. Considering there is already a lot of knowledge about materials obtained through conventional methods such as rolling and forging, once knowledge of comparative properties between these processes is developed, it can be established a relationship between them, and it is possible to develop the projects predicting characteristics. Khodabakhshi et al. (2019) compared the microstructure, hardness (Figure 30), and tensile strength characteristics of austenitic (316L) and martensitic (410L) stainless steel samples produced by L-DED with the same rolled materials. The axial traction test was performed by loading the samples transverse to the deposition layers (in the z-axis). The main metallurgical characteristics observed in materials made by AM were higher grain refining, higher microstructural heterogeneity, higher anisotropy (caused by directional solidification), and higher martensite formation. However, a decrease in micro-segregation was observed due to rapid cooling. Hardness per AM decreased by 20% in 316L and increased by 25% in 410L relative to laminated materials. This increase is due to the material being martensitic in parallel with the high cooling rate of the AM process. The effect of the strain rate variation did not vary significantly at 316L between the laminated material and that made by AM. For 410L a strong dependence on strain rate was observed.

Figure 30 – Indentations in regular materials and processed by AM.



Source: [74].

There are even other approaches to the L-DED process, beyond its current limitations, as in the study by Weng et al. (2019). He proposes to manufacture rods in the z-direction using 316L and L-DED and expects the technique to lay the groundwork for the deposition of wire structures or structures more efficiently than a traditional layer-by-layer deposition. The technique consists of continuous deposition in the z-direction, without the regular deposition of passes. The rods can even be used as support for complex structures. Microstructure and mechanical properties were evaluated. A two-phase microstructure (γ/δ) was obtained and the appearance of the δ phase was beneficial to the mechanical properties. Six tensile specimens were tested, and although voids and inclusions were found, they demonstrated a ductile fracture with tensile stress between 539 and 608 MPa [75].

Table 2 and Chart 3 demonstrate the processing parameters used in the articles discussed here and a summary of their purpose and contribution, respectively.

Table 2 – Processing parameters for L-DED found in the studied papers.

BIBLIOGRAPHY	POWER W(spot)	SPEED [mm/min]	FEEDRATE [g/min]	MATERIAL
[68]	1500	636	12	316
[69]	1400 (3 mm)	1000	14	316L 45-105 μm
[75]	34,3(0,3 mm)	24	3,09	316L 20-53 μm
	34,3(0,3 mm)	24	2,81	
	34,3(0,3 mm)	24	2,46	
	45,2(0,3 mm)	24	2,81	
	45,2(0,3 mm)	30	2,81	
	45,2(0,3 mm)	36	2,81	
[70]	650	360	8,52	316L 45-90 μm
	650	720	8,52	
	1300	360	8,52	
	1300	720	8,52	
[73]	1200 (2 mm)	900	6,8	316L 11-307 μm
[71]	700	650	4,5	316L 45-150 μm
	800	850	5,5	
	900	1050	6,5	
[74]	800 (2mm)	800	9	316L e 410L
[72]	500 (2 mm)	600		316L
	700 (2 mm)	1000		
	900 (2 mm)	1100		
	1100 (2 mm)	1300		
	1200 (2 mm)	800		

Source: Author (2019).

Chart 3 – Summary of approached articles.

BIBLIOGRAPHY	GOAL AND APPROACH	CONTRIBUTION
[68]	Evaluate the printability of 316 stainless steel using L-DED, SLM, and DED-MAG technologies.	The L-DED process was considered with intermediate performance in all evaluated aspects (residual stress, distortion, chemical composition variation, lack of fusion, layer thickness).
[69]	316L block construction by L-DED. Characterize porosity, density, and microstructure by microscopy and x-ray tomography. Microhardness and mapping to evaluate the solidification mode.	Characterization of a block produced by AM. Variation of bead width as a function of layer height, porosity distribution along with height, as well as pore geometry. Microstructural analysis to evaluate the solidification process, track body hardness, and fusion line.
[75]	The technique reported in this document is expected to lay the groundwork for the deposition of wire structures or structures more efficiently than traditional layer-by-layer directed energy deposition, continuously depositing in the z-direction.	A new strategy of continuous deposition in the z-direction was used. A two-phase microstructure (γ/δ) was obtained and the appearance of the δ phase was beneficial for mechanical properties.
[70]	Establish the influence of manufacturing orientation on the microstructure and mechanical properties of parts produced with 316L by L-DED.	A vertical and a horizontal block were produced, 3 tensile samples were taken from each of them (25x6x3 mm). The yield stress by AM was higher than the forged material, but the tensile stress was lower. Overall, resistance was higher in horizontal samples. The vertical samples presented higher ductility.
[73]	Perform a repair on a 316L plate using the L-DED process. Apply the finite element method to predict the behavior of the molten pool and evaluate the thermal influence of previous layers on the hardness and microstructure of the first line of the first layer, at 3 distinct points.	It was concluded that the effect of heat accumulation has a significant influence on the size and temperature of the melt pool. Hardness varies with grain refining, therefore, varies with proximity to previous beads. The model had a good response by predicting the geometry of the repaired area.
[71]	Check the possibility of repairing, using L-DED, damaged parts of 316L originally produced by SLM, maintaining or improving the mechanical characteristics and discontinuities.	Repairs with 316 by L-DED with 0,5; 1 and 2 mm deep grooves were evaluated, on hot-rolled steel substrate and another produced by GMP. Good results were obtained only with 0.5 mm deep grooves.
[74]	To compare the microstructural, hardness, and tensile strength characteristics of austenitic (316L) and martensitic (410L) stainless steel samples with the same rolled materials.	The main metallurgical characteristics observed in materials made by AM were higher grain refining, higher microstructural heterogeneity, higher anisotropy, and higher martensite formation. However, a decrease in micro-segregation was observed due to rapid cooling.
[72]	To evaluate the mechanical and microstructural characteristics of L-DED repairs using 316L, by adding two powders with different chemical compositions.	It was observed that even in the case of two powders of 316L, a change in chemical composition can significantly modify the mechanical characterization results obtained, including altering the fracture mechanics of the samples.

Source: Author (2019).

Analyzing all the studies previously exposed, it was observed that most authors use designs of experiments with a low number of experiments and also do not extend the results to continuous analysis. Using that approach there is an elevated risk of do not consider good processing parameters that are out of the range that was approached. Another difficulty was to define the selection criteria adopted by each author. Many times it was not clear, and when it was, it was different for many authors. Considering these facts, it was considered necessary to establish a pattern for selection criteria and to create a clear method to select processing parameters applied to the L-DED technology.

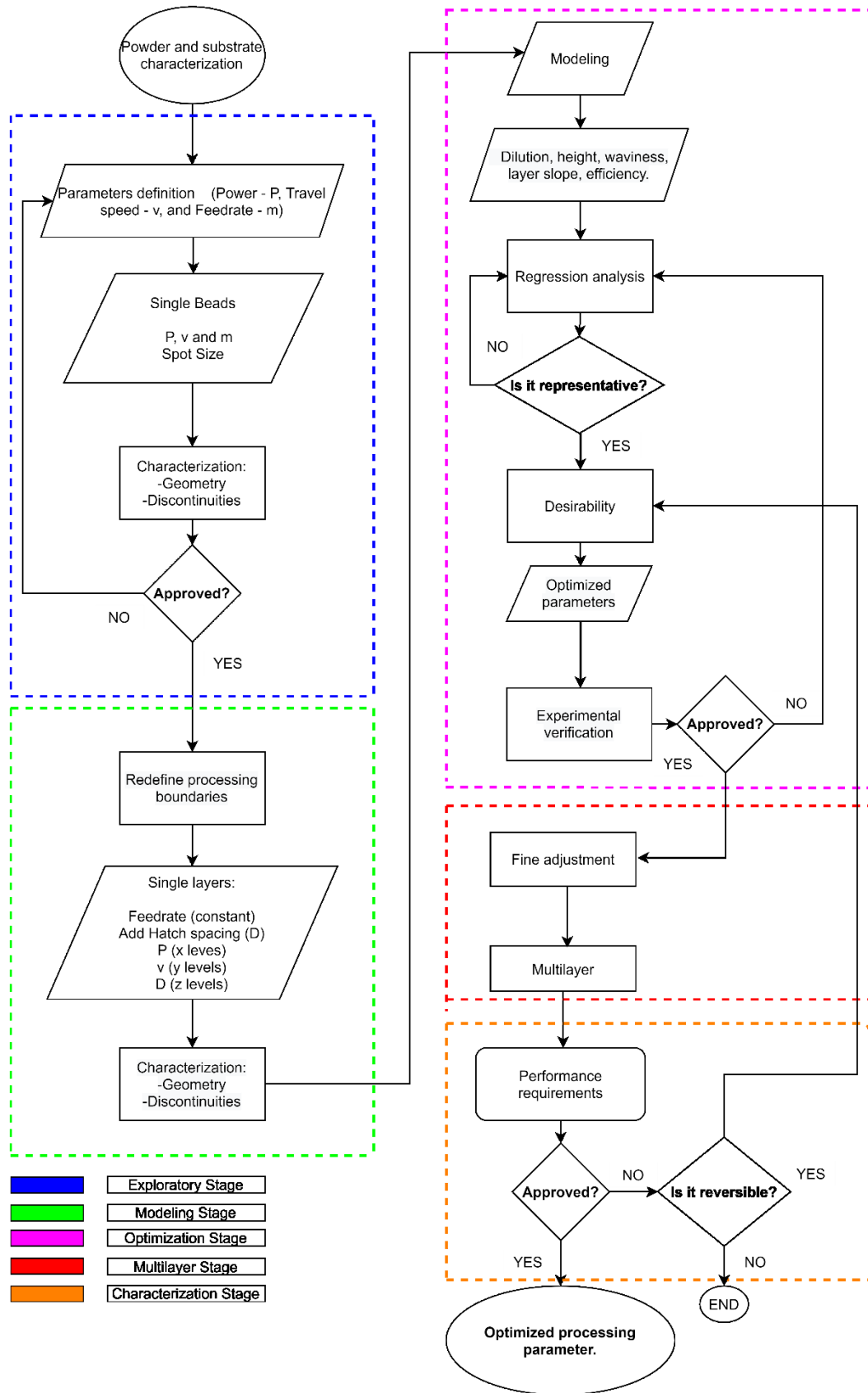
3 METHODOLOGY

The main idea of this work is to develop a methodology that can be applied in any set of equipment and any alloy using the L-DED process. The methodology proposes how to select processing parameters using L-DED technology. It consists of a quick analysis of single beads moving on to a more detailed analysis of the single layers, which will provide data for regression analysis. Subsequently, desirability criteria will help to select an optimized parameter that will be extrapolated to multiple layers. Considering that, in this section, only general instructions were given, it was not described any model of equipment or any range of parameters used (these details will be described in the next chapter).

Figure 31 shows the general flowchart of the proposed methodology. The first step (the characterization of the metallic powder) is important because once known powder features, it is possible to understand and explain some behaviors that may be observed during the process or the characterization. Even today these relations are not very clear, it is important to create a database to help their understanding in the future.

After powder characterization, some preliminary tests may be done to better understand the behavior of that material in a specific setup, or under specific circumstances. This step is not mandatory. The methodology itself starts defining a group of parameters that cover all the boundaries of the process for specific material and equipment setup and single beads are deposited with them. In sequence, a good processing window is selected and single layers (sequence of single beads laterally deposited with an overlapping portion) are deposited based on single beads results. The layers are analyzed and are used as input for regression analysis. The desirability criteria are defined based on what is expected for that parameter. Based on that, an algorithm gives an optimized parameter, which tries to attend to all the criteria previously set. If it was impossible to find a parameter to attend to the criteria, or the results are inconsistent, the regression or/and desirability must change, and this loop must be redone until a satisfactory result be reached. Once established the optimized parameter, it is necessary to verify the theoretical parameter and its outputs with the real deposited layer, comparing the results to assure that the model represents the behavior of the process. The last stage of parameter development consists of building a simple multilayer geometry, making it possible to analyze the bond and the presence of defects between layers (it could be a cubic or parallelepiped geometry). In that stage, some adjust to the layer thickness may be done to achieve better results.

Figure 31 – Methodology flowchart.



Source: Author (2019).

Once defined all the parameters for processing, samples are built, to analyze the performance of the parts, taking into account their application (e.g. tensile, fracture, hardness, and microstructure).

3.1 EXPLORATORY STAGE

This stage begins with the gathering of information on the material and on the application, which will be necessary to support the decisions along with the methodology. Material information includes: parameter ranges already studied in the literature, gases used for processing, phase diagrams, predictive diagrams, tendency to crack, and other possible discontinuities. Regarding the application, one must look for mechanical, tribological, corrosion, and shape requirements, beyond the degree of tolerance to the presence of discontinuities and imperfections.

The substrate must be selected according to the filler metal. The most similar the better. Similar materials decrease the chance of defects and discontinuities, tend to have a better metallurgical bonding and a closer thermal distortion in post-processing steps. Another important feature is the substrate dimensions. The size of the substrate directly affects how heat dissipation is conducted, so far, depending on the size and time of the experiment, it may significantly affect the results. During experiments of single beads and single layers, the chemical composition of the substrate is more relevant, because feed material and substrate material will be mixed. When building multiple layers, the composition of the substrate is not as important as the first layer, because the interaction with the substrate decreases. When building samples or parts that will pass through heat treatment, it is necessary to be careful about heat distortions. If the materials have much different behavior when submitted to heat treatment, cracks and distortions may occur.

Even before the experiments start, the substrates and powders to be used must be characterized to guarantee the quality of the materials. The substrates must undergo chemical characterization, while the powders are subjected to chemical analysis, morphological analysis, and, if possible, rheological analysis. Adequate stock and handling procedures for these materials must be followed.

This stage also includes the possibility of carrying out preliminary tests to clarify any doubts before the start of structured experiments. These tests may be of any kind, that helps to

understand the material behavior under the processing conditions. The main idea about the preliminary tests is to carry out qualitative results to the Exploratory Stage.

In the L-DED process, the single bead is the most basic geometry found. It is not guaranteed that a good quality of a single bead will provide a good quality part, but it is more accurate to say that a single bead with bad quality will carry these problems to the next stages, and consequently to the final part. Single beads experiments are quick to plan, program, and execute. Considering the previous facts, it is possible to affirm that a single bead is an ideal approach to start a methodology.

As it is a stage whose goal is to indicate approximately the region of a stable process, the suggestion is to carry out a full factorial experiment (because with more experiments it will be easier to select the window to the next stage), varying the levels of power, travel speed, and feedrate with simple and fast characterizations. It is recommended to deposit single beads with a length between 25 mm and 100 mm, depending on the spot size used. Longer beads are desirable because it is easier to reach the process stability (different machines may have different dynamics for the acceleration of the head).

The selection of the spot size depends on the study's approach, and the machine setup and resources available. If it is desired to prioritize productivity, a higher spot size must be used. If it is desired to prioritize resolution, a small spot size must be used. Considering that there are many variables to control the process, it is recommended that the spot size remain constant. If it is needed to obtain an optimized parameter for productivity and another one for resolution, it may be necessary to apply the methodology twice, using two different spot sizes. Sometimes it is possible to achieve both parameters (productivity and resolution) in only one application of the methodology, depending on the behavior of the alloy. Chart 4 shows the main factors of the Exploratory Stage, the details are described below.

Chart 4 – Main factors of Exploratory Stage.

Experiment	Full factorial.
Samples	Single beads.
Variables	Power, travel speed, powder feedrate.
Characterization	Visual inspection, dye penetrant inspection, height measure.
Criteria	Convexity, regularity, detachment, process stability, cracks, surface porosity, height.
Output	Processing window.

Source: Author (2019).

The recommendation is that the laser power and travel speed ranges should be wide, with four or five levels for each one. For the material feedrate⁵, it is suggested a more restricted range, such as two or three levels (each additional level increases the number of experiments significantly). If a high productivity parameter is being developed, high feedrates should be used, considering this is the main factor of productivity, defined as the rate of material deposited per unit of time. If the parameter being developed is intended for high resolution, lower feedrates should be used.

In this stage of methodology, each experimental point only needs to be performed once. The reproduction will only be recommended for points that present anomalous behavior in the characterization, that is, outside the expected.

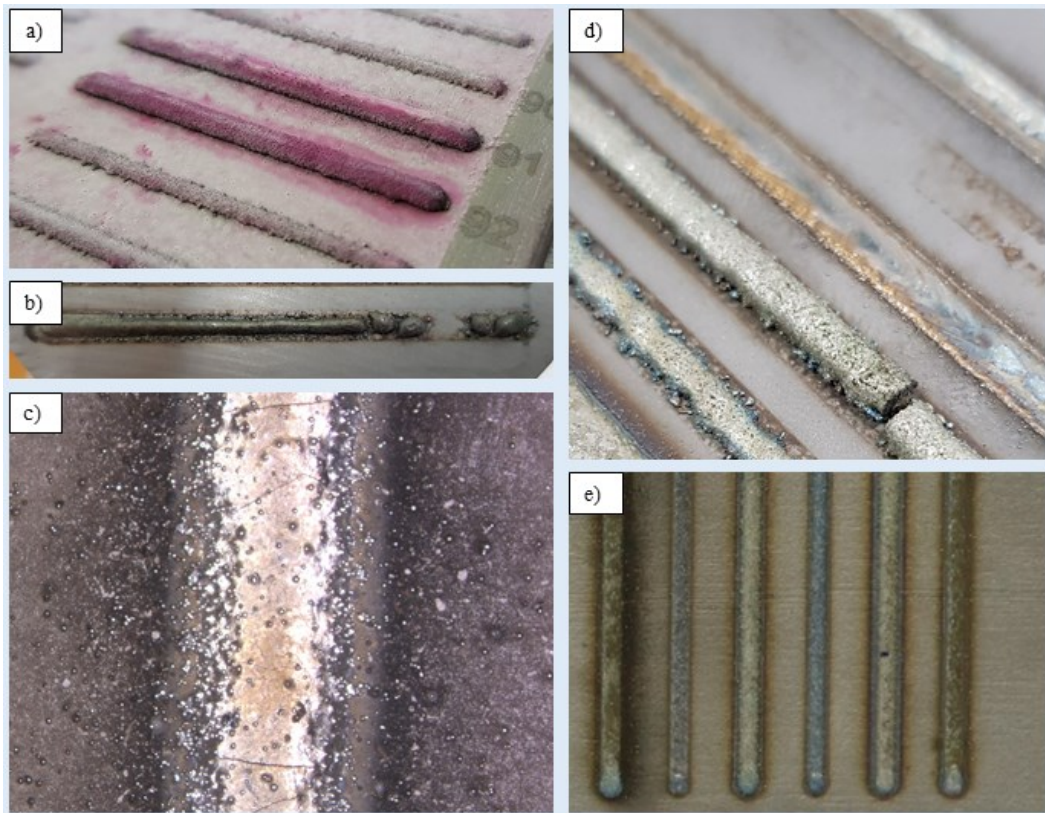
In some cases, it may be interesting to assess the effect of some other parameter⁶. It can be included in the factorial design as an additional factor or replacing one of the previously recommended processing parameters. Another possibility, if this factor has a small influence on the geometric properties of the bead, is to study his effect after the Exploratory Stage or the Modeling Stage⁷. For the evaluation of the deposited single beads, it will be checked, as a qualitative performance, the convexity, the presence of irregularities, detachment, process stability, porosity, cracks, and height. Convexity, irregularities, and detachment will be analyzed by visual inspection (Figure 32 “a”, “b” and “d”, respectively). A stereoscope should be used to assist in this task. It may be considered high convexity when the width of the bead bonded to the substrate is smaller than the highest height of the bead (high aspect ratio). It may be hard to see without a cross-section, so just the parameters that show a high level of convexity are classified. Irregularities are non-symmetric or non-continuous beads. Detachment happens when there is no physical bond between the bead and the substrate. Process instability may be observed during the process and is defined as some event that will not generate a usable parameter or may damage the equipment. Porosity and cracks (Figure 32 “e” and “c” respectively) will be observed with the help of dye penetrant inspection (here it is considered surface porosity).

⁵ As stated in the section 2.1.1, the terminology *feedrate* will be used to represent the amount of material expelled by the nozzle during the processing. It may be expressed as *feedrate* or *material feedrate* along the text.

⁶ For example: the amount of a shielding gas.

⁷ For example, the effect of the nitrogen content of the shielding gas on the austenite ratio of duplex steel can be assessed as in the latter case, using the optimal modeling point, since nitrogen must have a minimal effect on other deposition characteristics.

Figure 32 – Problems observed on single beads: (a) high convexity, (b) irregularity, (c) cracks, (d) detachment, and (e) surface porosity.

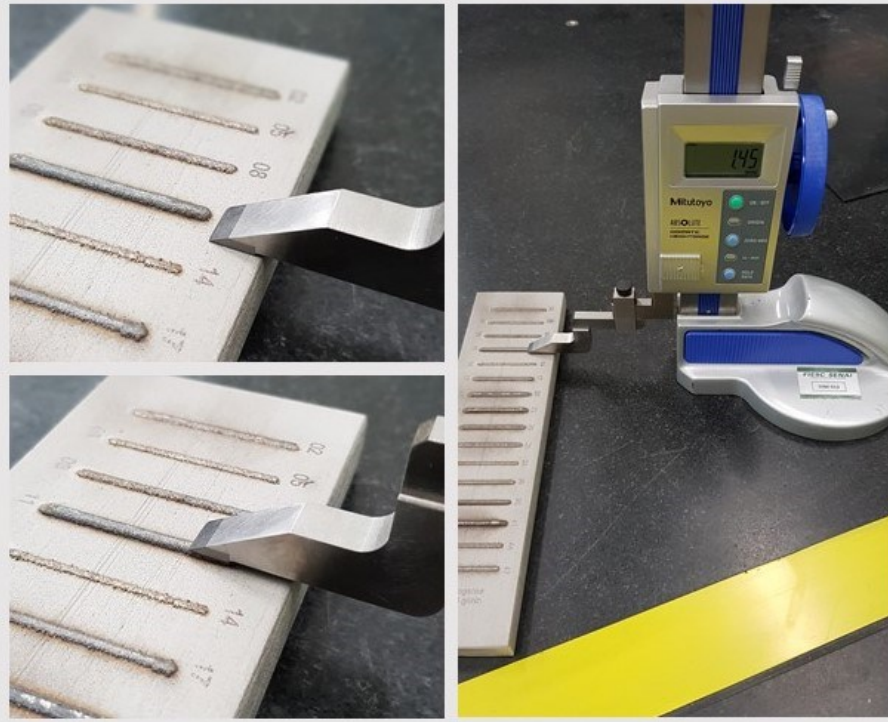


Source: Author (2020).

The last item is the height. For parameters prioritizing higher productivity, for example, it is desired height as big as possible. So, a minimum value may be set as a cutting criterion. Height measure may be done using a micrometer or a height caliper gauge, as shown in Figure 33. Applying that concept is much faster than preparing the cross-section of all the single beads, saving time and resources that may be spent in the layer analysis, which is much more representative when compared to the final building parts.

The level of requirement adopted to assess the criteria is subjective and will depend on the general quality of the depositions, the application to which it will be subjected, and the level of maturity about the alloy, the process, and the equipment used. Also, depends on the experience of the operator and responsible for analysis. However, it is important to state that this methodology stage is executed as an exploratory goal and the results are not decisive for the selection of the final optimized parameter.

Figure 33 – Height measure of a single bead using a height caliper gauge.



Source: Author (2020).

The results can be presented in the form of tabular maps of power per travel speed, one for each feedrate, and can follow the example of Figure 34. It is proposed a scheme of colors and letters to describe all the characteristics of each bead. On the right side of the figure, there is a subtitle explaining the meaning of each color and letter, on the left, there is an example of a tabular map, to evaluate and select parameters. The colors are disposed of in order of gravity, in which green is the best and purple is the worst case. Red and purple are automatically discarded. Another colors may be included depending on the situation. Pores and cracks are not excluding factors, once their formation dynamics change a lot in multiple layers deposition.

Depending on the application, other properties may be important at this stage, such as microstructure, microhardness, and the presence of other defects. As this point is only intended to indicate the region to be studied in greater detail in the Modeling Stage, so the use of simpler and faster characterization techniques is suggested. If more time-consuming procedures are required (such as metallographic preparation), the suggestion is that they should be carried out only in part of the samples, as in the region that meets the properties evaluated in the visual inspection, or more spaced conditions.

Chart 5 – Main factors of the Modeling Stage.

Experiment	Full factorial.
Optimization	Desirability.
Samples	Single layers (10 beads each).
Variables	Power, travel speed, hatch spacing.
Characterization	Visual inspection, stereoscopy (cross-section), dye penetrant inspection.
Criteria	Dilution, height, waviness, layer slope, capture efficiency, porosity, cracks.
Output	Data for the response surfaces.

Source: Author (2019).

There are two possible approaches to quantify the distance between two beads deposited side-by-side. The first one is using “overlapping”. Overlapping is given by the percentage of the width of a bead that is deposited over the previous one. The second one is “hatch spacing”. Hatch spacing is the lateral distance between the deposited bead and the previous one. It may be noticed that overlapping depends on the width of the bead while hatch spacing is an absolute value. If the concept of overlapping was applied it would be necessary a different value for each deposition, which would significantly increase the programming and experimental time. Applying the concept of hatch spacing some values are previously set, which makes the experiments much faster. For example, applying overlapping in three levels for a 4x4 full factorial experiment would result in 48 different values. Applying three levels of hatch spacing they are just three.

The tendency to form cold cracks is reduced when switching to multiple beads and multiple layers, due to the lower cooling rate. That will also influence the disposition of voids. Due to these facts, if these discontinuities are observed, it will not prevent the selection of the parameters related to them. However, it will be considered when analyzing how those parameters are ranked, prioritizing those without defects.

In the Modeling Stage, the hatch spacing is added as a processing parameter. It is very important to set up the range properly, otherwise, it will not be possible to model the process properly. If the hatch spacing is too low, the beads will overlap too much, which will probably incur in lack of fusion with the previous layer. If it is too high, the beads will be too much spaced to each other, which will probably incur voids between beads (once there is not energy enough to melt the previous bead). The approach suggested here is to use the average width of all the selected parameters and set 20%, 35%, and 50% overlapping on the average. These three distances will be the hatch spacing of the Modeling Stage. In the case of using

more than three values of hatch spacing, it is desired that the difference between each value be always the same. It will make the visual analysis of the response surfaces easier.

By default, the surface of the samples is evaluated for the presence of cracks and surface porosity through macrography. Macrographies are also done on the cross-section where it will be evaluated the dilution, layer height, waviness, layer slope, and capture efficiency, using image analysis software. Other characteristics can be evaluated, depending on the material and the application.

The cross-section of the sample must be performed in its center after visual inspection. One of the faces must be prepared with sandpaper up to size 1200 grain size, later polished, and etched with the appropriate reagent, taking into account the processed alloy. Then, it will be possible to obtain a contrast between the deposited area and substrate, allowing the user to analyze all the desired factors. Measurements related to dimensional aspects should be performed using image processing software, such as ImageJ. It should also be observed the presence of pores and voids qualitatively.

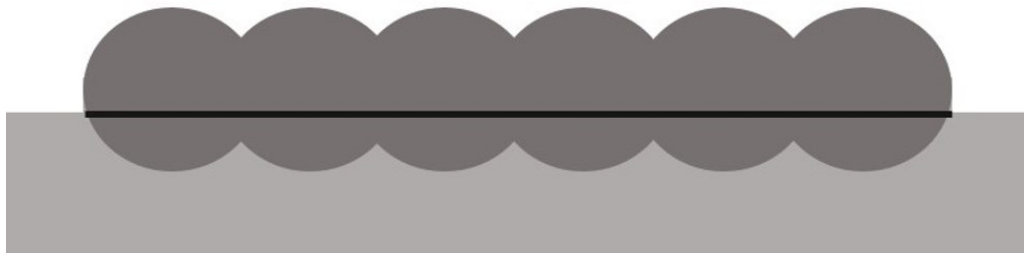
The data of the dimensional aspects are the most important information of all the Deposition Stage. There is a lack of information in the literature about which are the most important dimensional features and how to measure them. Because of that, it may be hard to replicate some study, once each person may measure some characteristics differently. It is important that all the measurement results be the same, or at least very close, independent of who is doing it. Trying to solve this problem, the main layer features and one proposed method to standard measurements of layers dimensional features will be presented below, to follow to the next stage with consistent data for regression analysis.

- a) Dilution (D) [%]: is the relation between the area of the previous layer or substrate that was refused and the total area. Dilution is expressed by equation 6:

$$D = \left(\frac{A_u}{A_t} \right) 100\% \quad (6)$$

where A_u [mm²] is the refused area (dark grey under the black line) and A_t [mm²] is the total area (dark grey) (Figure 35).

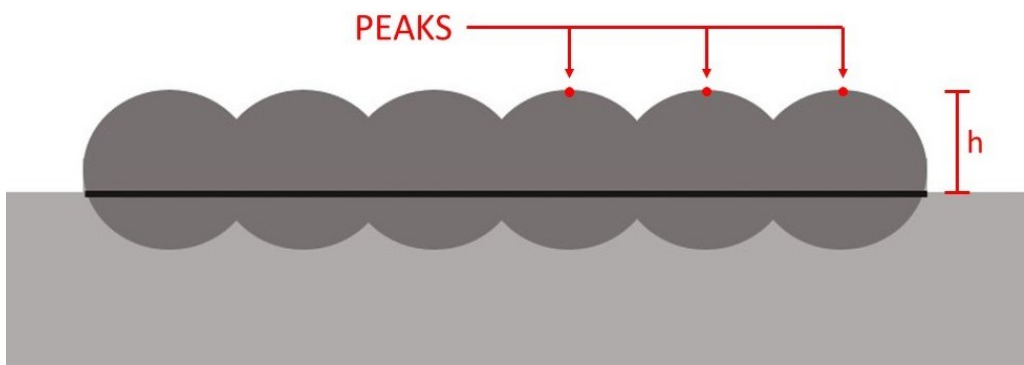
Figure 35 – Representative scheme of dilution in a single layer.



Source: Author (2019).

- b) Height (h) [mm]: the height is measured through the average distance between the substrate and the three last peaks of a layer, as shown in Figure 36. It is a very important measure, directly linked to the productivity of the building process.

Figure 36 – Representative scheme of layer height measurement.

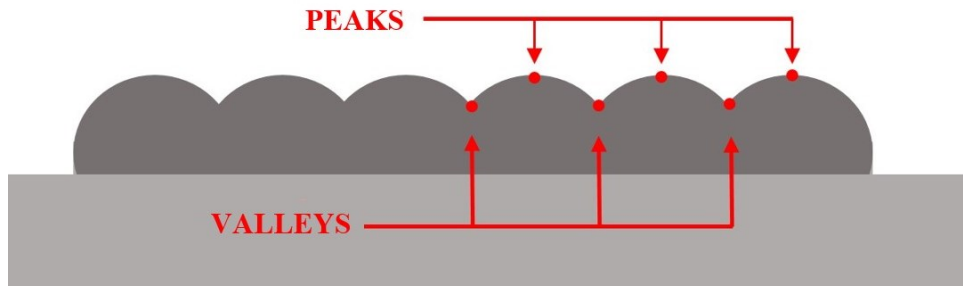


Source: Author (2019).

Height-variation (Δh) [mm]: it is the difference between the average of the height of the three last peaks ($\overline{h_p}$) and the three last valleys ($\overline{h_v}$) (Figure 37). From all of these measures, this is the only one that is not an input for the desirability, it is just an input to calculate waviness.

$$\Delta h = \overline{h_p} - \overline{h_v} \quad (7)$$

Figure 37 – Representative scheme of height-variation.



Source: Author (2019).

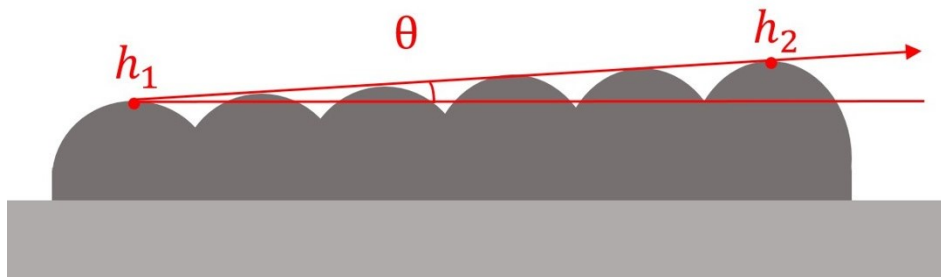
- c) Waviness ($\Delta h'$) [%]: it is expressed by the relation between height-variation and height. Once this parameter is a percentage, it gives a sensibility to how wavy is the surface, and how deep are the valleys considering the total height. In other words, it expresses how close the top of the layer is to a perfectly flat surface. It is expressed by equation 8:

$$\Delta h' = \left(\frac{\Delta h}{h} \right) 100\% \quad (8)$$

- d) Layer slope (θ) [degrees]: it is the angle of a straight line, nearly tangent to the layer's surface, with the horizontal. The points selected to do the measure must be the first and the last peaks. Considering that ten beads are deposited to form one layer, the distance used to calculate the angle must be the total width of the layer (W) minus half a bead from each side. In other words, it is considered 90% of the total width. This angle must be as smallest as possible, otherwise, it may cause geometrical distortions on the final part.

$$\theta = \tan^{-1} \frac{(h_2 - h_1)}{(0.9W)} \quad (9)$$

Figure 38 – Representative scheme of layer slope.



Source: Author (2019).

- e) Capture Efficiency (η) [%]: this is the relation between the most relevant parameters involved in the process that express the amount of powder that reach the melt pool, is melted, and becomes a properly deposition. It is given by the following equation:

$$\eta = \frac{A_o v \rho}{10^2 \dot{m}} \quad (10)$$

where A_o [mm²] is the cross-section area over the substrate line, v [mm/min] is the travel speed, ρ [g/cm³] is the density of the metal powder and \dot{m} [g/min] is the feedrate. The constant (10^2) has the function of split the area into ten parts (10 single beads overlapped), adapt the unit of density, and transform the final result into a percentage.

After all the measurements were done the data is put in a table linking the processing parameters to their corresponding characteristics. These data are the input for regression analysis.

3.3 OPTIMIZATION STAGE

After single layers deposition and measurements, the next stage is to develop a regression analysis, that will link all the outputs to model the process behavior, create response surfaces and make it possible to predict intermediary behaviors. These tasks are done aided by software like R-Statistics.

The regression analysis allows starting from a group of experimental data and estimates an equation that better describes the behavior of a system inside the limits of the input data. At the end of the regression, it is desired to found one or more equations, as expressed in Equation 11.

$$Properties \rightarrow f(Parameters) \quad (11)$$

It is a method that allows verifying the influence of a variable (input) on the response (output) of a system, generating an equation that better describes this correlation. The most studied case is linear regression analysis. However, to any kind of relationship between variables, the regression is obtained in the same way, minimizing mean squared error [76].

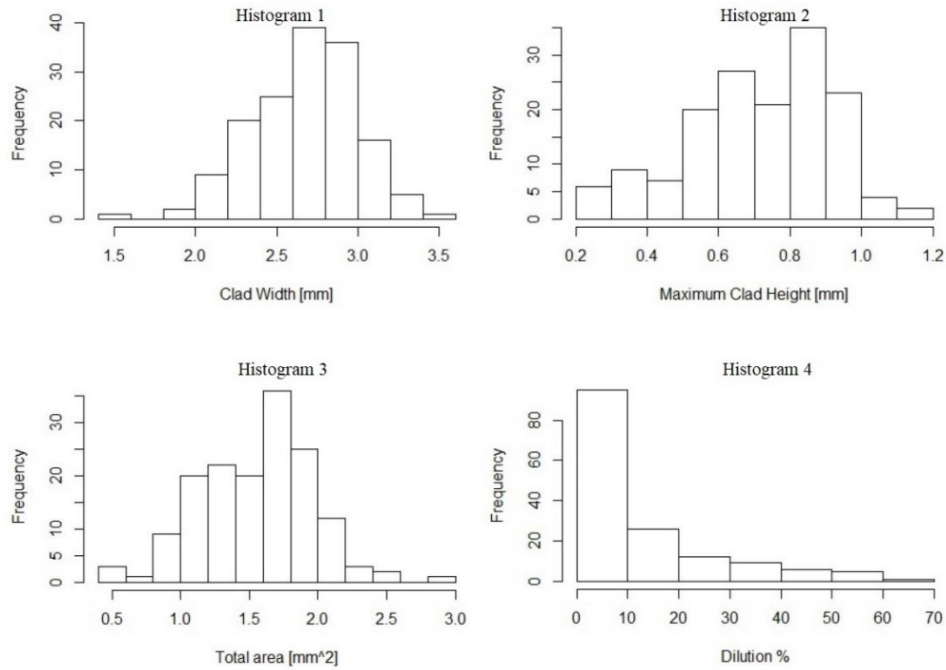
In the beginning, it is necessary to define the kind of relation between the variables and the responses (linear, quadratic, cubic, sinusoidal, logarithmic, etc). Considering X the input values, Y the response of the system to each X , Y' the estimated values of the regression for each X , and N the number of values analyzed, the mean squared error may be calculated as following [77]:

$$\text{MSE} = \frac{\sum_{i=1}^N (Y_i - Y'_i)^2}{N} \quad (12)$$

The analysis must be done considering many facts in parallel, such as the trend, MSE, p-value among other characteristics [78]. There is not a specific number of MSE and p-value that is acceptable, it must be seen the best fit of the response surface to the plotted points, and at the same time the best representation of the trend of each variable response. This loop needs to be repeated as many times as necessary until an acceptable result is achieved. This algorithm is based on a polynomial multiple regression using the Minimum Square Errors method. The initial format of the regression is a cubic polynomial with all first-order, second-order, third-order terms, as well as the first-order and second-order interaction terms. With this polynomial as a base, the algorithm goes into a loop, searching the regression, checking if the p-values of all terms are less than 0.001 (this value must be adjusted according to the behavior observed by the user), and, if not, removing the term with the highest p-value to repeat the loop. When all terms have a p-value lower than 0.001, the algorithm stores this regression and proceeds to calculate the regression of the next properties. At the end of the regression analysis, the list with models for all properties is available.

For the definition of the regression analysis applied to the L-DED process, it is recommended to use a polynomial of the second or third degree. It is also recommended to plot a histogram before the desirability application. Analyzing the histogram it is possible to see the gaps that happen more frequently. This way will be easier to set the targets, avoiding zones very hardly achieved, or where the representation of the regression may be poorer. The histogram must show the frequency of a gap for each output that is important like shown in the arbitrary example in Figure 39.

Figure 39 – Histograms of outputs.



Source: Author (2019).

As previously said, desirability is a function used to analyze multiple factors simultaneously and obtain the best match between them. The first proposal of the desirability function was done by Harrington in 1965 [79] and suffered many modifications until it becomes the model used here, purpose by Derringer and Suich in 1980 [80].

The desirability function transforms each estimated response variable Y_i to a desirability value d_i where $0 \leq d_i \leq 1$. The closer Y_i is to the wanted value the closer d_i is to 1. Many setups are used in the desirability function, depending on the approach to the response variable. For binary response (acceptable or unacceptable) d_i must be defined as 1 for acceptable and 0 for unacceptable. In the case where Y_i is acceptable just under a specific value, the desirability must assume the shape of equation 13, where S_i is the superior limit. By the opposite way, in the case where Y_i is acceptable just over a specific value, the desirability must assume the shape of equation 14, where I_i is the inferior limit.

$$d_i(Y_i) = \{1 \text{ se } Y_i \leq S_i \quad 0 \text{ se } Y_i > S_i \quad (13)$$

$$d_i(Y_i) = \{0 \text{ se } Y_i \leq I_i \quad 1 \text{ se } Y_i > I_i \quad (14)$$

For cases where there is an optimal value desirable (target T_i), that is, the closer to a specific value the better, the desirability must assume the shape of equation 15, where I_i and

S_i are the inferior and superior limits respectively, while “s” and “t” are the coefficients that indicate how fast the desirability decays as long as it gets further from the target.

$$d_i(Y_i) = \begin{cases} 0 & \text{if } Y_i < I_i \\ \left(\frac{Y_i - I_i}{T_i - I_i}\right)^s & \text{if } I_i \leq Y_i \leq T_i \\ \left(\frac{Y_i - S_i}{T_i - S_i}\right)^t & \text{if } T_i \leq Y_i \leq S_i \\ 0 & \text{if } Y_i > S_i \end{cases} \quad (15)$$

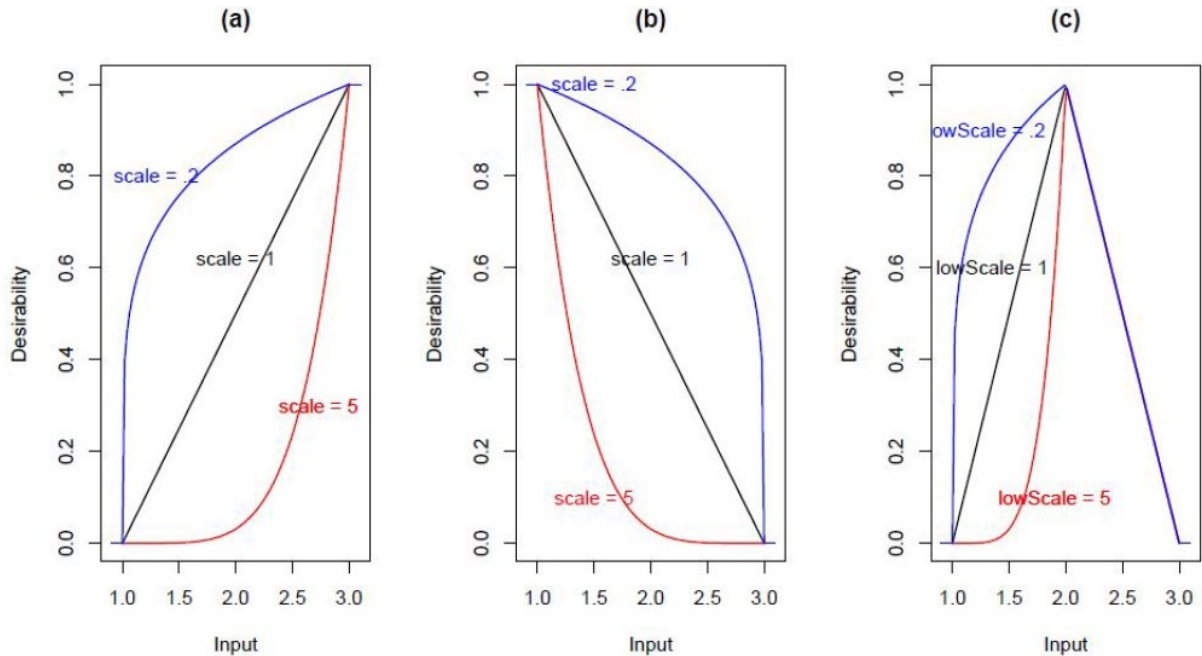
In the last case, when it is desired to maximize Y_i until T_i , and after that, it does not change the results anymore, it is possible to use equation 16. In the opposite way, when it is desired to minimize Y_i until T_i , it is possible to use equation 17.

$$d_i(Y_i) = \begin{cases} 0 & \text{if } Y_i < I_i \\ \left(\frac{Y_i - I_i}{T_i - I_i}\right)^s & \text{if } I_i \leq Y_i \leq T_i \\ 1 & \text{if } Y_i > T_i \end{cases} \quad (16)$$

$$d_i(Y_i) = \begin{cases} 1 & \text{if } Y_i < T_i \\ \left(\frac{Y_i - S_i}{T_i - S_i}\right)^t & \text{if } T_i \leq Y_i \leq S_i \\ 0 & \text{if } Y_i > S_i \end{cases} \quad (17)$$

The exponents “s” and “t” may vary according to how closer to the target is needed to accept Y_i , it is called sensitivity. The higher the exponent (higher than 1) the more restricted is the system, the lower the exponent (lower than 1) the more acceptable the system is for values further from the target, and when the exponent is equal to 1 the system is linear. Figure 40 shows a graphical representation of the behavior of sensitivity from values lower, equal, and higher than 1. It also shows a maximization, a minimization, and a target distribution. It is possible to merge more than one distribution of desirability for one response variable, making it possible to adequate the criteria for basically any situation.

Figure 40 – Figure (a) represents maximization desirability, (b) represents minimization desirability, and (c) represents target desirability. Both of them show high, low, and standard sensitivity.



Source: [81].

The selection of the profiles of desirability such as the definition of the proper sensitivity is very important and has a great impact on the final results and characteristics of the optimized parameter. They will change according to the alloy that is being used, the equipment, among other variables. If the optimized parameter's features are not satisfactory, it is recommended to change some of these factors to get closer to the desired characteristics.

The desirability function approach is a method for simultaneous evaluation of multiple responses, by assigning to each a desirability score and multiplying all individual desirability scores to reach global desirability for a given condition. Global desirability is an index of how close the combination of all the characteristics is to the perfect situation, where the worst scenario is 0 and the best scenario is 1. It is given equation 18.

$$D = (d_1(Y_1) \times d_2(Y_2) \dots d_k(Y_k))^{1/k} \quad (18)$$

As described in the flowchart shown in Figure 31, there are some steps after the optimized processing parameter was obtained. First, the optimized parameter must be verified, throughout the deposition of a single layer with triplicate. They must be cut in cross-section and sandpaper prepared to analyze the geometrical features in a microscope. The

outputs must be close to what was predicted in the model, or into a previously established acceptable range, otherwise, the model must be improved and the optimal parameter must be redone.

3.4 MULTILAYER STAGE

After obtaining and verifying the optimized parameter, the Multilayer Stage begins. Additional tests may be necessary to obtain improvements in the characteristics of the optimized layer through sensitive changes in the processing parameters. The analysis of the need and which tests will be carried out are up to the user. After this stage, the multilayer tests are actually started. The objective is to stipulate the best overlapping rate of layers by analyzing the relationship between productivity and the presence of defects (mainly pores and lack of fusion). To do that it is necessary to build a simple multilayer geometry (as a block with $30 \times 30 \times 30 \text{ mm}^3$) using the predicted thickness, cut a cross-section, and analyze the presence of pores and lack of fusion voids. If the quality is not satisfactory, the layer height is decreased by 5%, successively, until a good quality is achieved. When analyzing the presence of defects it is possible to discard the three or four first layers, once the substrate is previously cold, and the system is not in a permanent regime.

3.5 CHARACTERIZATION STAGE

Once known the best layer thickness it is possible to build the samples to do all the characterization that is desired, such as tensile, compression, impact, hardness, microstructure, porosity, etc.

4 MATERIALS AND METHODS

The previous chapter explained how to apply the methodology proposed. The current chapter aims to explain all the relevant details related to the processes and equipment used to develop this study. The sequence adopted to go along with it is exposed in the flowchart shown in Figure 41.

4.1 POWDER CHARACTERIZATION

The metallic powder used for this study was a gas atomized Höganäs 316L with a size distribution between 50-150 μm . It was analyzed the powder chemical composition, particle size distribution (PSD), morphology, and presence of pores. The chemical characterization was performed with the Inductively Coupled Plasma Optical Emission Spectrometry (ICP-OES) technique. It is necessary to have a pattern of the material to compare the results. The reference material used was AISI 316L certified by IPT 98 (ATTACHMENT A – Reference material certificate). The equipment was an AGILENT ICP-OES 710. The results are shown in the table below:

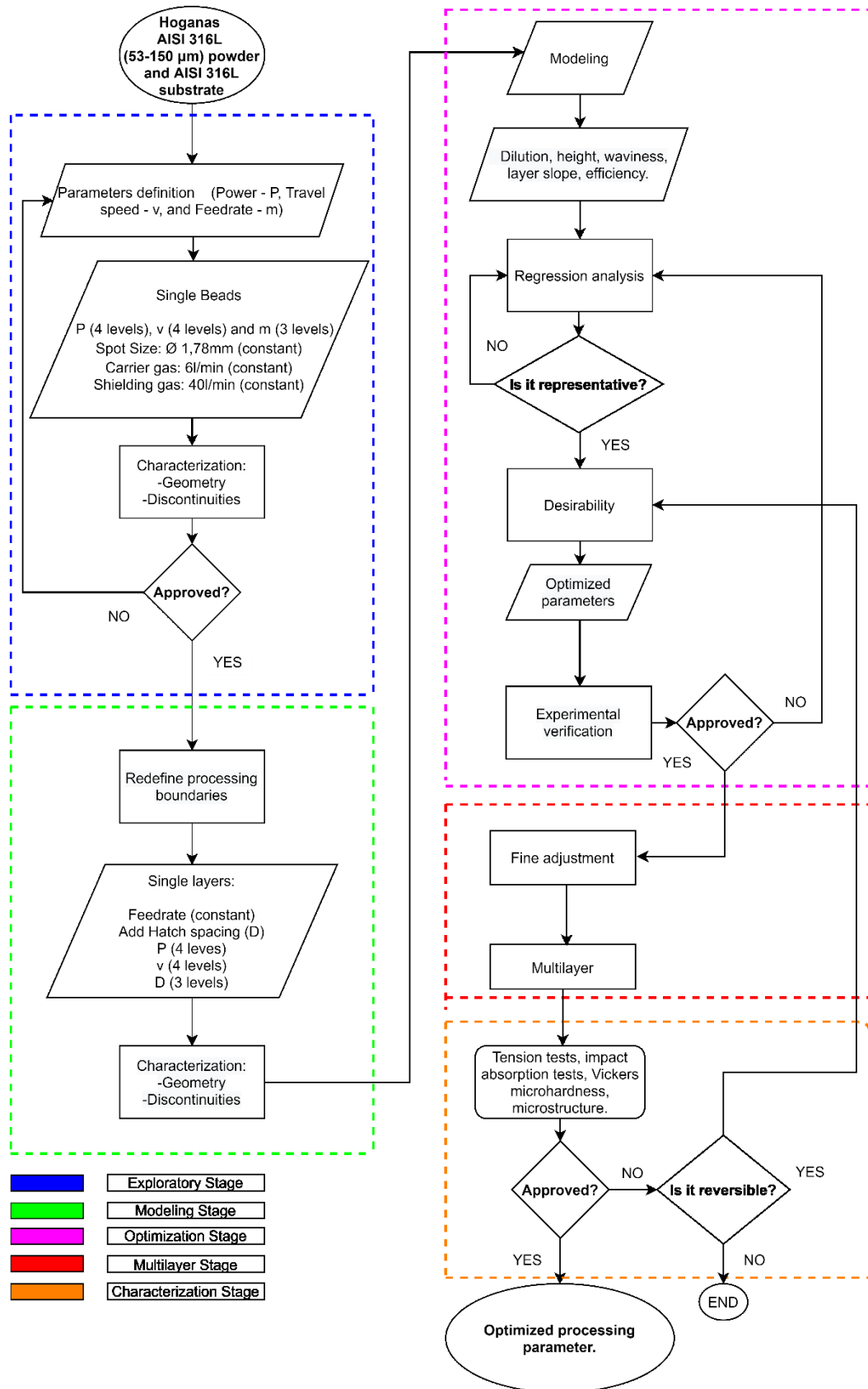
Table 3 – 316L powder chemical composition.

	Cr	Ni	Mo	Mn	Si	P	S	C
316L Höganäs Powder (measured)	17.18 ± 0.08	13.1 ± 0.1	2.56 ± 0.02	1.45 ± 0.01	0.63 ± 0.04	0.025 ± 0.001	0.012 ± 0.002	NA
AISI 316L [82]	16.0-18.0	10.0-14.0	2.00-3.00	2.00	1.00	0.04	0.030	0.03

Source: Author (2019).

For the grain size distribution and circularity analysis, it was employed a dynamic image analysis method. It consists of homogeneously immerse the particles into a liquid, then they go through a thin cell in the optical path. The cell is hit by a light source and the profile of the particles is projected and captured by a high-resolution camera with a focusing lens. The software provides some geometrical and statistical models to analyze shape and size distribution. The model used in this work is named Equivalent Circular Area (ECA). It represents the projected area of each particle as a perfect circle with the same area, giving an Equivalent Circular Diameter (ECD). Thus it is possible to define the grain size distribution of the powder. It is also possible to calculate the circularity, as a relation between the projected area and the area of a mathematically perfect circle.

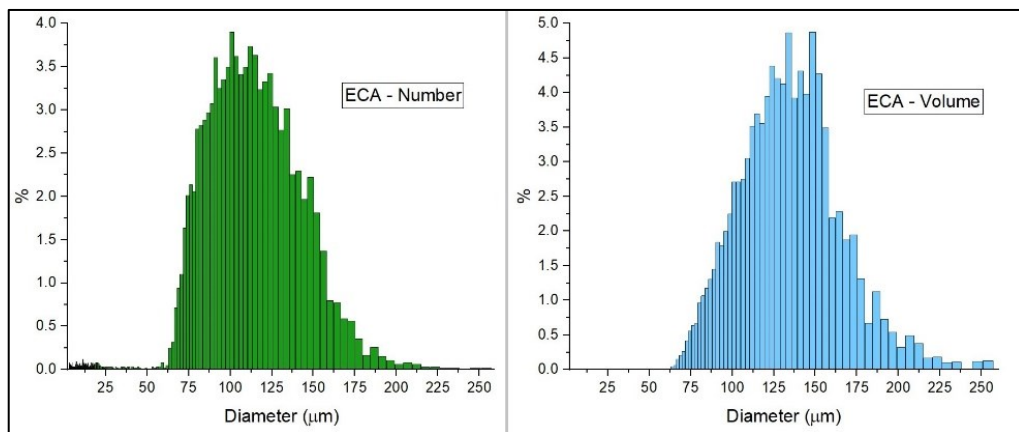
Figure 41 – Flowchart of the applied method.



Source: Author (2019).

The equipment that was used to perform the analysis was a Particle Insight of Vision Analytical, with a software Particle Shape Analyzer 2.55. The samples were taken according to the ASTM B215 standard [83] and it was analyzed an amount of 8562 particles. The results are given in terms of number and volume. The main difference between them is that “number” counts the number of particles for each diameter and “volume” projects a volume based on the ECA, giving an idea of how each particle impacts the total volume analyzed. The distributions are shown in Figure 42.

Figure 42 – Equivalent circular diameter of metallic powder exposed by number (left) and volume (right).



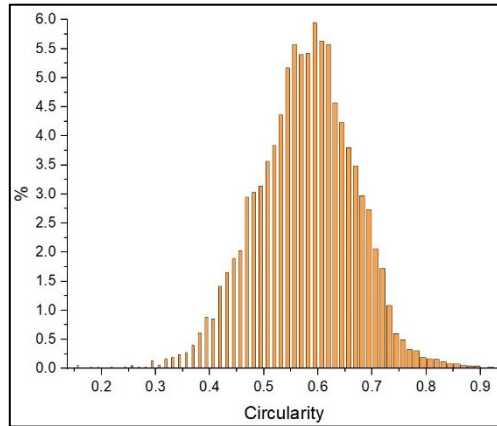
Source: Author (2019).

In the number evaluation, it was found a mean of 105.6 μm and a mode of 101.1 μm . Analyzing the distribution is possible to see a little number of particles with a low ECD (around 3 and 30 μm). They may be really small particles, little bubbles captured during the acquisition of images, or even satellite particles detached. The distribution was concentrated and the mode and mean were close to the median, so it was considered a good particle distribution. Looking at the volume distribution it was observed that those little particles disappeared. It was concluded that those particles are not relevant in the final volume of material that will be processed.

Another feature analyzed was circularity, shown in Figure 43. It was observed a mean of 0.575 and a mode of 0.594. The D_n50 is the equivalent diameter below which 50% of the number of particles is inside. The D_v50 is the equivalent diameter below which 50% of the volume of particles is inside. Both these values and the most important information about Particle Insight Analysis are shown in Table 4 (the analysis are made based on a Gaussian

distribution). The complete report may be seen in ATTACHMENT B – Particle Insight Report.

Figure 43 – Circularity of the metallic powder.



Source: Author (2019).

Table 4 – 316L powder characteristics obtained through Particle Insight Analysis.

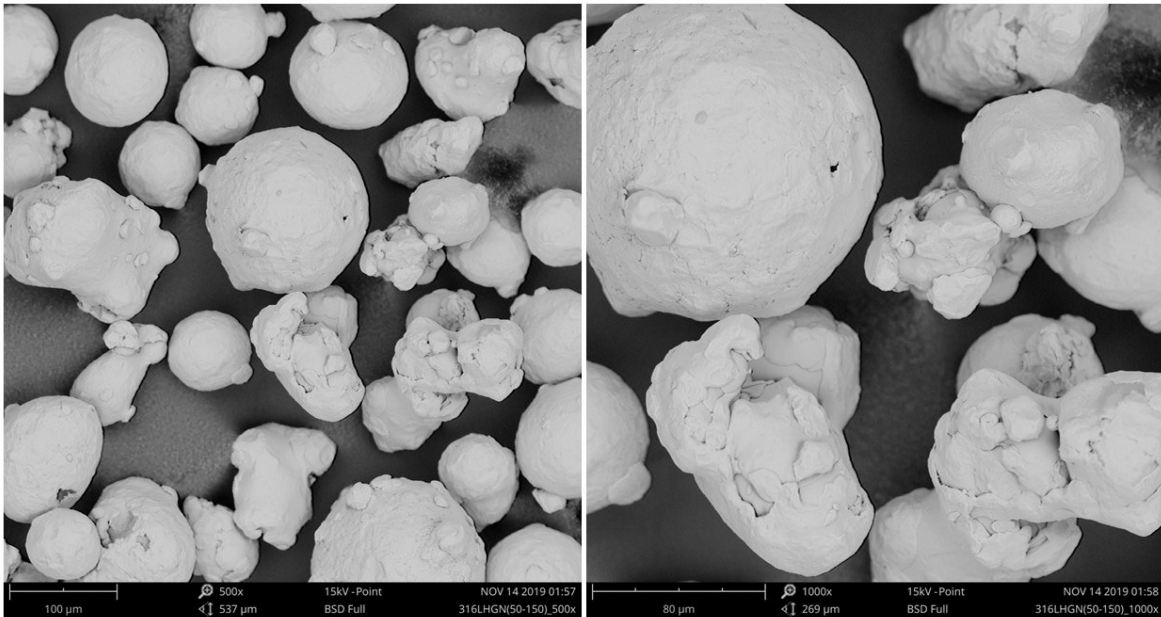
Number of particles analyzed: 8562			
Minimum equivalent diameter		3 μm	
Maximum equivalent diameter		292.9 μm	
Mean equivalent diameter		105.6 μm	
Standard deviation		31.9 μm	
Mode		101.1 μm	
Circularity (mean)		0.575 μm	
Number Analysis		Volume Analysis	
D_n10	74.3 μm	D_v10	91.4 μm
D_n50	104.3 μm	D_v50	127.8 μm
D_n90	145.4 μm	D_v90	167.2 μm

Source: [84].

The morphology of the powder was also performed with a Field Emission Gun - Scanning Electronic Microscopy (FEG-SEM) analysis, and is shown in Figure 44. The equipment used was a Zeiss Supra 55VP, working energy 0,1-30 kW, and working distance 1-20 mm. Most particles showed good spheroidicity but there were some with an elongated shape. There were also a great number of satellite particles. Both of these characteristics may difficult the flowability of the powder. Some surface pores were observed. These pores were better analyzed with cross-section preparation. Some powder was put into bakelite, ground, and polished. The cross-section was analyzed using a Zeiss Axio Imager M2m (50-1000x

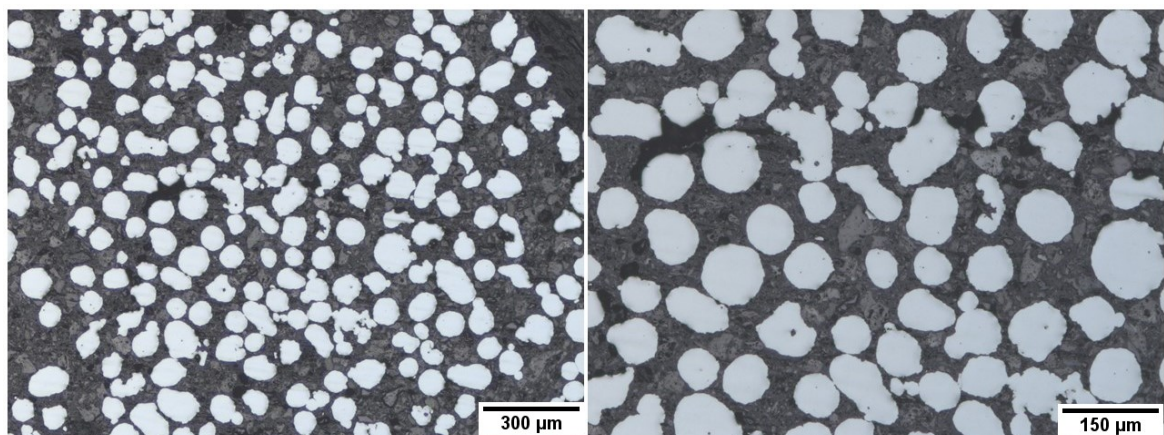
magnification) optical microscope and is shown in Figure 45. It was identified small pores inside of the particles, with dimensions between 3 and 30 μm . These pores may be transferred to the final part. When analyzing the layers or multilayers porosity that characteristic must be considered.

Figure 44 – FESEM morphology analysis, 500x (left) and 1000x (right) magnification.



Source: Author (2019).

Figure 45 – Optical microscopy of powder cross-section for pores evaluating, 50x (left) and 100x (right) magnification.



Source: Author (2019).

It is important that all the characterization of the metallic powder be analyzed together, considering that each one complements the other. There is not an acceptable range

or cut-off criteria. All the results must be analyzed qualitatively, at least until there is a database enough for this kind of material, this process, and this equipment setup, that enables to compare the results. Taking it to account, the characterizations previously exposed are important to help to create a database that may help to understand the relation between powder features with its processability and the characteristics of the final parts obtained.

4.2 SUBSTRATE CHARACTERIZATION

The base material (substrate) was defined taking into account the filler metal selected for this work. The characteristics of the substrate are important especially in the Modeling Stage, where the single layers are deposited. The chemical composition of the substrate was quantified with the Optical Emission Spectrometry (OES) technique. In this method, the elements are excited by an electrical discharge that produces plasma over the material. These elements produce some radiation that can be measured, identifying the elements and their amount. The equipment employed was the Oxford Foundry-Master Pro, using between 3 and 4 bar of argon pressure. The results are shown in Table 5:

Table 5 – 316L substrate chemical composition.

	Cr	Ni	Mo	Mn	Si	P	S	C	N
316L Substrate	16.375 ±0.3403	10.875 ±0.5315	1.9975 ±0.025	1.2225 ±0.078	0.495 ±0.048	0.0298 ±0,0022	0.0013 ±0,0005	0.0225 ±0,005	NA
ASTM A240 [85]	16.0-18.0	10.0-14.0	2.00-3.00	2.00	0.75	0.045	0.030	0.03	0.10

NA - not analyzed.

Source: Author (2019).

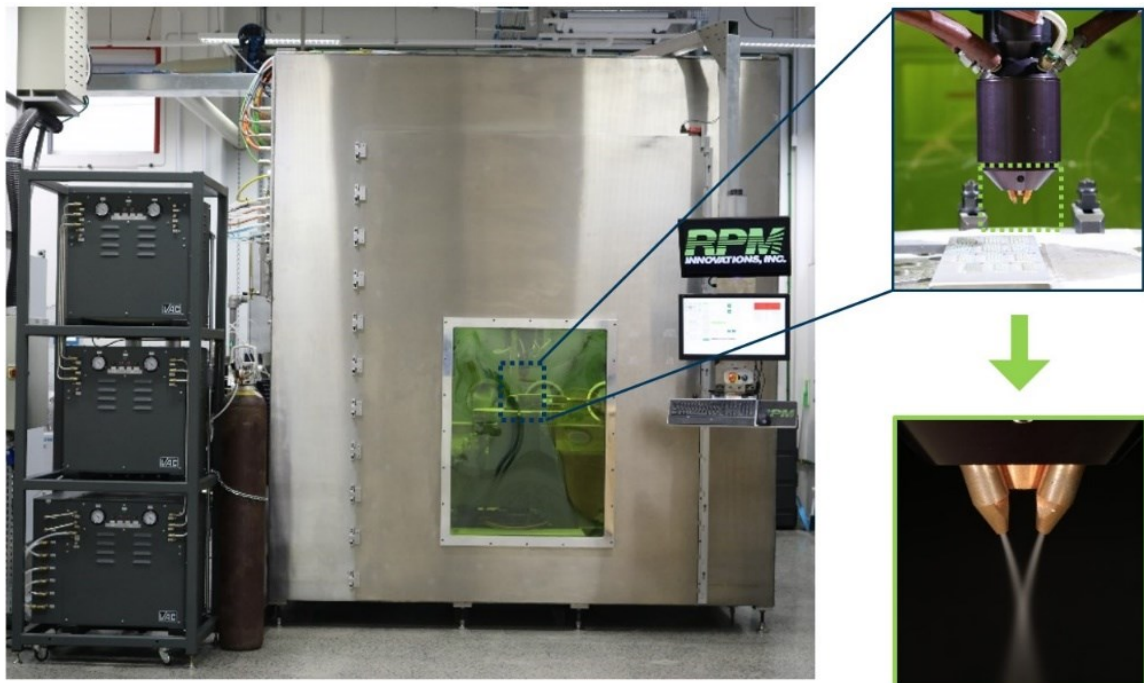
The substrate was provided in bars of 76x16x6000 mm. They were cut into sections of 250 mm length using a Timemaster 10” Horizontal Band Saw. To maintain the same heat dissipation conditions in all of the used substrates, the length of the plates was maintained constant with a maximum tolerance of ±3 mm. The reflection is another feature related to the substrate that is very much relevant to the process. If the surface of the substrate is not opaque enough, the laser beam may reflect too much, which will decrease the amount of energy absorbed by the substrate. To standardize the surface condition, all the plates were blasted with a micro-blasting machine, model Iepco Peenmatic 620, using iron shot model MS 90 150 A with size distribution between 75-150 µm. The opacity and homogeneity of the surface

were visually inspected. To avoid contaminations, once blasted, the surfaces were cleaned using a paper towel and ethyl alcohol 96.

4.3 EXPLORATORY STAGE

The Exploratory Stage was carried based on the methodology described in Chapter 3. The powder was dried in a dry heat sterilizer (TECNAL TE-393/2) at 80 °C for 4 hours. For that procedure, it was used a 2000 ml beaker to dry 3 kg of powder. The powder feeder was previously cleaned to avoid cross-contamination between the powder previously used. Bag tests⁸ were carried before the depositions to assure the correct federate. The test ends just after two consecutive measurements with the correct feedrate $\pm 0,3$ g. For all the deposition of this study, it was used an RPM Innovations 535 deposition system with a 25° nozzle (Figure 46), which the main characteristics are exhibited in Table 6. This equipment is powered by a 3000 W laser source (IPG Photonics YLS-3000-CT). The laser source and optical set features are described in Table 7.

Figure 46 – RPM Innovations 535 with 25° nozzle.



Source: Author (2021).

⁸ Bag test is a calibration that consists on capturing the powder expelled by a nozzle during one minute using a plastic bag. After that, the powder is weighted. The device is adjusted and the procedure is repeated until he desired mass be achieved.

Table 6 – RPM Innovations 535 features.

Characteristic	Value	Unit
Axes	5	-
Max travel speed	3810	mm/min
Movement precision	0.025	mm
Max building dimensions	1524 x 914 x 1524	mm ³
Oxygen level (purged)	< 5	ppm

Source: [86].

Table 7 – Laser source and optical set features.

Solid-state laser	Ytterbium-doped Optical Fiber
Transmission	Optical fiber
Fiber core diameter	300 μ m
Collimator lens	38.1 x 103.0 - P/N: 900-0300-120-A
Focus distance	229.09 mm
Spot size	800.5 μ m
Power	3000 W
Wavelength	1064 nm
BPP	10.02

Source: [86, 87].

The processing windows were defined based on previous knowledge about the equipment and alloy. It was set four levels of power, four of scanning speed, and three of powder feedrate. The laser spot diameter remained constant. Table 8 shows all the parameters.

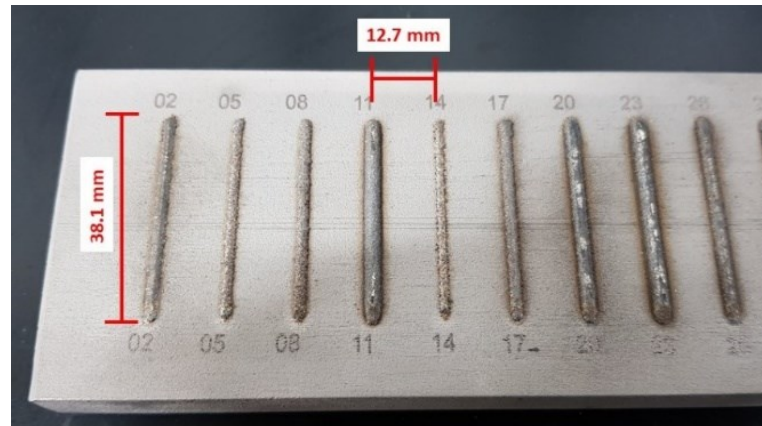
Table 8 – Exploratory Stage parameters.

Spot size [mm]	1.78
Power [W]	1000 / 1400 / 1800 / 2200
Travel speed [mm/min]	500 / 1000 / 1500 / 2000
Feedrate [g/min]	20 / 30 / 35

Source: Author (2020).

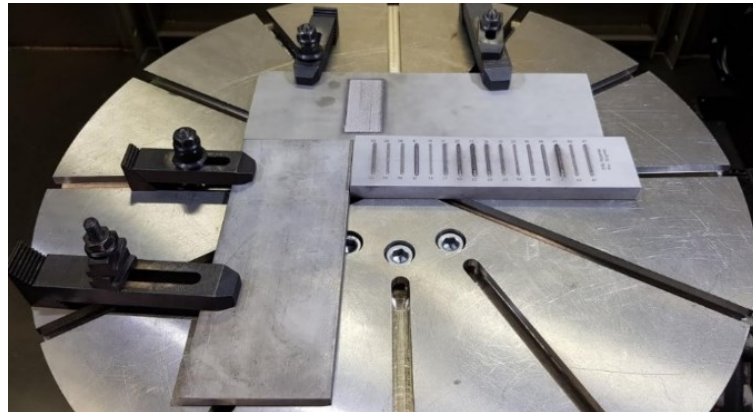
It was deposited a total of 48 single beads. They were made with 38,1 mm length and 12,7 mm spaced each other, as seen in Figure 47. Three substrates were used, with 16 single beads each. After each deposition, the substrate was changed, maintaining the temperature of the substrate similar in all the depositions. Two plates were fixed on the working table to guarantee that the positioning of the substrates was always the same, as shown in Figure 48.

Figure 47 – Exploratory Stage deposition.



Source: Author (2020).

Figure 48 – Substrate positioning setup.



Source: Author (2020).

For the single beads it was not necessary to measure the temperature before each deposition, considering that by touching, the substrate was cold enough just cooling along the time between the depositions. The order of the processing parameters chosen was aleatory, and they were noted during the process, to link each bead number to its corresponding parameter.

The next step was the application of die penetrant liquid to observe the presence of cracks, pores, and lack of fusion. The die penetrant liquid (METAL-CHEK VP30) was applied over the surface and let to penetrate for 10 minutes. After that, the surface was washed with running water and cleaned with a brush to remove the excess of the product. The samples were dry using compressed air. After dried, the revealing liquid was applied (METAL-CHEK D70) and let act for 30 minutes. Then, it was possible to visualize the presence of defects by visual inspection.

After finished the die penetrant liquid inspection, the height was measured. In this case, the measure was done using a digital height caliper gauge (MITUTOYO HDS 0-300 mm). Two measures were done, one by each side of the substrate (beginning and end of the bead). The average was used to define the total height.

Using all the previous information it was possible to select the processing window that would be used in the next stage of the methodology. Once the processing window was selected, all the selected single beads had their width measured. That information was used as an input to define the hatch spacing in the Modeling Stage. Width measures were done by taking top pictures using a Stereoscope (ZEISS Discovery V8) with 10x magnification. The images were analyzed using ImageJ (an open-source software) for measuring the widths.

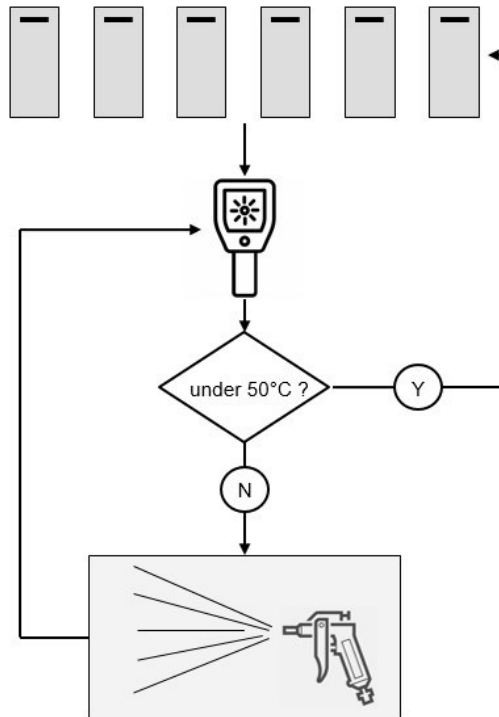
4.4 MODELING STAGE

In the previous stage, a processing window was selected. The limits of this experiment were set aiming to extrapolate the limits of the “good window” previously selected. That approach guarantees that any good processing zone was left behind. The power range was set between 900 and 1900 W and the travel speed between 762 and 1778 mm/min, both varying in four levels. The mas flow was constant in 30 g/min and there was another variable introduced, the hatch spacing. Hatch spacing was tested in three levels, maintaining the same number of samples (48) of the Exploratory Stage. To define the values of hatch spacing it was calculated the average width of all the selected single-beads. Using the average width it was set the three levels of hatch spacing as 20, 35, and 50 percent of overlapping (applied to the average), which was considered a good range to contemplate all the possible good results. Using that range it was expected to obtain most layers with processable results. It was decided to use 6 substrates. The same procedures for drying powder, feedrate calibration, and substrates positioning were adopted.

The heat input linked to the deposition of single layers is considerably higher than single beads. It was necessary to be careful and guarantee that this temperature variation did not have any significant influence on the final results. To assure that, it was set a deposition strategy. Three random parameters were deposited, one on each substrate, and before the first substrate was used again all of them had their temperature measured using a thermal camera (IRISYS IRI4030-00). The experiments continue just after all of them had their temperature under 50 °C as represented by the scheme in Figure 49. An argon flow was used to help to

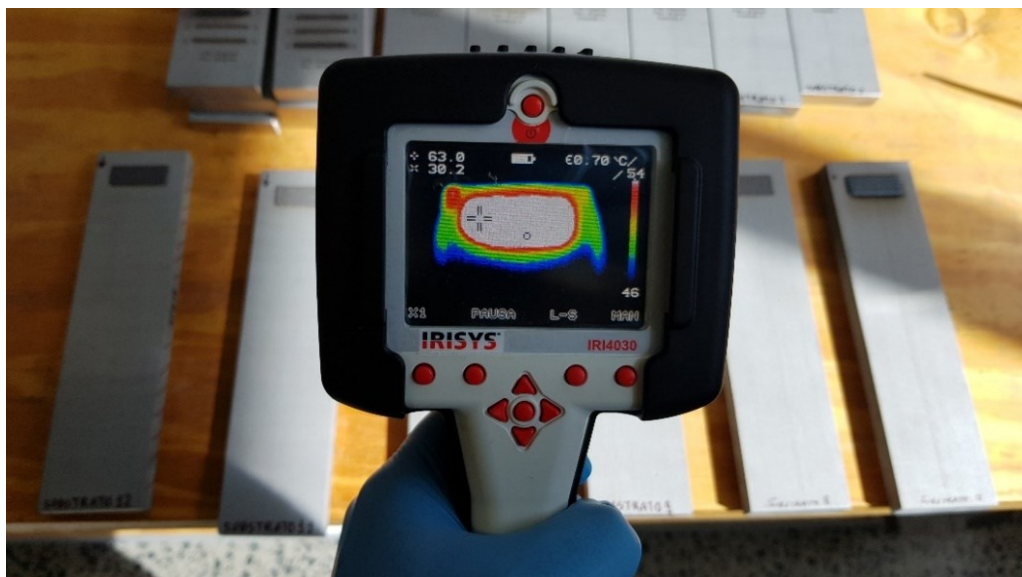
cool down the substrates, and the emissivity used in the camera was 0,7. Figure 50 exhibits a thermal camera measurement done during that procedure.

Figure 49 – Substrate heating control.



Source: Author (2020).

Figure 50 – Thermal camera inspection to assure temperature homogeneity in the Modeling Stage.



Source: Author (2020).

After the deposition, the samples were laser marked and it was applied a die penetrant inspection just as previously described in the Exploratory Stage. The leaving of die penetrant inspection was washed and the substrates with the deposited layers were cut in cross-section. The layers were separated from each other and cut in half using a horizontal band saw. After that, they were hot embedded in bakelite (AROTEC PRE 40). The surfaces prepared were always those cut with the cut-off, because they had a better surface finishing. The preparations were done using a grinding and polishing machine (AROTEC Aropol 2V) with 80, 220, 400, 600, 1200 sandpapers, and polished with diamond polishing paste (CHRISTENSEN RODER JP-1). The etches were made with hydrochloric acid (4 g CuSO_4 + 20 ml HCl + 20 ml H_2O) for around eight seconds and stopped in water. The macrographs were done using a Stereoscope (ZEISS Discovery V8) using 10x magnification.

With the macrographs in hand, all the measurements were taken using ImageJ software. The results were recorded in a spreadsheet and were the input data for the regression analysis.

4.5 OPTIMIZATION STAGE

The software responsible for carrying out the regression analysis was R-Statistic. It was chosen a polynomial of the third degree for the regression analysis. It appeared to be a good option because a polynomial of the second degree is very hard to fit the response, because of its limited shape. With a polynomial of the fourth degree or higher what happens is the opposite, the surface suffers too abrupt changes, which is called overfitting. Overfitting is undesirable because it makes the trends harder to analyze. Regression analysis is iterative, so the quality of the results will depend on the domain that the user has over the tool and the physics of the process. It is desirable to achieve response surfaces that better describe the trending of the manufacturing process. The number of variables and the p-value were adjusted, minimizing overfit. The surface was analyzed and compared to the physics of the process, to see if the trendings made sense. The number of terms of the polynomial was adjusted changing the p-value until a satisfactory result was obtained.

The desirability was defined according to what was needed from the process to achieve a final part with the desired features. Five desirability criteria were used, which together formed the global desirability. They were dilution, waviness, height, capture efficiency, and layer-slope. The limits defined for each one are exposed in section 5.1.3, where there is a discussion linking the limits to the results obtained.

Once the optimal parameter was obtained, it was necessary to verify it, to check if the model corresponded to reality. It was done through the deposition of a layer using the parameter that was obtained. The layer was cut in cross-section, prepared, and measured in the stereoscope. The results measured were compared to those that were predicted. The parameter was verified to see if all the outputs attended to the range previously set for desirability. It was not defined a range around the predicted outputs, once the prime goal was to attend the desirability criteria.

4.6 MULTILAYER STAGE

The approach used was to deposit simple multilayer geometries in block shape (25.4 mm x 25.4 mm base x 12.7 mm height) varying the overlayer from 0% to 25% at the step of 5%. The blocks were analyzed about the presence of pores and voids aiming to find the best balance between productivity and quality.

4.7 CHARACTERIZATION STAGE

Samples were deposited to furthermore be submitted to tensile test, impact absorption test, Vickers microhardness, microstructure, and porosity. After that, all the related analyses were carried. The specifications of each characterization are described in Table 9.

Table 9 – Specifications of the characterizations.

	Number of samples	Number of conditions	Standard	Equipment
Tension test	9	3	ASTM E8 ¹⁰	Instron 5988
Impact absorption test	9	3	ASTM E23	Instron Charpy Impact Tester
Vickers microhardness	4	1	ASTM E384	Wilson Knoop/Vickers Tester 402MVD
Microstructure (OM)	4	2		Zeiss Axio Imager M2m
Porosity (OM)	4	1		Zeiss Axio Imager M2m

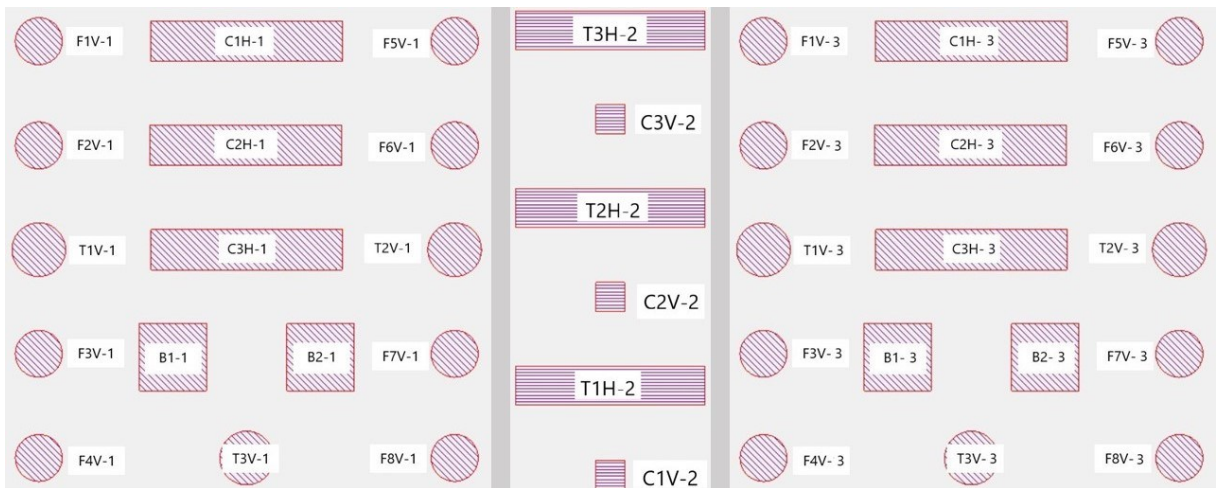
Source: Author (2020).

The deposition was done in three separate manufacturing buildings. Build 1 includes 8 samples for fatigue behavior (that will not be analyzed in this study), 3 samples for tensile (built vertically), 3 samples for impact absorption (built horizontally), and two blocks for

¹⁰ Specimen 2.

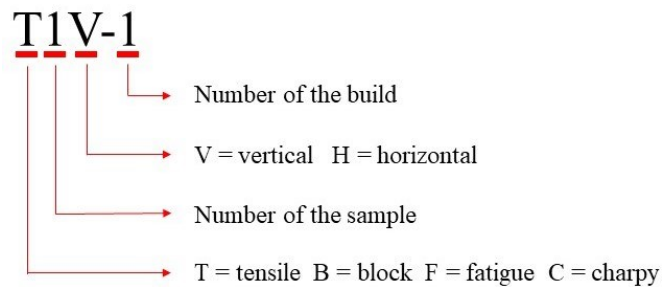
microstructure analysis and microhardness. Build 2 includes 3 samples for tensile (built horizontally) and 3 samples for impact absorption (built vertically). Build 3 was deposited aiming to compare the results before and after heat treatment. It has the same configuration as build 1 to maintain all the characteristics of cooling rate, dwell time, and other features inherent to the process. After the buildings were finished, builds 1 and 2 were sent for the heat treatment of stress relief for 6 hours at 550 °C and solubilization for 2 hours (1 hour for a soak and 1 hour for the treatment) at 1070 °C and cooling under 260 °C in saline solution (the graphics for the heat treatment of stress relief and solubilization may be accessed in ATTACHMENT C – Stress Relief Heat Treatment Report and ATTACHMENT D – Solubilization Heat Treatment Report respectively). Figure 51 shows the nomenclature for each sample (the sequence of deposition is exhibited in ATTACHMENT E – Sequence for the Deposition of Specimens). The meaning of the nomenclature is explained in Figure 52.

Figure 51 – Sample nomenclature for build 1 (left), build 2 (center), and build 3 (right).



Source: Author (2020).

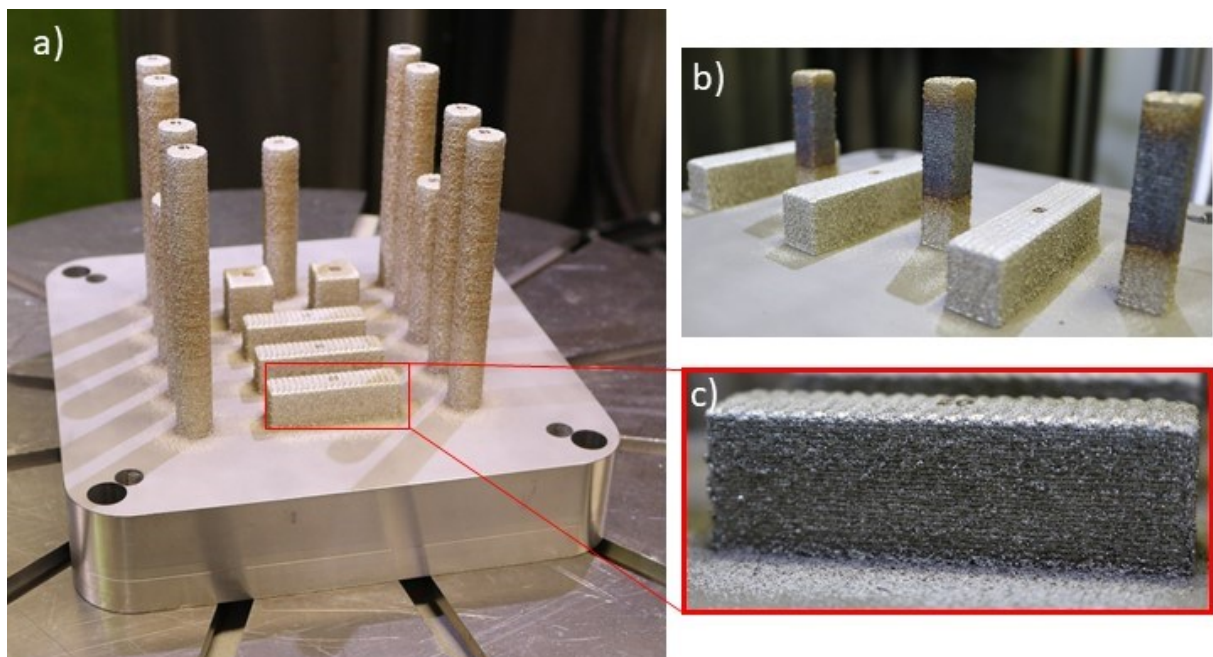
Figure 52 – Sample nomenclature.



Source: Author (2020).

The samples had 1 mm overbuild in each direction for machining. It was also included 4 mm on height to remove the first 4 mm of deposition. This strategy aims to remove the first layers that generally have a higher amount of pores due to higher cooling rates. The tensile samples were modeled in a circular cross-section shape when deposited vertically and a square cross-section shape when deposited horizontally. That strategy was taken aiming to keep the building as more homogeneous as possible. Considering the process limitations, the horizontal samples for tensile analysis would have a more heterogeneous stress distribution if deposited with a rounded size. The hatching angle variation was set at 45 degrees, forming a configuration of 0/45/90/135/180/225/270/315 that was repeated until the end of the deposition. In Figure 51 it is possible to see hatch angles of 0° (center) and 135° (right and left). There was no dwell time between layers for build 1. In build 2, it was set 10 seconds of dwell time between layers after finished the tensile samples. Once the tensile samples were finished, the time between depositions of the charpy samples would be different, so would be the heat input on them. The dwell time was set to try to decrease the difference between these two different processing conditions. In Figure 53 it is possible to see the samples in the “as-built” condition. The magnification exhibits the finishing condition of an impact absorption sample.

Figure 53 – Buildings of samples. Build 1 (a), build 2 (b), and magnification on the surface of an impact absorption sample from build 1 (c).



Source: Author (2020).

4.8 CALIBRATIONS

To guarantee the repeatability of the process, such as its accuracy, it was necessary to do some calibrations. That way it was possible to assure that every variation observed in the final parts was related to the process conditions and was not related to equipment inconsistencies.

4.8.1 Laser Power

The calibration consists of getting 10 values of laser power, varying from 10% to 100% through a power meter. After that, the measured output was compared to the output shown by the software. In sequence, a correction table was applied to fix the inconsistencies. The main goal was to guarantee that the programmed power was the same that the power emitted.

During this procedure, it was used a PRIMES PMT 70icu power-meter and two measures of each power level were done. It was necessary to position the power-meter over thermally insulating material to avoid heat dissipation to the table. It was used a polystyrene plate for that. It was also necessary to cool the power meter until 25 °C after each measurement, emerging it in cold water. After that, the power-meter was dried using compressed air. Figure 54 shows a laser power measurement being acquired.

Figure 54 – Laser power calibration procedure.

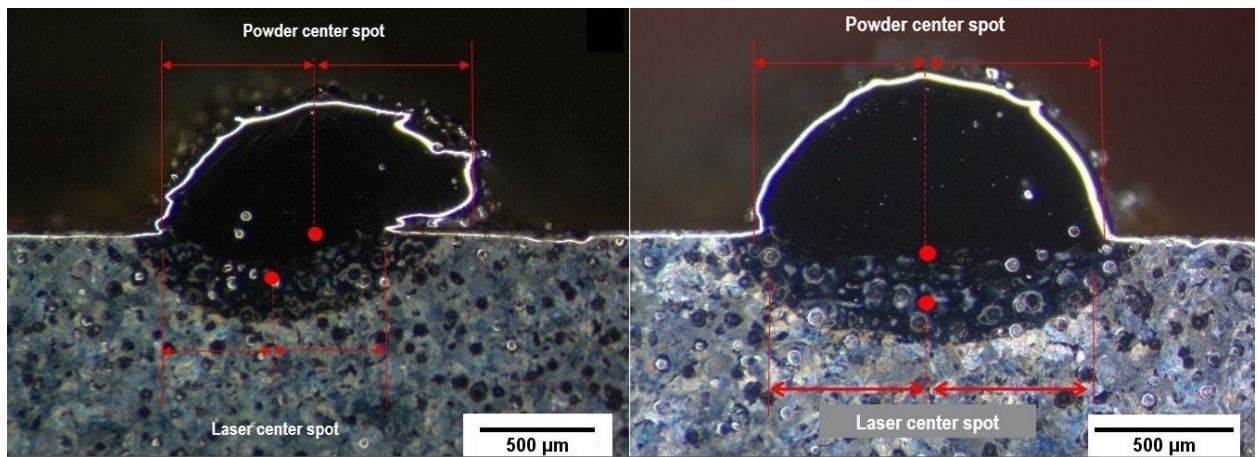


Source: Author (2019).

4.8.2 Laser and powder spots alignment

The Laser beam and the powder spot must be concentric, otherwise, some distortions on the single bead may be observed, which can generate defects and distortions on the final part. Figure 55 exhibits the difference between the cross-section of a single bead with powder spot and laser spot misaligned and after adjusted, using the same processing parameters and conditions. The difference between them is very clear, showing the importance of this procedure.

Figure 55 – Difference between the cross-section of a single bead with powder and laser spot misaligned (left) and aligned (right).



Source: Author (2019).

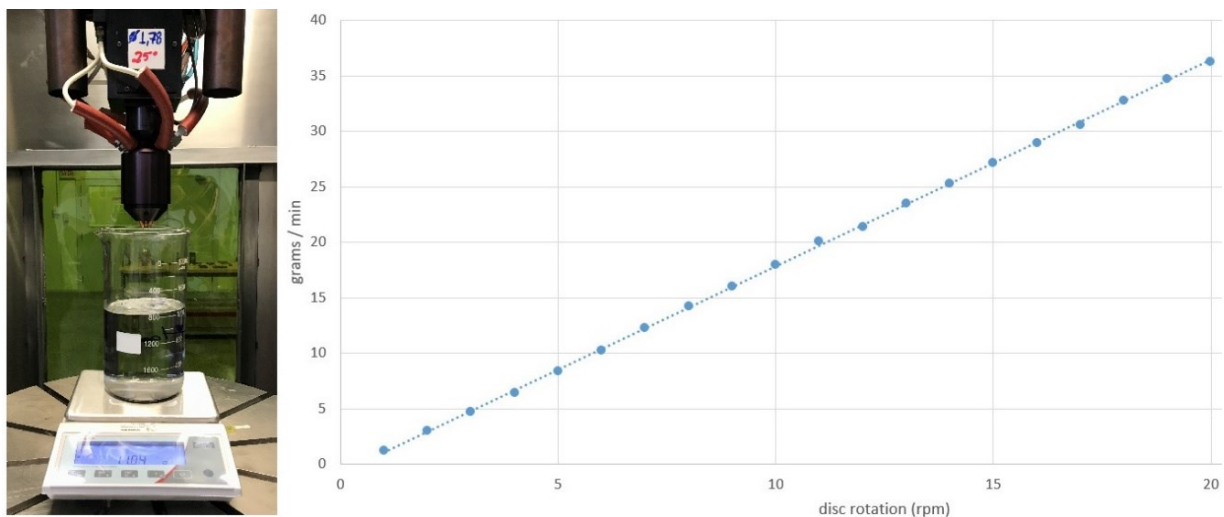
The procedure consists of painting part of a substrate using a permanent marker. After that, the headstock was positioned over the painted area, with the correct stand-off distance, and the powder feeder was turned on for a while, long enough to take off the painting of the incident area. In sequence, a fast laser pulse is performed. The center of the two marks was compared, and if they were not the same, some adjustments were done. The powder focus position cannot be modified, because it is fixed. What was done was to centralize the laser beam to the powder spot by moving the turning mirror. The turning mirror is responsible for turning the collimated laser beam coming from the fiber output to the processing direction. The procedure was repeated until both spots were in the same place.

4.8.3 Powder Feedrate

The metallic powder used as an additive material is fed by the powder feeder system. It consists of a perforated disc that spins in contact with the metallic powder. With the assistance of carrier gas, the powder is carried until the nozzle, where the deposition process happens. The amount of powder that is delivered to the melt pool is defined by the rotation of the perforated disc. It was necessary to calibrate the curve that links the rotation of the powder feeder to the corresponding feedrate.

The procedure consists of letting the powder flow steady (around 30 seconds) and after that move the headstock over a beaker filled with water. The height between the surface of the deposition nozzles and the edge of the beaker was as smallest as possible. By doing that procedure the losses to the atmosphere were irrelevant. The mass flow stayed for two minutes into the water. The beaker was positioned over an electronic scale. The procedure was repeated from 1 to 20 rpm at the step of 1 rpm. In the end, the results were plot, relating the rotation with the powder feedrate. Before any change of feedrate in a group of depositions, the necessary rotation was calculated based on the calibration and a bag test was performed to assure the correct powder feedrate. The arrangement of the procedure and the corresponding results are shown in Figure 56.

Figure 56 – Feedrate calibration arrangement (left) and resultant straight (right).



Source: Author (2019).

5 RESULTS AND DISCUSSIONS

This section will be split into three parts. The first section will show the results obtained from the application of the methodology. These results led to the optimized parameter that was used to build the samples. The second section will exhibit the characterization results aiming to verify the capability of the methodology on producing parts with good mechanical properties. The third section will show the lessons learned from the first try on the application of the methodology. Some problems were observed in this first try, which required some changes in the methodology, leading to the final shape exposed in chapter 4.

5.1 METHODOLOGY

The results for the application of the methodology will be exhibited according to the stages previously exposed in chapters 3 and 4.

5.1.1 Exploratory Stage

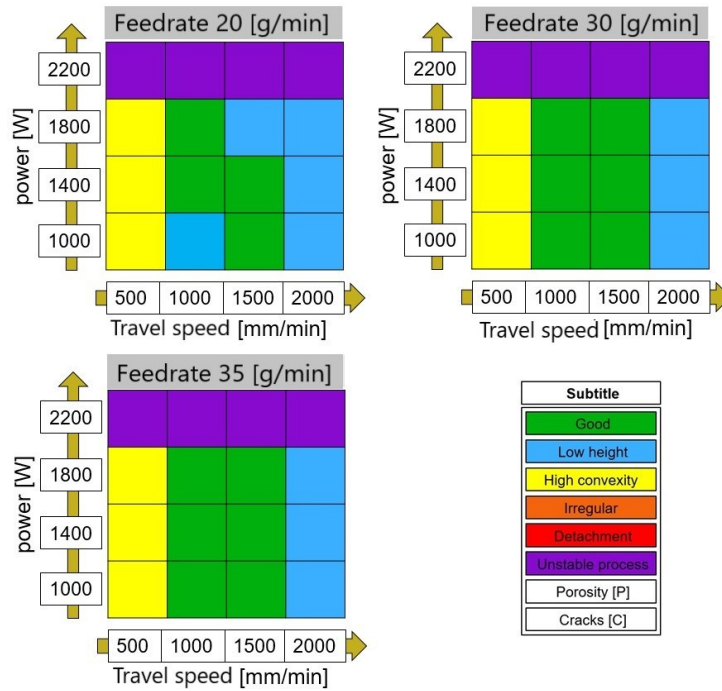
The single-beads categorization was made according to Figure 57. All the depositions using the highest power (2200 W) exhibited an unstable process. It was observed through the excess of spatter and what appears to be starting the formation of a keyhole. These parameters were discarded because they could damage the focusing lens and in a long time deposition would generate distortions due to the high heat input. A constant behavior was also observed in the lowest travel speed (500 mm/min) where all the single beads had high convexity¹¹. The low speed delivers higher energy and a higher amount of powder per unit of length, resulting in higher and more convex single beads. On the other hand, the single-beads with the highest travel speed (2000 mm/min) showed a low height¹². This case is exactly the opposite of the previous one, with lower energy and amount of powder per unit of length, resulting in low and flat single-beads. Considering the color graphics changes vertically and not horizontally, it is possible to affirm that the travel speed has much more influence on the shape of the single-beads than the power. That behavior is because travel

¹¹ The images of all single beads may be accessed in APPENDIX A – Single Beads Images and the processing parameters may be seen in APPENDIX B – Processing Parameters used in Exploratory Stage.

¹² The height measured on all the single beads are available in APPENDIX C – Single Beads Height.

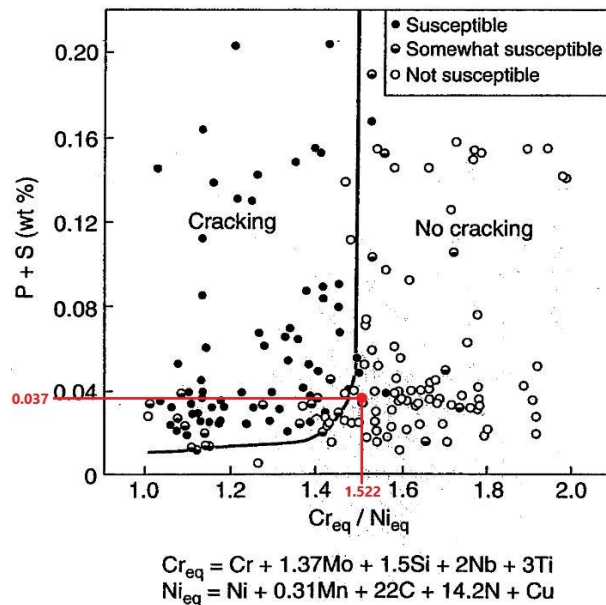
speed interferes in more than one behavior (line energy and powder delivery per length) while the laser power just interferes with the amount of energy delivered. It was not observed any surface pores and cracks through die penetrant liquid. The lack of cracks was expected according to the application of the Suutala Diagram (Figure 58).

Figure 57 – Single-beads categorization.



Source: Author (2019).

Figure 58 – Application of the Suutala Diagram.



Source: Adapted from [18].

Two good processing windows may be easily observed, one with 30 g/min and one with 35 g/min. It was decided to move on with the 30 g/min window, once the 35 g/min window did not represent a great improvement of height and the feeding system for that feedrate started to show some instability, once it was very close to the maximum feeding rate of the powder feeder. It was decided to set the range of power between 900 and 1900 W so it extrapolates the limits previously set. The same was done with the travel speed, varying from 762 to 1778 mm/min. Both were split into four levels, making it possible to obtain a good number of points for the regression analysis.

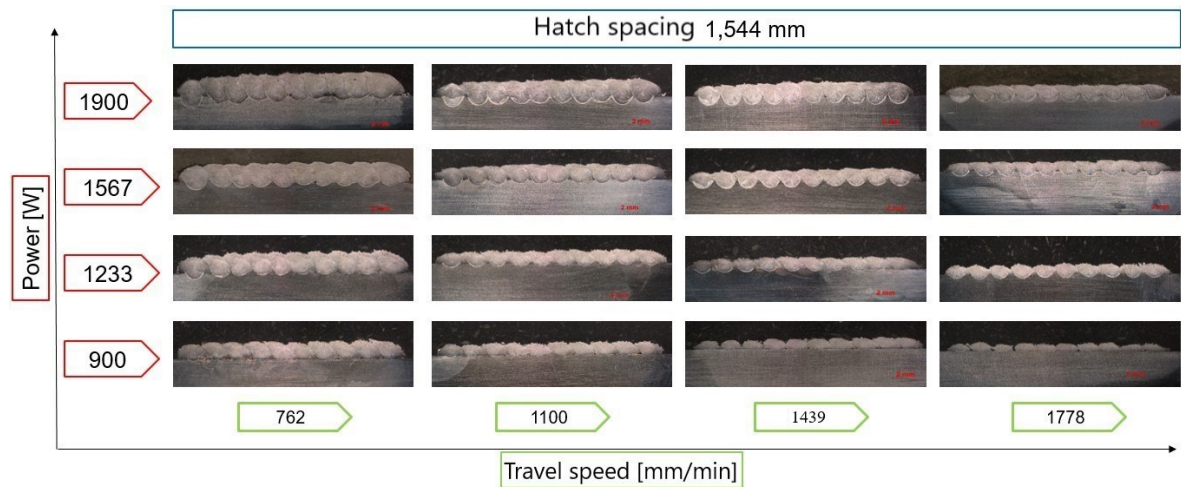
5.1.2 Modeling Stage

At this stage, the feedrate remained constant (30 g/min) and the windows were split into the three levels of hatch spacing (1.544, 1.254 e 0.965 mm)¹³. The cross-sections of 1.544 mm of hatch spacing are shown in Figure 59¹⁴. The two extremes of shape were observed in this window. The first one (1900 W and 762 mm/min) had a higher thickness because single beads were too big at a point that they began to overlap more and more. The last bead had almost no dilution because most of the energy was used to melt the previous bead and there was no energy enough to melt the substrate. The opposite occurred with low power and high speed (900 W and 1778 mm/min). The beads were small and in this situation, the hatch spacing was big enough to completely separate some of them. The amplitude of the tested window was intentionally planned so that it was possible to model the behavior of the process with a greater range of behavior and, thus, make it possible to obtain an optimized parameter.

¹³ The three levels of hatch spacing were calculated based on the mean width of all selected single beads, applying 20%, 35%, and 50% overlapping. The width measured on single beads are available in APPENDIX D – Single Beads Width. The values for all parameters Modeling Stage is available in APPENDIX E – Modeling Stage Parameters.

¹⁴ The cross section of all single layers is available in APPENDIX G – Single Layers cross-sections.

Figure 59 – Cross-sections of single layers.

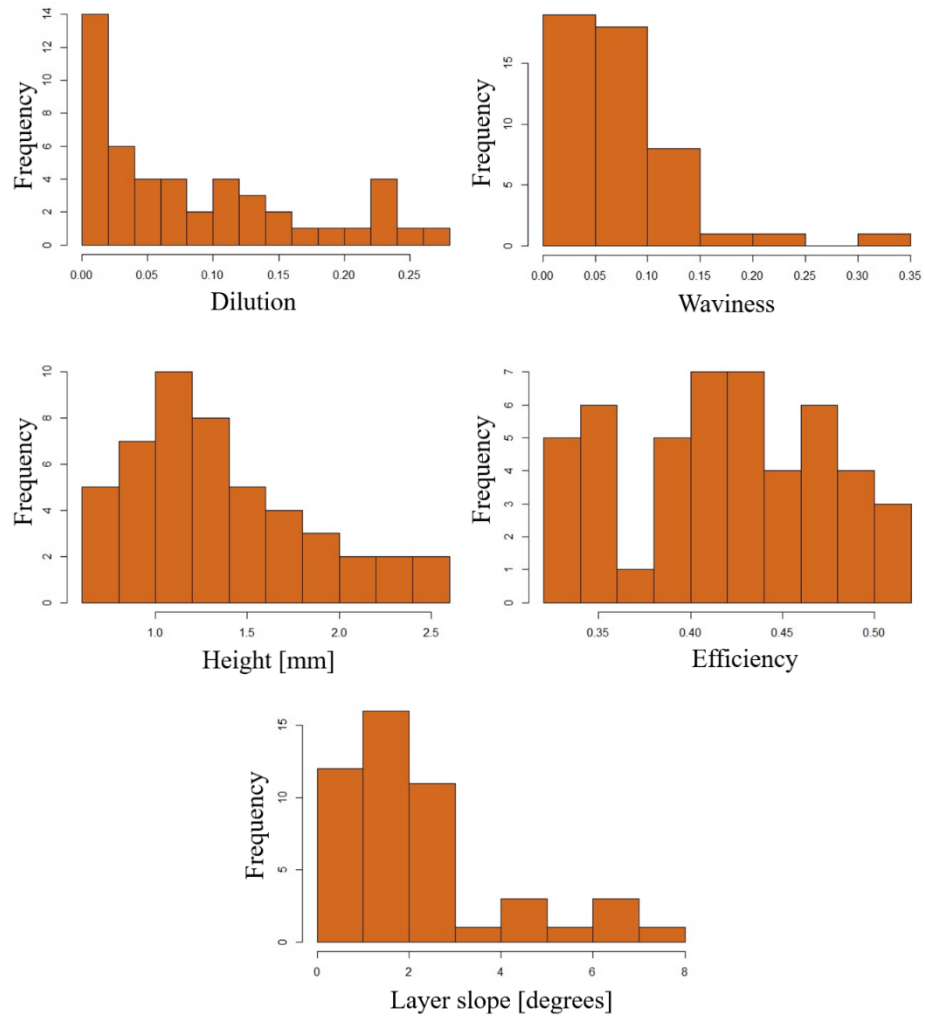


Source: Author (2020).

After the measurement of all the layers¹⁵, it was possible to plot a histogram for each output that was analyzed. Using this tool it was easier to have a holistic view of the cross-section characteristics, as exposed in Figure 60. It was possible to see many occurrences of 0% dilution. This behavior was seen often when the hatch spacing was too low, so the heat from the laser beam was majorly dissipated to the previous bead and there was no power enough to melt the substrate and cause a metallurgical bond. The layer slope was another output that corroborates the fact that the hatch spacing was too low. Even most depositions were under the maximum accepted angle, there were many occurrences of higher angles, which led to distortions and process instabilities. It was possible to observe these two behaviors in Figure 61. Height, waviness, and capture efficiency did not show to be limiting factors for the selection of the optimum processing parameter.

¹⁵ The results for the measurements of all single layers is available in APPENDIX H – Single Layers Measurements.

Figure 60 – Histograms of cross-section measurements.



Source: Author (2020).

Figure 61 – Cross-section of deposition with high layer slope and decreasing dilution due to low hatch spacing (the deposition starts from the left).



Source: Author (2020).

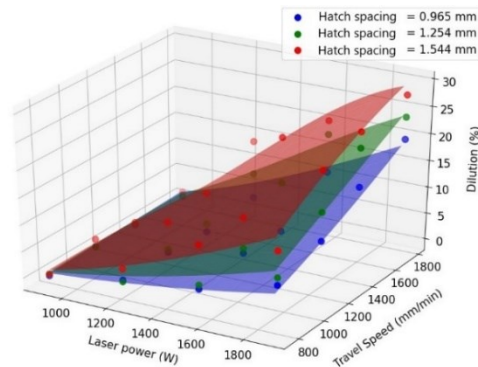
5.1.3 Optimization Stage

The intend of using multiple regression is to link the processing parameters to the final part characteristics. For that representation to have a good quality, it is necessary that the response surface be as close as possible to the dots that represents the experiments, but without overfitting. The suitability of the experiments' data to the surface response is given by the R-square adjusted. When the overfit occurs it is not possible to use the regression for predicting a behavior once the response has good mathematic suitability but very bad physical suitability. Adjusting the parameters of the regression it was possible to achieve all the responses without overfitting trend. The minimum R-square obtained was 0.88 and the minimum adjusted R-square was 0.87. These two information heads to regression surfaces that represent very well the physical phenomenons present in the process, correlating the input processing parameters to the output geometrical characteristics.

An important factor related to regression analysis is the p-value. It is a number that can indicate how much a model is incompatible with its source data. Informally, the closer the p-value is to zero the better. It is usually recommended to use less than 0.5. These results were obtained using a p-value in the order of 10^{-16} , which shows that the regressions are robust, with a very low probability of discrepancies. All the regression analysis are described one by one below:

- a) Dilution: The inclination of the curve is sharper in the travel speed axis, which indicates that travel speed had more influence on dilution than power variation. The bigger is the power, the more separated are the plans, so the increase of power makes the difference of dilution for each hatch spacing more evident. For the same power, varying the travel speed, the spacing between plans remains approximately constant, which indicates a linear behavior of dilution variation through the increase of travel speed in all the hatch spacing. The smaller is the hatch spacing the smaller is the dilution. This behavior is due to the power from the laser beam that is more delivered to remelt the previous bead when the hatch spacing is low. Once the hatch spacing is increased more power is delivered to the substrate, increasing the dilution. The surface curves are very smooth and intercepted most dots, indicating a good representation of the phenomenon.

Figure 62 – Regression analysis for dilution.



Source: Author (2020).

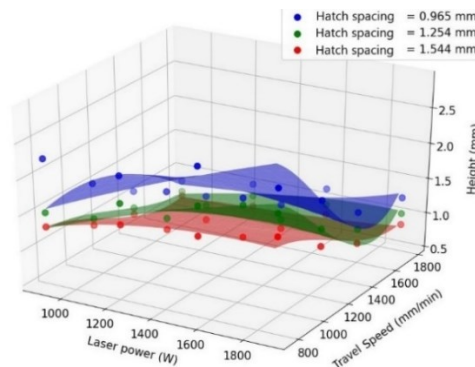
R-squared 0.9822

Adjusted R-squared 0.9796

$$Dilution [\%] = -5.89e^{-17}P^3V^2H^2 + 4.56e^{-17}P^3V^2H + 1.41e^{-14}P^3VH^2 + 1.22e^{-13}P^2V^2H^2 - 6.72e^{-14}P^2V^2H - 5.07e^{-11}PV^2H^2 \quad (19)$$

- b) Height: The plans are separated which indicates that hatch spacing had a strong influence on height. That makes sense once the variation of overlapping on the beads significantly affects layer height. The inclination of the surfaces is higher in the travel speed axis when compared to the power axis, leading to the conclusion that travel speed has more influence on the final height. Low hatch spacing makes the beads overlap more so higher heights are observed on them. Using high speeds the beads are too small making some of them completely separated from each other, where is not even possible to consider as a uniform layer, resulting in low layer heights.

Figure 63 – Regression analysis for height.



Source: Author (2020).

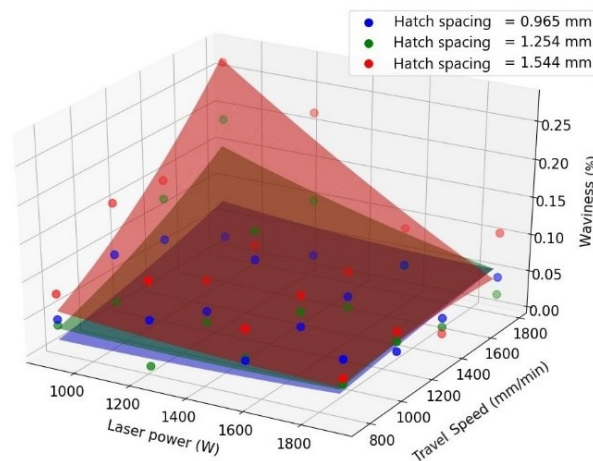
R-squared 0.9973

Adjusted R-squared 0.9962

$$\begin{aligned}
\text{Height [mm]} = & 2.09e^{-12}P^3VH^3 - 2.97e^{-12}P^3VH^2 - 8.64e^{-9}P^2VH^3 + 1.22e^{-8}P^2VH^2 + 1.11e^{-5}PVH^3 \\
& - 1.57e^{-5}PVH^2 + 4.14e^{-4}PH^2 - 3.11e^{-9}V^3H^2 + 5.33e^{-9}V^3H - 2.15e^{-6}V^2H^3 \\
& + 1.63e^{-5}V^2H^2 - 2.17e^{-5}V^2H - 1.51e^{-2}VH^2 + 2.38e^{-2}VH
\end{aligned} \quad (20)$$

- c) Waviness: It is clear that the waviness of the surface is strongly linked to hatch spacing. The higher the hatch spacing the more distance single-beads are from each other and the higher is the waviness. This behavior becomes more evident in smaller beads, which are those with low power and high travel speed.

Figure 64 – Regression analysis for waviness.



Source: Author (2020).

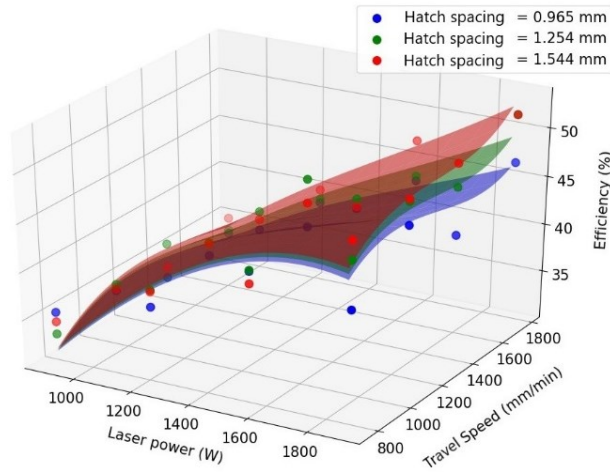
R-squared 0.8847

Adjusted R-squared 0.8742

$$\begin{aligned}
\text{Waviness [\%]} = & 1.18e^{-20}P^3V^3H^3 - 1.80e^{-13}P^2V^2H^2 + 5.31e^{-14}P^2V^2H + 6.25e^{-11}P^2VH^2 \\
& + 1.06e^{-10}PV^2H^2
\end{aligned} \quad (21)$$

- d) Capture Efficiency: The plans are very close to each other so the hatch spacing has a low influence on capture efficiency. The variation of the plans is higher in the power axis when compared to the travel speed axis which indicates that power has a stronger influence on this result. Increasing the power the energy delivered to the melt pool is increased, making the melt pool bigger. With a bigger melt pool, more powder is captured, increasing the capture efficiency of the process.

Figure 65 – Regression analysis for capture efficiency.



Source: Author (2020).

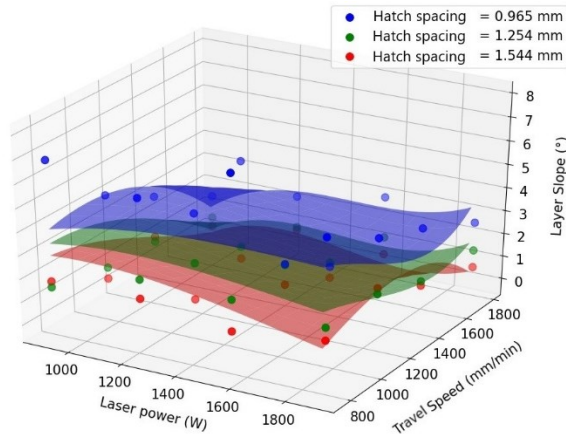
R-squared 0.9992

Adjusted R-squared 0.9989

$$\begin{aligned}
 \text{Capture efficiency [\%]} &= -2.97e^{-20}P^3V^3H^3 + 1.85e^{-16}P^3V^2H^2 - 2.43e^{-13}P^3VH^2 + 3.24e^{-10}P^3H^2 \\
 &- 2.87e^{-10}P^3H + 6.29e^{-17}P^2V^3H^3 - 3.86e^{-13}P^2V^2H^2 + 5.06e^{-10}P^2VH^2 \\
 &+ -8.09e^{-7}P^2H^2 + 6.74e^{-7}P^2H + 2.86e^{-4}PH^2 - 1.75e^{-4}VH^2 + 2.53e^{-4}V
 \end{aligned}
 \tag{22}$$

e) Layer slope: Once the surface is closely parallel to the “power x travel speed” plan it is not possible to link the variation of any of these inputs to layer slope. However, the plans are distanced from each other which indicates that the hatch spacing influences layer slope. It makes sense considering the overlapping effect previously explained.

Figure 66 – Regression analysis for capture layer slope.



Source: Author (2020).

R-squared 0.9344

Adjusted R-squared 0.9213

$$\begin{aligned}
 \text{Layer slope [degrees]} & \\
 &= -1.18e^{-8}V^3H^2 + 1.82e^{-8}V^3H - 2.04e^{-5}V^2H^3 + 9.12e^{-5}V^2H^2 - 9.33e^{-5}V^2H \\
 &+ 3.86e^{-2}VH^3 - 1.33e^{-1}VH^2 + 1.15e^{-1}VH
 \end{aligned} \tag{23}$$

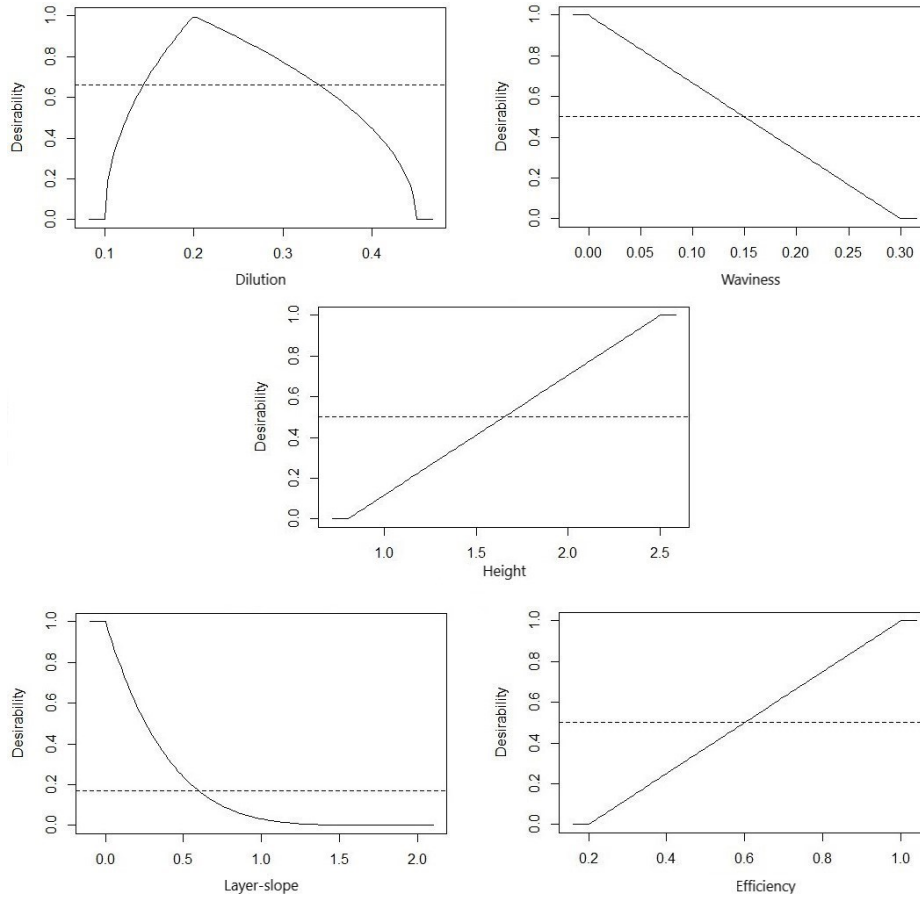
After the regression analysis was obtained an algorithm was run to apply the desirability criteria (exposed in Table 10) and find the processing parameters that give the best combination of characteristics. The dilution was set as a target function, because too low dilution may cause a lack of fusion. On the other hand, too high dilution may imply problems of heat management during deposition. The maximum waviness admitted was 30%, because values over than this are linked to void formation and porosity. The capture efficiency was set as a minimum of 20% because with this setup the highest values are around 40%. Layer slope directly impacts geometrical distortions, so it was admitted a max of 2 degrees. It was also set the sensitivity of 5 because it is very critical. Layer height must be as higher as possible, keeping great quality in the deposition. However, it was set a maximum value, close to the maximum height observed. It was done aiming to differ the desirability of two different heights and simultaneously do not decrease the global desirability. The minimum criteria established was 0.8 millimeters. Table 10 represents all the limits and their function for each variable. Figure 67 exhibits the plot of the desirability functions where it is possible to have a better understanding of how the acceptable range is distributed for each situation.

Table 10 – Desirability configuration.

Output	Type	Minimum	Target	Maximum	Sensitivity 1	Sensitivity 2	Unit
Dilution	Target	10	20	45	0.5	0.5	%
Waviness	Minimum	0	-	30	1	-	%
Height	Maximum	0.8	-	2.5	1	-	mm
Capture Efficiency	Maximum	20	-	100	1	-	%
Layer-slope	Minimum	0	-	2	5	-	degrees

Source: Author (2020).

Figure 67 – Desirability distributions.



Source: Author (2020).

It was necessary to make a deposition using the processing parameters previously obtained and compare the results to assure the methodology works and the characteristics match the predicted. The comparison is shown in Table 11. The difference was low for all features when comparing absolute results. When comparing percentage results layer slope exhibited a high difference. It was expected that layer slope and height exhibit the worst behavior when compared to the other features considering that their regression was more heterogeneous. Additionally, layer slope and waviness have low numbers, which makes the percentage analysis more sensible. In general, the model was able to predict the general behavior of the deposited layer.

Table 11 – Comparison between predicted and real characteristics.

Global desirability: 0.373		Power: 1900 [W]		
Travel speed: 1404.8 [mm/min]		Hatch spacing: 1.379 [mm]		
Property	Predicted	Real	Difference	Difference

			(absolute)	(percentage)
Dilution [%]	22	20.5	-1.5	-6.82
Waviness [%]	0.6	0.5	-0.1	-16.67
Height [mm]	1.09	1.23	0.14	12.84
Capture Efficiency [%]	50.09	52.08	1.99	3.97
Layer slope [°]	0.688	1.109	0.421	61.19

Source: Author (2020).

5.1.4 Multilayer Stage

After the single-layer, a simple multilayer geometry was deposited to find out the best overlayer observing the presence of pores and voids. As seen in Figure 68 the block was deposited with 5% (b), 10% (c), 15% (d), 20% (e), and 25% (f) of overlayer based on the height measured in the verification deposition. For 5%, 10%, and 15% of overlayers it was observed lack of fusion in most layers. No lack of fusion was observed when using 20% and 25% overlayer and the last one presented a higher number and size of pores, which lead to select the 20% overlayer parameter¹⁶. Increasing the overlayer the dilution is also increased, which leads to the decreasing of pores and voids. Figure 68 presents the single layer and the cross-section of the multilayer geometries for 0% and 20% overlayer.

¹⁶ The cross-section images for all multilayer geometries varying overlayer is available in APPENDIX I – Multilayer Geometry Depositions.

Figure 68 – Verification of the predicted single-layer (a) and the blocks using 5% (b), 10% (c), 15% (d), 20% (e), and 25% (f) of overlayer.



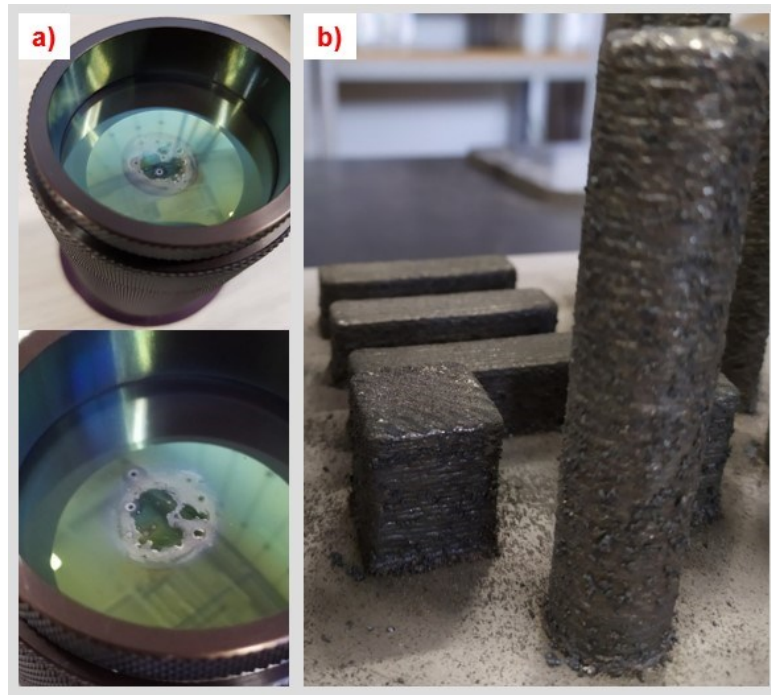
Source: Author (2020).

5.1.5 Restraining the process boundaries

It was deposited three samples for impact absorption analysis, three for tension analysis, two blocks for microstructure and microhardness, and four samples for fatigue behavior (that will not be approached in this study). Despite the regression predicts well the behavior of the single-layer it does not predict the impact of a long way deposition and its consequences. The high density of energy delivered to the process generated soot on the surface (Figure 69). The parameters selected exhibited too much spatter, which in the beginning was believed to be acceptable but ended damaging permanently the focusing lens. It is also possible to see soot on the surface of the lens, indicating that the processing

parameter was too aggressive for the current setup. It is important to point that the problem was not caused by a bad prediction given by the methodology, once the results matched what was expected. The problem was the result of a bad understanding of the limits that the machine could work for a long time under those conditions. The methodology does not consider these limits. It is up to the user to analyze which processing characteristics may be dangerous to the equipment.

Figure 69 – Damaged lens (a) and samples with soot (b).



Source: Author (2020).

Trying to understand and minimize the spatter effect some high-speed videos were made. It was evaluated the variation of spatter and other effects that may cause instabilities in the process through the variation of power input. The videos were recorded using a Phantom Miro R311 high-speed camera using 9000 fps with a resolution of 512 x 320p. It was analyzed five levels of power (1900, 1700, 1500, 1300, and 1100 W) and it was observed the starting of vapor capillary in all situations. However, the intensity and frequency decreased at the same time the power was decreased. For the power of 1300 W and 1100 W, the behavior was very similar, so it was decided to move on using the power of 1300 W.

Considering that the results obtained matched the prediction given by the regression analysis it was decided to use the same regression but limiting the window to the power of 1300 W. The desirability criteria remained the same and the new optimized processing

parameter obtained such as its characteristics and its comparison to the verification layer are shown in Table 12. It is also necessary to make it clear that the original investigated window ranged from 1100W to 1900W. Therefore, there was a good representation of the behavior of the process for a wide window. When the power was limited, the experiment window and consequently the amount of data decreased dramatically, since the minimum power was 1000 W. Therefore, being close to the edge of the window and with a low density of data, the representation of the process behavior is impaired. To improve this behavior, a new set of experiments with intermediate powers from 1000 W to 1300 W would be necessary.

Table 12 – Comparison between predicted and real characteristics of the new optimized parameter.

Global desirability: 0.142 Travel speed: 1446 [mm/min]		Power: 1300 [W] Hatch spacing: 1.483 [mm]		
Property	Predicted	Real	Difference (absolute)	Difference (percentage)
Dilution [%]	10.4	23.0	12.6	121.1
Waviness [%]	9.6	4.8	-4.8	-50
Height [mm]	0.865	0.823	0.042	-4.85
Capture Efficiency [%]	41.48	34.2	-7.28	-17.55
Layer slope [°]	0.810	0.706	-0.104	-12.84

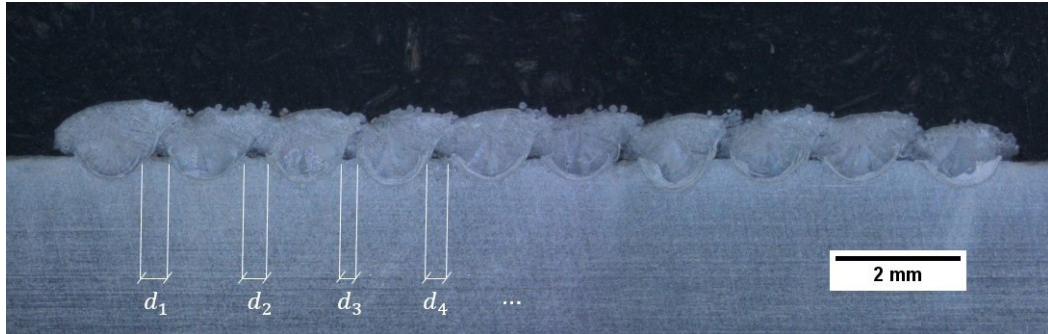
Source: Author (2020).

Most characteristics were well predicted when analyzing the absolute difference, except by dilution and capture efficiency. Observing the single-layer verification deposition it is possible to see that the beads are too spaced each other, which causes a direct impact on the dilution. It was decided to refine the hatch spacing, expecting to improve the bonding between beads and decrease the number of pores, voids, and lack of fusion. This refinement was predicted in the methodology in the Multilayer Stage. As previously said, the adjustments (if necessary) depends on the analysis of the user and his capability in identifying the weakness of the optimized layer that was obtained and how to improve it, helped by the trends given by regression analysis.

When the beads are very widely spaced with each other there is a gap in the overlapping area where there is no energy enough to melt the previous bead and the substrate. By applying that concept, equalizing all of those distances to zero would solve the problem of unmelted areas. The strategy adopted to achieve the ideal hatch spacing was to measure all the

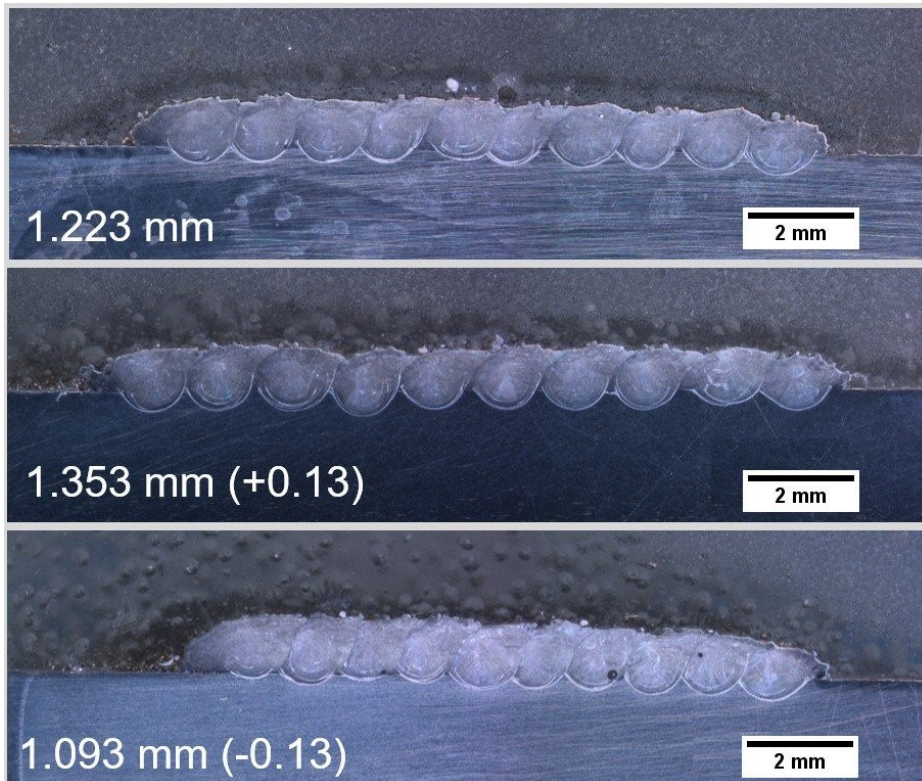
distances of the gaps (as shown in Figure 70) and subtract their mean from the original hatch spacing. The mean distance obtained was 0.26 mm leading to the hatch spacing of 1.223 mm. It was also set a range of ± 0.13 mm to guarantee the best configuration was achieved. The three depositions of hatch spacing refinement are shown in Figure 71.

Figure 70 – Verification single-layer with very widely spaced beads.



Source: Author (2020).

Figure 71 – Hatch spacing refinement.



Source: Author (2020).

The strategy of hatch spacing refinement worked very well and good layers were obtained with just a few adjustments. As expected, the layer with a hatch spacing of 1.093

mm exhibited a higher slope, once the beads are too close to each other and start to overlap too much. The opposite behavior was not observed when using 1.353 mm which presented a low waviness, low layer slope, and no presence of lack of fusion, pores, and voids, such as the 1.223 mm hatch spacing.

The characteristics of the new optimized parameter after the experiments of hatch spacing are exposed in Table 13. For the hatch spacing of 1.093 mm, the layer slope exceeded the maximum acceptable value of two degrees, declassifying that parameter. Comparing the global desirability of the two other parameters it is not possible to assure which one is the best. The values of desirability are very close and considering the variations, it is not possible to say they are different. Additionally, the targets previously set are estimates, so they are not necessarily the best condition for that feature, but an approximation, adding some uncertainty around the final result. Considering the previous factors, the selection criteria adopted was the lowest layer-slope. It will cause a higher impact on geometrical stability, so it is considered more critical.

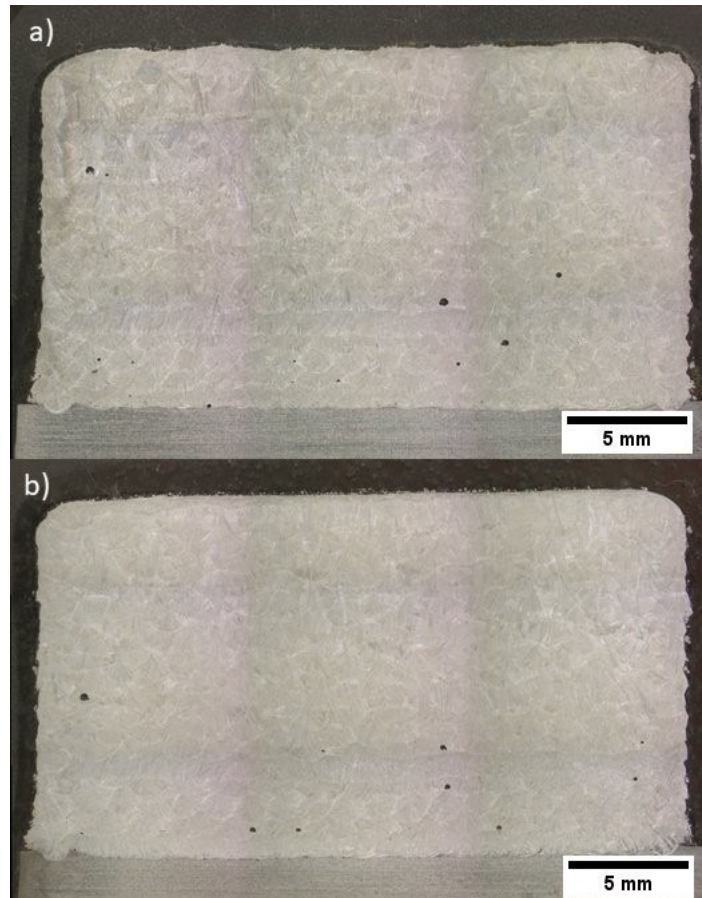
Table 13 – The characteristics of the new optimized parameter for the three layers of the additional experiment of hatch spacing adjustment.

	1.223		1.353 (+0.13)		1.093 (-0.13)	
	Value	Desirability	Value	Desirability	Value	Desirability
Dilution [%]	19.1	0.955	26.8	0.853	15.0	0.704
Waviness [%]	9.8	0.673	16.3	0.457	9.7	0.677
Height [mm]	0.915	0.068	0.814	0.008	1.114	0.185
Efficiency [%]	40.4	0.255	38.7	0.234	41.8	0.272
Layer slope [°]	1.228	0.009	0.691	0.120	2.613	0
Desirability	0.157		0.155		0	

Source: Author (2020).

After all the features for a single layer were defined, the overlayer was selected. Considering that previous tests exhibited a huge difference over 20% overlayer, it was decided to use 20% and 25% on the first try, and if necessary try other values. Figure 72 exhibits the cross-section for 20% overlayer (a) and 25% overlayer (b). The presence of pores was very similar on both overlayers, and no lack of fusion was observed. In (b) it is possible to see higher dimensional stability and lower waviness on the surface, which leads to its selection.

Figure 72 – Verification block for 20% (a) and 25% (b) overlayer.



Source: Author (2020).

5.2 CHARACTERIZATION

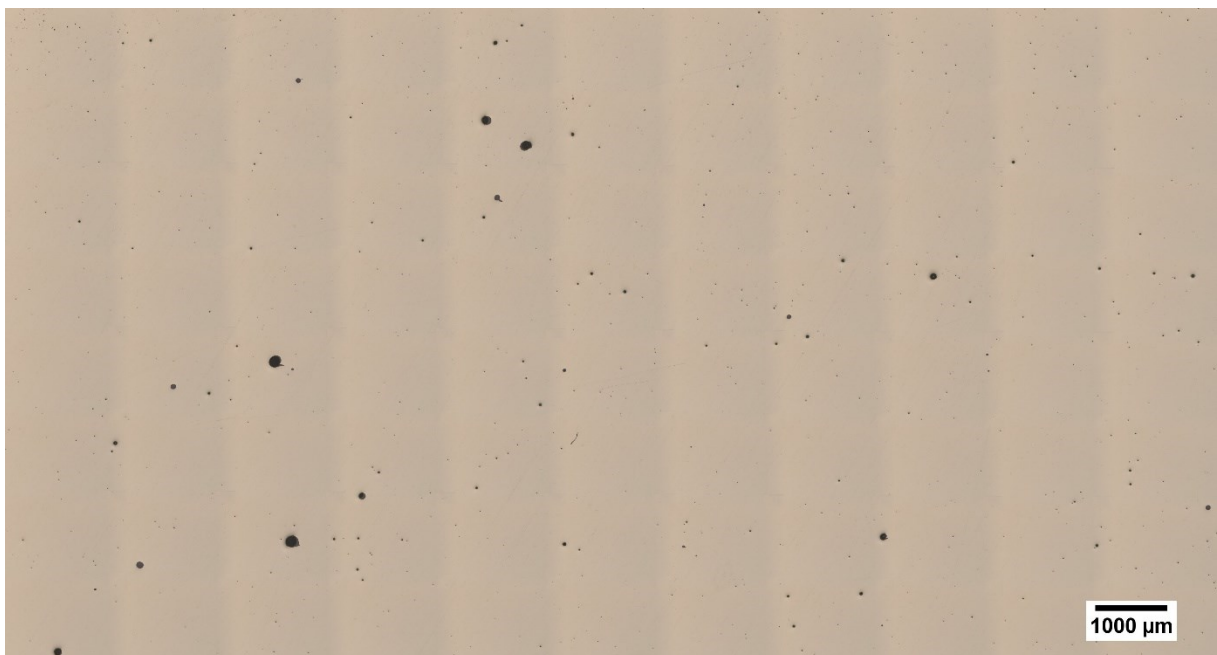
The results obtained from the characterization of the samples described in section 4.7 are discussed below.

5.2.1 Porosity

It was analyzed the presence of pores and voids after the heat treatment of stress relief and solubilization in the B1-1 sample. The preparation includes grinding with 80, 220, 400, 600, 1200 sandpapers, and polishing with diamond polishing paste. The polished surfaces were not etched because it is easier to quantify the porosity with higher contrast. The quantification was made using the software Axio Vision where the pores are automatically selected. However, the level of contrast is manually set, which allows a configuration for selecting as many pores and voids as possible without considering noisy data.

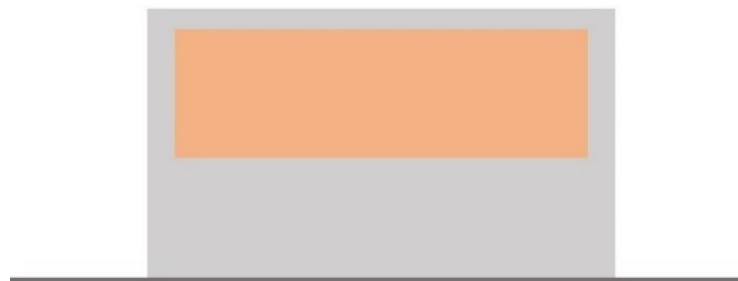
Figure 73 exhibits the porosity of the heat-treated sample. The analysis was made considering the top half of the sample, once the first layers may suffer from a lack of fusion due to higher cooling rates. Figure 74 exemplifies the area used to perform the porosity analysis. The quantification of density was made by image analysis, considering non-solid all the darker areas. Most defects have a rounded shape, which is good in terms of avoiding crack propagation. It was obtained 99.86% of density and the pores and voids size distribution (maximum diameter) is showed in Figure 75.

Figure 73 – Porosity of the heat-treated sample using a 50x magnification mosaic.



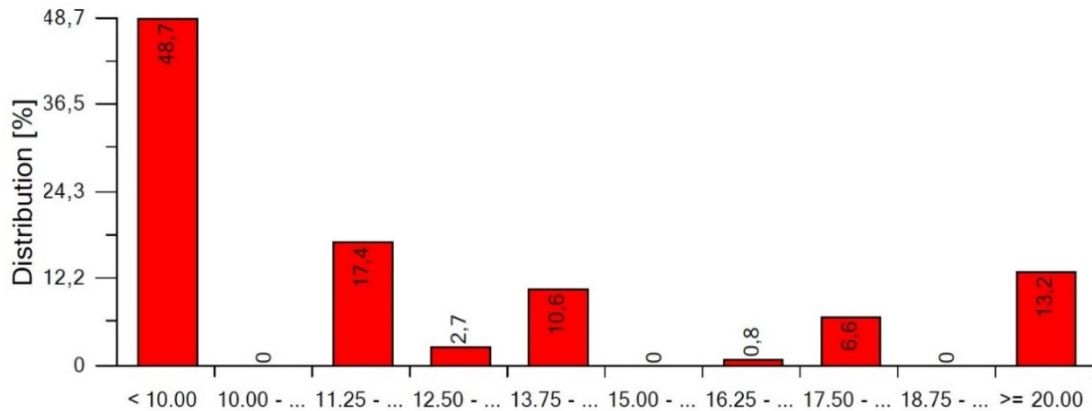
Source: Author (2020).

Figure 74 – The orange rectangle represents the area used to perform the porosity analysis.



Source: Author (2020).

Figure 75 – Pores and voids size distribution.



Source: Author (2020).

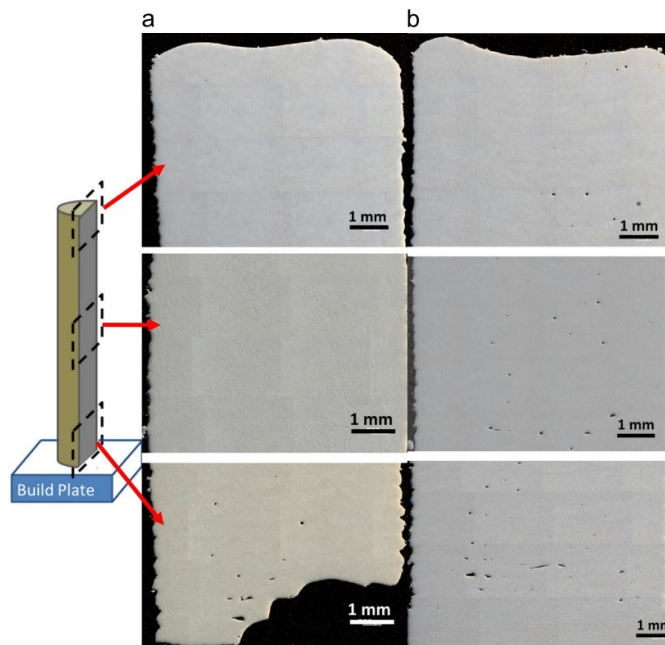
Almost half of the pores have a diameter below 10 μm and just 13,2% are over 20 μm . Despite the incidence of small pores must be even bigger, considering that the image analysis can not select small pores very well due to the resolution of capture. Even the biggest pores are the most critical, the characteristics of all pores may cause important impacts on final results. Previous studies show that smaller pores may be inclusions [88-92]. The inclusions are categorized into fine (below 2 μm) and coarse oxides (around 5 μm). Fine oxides are rich in S and O and coarse oxides are rich in S, O, and Mn [88, 90]. There are still reports of the presence of Mo-rich oxides in the literature [93]. Additionally, the presence of these oxides is linked to mechanical properties, increasing the strength, and decreasing the elongation of the component [88, 90]. It is believed that major defects present in the sample are pores and not oxides, considering that the atmosphere of deposition was composed of argon with a low amount of oxygen (below 50 ppm). Additionally, after better polishing the samples it was possible to observe that some of what was believed to be very small pores or inclusions were actually residual particles from grinding. It is also important to point that the cross-section analysis is a punctual approach for porosity quantification, not necessarily representing the behavior in all the volume analyzed or even on all the building parts. Even the image analysis is not the best technology available for porosity quantification due to the previous factors, it is important to achieve a basic idea about that characteristic. The results of porosity will be analyzed together with the tensile tests to get a conclusion¹⁷.

YADOLLAHI et al. (2015) study the effects of dwell time and heat treatment on the mechanical and microstructural properties of samples produced by L-DED using 316L. The effect of dwell time is obtained by doing the first deposition of just one sample and the second

¹⁷ The complete report for porosity is available in ATTACHMENT F – Porosity Report.

with nine samples together. In this study, many samples are built together, so it may be said that the results are closer to the nine build deposition. Figure 76 exposes the variation of porosity along with the height of the sample. Comparing the blocks used to analyze porosity in this study and its position related to the other samples (seen in Figure 53-a) to Figure 76 it is possible to affirm that the bottom of the nine-build sample is the best comparison. It is easy to observe that porosity decreases as long as the height increases. With that result in mind, it is believed that the blocks that will be following analyzed represent the worst scenario of porosity present in all the samples of this study.

Figure 76 – Porosity observed for (a) single-built (not heat-treated) and (b) nine-built samples at three different regions (bottom, middle, and top).

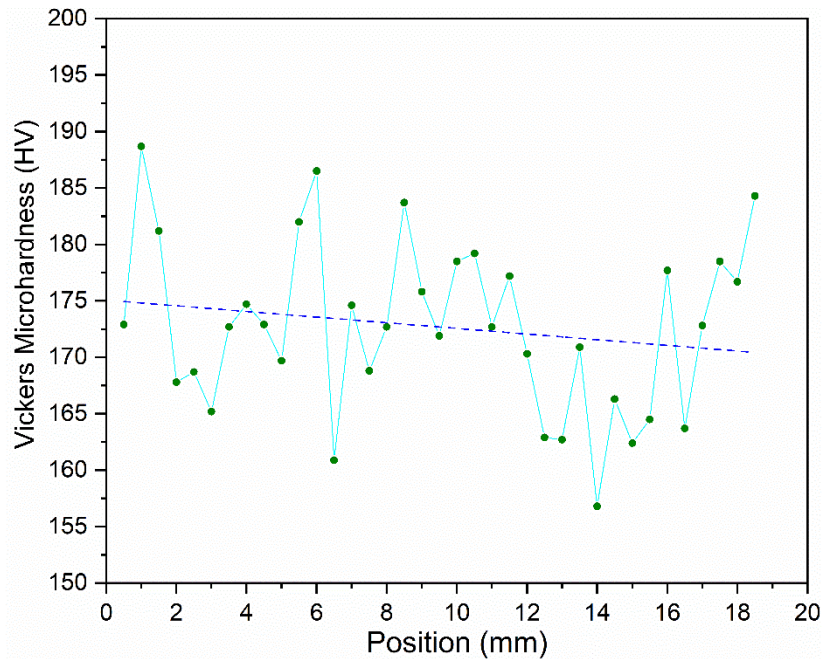


Source: [88].

5.2.2 Microhardness profile

The microhardness profile was done in the B2-1 heat-treated specimen using a 500 g load for 10 seconds, and spacing of a half-millimeter from each other in the positive direction of the z-axis (building direction). The sample was removed from the substrate, discarding the first 4 millimeters according to the procedure performed on the specimens. A distance of half a millimeter from the edges was adopted. The average microhardness obtained from 37 indentations was 173 HV with a standard deviation of 8HV. The distribution of the measurements is exposed in Figure 77.

Figure 77 – Microhardness profile.



Source: Author (2020).

Considering that the first value from the trend line (175 HV) and the last one (173 HV) are both into the confidence interval (173 ± 3.17 for 99%) it is possible to assume that the average does not change along with the height of the building part, and there is no significant variation of microhardness. The variation observed was due to the anisotropic microstructure, which is a characteristic of the L-DED process. There are regions with significantly different grain size distribution, which directly affects the results of microhardness. The reasons for that variation are explained in section 5.2.3.

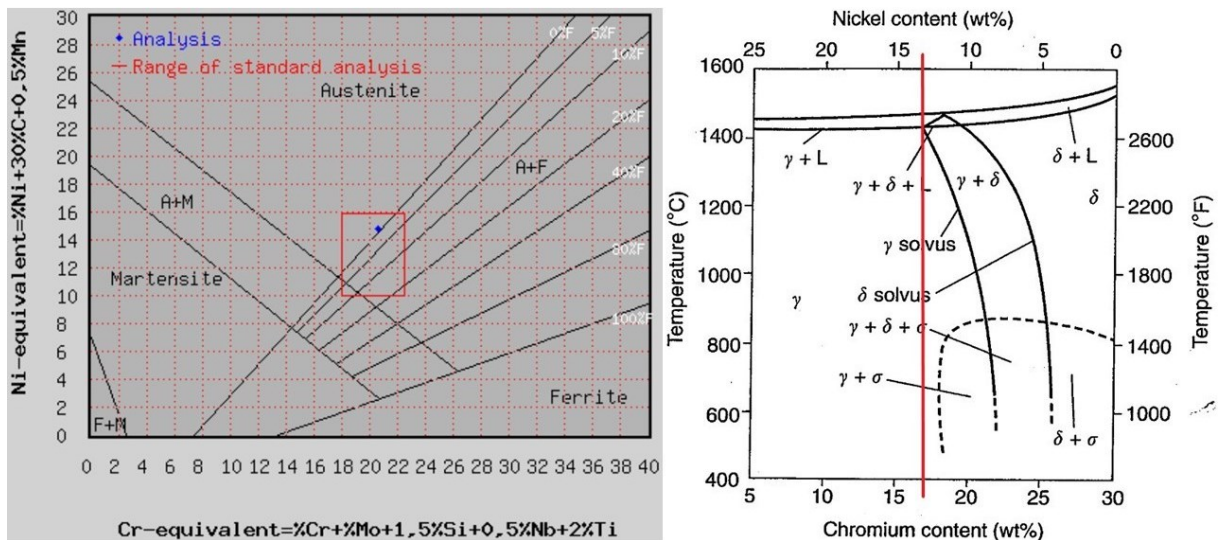
Comparing the results to the literature it is possible to observe that the microhardness is close to casting material (170 HV) [67]. The values for AM parts build with 316L vary a lot, going from 190 HV to 370 HV [67]. However, these values are obtained from as-built components. The heat treatment of solubilization tends to reduce the hardness of the material, therefore, it is believed that the component studied here would have values according to the literature if the hardness was evaluated without the heat treatment. It was preferred to do the measurements after the heat treatment because it is the real condition of most final parts produced by L-DED.

5.2.3 Microstructure

The microstructure analysis was carried aiming to understand the characteristics of the parts produced by L-DED in 316L and link them to their mechanical behavior. Two conditions were analyzed: as-built and heat-treated. The as-built sample characteristics indicate what happened during the process, which is modified after the heat treatment. The heat-treated sample can show what was modified and link it to mechanical behavior and show the advantages and disadvantages of the heat treatment.

The chemical composition of the alloy used in this study indicates an austenitic microstructure. However, using Schaeffler and the pseudobinary diagrams it is possible to see that the microstructure prediction is on the limit of the formation of δ -ferrite (Figure 78). Considering that L-DED is a process with high cooling rates ($<10^3$ K/s) that is far from the equilibrium conditions (which increases the error related to the predictive diagrams) that may exist ferrite phases in the final parts [94].

Figure 78 – Schaeffler Diagram (left) and a pseudobinary diagram for 70% iron (right) analysis using the metallic powder composition.



Source: [95] and adapted from [18].

It is possible to see that the as-built arrangement exhibits cellular and columnar-dendritic morphology (Figure 79) which is very similar to the arrangement obtained in the welded fully austenitic solidification (Figure 18). Considering the similarity it is possible to conclude that the L-DED process resulted in a majorly austenitic microstructure and if there is some δ -ferrite it is present in a very low amount.

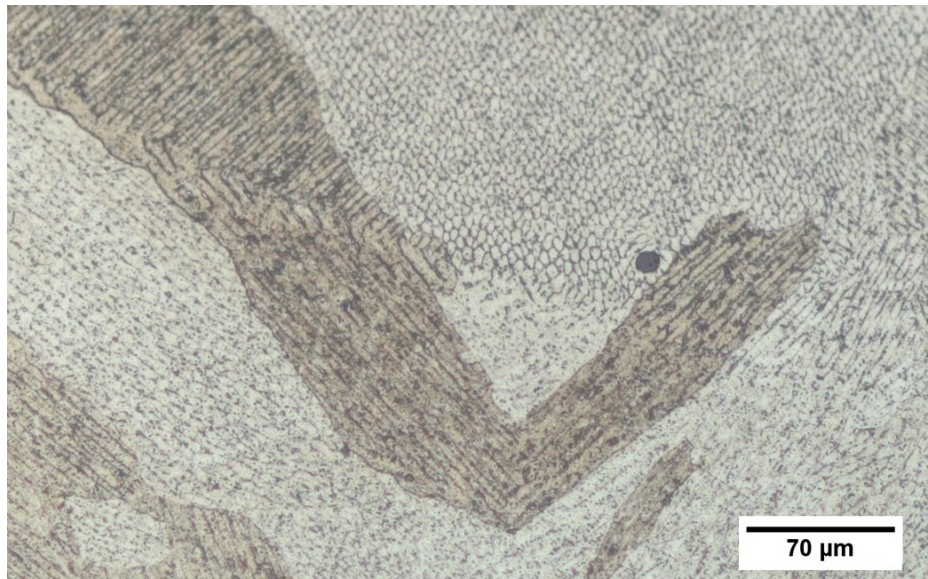
Figure 79 – Microstructure of as-built sample (200x magnification).



Source: Author (2020).

Bearing in mind that the cooling rate obtained in the process is directly proportional to the grain refining [13, 35] it can be said by comparing Figure 79 and Figure 18 that the L-DED process, with the set of selected parameters, provides a higher cooling rate compared to what is typically obtained in arc welding processes. It may also be confirmed by the absence of equiaxial dendritic structures. The dashed line in Figure 79 indicates the boundary of a bead and in the circled area it is possible to see an epitaxial growth during the solidification related to the previously deposited layer. The same behavior was observed by Zhang et al. [25] processing 316L by L-DED. The orientation of the grains varies drastically in a very short space, which is a characteristic inherited by the scanning strategy. Figure 80 shows the transition of the kind of grains observed, exhibiting a columnar solidification (faster cooling) near the base of a bead turning into cellular (slower cooling).

Figure 80 – Microstructure of as-built sample (200x magnification).



Source: Author (2020).

When a single bead is deposited beside the previous one to form a layer, part of the previous bead is remelted, refining the grain size of that structure. In Figure 81 it is possible to see the difference between the grain size of a remelted zone between beads (indicated by “A”) and a zone in the center of the bead that was not remelted (indicated by “B”).

“Carbon is normally considered an undesirable impurity in austenitic stainless steel. While it stabilizes the austenite structure, it has a great thermodynamic affinity for chromium. Because of this affinity, chromium carbides, $M_{23}C_6$, form whenever carbon reaches levels of supersaturation in austenite, and diffusion rates are sufficient for carbon and chromium to segregate into precipitates” [96]. Intermetallic phases may precipitate, decreasing tenacity and corrosion resistance. However, these precipitations need time to occur [96]. Considering the rapid cooling of the process it is unlikely to happen, but the accumulation of heat during the process may elevate the temperature of the building part, and that hypothesis may not be discarded. In Figure 82 it is possible to see some discontinuity in the intercellular region, which is believed to be microsegregation. Many authors diverge about the impact of cooling rates on microsegregation. The characterization of microsegregation is based on the analysis of the final parts only [97]. The results obtained from tension testing and impact absorption will make it possible to attest to the occurrence of embrittlement resulting from microsegregation.

Figure 81 – Microstructure of as-built sample (100x magnification).



Source: Author (2020).

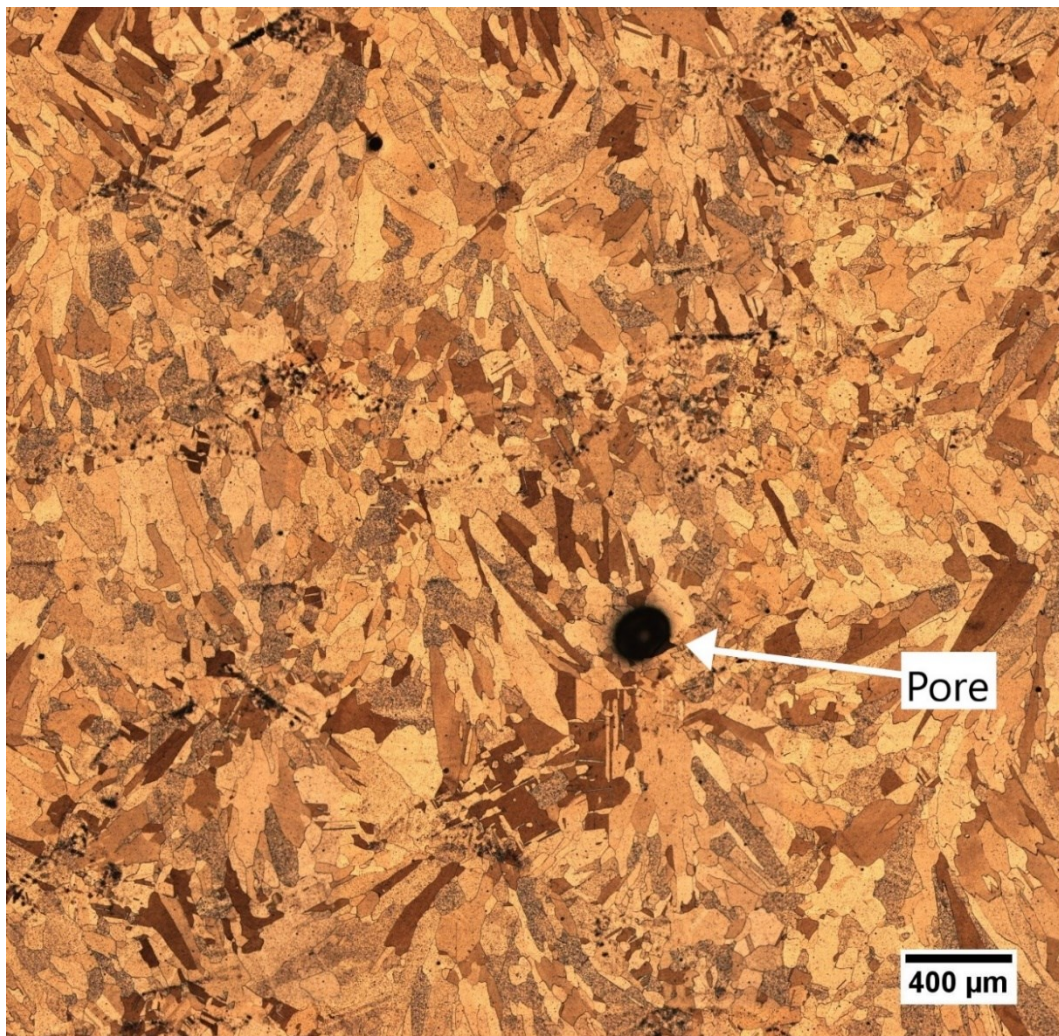
Figure 82 – Microstructure of as-built sample (500x magnification).



Source: Author (2020).

Figure 83 exhibits the microstructure of the sample after the solubilization heat treatment. The microsegregation was not observed, so it is believed that the heat treatment was able to dissolve them. The average grain size was bigger when compared to the as-built sample. That is easy to observe when comparing Figure 81 and Figure 83. Figure 81 exhibits finer grain size even with double magnification. That characteristic was expected once the solubilization maintained the sample at 1070 °C for two hours, allowing grain growing. It is also possible to observe that the morphology is more isotropic when compared to “as-built” samples, with fewer elongated grains. During the etching with hydrochloric acid (4 g CuSO_4 + 20 ml HCl + 20 ml H_2O) it was possible to have an idea of the corrosion resistance variation between the samples. The first sample (as-built) took around eight seconds to exhibit the microstructure while the heat-treated sample took around fifty seconds. That shows the solubilization was capable of significantly improve the corrosion resistance of the material.

Figure 83 – Microstructure mosaic of the heat-treated sample (50x magnification).

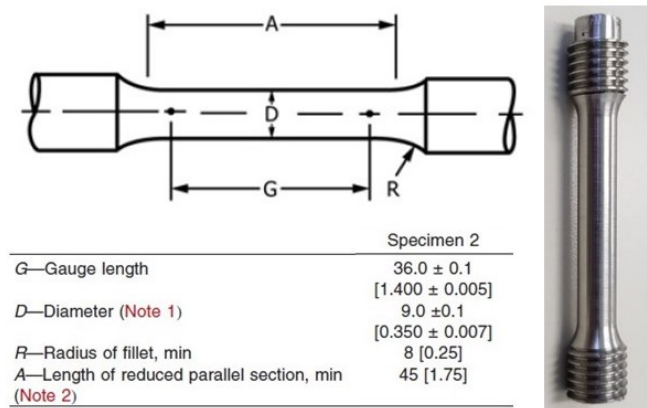


Source: Author (2020).

5.2.4 Tensile testing

Considering that the deposition process generates anisotropic behavior it is necessary to compare the results between vertically (builds 1 and 3) and horizontally (build 2) deposited samples. The orientation of the sample on the substrate is not relevant once there is a 45 degrees variation between the orientation of each layer. The tension testing aims to compare the mechanical behavior of the samples to wrought material and to the literature for L-DED technology. It was also desired to compare the behavior before (build 3) and after heat-treatment (build 1 and 2). Nine samples were tested, where 6 were built vertically and 3 horizontally. The vertically built samples were tested with (3 samples) and without (3 samples) heat-treatment. The tests were carried according to ASTM A370 and the samples were built according to ASTM E8 where specimen 2 was chosen. It was applied an elastic speed of 3.75 mm/min and a plastic speed of 12 mm/min. A laser extensometer was used to measure the deformation and the 0.2% offset method was applied to determine the yield strength and elastic modulus.

Figure 84 – Specimen 2 dimensions (left) according to ASTM E8 and after machined (right).



Source: Adapted from [99].

Table 14 shows the results of tension tests. The values presented refer to the average/standard deviation. The abbreviation “HT” means “heat-treated” and “AB” means “as-built”. The low standard deviations obtained from the results of yield strength and ultimate strength show very consistent data in all situations. This fact indicates that even with the porosity, discontinuities, and anisotropy, it is possible to predict the behavior of the material under axial stress. All the results were higher than the minimum requirements for wrought material, according to ASTM A276.

Table 14 – Tension tests results.

	Yield strength [MPa]	Ultimate strength [MPa]	Elastic modulus [GPa]	Elongation [%]
Vertical (HT)	298 / 0.82	575.3 / 1.25	203.3 / 32.27	53.7 / 0.47
Horizontal (HT)	304.7 / 1.89	602.3 / 0.47	179.0 / 5.72	50.3 / 0.47
Vertical (AB)	380.7 / 1.89	604.7 / 1.25	151.3 / 9.10	45.7 / 6.85
ASTM A276 [100]	170	485	-	40

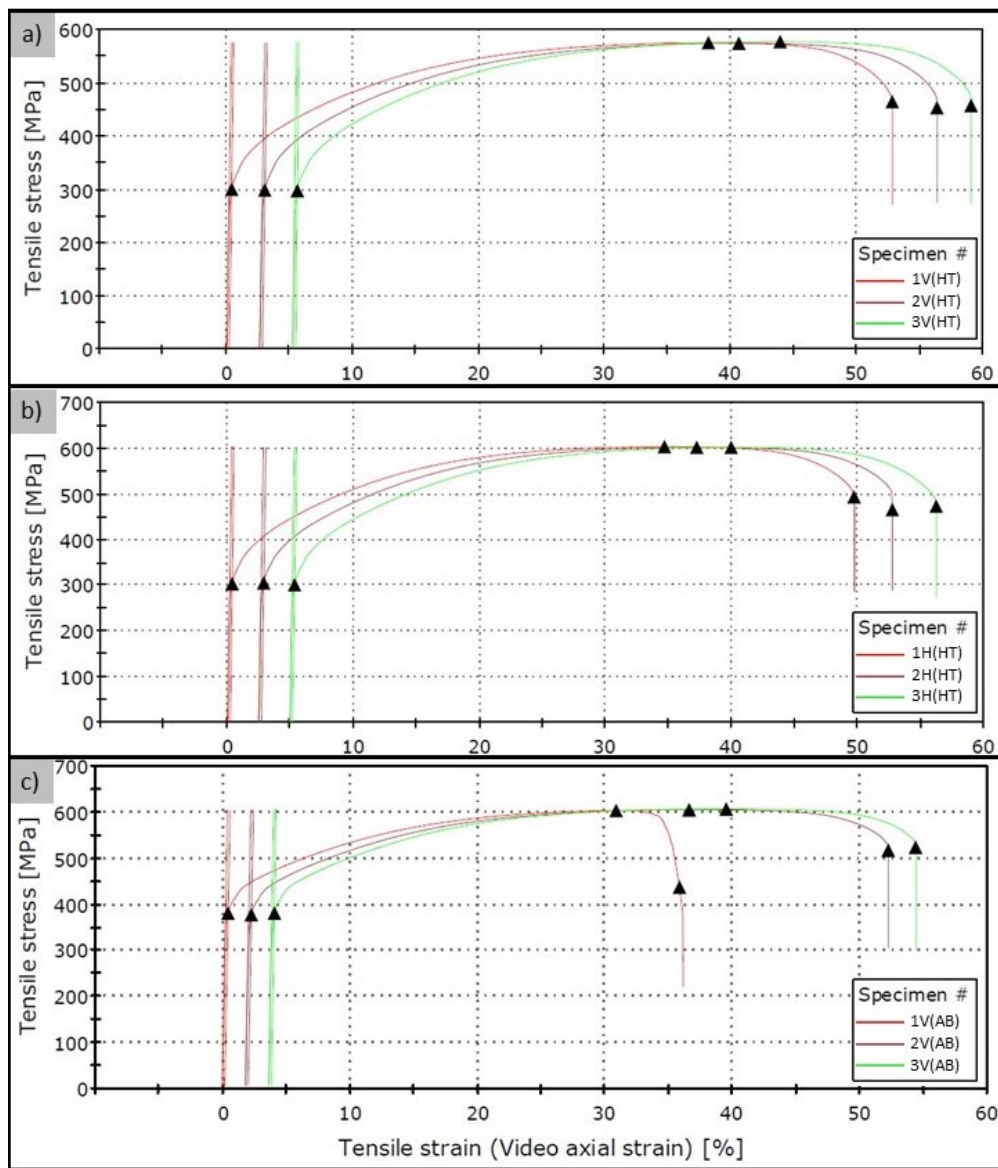
Source: Author (2020).

Comparing the yield strength of HT samples, there was not a significant difference between vertical and horizontal specimens. Vertical samples had grain growth preferably in the axial direction while horizontal samples had layers building parallel to the axial direction, minimizing the effect of discontinuities between layers. The solubilization makes the grain distribution more homogeneous, which may minimize the difference in building orientation between samples. The horizontal samples showed an ultimate strength of 4.7% higher than the vertical ones. That difference could be due to the anisotropy remaining from the deposition process, with a grain growth preferentially in the “z-axis” direction. The elongation of the vertical samples was 6.8% higher than the horizontal, which is an opposite effect of the grain growth tendency previously explained. Elastic modulus exhibited the highest standard deviation, and the results were considered not trustworthy. It is believed that the high standard deviation is due to the tensile test, which is not the most indicated to quantify the elastic modulus. Another explanation may be the anisotropy of the material, but it not the first hypothesis considering that all the other results are very similar. Figure 85 exhibits the curves of all the nine tests split into three groups: vertical heat-treated (a), horizontal heat-treated (b), and vertical as-built (c).

Compared to the heat-treated results, the as-built samples presented a 26.3% higher average yield strength. That behavior was expected due to the finer grain size previously presented and the higher presence of columnar grains. However, the ultimate strength remained very similar to horizontal HT (4.7% higher than vertical HT). That behavior may be explained by the presence of microsegregation exposed in Figure 82, which tends to fragilize the material. Such elongation as the fracture behavior was very similar in samples T2V-3 (AB) and T3V-3 (AB) when compared to heat-treated samples. Sample T1V-3 (AB) exhibited a different behavior when compared to all other samples (with or without heat treatment), as seen in Figure 86. The elongation (36%) was much lower when compared to the other

samples without heat treatment, samples 2 and 3 as-built (50% and 51% respectively). Furthermore, the surface of the fracture was flat and 45° (Figure 86 - right). A better evaluation of the fractured surface could be done to understand if the failure was caused by a defect or by a fragilization of the material. All the other ones presented fractures with ductile characteristics (Figure 86 - center and left). These results will be compared to the impact absorption test to achieve a better conclusion.

Figure 85 – Results of tension tests from vertical heat-treated (a), horizontal heat-treated (b), and vertical as-built (c) samples.



Source: Author (2020).

Figure 86 – Vertical HT sample T1V-1 (left), vertical AB sample T2V-3 (center), and vertical AB sample T1V-3 (right) showing the shape of the fracture after the tensile test. Only the right sample exhibits brittle behavior.



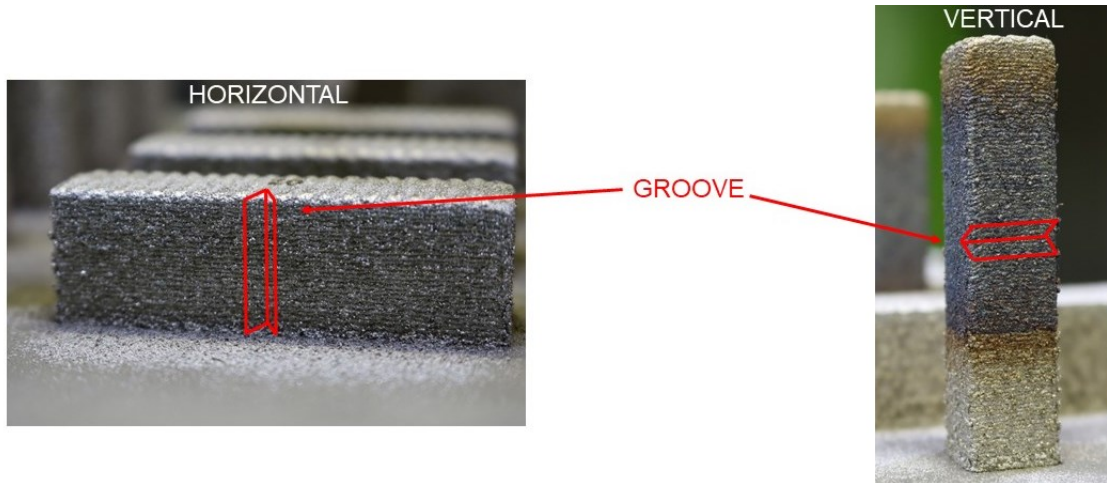
Source: Author (2020).

ASTM A240 covers stainless steel plates, sheets, and strips for pressure vessels and general applications including architectural, building, construction, and aesthetic applications. The standard defines the minimum values of 485 MPa, 170 MPa, and 40% for ultimate strength, yield strength, and elongation respectively. All the average results achieved significantly higher values when compared to the minimum stipulated by ASTM A240. The only exception was the elongation of sample T1V-3 (as-built).

5.2.5 Impact

The samples were built vertically and horizontally such as the tension samples. In the impact absorption test, it is desired to analyze the most critical behavior of the sample when submitted to an impact. With that concept in mind, the horizontal samples had the groove cut in the z-axis direction, parallel to grain growth preferential orientation (Figure 87).

Figure 87 – Groove position on impact absorption sample.



Source: Author (2020).

Table 15 shows the results of impact absorption tests and the comparison to the literature for AM and wrought 316L. All the samples exhibited ductile behavior. The standard deviation was low for all groups, showing that the defects and discontinuities did not make the material behavior unpredictable. The average of V(HT) was 16.9% higher than H(HT), which indicates that the parallel to grain growth preferential direction is the most critical situation. It was expected considering that the failure comes from intergranular adhesion. (HT) presented 19.2% higher energy absorption when compared to H(AB) samples. Even with lower energy absorption, the as-built samples results indicate there was not a significant fragilization of the material without heat treatment. It is believed that the difference is linked to the lower grain size of the material, making it more brittle (but still ductile) when compared to heat-treated. When comparing to the literature for AM, the results were similar for the H(HT), lightly higher for the V(HT) and lightly lower to the H(AB) samples. All the results for impact absorption were lower than those observed for wrought 316L. Figure 88 shows the fracture surfaces of all samples reinforcing the ductile behavior of the material. It is believed that the darker points observed in the fractured sample may be oxide inclusions, which may be initiation sites for microvoid formation, which may decrease impact toughness and mechanical resistance of the material, as observed in the study of Lou et al. [93].

Table 15 – Impact absorption results.

Vertical Heat-treated		Horizontal Heat-treated		Horizontal as-built	
Sample	Energy [J]	Sample	Energy [J]	Sample	Energy [J]
C1V-2(HT)	183.8	C1H-1(HT)	150.1	C1H-3(AB)	121.3
C2V-2(HT)	170.2	C2H-1(HT)	144.1	C2H-3(AB)	118.5
C3V-2(HT)	162.9	C3H-1(HT)	148.0	C3H-3(AB)	130.9
Average/ standard deviation	172.3 / 8.7		147.4 / 2.5		123.6 / 5.3
AM 316L [93]			130 – 150 [J]		
Wrought 316L [93]			Around 200 [J]		

Source: Author (2020).

Figure 88 – Ductile fracture of the impact absorption samples.

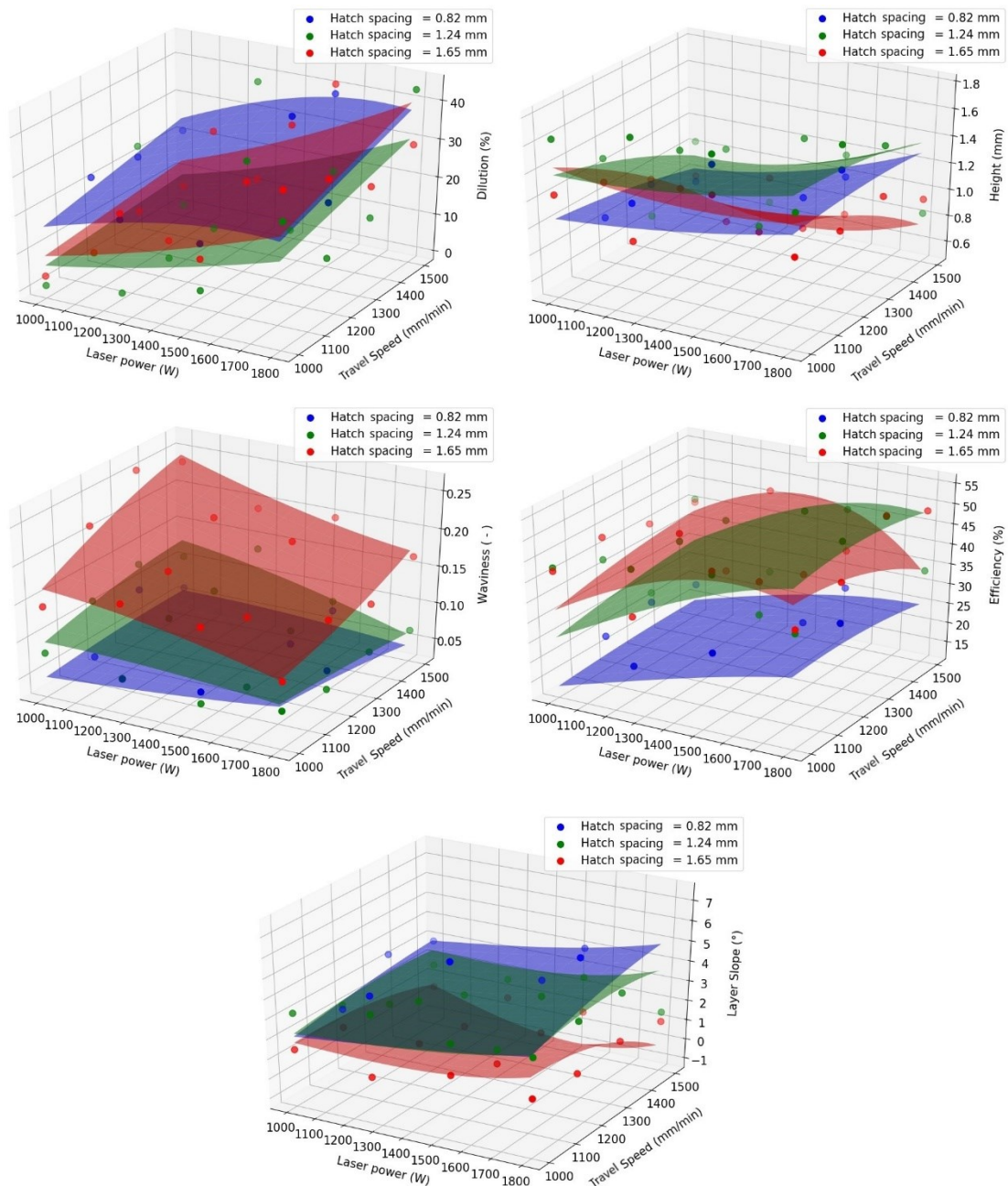


Source: Author (2020).

5.3 FIRST ATTEMPT OF METHODOLOGY APPLICATION (BAD SUCCEED)

The first idea for the deposition of the single beads in the Exploratory Stage was to set the range of parameters in a way that the depositions cover more possibilities of behavior as possible. It was selected a wide range of parameters when it comes to speed, power, and feedrate. It was believed that the substrate heating would not significantly impact the results, once the depositions were relatively fast. Considering that, the depositions were made in aleatory sequence, but with no waiting time to let the substrate cool down between depositions. In the Modeling Stage, the same strategy was adopted. In the regression analysis, it was observed some random behavior, and it was not possible to define a trend for some responses, as shown in Figure 89.

Figure 89 – Regression analysis for the first attempt of methodology.

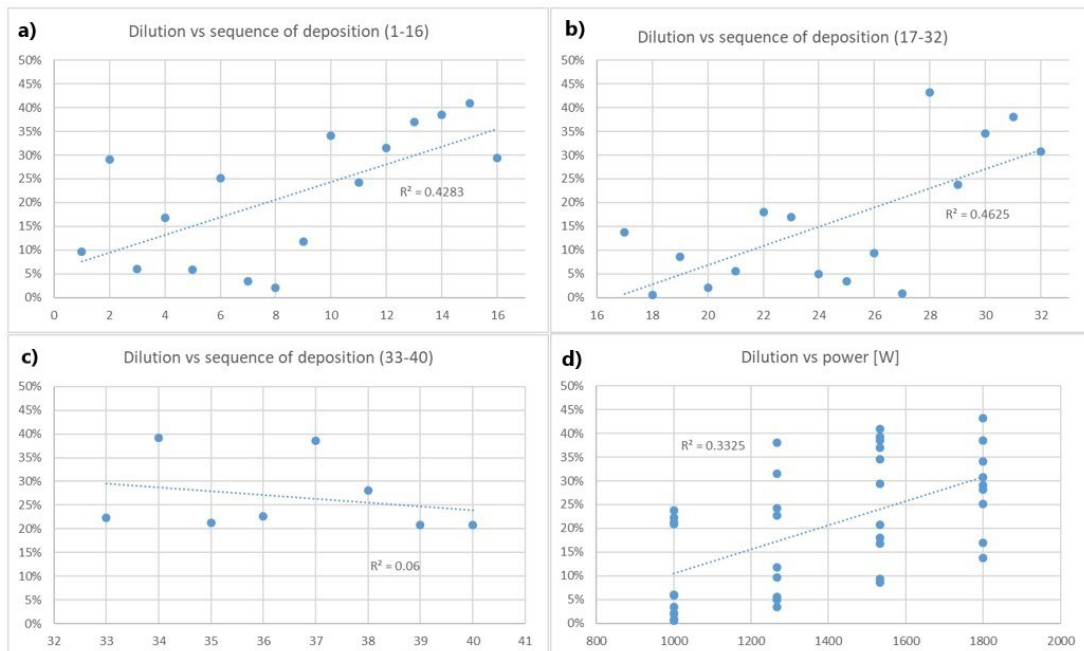


Source: Author (2019).

The dots (representing each experiment) do not follow a behavior that can be physically explained, according to the phenomena present in the process. Additionally, there are some discrepant dots, making a group of each hatch spacing mix to the others. It was also observed that the dots are too much spaced from the plan that represents it, so the regression will not correspond to the results obtained. Considering all these factors, a step back was necessary, to analyze what caused that unexpected behavior.

Among some possible reasons for the behavior observed, the most probable was that the sequence of deposition was heating the substrate, and it could impact the characteristics of the layers. It was analyzed the correlation between some inputs and outputs to verify the hypothesis. The deposition was made using three substrates. In the first one, it was deposited parameters 1 to 16, the second one received parameters 17 to 32, and the last one received the parameters 33 to 48. The parameters 41 to 48 do not appear in the graphics because they presented high deformation on their surface so they were disqualified from cross-section preparation. The numbers just express the sequence of deposition but the values for travel speed and power were chosen randomly. The correlation is related to the substrate heating so the graphics were split according to the substrate's deposition (Figure 90). The correlation factor between the sequence of deposition and the dilution was higher than the correlation between dilution and power in “a” and “b”. According to that, it is believed that the sequence of deposition had an impact on the results obtained, probably generated by substrate heating. The action adopted to solve the problem was to measure the substrate temperature and only move on once it was under 50 °C, as described in section 4.4.

Figure 90 – Correlation between the dilution and the sequence of deposition (a, b, and c) and between the dilution and power (d).



Source: Author (2020).

6 CONCLUSIONS

The group of geometrical characteristics selected for representing the single-layers was efficient to describe all the desired features without overlapping information. The illustrations were developed for explaining the correct way to measure the layers to minimize the chance of misinterpretations by the user and standardize the measuring process. That approach helped everybody involved in the methodology process to perfectly understand the characteristics that were being measured and how the measuring process is done.

The development of the methodology shows that the process is not mechanized, and requires from the user an understanding of the behavior of the alloy, the limitations of the equipment, and the understanding of which are the most important characteristics for each application. The method obtained helps the user to develop all of these knowledges and to achieve a better comprehension of all the processing parameters selection chain.

The application of the methodology allowed a better understanding of how some factors may influence the results of single-beads and single-layers. One good example was the necessity for changing the substrate after each deposition and measure the temperature. The trend was observed because substrate heating allowed good learning for not underestimate environmental conditions, and how they can have a direct impact on the results.

The selection of the processing parameter is highly dependent on the quality of all the stages previously developed. However, the multiple regression allows a little variation from the geometrical characteristics (as long they are random), once the response surfaces indicate the trend of the process. The regression analysis is a critical moment in the methodology and must be carried very carefully. Noises generated in this stage may incur results that can not be validated. Additionally, it is necessary to be careful with the desirability ranges, to define values possible to be achieved and correspond to the needs of the user. The additional tests for improving the optimized layer are important to be considered and depend on the sensibility and knowledge of the user.

The building of the samples using the selected parameter did not present many difficulties, being stable along all the process. Some care was taken with the position, quantity, and strategy used for the deposition of samples, aiming always to keep the maximum homogeneity possible.

The characterization of the samples resulted in 99.86% of density, and the morphology of the pores was majorly rounded, which decreases the chance of these pores being crack nucleators. The microhardness observed (172.7 HV) was lower than expected

(minimum of 190 HV) for AM manufactured parts. The microstructure observed was refined and highly anisotropic, which turned to coarser and more isotropic after heat treatment. Yield strength for heat-treated samples (around 300 MPa) was considerably higher than the minimum requirements for wrought material (170 MPa according to ASTM A276) and even higher for as-built samples (380.7 MPa). All the samples exhibited similar behavior except by T1V-3 that needs deeper fracture analysis to understand if it was due to a defect or fragilization. The results for elastic modulus were inconsistent, which is believed to be related to the tensile test. For further studies, it is recommended to use a compression test or another to quantify elastic modulus, once the tensile test is not the most indicated to quantify that property. The characterization of the samples exhibited, in general, consistent results. That may be seen by the similarity of the tension curves and the low standard deviation of all the results¹⁸. That achievement increases the credibility of the method, once the characterization showed a predictable behavior of the parts obtained. The mechanical behavior observed was predominantly ductile and higher than minimal wrought material requirements.

In an overview, the methodology purposed in this work can help the user in selecting processing parameters (power, travel speed, feedrate, hatch distance) applied to additive manufacturing of Laser Directed Energy Deposition technology, providing parts with high density (above 99%) and consistent mechanical behavior (low standard deviation).

Some suggestions for future works are to extend the methodology for the deposition of complex geometries, investigate other mechanical properties using different techniques (e.g. compression test, bending test, impulse excitation test), analyze the Elastic Modulus using a different technique (e.g. compression test), analyze the effect of stress concentration factor related to the pores and voids observed, apply the method using other alloys.

¹⁸ Except elastic modulus.

REFERENCES

- [1] ISO/ASTM, “52900:2015 - Standard Terminology for Additive Manufacturing – General Principles – Terminology,” *Iso/Astm*, vol. 52900, p. 9, 2015.
- [2] R. M. Mahamood, *Laser Metal Deposition of Metals, Alloys, and Composite Materials*. Cham, Switzerland.: Springer, 2018.
- [3] B. H. Jared *et al.*, “Additive manufacturing : Toward holistic design,” *Scr. Mater.*, vol. 135, pp. 141–147, 2017.
- [4] “Wohlers Report 2019 - 3D Printing and Additive Manufacturing: State of the Industry,” Fort Collins, Colorado., 2019.
- [5] H. Bikas, P. Stavropoulos, and G. Chryssolouris, “Additive manufacturing methods and modeling approaches: A critical review,” *Int. J. Adv. Manuf. Technol.*, vol. 83, no. 1–4, pp. 389–405, 2016.
- [6] D. Gu, *Laser Additive Manufacturing of High-Performance Materials*. Nanjing, China.: Springer-Verlag, 2015.
- [7] J. Scott, N. Gupta, C. Weber, and S. Newsome, “Additive Manufacturing: Status and Opportunities,” Washington, DC., 2012.
- [8] W. M. Steen and J. Mazumder, *Laser material processing*, 4th Editio. New York: Springer, 2010.
- [9] W. Zhang *et al.*, “Additive manufacturing of metallic components – Process, structure and properties,” *Prog. Mater. Sci.*, vol. 92, pp. 112–224, 2018.
- [10] M. Al-Makky and D. Mahmoud, “The Importance of Additive Manufacturing Processes in Industrial Applications,” in *17th International Conference on Applied Mechanics and Mechanical Engineering.*, 2016, p. 14.
- [11] American Society for Testing and Materials, “Standard Guide for Directed Energy Deposition of Metals, ASTM F3187,” 2016.
- [12] S. Donadello, M. Motta, A. G. Demir, and B. Previtali, “Monitoring of laser metal deposition height by means of coaxial laser triangulation,” *Opt. Lasers Eng.*, vol. 112, no. August 2018, pp. 136–144, 2019.
- [13] J. Iñaki, A. Lamikiz, M. Cortina, E. Ukar, and A. Alberdi, “Hardness , grainsize and porosity formation prediction on the Laser Metal Deposition of AISI 304 stainless steel,” *Int. J. Mach. Tools Manuf.*, vol. 135, no. August, pp. 53–64, 2018.
- [14] I. Jon and *et. al.*, “Instantaneous powder flux regulation system for Laser Metal Deposition,” vol. 29, pp. 242–251, 2017.

- [15] R. L. Deuis, J. M. Yellup, and C. Subramanian, "Metal-matrix composite coatings by PTA surfacing," *Compos. Sci. Technol.*, vol. 58, no. 2, pp. 299–309, 1998.
- [16] J. Tuominen, "Engineering Coatings by Laser Cladding – The Study of Wear and Corrosion Properties, Ph.D Dissertation," Tampere University of Technology, 2009.
- [17] R. Xie, D. Li, B. Cui, L. Zhang, and F. Gao, "A defects detection method based on infrared scanning in laser metal deposition process," *Rapid Prototyp. J.*, vol. 24, no. 6, pp. 945–954, 2018.
- [18] J. C. Lippold and D. J. Kotecki, "Austenitic Stainless Steels," in *Welding Metallurgy and Weldability of Stainless Steels*, vol. 2, no. 2, Jhon Wiley & Sons, 2005, pp. 141–229.
- [19] A. Dass and A. Moridi, "State of the Art in Directed Energy Deposition: From Additive Manufacturing to Materials Design," *Coatings*, vol. 9, no. 7, p. 418, Jun. 2019.
- [20] T. Mukherjee and T. DebRoy, "A digital twin for rapid qualification of 3D printed metallic components," *Appl. Mater. Today*, vol. 14, pp. 59–65, 2019.
- [21] M. M. Attallah, R. Jennings, X. Wang, and L. N. Carter, "Additive manufacturing of Ni-based superalloys: The outstanding issues," *MRS Bull.*, vol. 41, no. 10, pp. 758–764, 2016.
- [22] E. T. J. Lawrence, J. Pou, D. K. Y. Low, *Advances in Laser Materials Processing*. Woodhead Publishing Limited, 2010.
- [23] TRUMPF Werkzeugmaschinen, "Laser machining: Solid-state lasers." Germany, p. 120, 2007.
- [24] Cemar Line, "Laser Types and Operation." [Online]. Available: <https://www.cemarelectro.com/laser-safety/laser-types-and-operation/>. [Accessed: 11-May-2019].
- [25] K. Zhang, S. Wang, W. Liu, and X. Shang, "Characterization of stainless steel parts by Laser Metal Deposition Shaping," *J. Mater.*, vol. 55, pp. 104–119, 2014.
- [26] A. Segerstark, J. Andersson, and L. E. Svensson, "Evaluation of a temperature measurement method developed for laser metal deposition," *Sci. Technol. Weld. Join.*, vol. 22, no. 1, pp. 1–6, 2017.
- [27] Z. Yan, W. Liu, Z. Tang, X. Liu, N. Zhang, and M. Li, "Review on thermal analysis in laser-based additive manufacturing," *Opt. Laser Technol.*, vol. 106, pp. 427–441, 2018.
- [28] American Society for Testing and Materials, "Standard Terminology for Additive Manufacturing – General Principles – Terminology, ASTM 52900." pp. 1–9, 2015.
- [29] R. Igarar, "About Measuring Laser Power and Energy Output," *Coherent*. pp. 1–5,

- 2009.
- [30] J. C. Ion, *Laser Processing of Engineered Materials*. Elsevier Butterworth-Heinemann, 2005.
- [31] American Welding Society, “Standard Welding Terms and Definitions, AWS A3.0,” vol. 6, no. 2. Miami, Florida., p. 103, 2000.
- [32] “Ophir Photonics.” [Online]. Available: <https://www.ophiropt.com/blog/laser-measurement/a-shortcut-for-calculating-power-density-of-a-laser-beam/>. [Accessed: 01-Mar-2020].
- [33] A. Emamian, S. F. Corbin, and A. Khajepour, “The influence of combined laser parameters on in-situ formed TiC morphology during laser cladding,” *Surf. Coatings Technol.*, vol. 206, no. 1, pp. 124–131, 2011.
- [34] E. Toyserkani, A. Khajepour, and S. Corbin, *Laser Cladding*. Boca Raton, Florida.: CRC Press LLC, 2005.
- [35] U. O. B. de Oliveira, “Laser Treatment of Alloys: Processing, Microstructure and Structural Properties,” Netherlands Institute for Metals Research, Natal, Brazil., 2007.
- [36] D. Ding, Z. Pan, D. Cuiuri, and H. Li, “A multi-bead overlapping model for robotic wire and arc additive manufacturing (WAAM),” *Robot. Comput. Integr. Manuf.*, vol. 31, pp. 101–110, 2015.
- [37] Z. Chen *et al.*, “Anisotropy of nickel-based superalloy K418 fabricated by selective laser melting,” *Prog. Nat. Sci. Mater. Int.*, vol. 28, no. 4, pp. 496–504, 2018.
- [38] American Society for Testing and Materials, “Standard Terminology for Nondestructive Examinations, ASTM E1316,” vol. 02, no. June 2014. p. 39, 2019.
- [39] J. L. Song, Y. T. Li, Q. L. Deng, Z. Y. Cheng, and C. Bryan, “Cracking mechanism of laser cladding rapid manufacturing 316L stainless steel,” *Key Eng. Mater.*, vol. 419–420, pp. 413–416, 2010.
- [40] F. Sciammarella and B. Salehi Najafabadi, “Processing Parameter DOE for 316L Using Directed Energy Deposition,” *J. Manuf. Mater. Process.*, vol. 2, no. 3, p. 61, 2018.
- [41] M. Thomas, G. J. Baxter, and I. Todd, “Normalised model-based processing diagrams for additive layer manufacture of engineering alloys,” *Acta Mater.*, vol. 108, pp. 26–35, 2016.
- [42] M. Nabhani, R. S. Razavi, and M. Barekat, “An empirical-statistical model for laser cladding of Ti-6Al-4V powder on Ti-6Al-4V substrate,” *Opt. Laser Technol.*, vol. 100, pp. 265–271, 2018.
- [43] U. De Oliveira, V. Oceli, and J. T. M. De Hosson, “Analysis of coaxial laser cladding

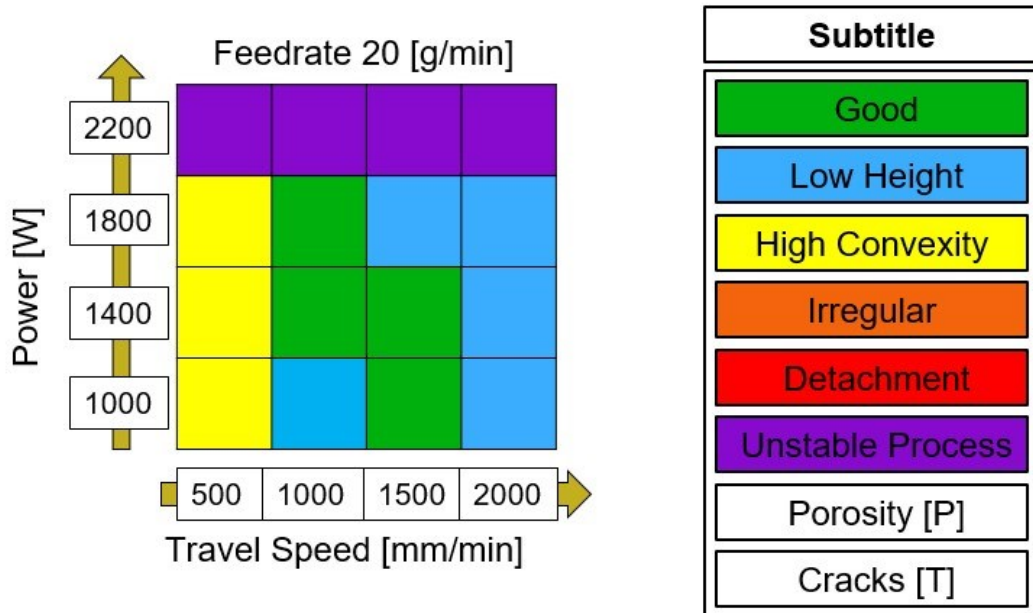
- processing conditions,” vol. 197, pp. 127–136, 2005.
- [44] B. Bax, R. Rajput, R. Kellet, and M. Reisacher, “Systematic evaluation of process parameter maps for laser cladding and directed energy deposition,” *Addit. Manuf.*, vol. 21, no. 2010, pp. 487–494, 2018.
- [45] L. Cao *et al.*, “Effect of laser energy density on defects behavior of direct laser depositing 24CrNiMo alloy steel,” *Opt. Laser Technol.*, vol. 111, no. August 2018, pp. 541–553, 2019.
- [46] A. Harooni, A. M. Nasiri, A. P. Gerlich, A. Khajepour, A. Khalifa, and J. M. King, “Processing window development for laser cladding of zirconium on zirconium alloy,” *J. Mater. Process. Technol.*, vol. 230, pp. 263–271, 2016.
- [47] A. Dass and A. Moridi, “State of the art in directed energy deposition: From additive manufacturing to materials design,” *Coatings*, vol. 9, no. 7, 2019.
- [48] J. Dawes, R. Bowerman, and R. Trepleton, “Introduction to the additive manufacturing powder metallurgy supply chain,” *Johnson Matthey Technol. Rev.*, vol. 59, no. 3, pp. 243–256, 2015.
- [49] L. Markusson, “Powder Characterization for Additive Manufacturing Processes,” Luleå University of Technology, 2017.
- [50] J. Gutjahr, “Análise do Reuso da Matéria-prima e sua Influência no Processo Laser Metal Deposition Aplicado à Manufatura Aditiva de Peças Metálicas,” Universidade Federal de Santa Catarina, 2020.
- [51] “Carpenter Additive.” [Online]. Available: <https://www.carpenteradditive.com/technical-library/>. [Accessed: 03-Mar-2020].
- [52] C. Kong, P. Carroll, P. Brown, and J. Scudamore, “The effect of average powder particle size on deposition efficiency, deposit height and surface roughness in the direct metal laser deposition process,” in *14th International Conference on Joining of Materials*, 2007.
- [53] Particulate Systems, “Particle Insight Brochure.” Norcross, Geórgia., p. 12, 2012.
- [54] Horiba scientific, “A Guidebook To Particle Size Analysis,” 2014.
- [55] I. Chang and Y. Zhao, *Advances in Powder Metallurgy: Properties, Processing and Applications*, First edit. Woodhead Publishing Limited, 2013.
- [56] T. ; Van Vliet and H. Lyklema, *Fundamentals of Interface and Colloid Science*, vol. IV. Elsevier, 2005.
- [57] M. Krantz, H. Zhang, and J. Zhu, “Characterization of Powder Flow: Static and Dynamic Testing,” *Powder Technol.*, pp. 239–245, 2009.

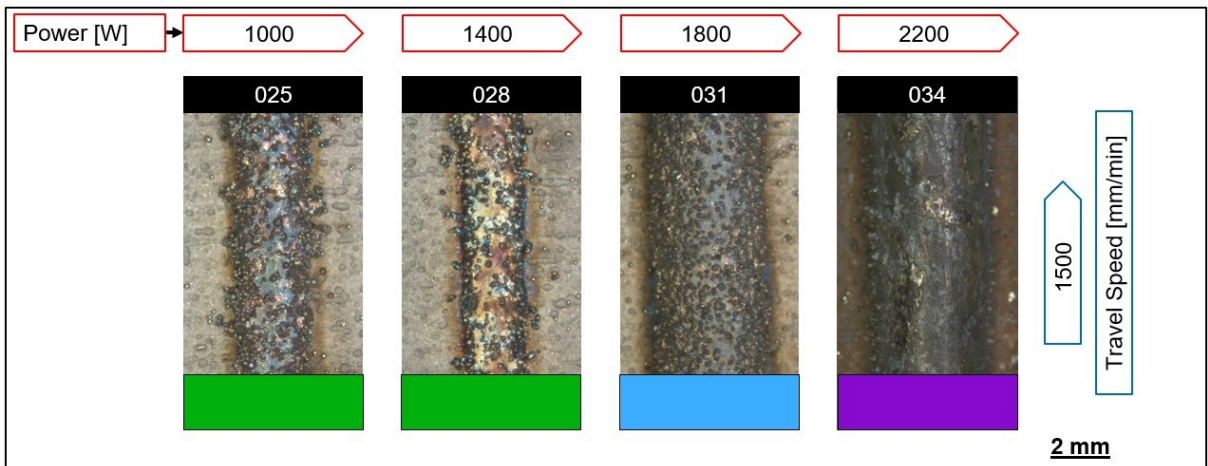
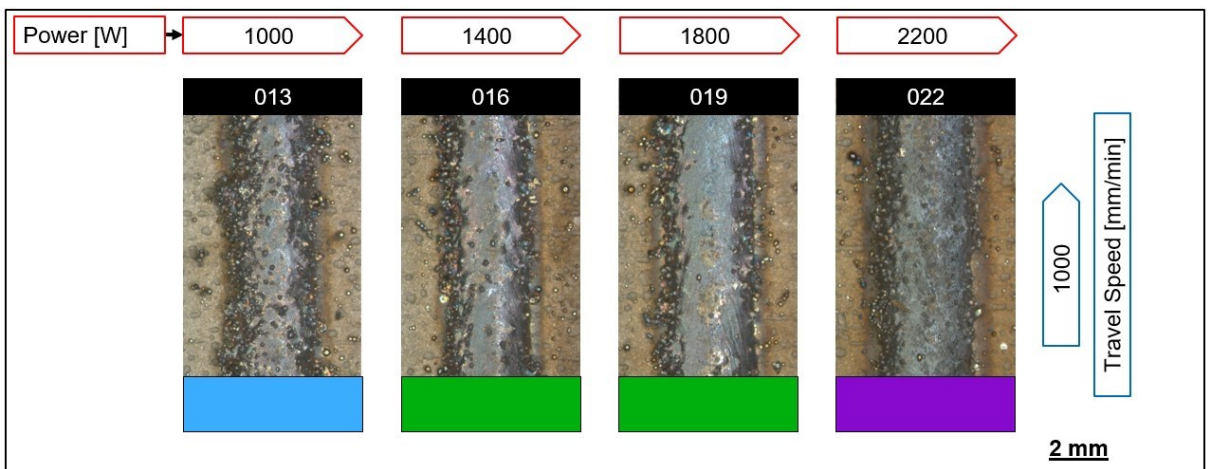
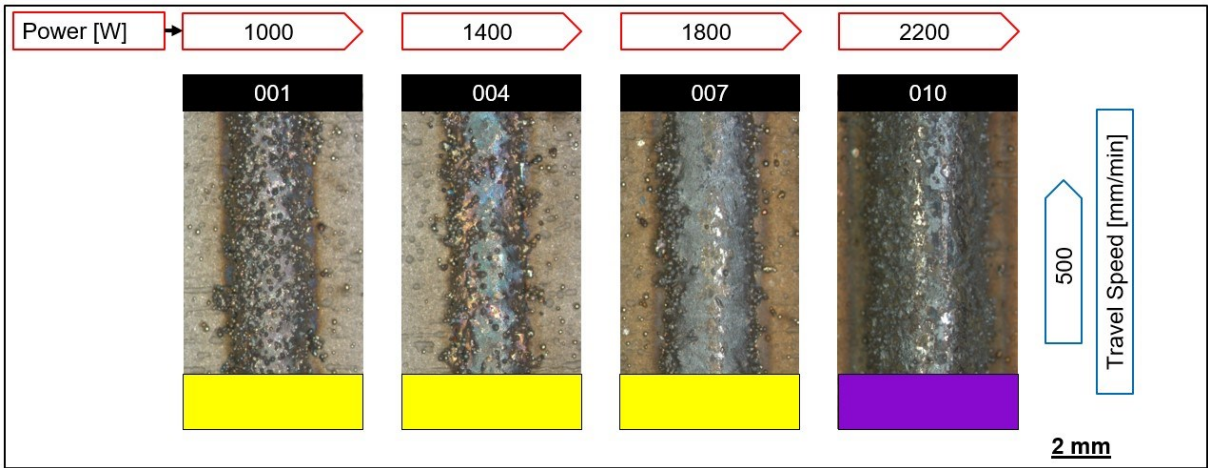
- [58] C. Zhong, J. Chen, A. Gasser, and R. Poprawe, “A comparative study of Inconel 718 formed by High Deposition Rate Laser Metal Deposition with GA powder and PREP powder,” *Mater. Des.*, pp. 386–392, 2016.
- [59] H. M. Carbó, “Aços Inoxidáveis: aplicações e especificações,” *Arcelor Mittal*. p. 29, 2008.
- [60] R. Singh, *Applied Welding Engineering*, 2nd Editio. 2015.
- [61] H. K. D. H. Bhadeshia and R. W. K. Honeycombe, *Steels: Microstructure and Properties*, 3rd Editio. Burlington, MA.: Elsevier Ltd, 2006.
- [62] W. D. Callister, *Ciência e Engenharia de Materiais: Uma Introdução*, 5ª edição. Rio de Janeiro - RJ, 2002.
- [63] D. F. Filho and V. A. Ferraresi, “Soldabilidade do aço inoxidável.” Barreiro - Portugal, p. 13, 2006.
- [64] A. Zeemann, “Soldagem dos aços Austeníticos,” *Infosolda*, p. 4, 2003.
- [65] P. J. Modenesi, P. V Marques, D. B. Santos, and C. Fortes, “Metalurgia da Soldagem.” ESAB, Contagem, MG., p. 48, 2001.
- [66] S. Kou, *Welding Metallurgy*, 2nd Editio., vol. 4, no. 3. New Jersey: John Wiley & Sons, 1972.
- [67] A. Saboori, A. Aversa, G. Marchese, S. Biamino, M. Lombardi, and P. Fino, “Microstructure and mechanical properties of AISI 316L produced by directed energy deposition-based additive manufacturing: A review,” *Appl. Sci.*, vol. 10, no. 9, 2020.
- [68] T. Mukherjee and T. DebRoy, “Printability of 316 stainless steel,” *Sci. Technol. Weld. Join.*, p. 8, 2019.
- [69] Z. En, E. Tan, J. Hock, L. Pang, J. Kaminski, and H. Pepin, “Characterisation of porosity , density , and microstructure of directed energy deposited stainless steel AISI 316L,” *Addit. Manuf.*, vol. 25, no. October 2017, pp. 286–296, 2019.
- [70] M. Mukherjee, “Effect of build geometry and orientation on microstructure and properties of additively manufactured 316L stainless steel by laser metal deposition,” *Materialia*, vol. 7, no. April, p. 100359, 2019.
- [71] W. J. Oh, W. J. Lee, M. S. Kim, J. B. Jeon, and D. S. Shim, “Repairing additive-manufactured 316L stainless steel using direct energy deposition,” *Opt. Laser Technol.*, vol. 117, no. December 2018, pp. 6–17, 2019.
- [72] G. F. Sun *et al.*, “Laser metal deposition as repair technology for 316L stainless steel : Influence of feeding powder compositions on microstructure and mechanical properties,” *Opt. Laser Technol.*, vol. 109, pp. 71–83, 2019.

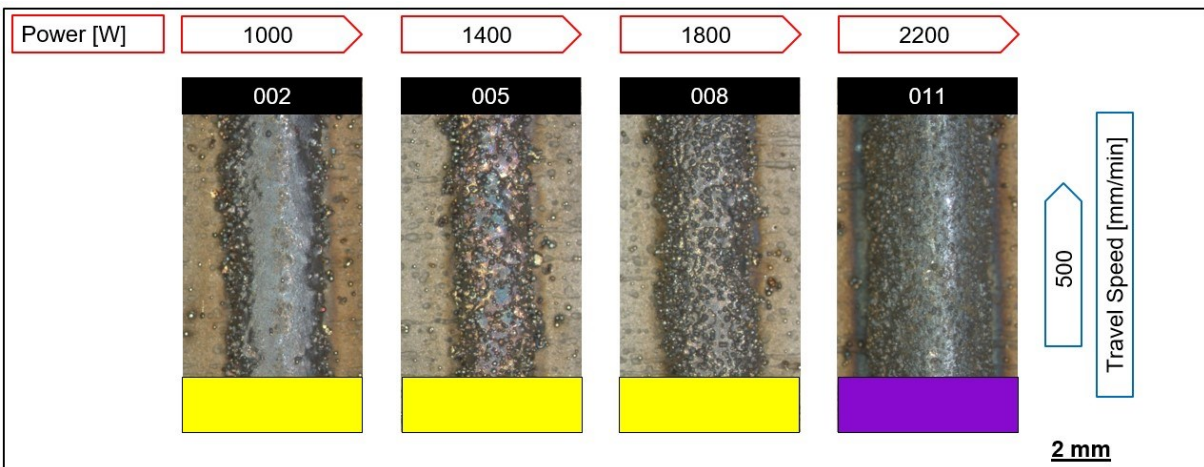
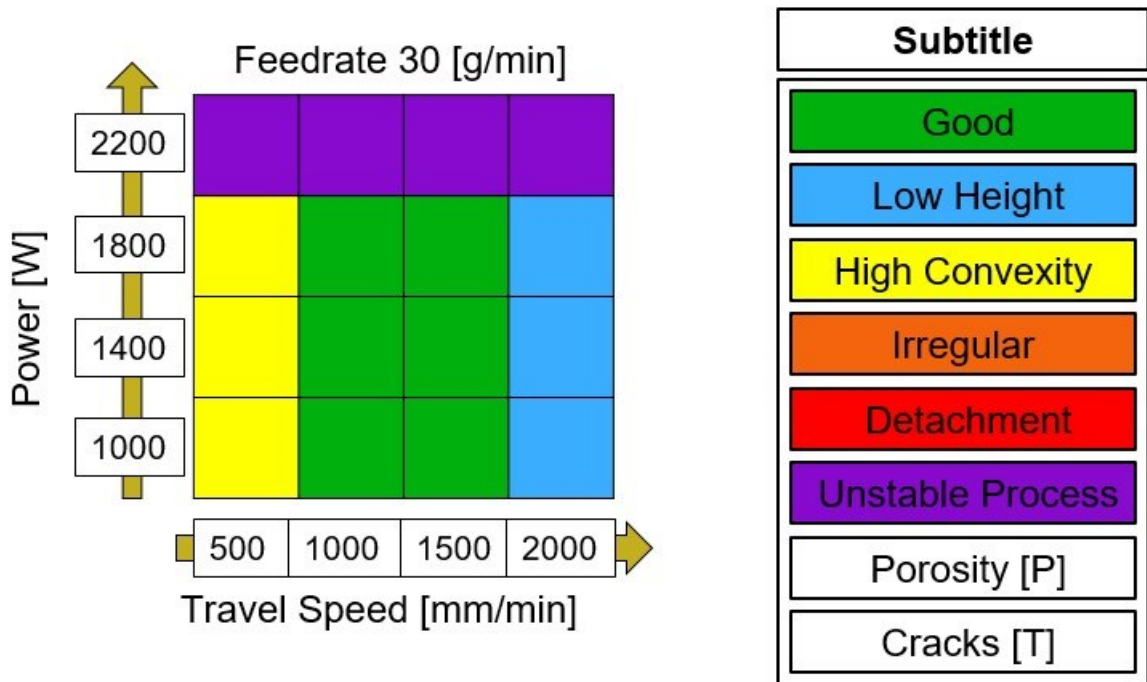
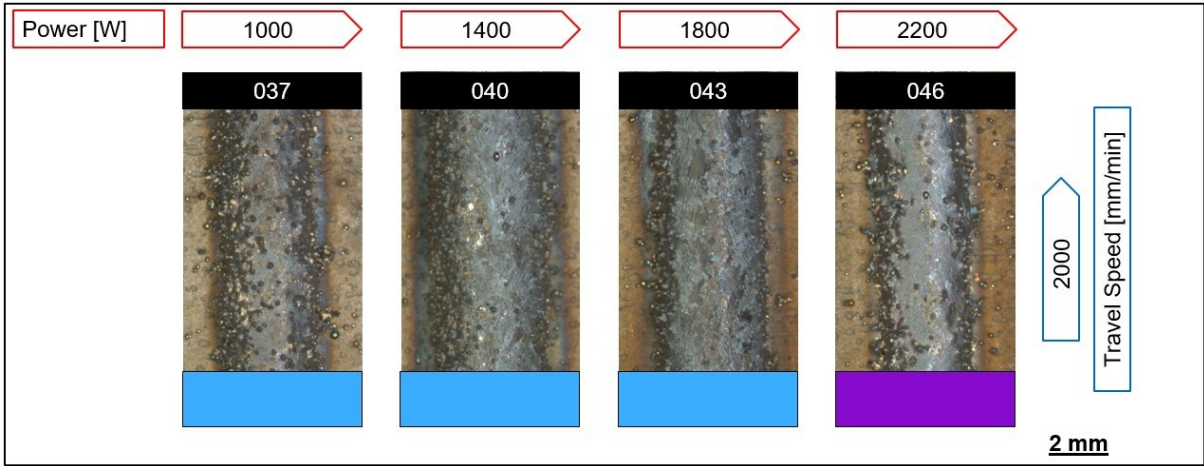
- [73] M. J. Zhan, G. F. Sun, Z. D. Wang, X. T. Shen, Y. Yan, and Z. H. Ni, “Numerical and experimental investigation on laser metal deposition as repair technology for 316L stainless steel,” *Opt. Laser Technol.*, vol. 118, no. March, pp. 84–92, 2019.
- [74] F. Khodabakhshi, M. H. Farshidianfar, A. P. Gerlich, M. Nosko, V. Trembošová, and A. Khajepour, “Microstructure, strain-rate sensitivity, work hardening, and fracture behavior of laser additive manufactured austenitic and martensitic stainless steel structures,” *Mater. Sci. Eng. A*, vol. 756, no. April, pp. 545–561, 2019.
- [75] F. Weng, S. Gao, J. Jiang, J. J. Wang, and P. Guo, “A novel strategy to fabricate thin 316L stainless steel rods by continuous directed energy deposition in Z direction,” *Addit. Manuf.*, vol. 27, no. March, pp. 474–481, 2019.
- [76] G. A. F. Seber and A. J. Lee, *Linear Regression Analysis*. Wiley, 2003.
- [77] S. Chatterjee and A. S. Hadi, *Regression Analysis by Example*, 5th editio. Wiley, 2012.
- [78] R. L. Wasserstein and N. A. Lazar, “The ASA’s Statement on p-Values: Context, Process, and Purpose,” *Am. Stat.*, vol. 70, no. 2, pp. 129–133, 2016.
- [79] L. S. Aft, *Fundamentals of Industrial Quality Control*, 3rd editio. CRC Press, 1997.
- [80] G. Derringer and R. Suich, “Simultaneous Optimization of Several Response Variables,” *J. Qual. Technol.*, vol. 12, no. 4, pp. 214–219, 1980.
- [81] M. Kuhn, “The desirability package.” 2016.
- [82] Instituto de Pesquisas Tecnológicas, “Certificado De Material De Referencia IPT 98.” São Paulo, p. 3, 2011.
- [83] American Society for Testing and Materials, “Standard Practices for Sampling Metal Powders, ASTM B215.” p. 4, 2008.
- [84] Particle Shape Analyzer 2.55, “Particle Insight Analysis,” 2019.
- [85] American Society for Testing and Materials, “Standard Specification for Chromium and Chromium-Nickel Stainless Steel Plate , Sheet , and Strip for Pressure Vessels and for General Applications, ASTM A240.” p. 12, 2020.
- [86] RPM Innovations, “RPM Innovations 535 - data sheet,” 2017.
- [87] IPG Photonics, “YLS-3000-CT data sheet,” 2015.
- [88] A. Yadollahi, N. Shamsaei, S. M. Thompson, and D. W. Seely, “Effects of process time interval and heat treatment on the mechanical and microstructural properties of direct laser deposited 316L stainless steel,” *Mater. Sci. Eng. A*, vol. 644, pp. 171–183, 2015.
- [89] A. Saboori *et al.*, “Critical Features in the Microstructural Analysis of AISI 316L Produced By Metal Additive Manufacturing,” *Metallogr. Microstruct. Anal.*, vol. 9, pp.

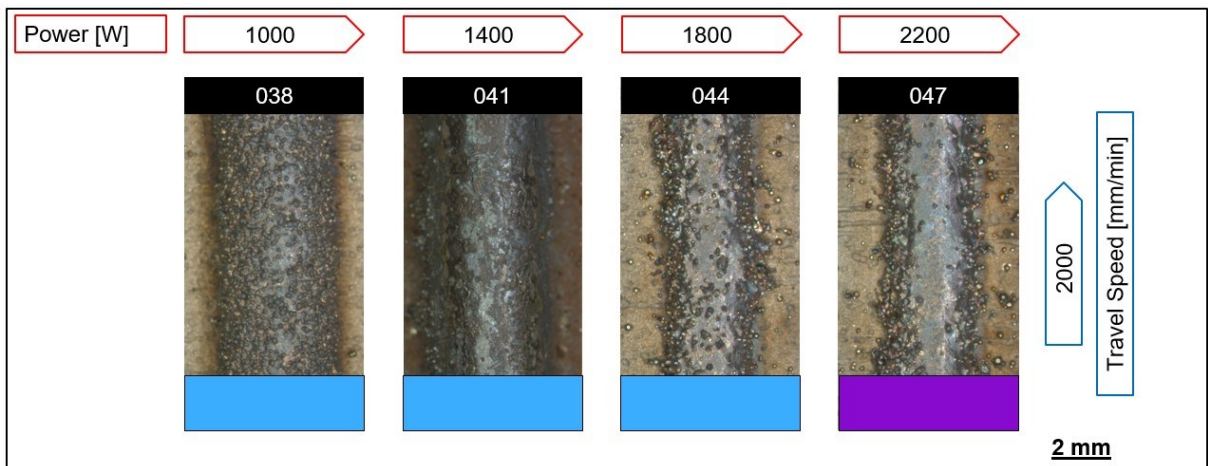
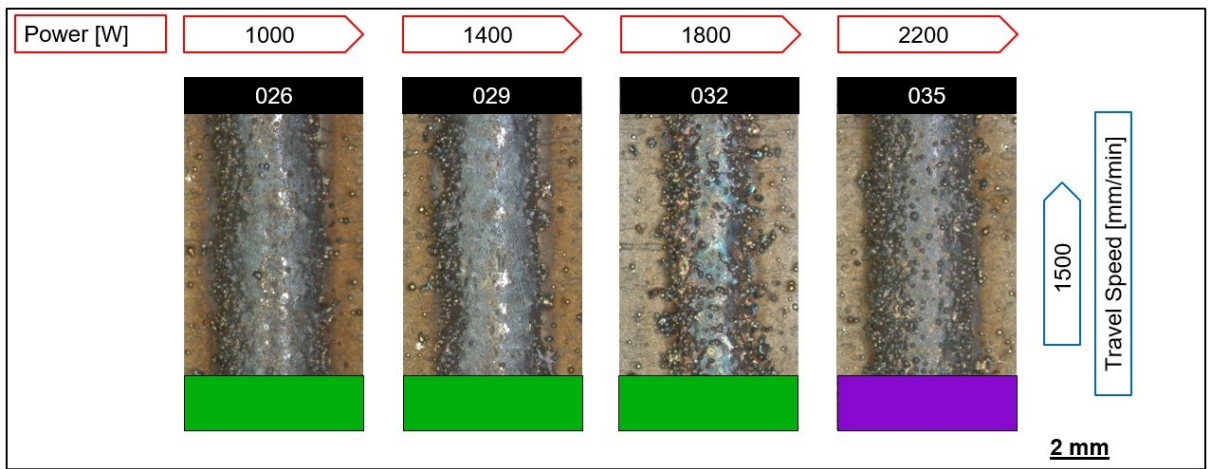
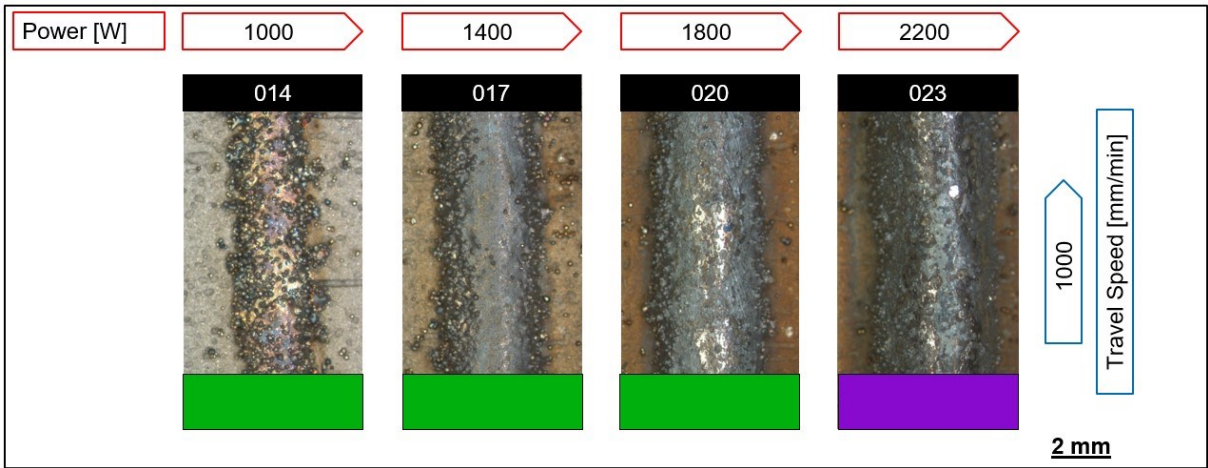
- 92–96, 2020.
- [90] A. Aversa *et al.*, “The role of Directed Energy Deposition atmosphere mode on the microstructure and mechanical properties of 316L samples,” *Addit. Manuf.*, vol. 34, no. February, p. 101274, 2020.
- [91] M. Ma, Z. Wang, and X. Zeng, “A comparison on metallurgical behaviors of 316L stainless steel by selective laser melting and laser cladding deposition,” *Mater. Sci. Eng. A*, vol. 685, pp. 265–273, 2017.
- [92] P. Ganesh *et al.*, “Studies on pitting corrosion and sensitization in laser rapid manufactured specimens of type 316L stainless steel,” *Mater. Des.*, vol. 39, pp. 509–521, 2012.
- [93] X. Lou, P. L. Andresen, and R. B. Rebak, “Oxide inclusions in laser additive manufactured stainless steel and their effects on impact toughness and stress corrosion cracking behavior,” *J. Nucl. Mater.*, vol. 499, pp. 182–190, 2018.
- [94] D. Herzog, V. Seyda, E. Wycisk, and C. Emmelmann, “Additive manufacturing of metals,” *Acta Mater.*, vol. 117, pp. 371–392, 2016.
- [95] “Schaeffler diagram analysis.” [Online]. Available: <https://migal.co/en/service/welding-calculators/schaeffler-diagram-for-standard-analysis>.
- [96] ASM International, “Stainless Steels for Design Engineers,” 2008.
- [97] F. Wang, D. Ma, and A. Bührig-Polaczek, “Microsegregation behavior of alloying elements in single-crystal nickel-based superalloys with emphasis on dendritic structure,” *Mater. Charact.*, pp. 311–316, 2017.
- [98] American Society for Testing and Materials, “Standard Test Methods and Definitions for Mechanical Testing of Steel Products, ASTM A370.” p. 50, 2019.
- [99] American Society for Testing and Materials, “Standard Test Methods for Tension Testing of Metallic Materials, ASTM E8.” p. 30, 2016.
- [100] “Standard Specification for Stainless Steel Bars and Shapes, ASTM A276,” *American Society for Testing and Materials*, vol. 10. pp. 1–7, 2017.

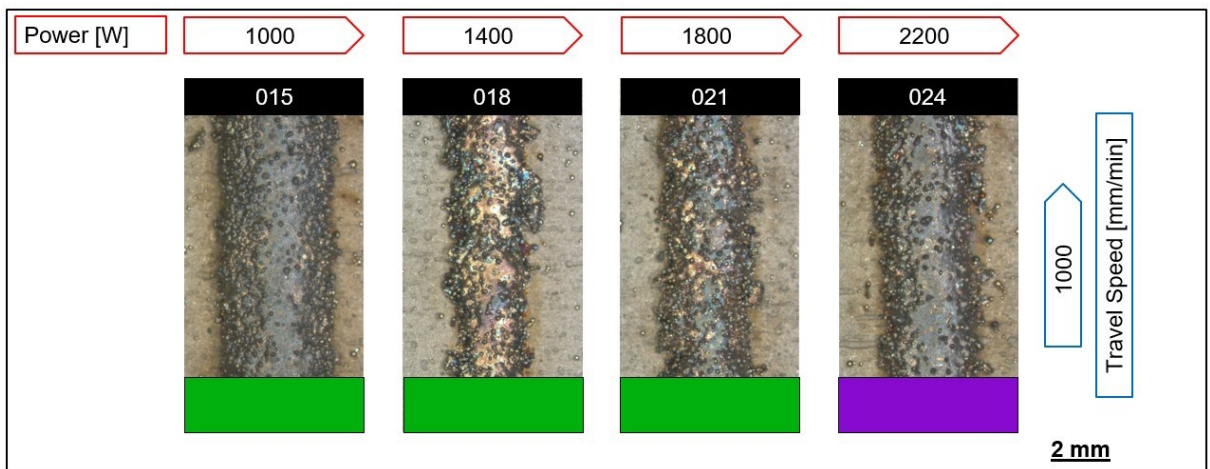
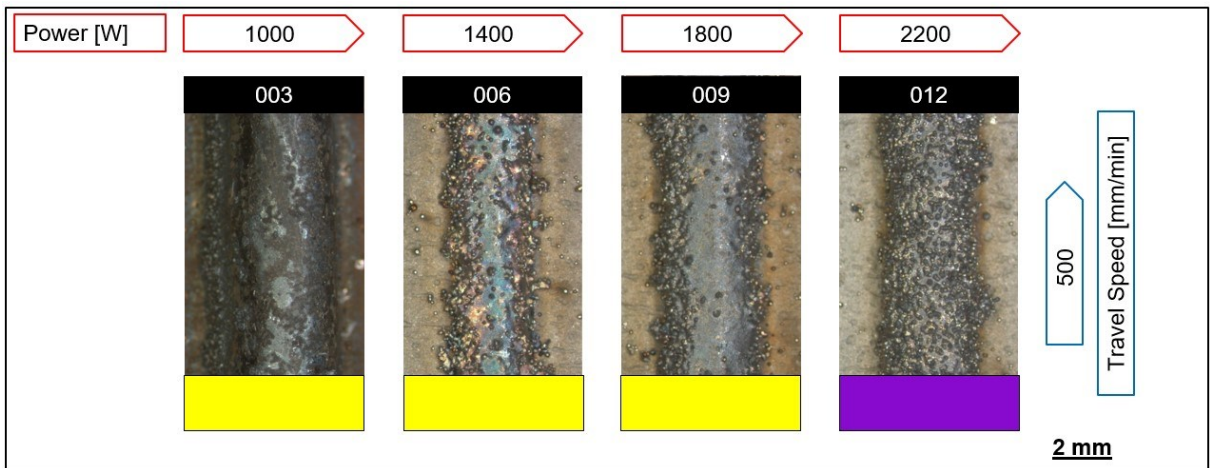
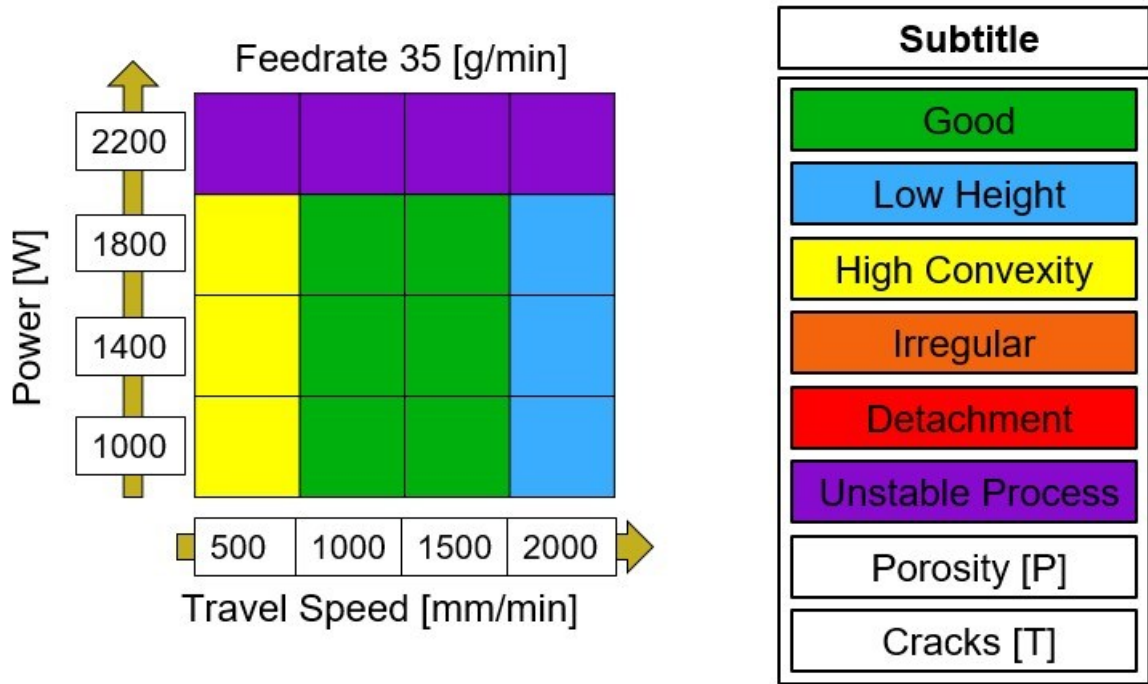
APPENDIX A – Single Beads Images

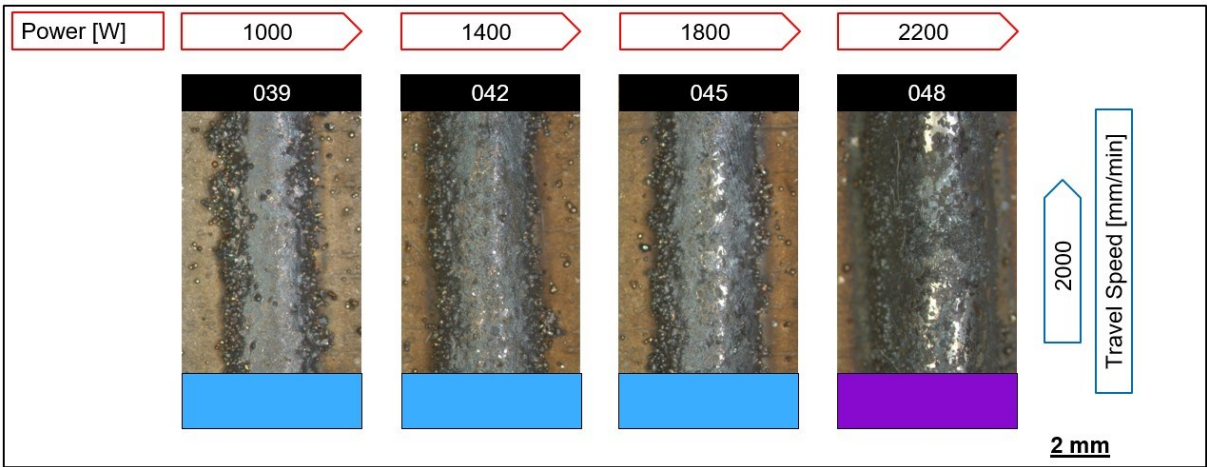
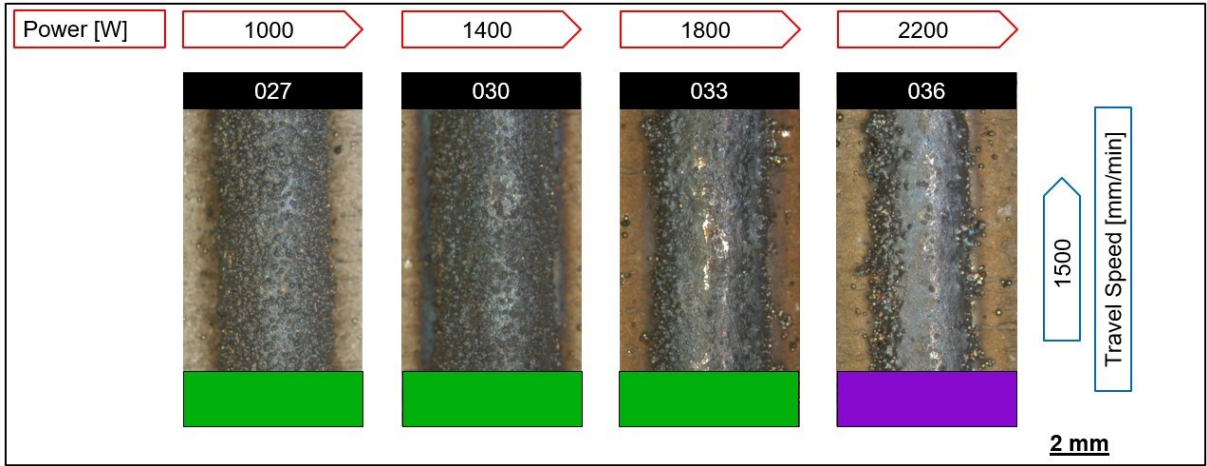












APPENDIX B – Processing Parameters used in Exploratory Stage

Laser Spot diameter = 1.78 mm | nozzle 25° | substrate = 316L

feedrate = 20 g/min				
	500 mm/min	1000 mm/min	1500 mm/min	2000 mm/min
1000 W	31	1	25	28
1400 W	40	37	13	4
1800 W	10	22	46	16
2200 W	34	43	7	19

feedrate = 30 g/min				
	500 mm/min	1000 mm/min	1500 mm/min	2000 mm/min
1000 W	38	8	5	14
1400 W	11	35	44	32
1800 W	23	26	17	47
2200 W	41	20	29	2

feedrate = 35 g/min				
	500 mm/min	1000 mm/min	1500 mm/min	2000 mm/min
1000 W	27	12	21	18
1400 W	30	15	24	6
1800 W	48	42	9	39
2200 W	3	33	45	36

APPENDIX C – Single Beads Height

Laser Spot diameter = 1.78 mm nozzle 25° substrate = 316L				
feedrate = 20 g/min				
	500 mm/min	1000 mm/min	1500 mm/min	2000 mm/min
1000 W	1.49	0.67	0.71	0.48
1400 W	1.57	0.88	0.72	0.41
1800 W	1.62	0.85	0.65	0.57
2200 W	1.67	0.89	0.55	0.49
feedrate = 30 g/min				
	500 mm/min	1000 mm/min	1500 mm/min	2000 mm/min
1000 W	1.53	0.90	0.70	0.65
1400 W	1.62	0.90	0.76	0.62
1800 W	1.78	0.96	0.77	0.65
2200 W	1.81	1.09	0.65	0.59
feedrate = 35 g/min				
	500 mm/min	1000 mm/min	1500 mm/min	2000 mm/min
1000 W	1.70	0.98	0.81	0.61
1400 W	1.93	1.09	0.75	0.55
1800 W	2.12	1.05	0.78	0.68
2200 W	2.09	0.96	0.73	0.58

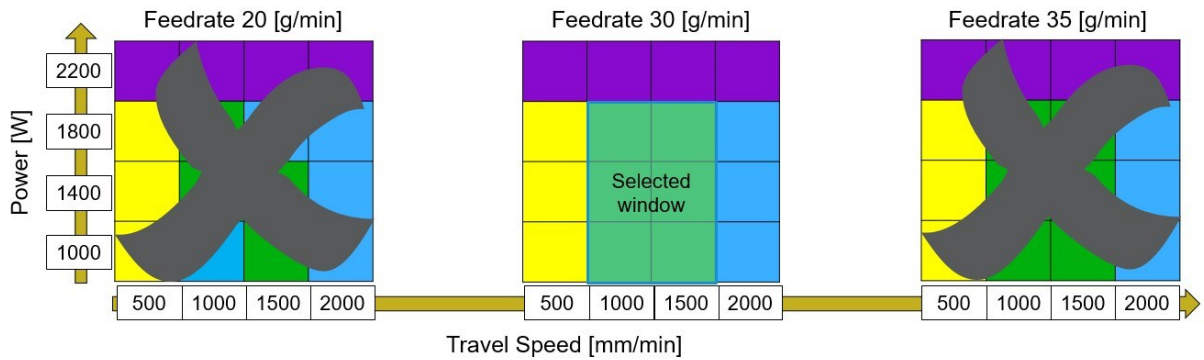
The blue cells are the parameters considered as “low height” (under 0.7 mm). The heights are expressed in millimeters.

APPENDIX D – Single Beads Width

Parameter	Height [mm]	Width [mm]	Aspect ratio
5	0.70	1.65	2.36
8	0.90	1.85	2.06
17	0.77	1.95	2.53
26	0.96	2.15	2.24
35	0.90	2.15	2.39
44	0.76	1.83	2.41

The width was measured only for the selected single beads. The average width of all selected single beads was used to calculate the 3 hatch distances used in the Modeling Stage.

APPENDIX E – Modeling Stage Parameters



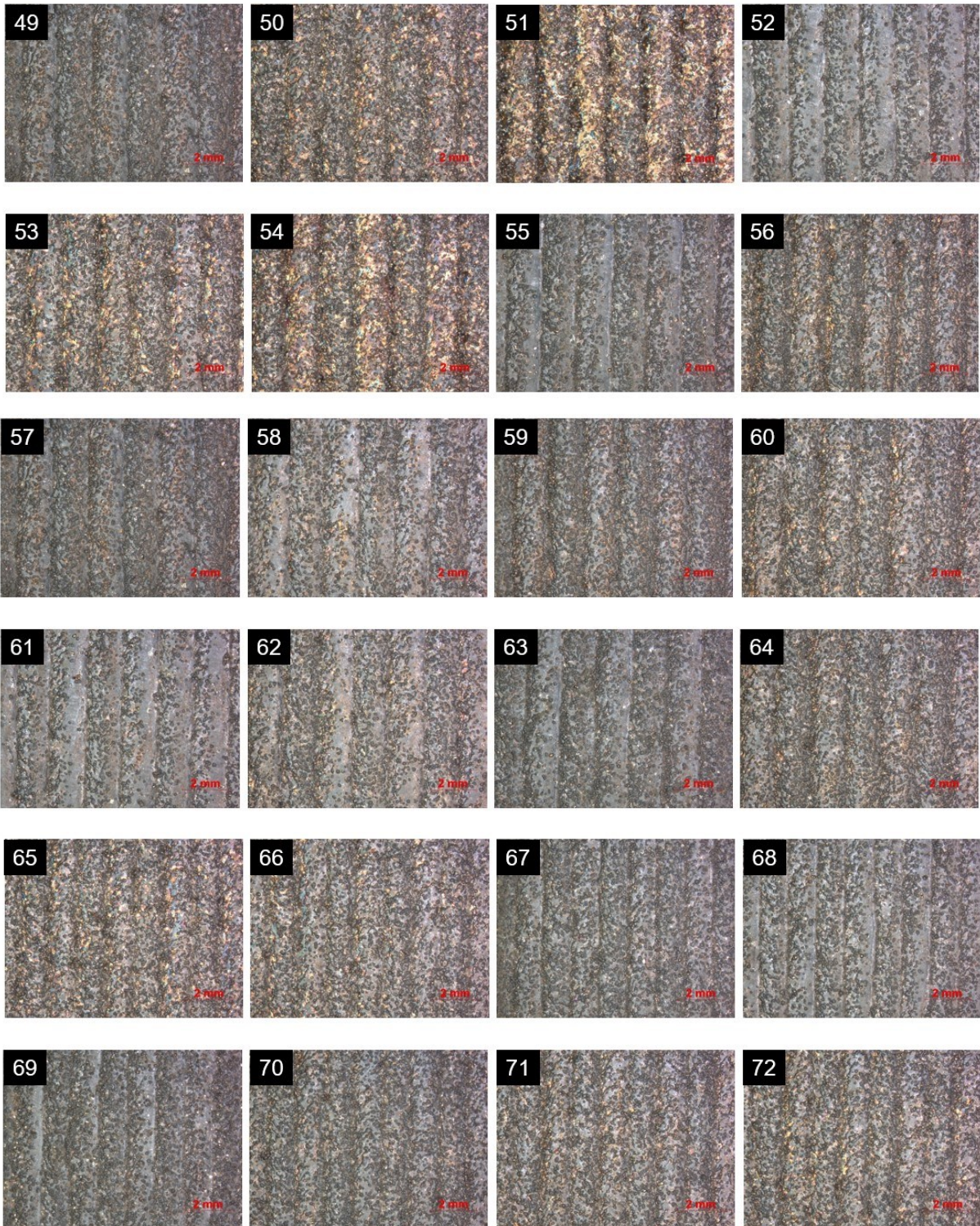
Laser Spot = 1.78 mm | nozzle 25° | substrate = 316L

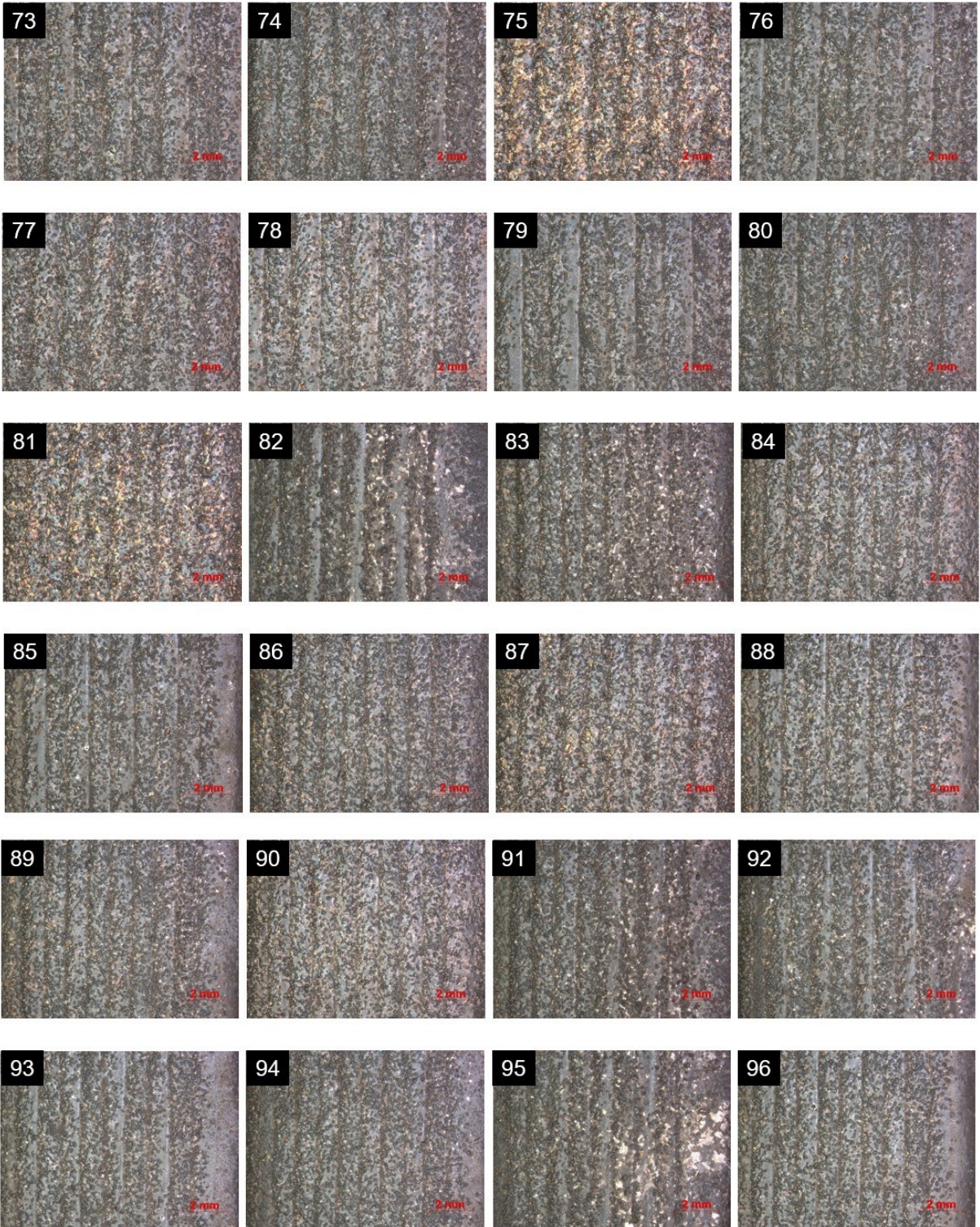
feedrate = 30 g/min 17.1 rpm D=1.5441 mm				
	762 mm/min	1100 mm/min	1440 mm/min	1778 mm/min
900 W	56	50	54	51
1233 W	59	64	60	53
1567 W	49	57	58	62
1900 W	63	55	52	61

feedrate = 30 g/min 17.1 rpm D=1.2545 mm				
	762 mm/min	1100 mm/min	1440 mm/min	1778 mm/min
900 W	70	72	65	75
1233 W	74	77	71	66
1567 W	80	67	73	78
1900 W	69	76	79	68

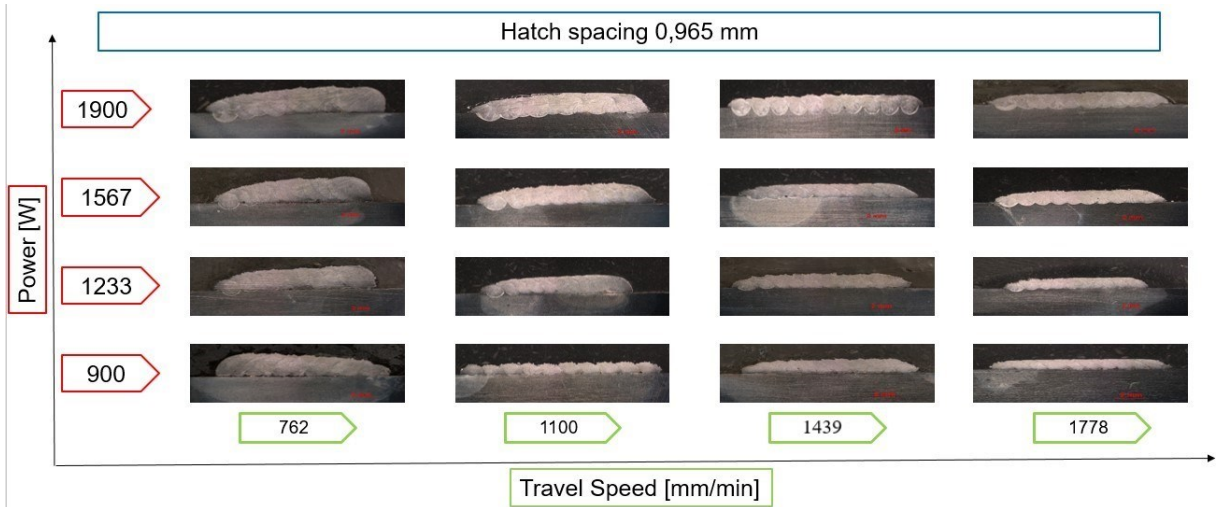
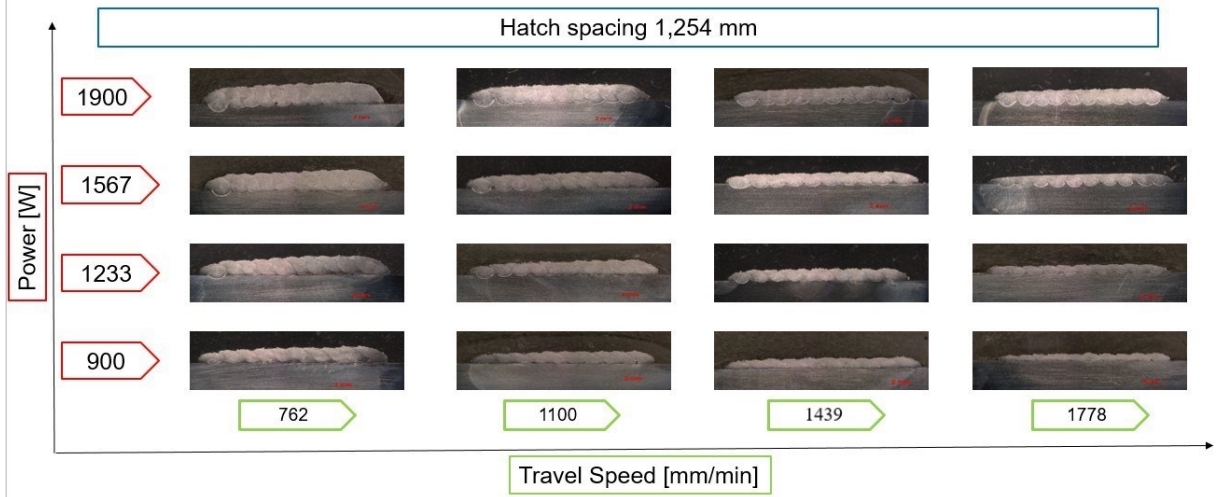
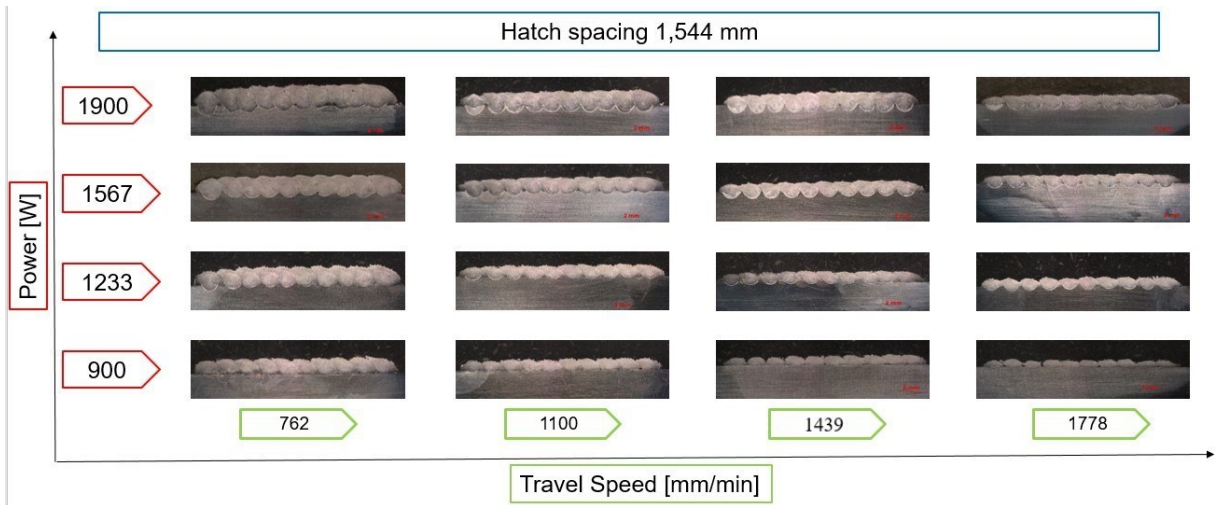
feedrate = 30 g/min 17.1 rpm D=0.09649 mm				
	762 mm/min	1100 mm/min	1440 mm/min	1778 mm/min
900 W	83	86	87	81
1233 W	91	89	84	90
1567 W	95	94	96	88
1900 W	82	92	93	85

APPENDIX F – Single Layers top images





APPENDIX G – Single Layers cross-sections



APPENDIX H – Single Layers Measurements

Sample	Power (W)	Travel Speed (mm/min)	Feedrate (g/min)	Hatch spacing (mm)	density (g/cm ³)	density (g/mm ³)	Total area (mm ²)	Top area (mm ²)	Bottom area (mm ²)	Dilution (%)	Width (mm)	Height (mm)	Mean height of the valleys (mm)	First peak (mm)	Peaks (3 last in mm)	Valleys (3 last in mm)	Height variation	Waviness	Efficiency	Layer slope (°)				
49	1567	762	30	1.544	8	0.008	27.93	24.592	3.338	12%	16.228	1.645	1.500	1.327	1.634	1.655	1.666	1.478	1.490	1.531	0.145	10%	56%	1.330
50	900	1100	30	1.544	8	0.008	13.909	13.667	0.242	2%	15.948	0.951	0.801	0.808	0.954	0.965	0.954	0.763	0.847	0.794	0.150	17%	46%	0.503
51	900	1778	30	1.544	8	0.008	8.674	8.596	0.078	1%	15.875	0.630	0.463	0.573	0.695	0.597	0.597	0.491	0.387	0.512	0.166	31%	41%	0.096
52	1900	1400	30	1.544	8	0.008	21.235	15.737	5.498	26%	8.047	1.023	1.003	0.819	1.046	1.026	0.996	1.005	1.014	0.990	0.020	1%	59%	1.400
53	1233	1778	30	1.544	8	0.008	11.39	9.843	1.547	14%	7.406	0.687	0.537	0.601	0.725	0.653	0.684	0.543	0.502	0.565	0.151	11%	47%	0.713
54	900	1400	30	1.544	8	0.008	10.517	10.465	0.052	0%	7.641	0.771	0.655	0.591	0.788	0.799	0.727	0.575	0.669	0.722	0.116	8%	38%	1.133
55	1900	1100	30	1.544	8	0.008	25.772	19.796	5.976	23%	7.492	1.333	1.247	1.036	1.347	1.316	1.337	1.223	1.244	1.275	0.086	3%	58%	2.556
56	900	762	30	1.544	8	0.008	19.911	19.855	0.056	0%	7.485	1.320	1.214	1.078	1.299	1.372	1.289	1.253	1.139	1.250	0.106	4%	40%	1.794
57	1567	1100	30	1.544	8	0.008	21.379	18.858	2.521	12%	7.524	1.235	1.129	0.985	1.270	1.229	1.207	1.115	1.126	1.147	0.106	4%	58%	1.878
58	1567	1400	30	1.544	8	0.008	17.674	13.748	3.926	22%	16.469	1.010	0.932	0.736	1.006	1.048	0.975	0.869	0.952	0.975	0.078	9%	51%	0.924
59	1233	762	30	1.544	8	0.008	23.954	22.899	1.055	4%	16.189	1.576	1.380	1.172	1.586	1.493	1.649	1.365	1.387	1.387	0.196	14%	47%	1.875
60	1233	1400	30	1.544	8	0.008	13.967	12.706	1.261	9%	16.417	0.913	0.834	0.664	0.934	0.892	0.913	0.795	0.849	0.857	0.079	10%	47%	0.965
61	1900	1778	30	1.544	8	0.008	17.51	12.7	4.81	27%	16.176	0.859	0.768	0.694	0.845	0.877	0.854	0.739	0.741	0.824	0.091	12%	68%	0.630
62	1567	1778	30	1.544	8	0.008	14.522	11.59	2.932	20%	16.394	0.782	0.714	0.632	0.799	0.812	0.736	0.763	0.712	0.668	0.068	10%	58%	0.404
63	1900	762	30	1.544	8	0.008	32.833	28.269	4.564	14%	16.787	1.866	1.772	1.358	1.886	1.878	1.834	1.751	1.751	1.814	0.094	6%	57%	1.805
64	1233	1100	30	1.544	8	0.008	17.836	16.419	1.417	8%	16.342	1.116	1.028	0.944	1.119	1.182	1.048	1.004	1.046	1.035	0.088	9%	48%	0.405

Sample	Power (W)	Travel Speed (mm/min)	Feedrate (g/min)	Hatch spacing (mm)	density (g/cm ³)	density (g/mm ³)	Total area (mm ²)	Top area (mm ²)	Bottom area (mm ²)	Dilution (%)	Width (mm)	Height (mm)	Mean height of the valleys (mm)	First peak (mm)	Peaks (3 last in mm)	Valleys (3 last in mm)	Height variation	Waviness	Efficiency	Layer slope (°)		
65	900	1400	30	1.254	8	0.008	11.283	11.256	0.027	0%	13.286	0.866	0.758	0.715	0.836	0.730	0.772	0.109	13%	42%	0.920	
66	1233	1778	30	1.254	8	0.008	10.363	9.601	0.762	7%	13.316	0.842	0.758	0.649	0.847	0.824	0.751	0.760	0.084	12%	46%	0.837
67	1567	1100	30	1.254	8	0.008	21.075	19.803	1.272	6%	14.033	1.689	1.581	1.106	1.668	1.691	1.707	1.564	0.107	8%	58%	2.724
68	1900	1778	30	1.254	8	0.008	16.592	12.703	3.889	23%	13.907	1.019	0.997	0.695	1.036	1.026	0.976	0.990	0.022	2%	60%	1.373
69	1900	762	30	1.254	8	0.008	29.829	27.144	2.685	9%	14.602	2.182	2.087	1.546	2.209	2.251	2.085	2.169	0.095	5%	55%	2.349
70	900	762	30	1.254	8	0.008	19.172	19.111	0.062	0%	13.730	1.521	1.463	1.067	1.597	1.566	1.483	1.400	0.058	4%	39%	1.544
71	1233	1400	30	1.254	8	0.008	13.382	12.966	0.416	3%	13.658	1.125	1.005	0.798	1.157	1.104	0.982	1.011	0.120	13%	48%	1.473
72	900	1100	30	1.254	8	0.008	13.895	13.863	0.032	0%	13.388	1.048	1.023	0.819	1.079	1.037	1.027	1.008	0.025	2%	41%	0.989
73	1567	1400	30	1.254	8	0.008	16.259	14.005	2.254	14%	13.417	1.139	1.107	0.782	1.146	1.157	1.115	1.129	0.033	3%	52%	1.580
74	1233	762	30	1.254	8	0.008	23.467	23.007	0.46	2%	14.155	1.872	1.853	1.182	1.959	1.876	1.902	1.876	0.019	1%	47%	2.697
75	900	1778	30	1.254	8	0.008	8.286	8.266	0.02	0%	13.192	0.689	0.560	0.571	0.664	0.728	0.675	0.574	0.129	21%	39%	0.502
76	1900	1100	30	1.254	8	0.008	23.358	19.701	3.657	16%	14.240	1.577	1.497	1.048	1.563	1.605	1.563	1.522	0.080	6%	58%	2.301
77	1233	1100	30	1.254	8	0.008	16.918	16.443	0.475	3%	13.896	1.278	1.250	0.871	1.275	1.254	1.306	1.271	0.029	2%	48%	1.992
78	1567	1778	30	1.254	8	0.008	12.963	10.683	2.28	18%	13.929	0.929	0.897	0.643	0.961	0.930	0.897	0.876	0.033	4%	51%	1.161
79	1900	1400	30	1.254	8	0.008	19.45	14.983	4.467	23%	13.823	1.226	1.192	0.813	1.230	1.293	1.156	1.189	0.035	3%	56%	1.579
80	1567	762	30	1.254	8	0.008	26.575	25.377	1.198	5%	14.592	2.062	1.960	1.410	2.085	2.076	2.024	1.991	0.101	6%	52%	2.677

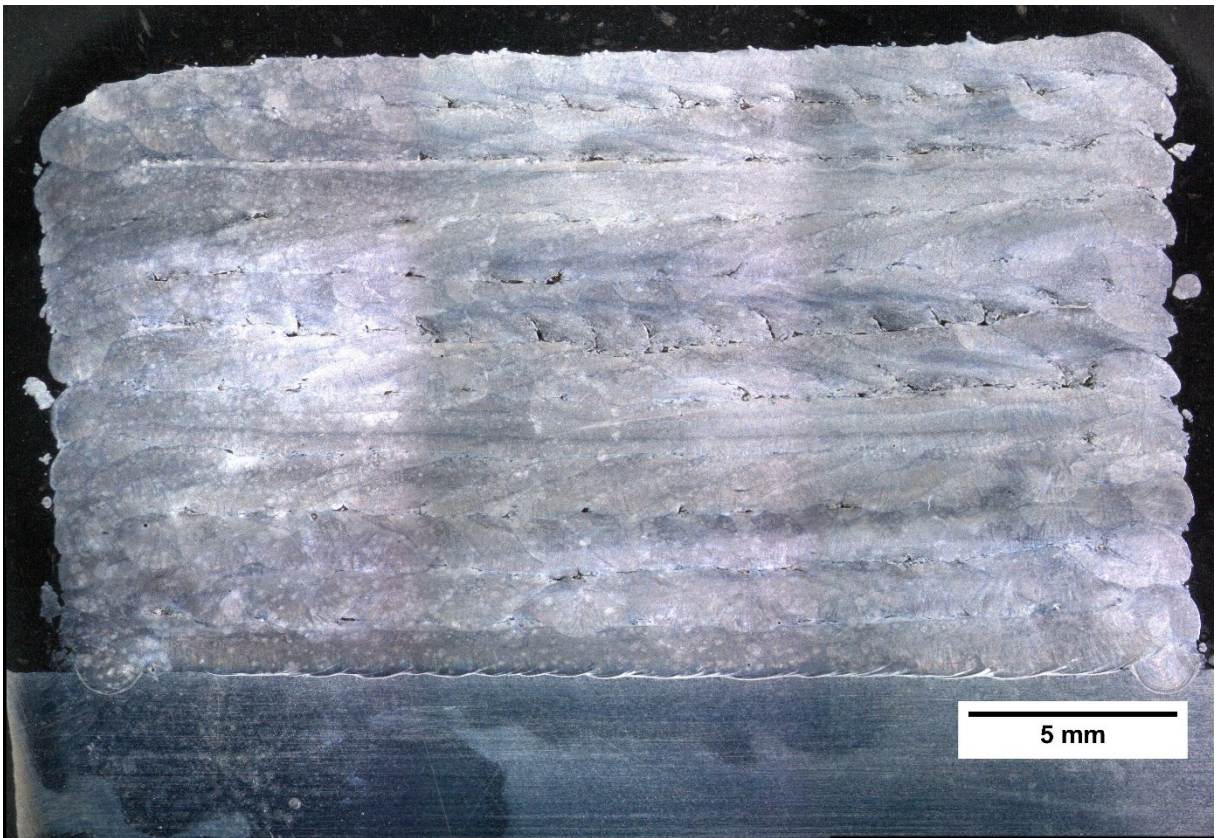
Sample	Power (W)	Travel Speed (mm/min)	Feedrate (g/min)	Hatch spacing (mm)	density (g/cm ³)	density (g/mm ³)	Total area (mm ²)	Top area (mm ²)	Bottom area (mm ²)	Dilution (%)	Width (mm)	Height (mm)	Mean height of the valleys (mm)	First peak (mm)	Peaks (3 last in mm)	Valleys (3 last in mm)	Height variation	Waviness	Efficiency	Layer slope (°)	
81	900	1778	30	0.965	8	0.008	8.188	8.188	0	0%	10.589	0.848	0.827	0.591	0.834	0.834	0.021	3%	39%	1.467	
82	1900	762	30	0.965	8	0.008	26.317	24.312	2.005	8%	11.275	2.520	2.328	1.410	2.498	2.132	2.479	0.191	9%	49%	6.064
83	900	762	30	0.965	8	0.008	20.431	20.431	0	0%	11.026	2.273	2.169	1.067	2.280	2.103	2.238	0.104	6%	42%	6.906
84	1233	1400	30	0.965	8	0.008	12.57	12.367	0.203	2%	4.442	1.258	1.173	0.809	1.285	1.167	1.179	0.085	3%	46%	5.202
85	1900	1778	30	0.965	8	0.008	14.262	11.501	2.761	19%	11.181	1.251	1.195	0.767	1.255	1.177	1.187	0.056	5%	55%	2.595
86	900	1100	30	0.965	8	0.008	13.638	13.592	0.046	0%	11.264	1.558	1.421	0.767	1.545	1.303	1.458	0.137	11%	40%	4.141
87	900	1400	30	0.965	8	0.008	10.108	10.108	0	0%	10.550	1.112	1.034	0.632	1.141	1.079	1.115	0.077	8%	38%	2.912
88	1567	1778	30	0.965	8	0.008	11.793	10.561	1.232	10%	10.860	1.162	1.121	0.643	1.140	1.202	1.145	0.042	4%	50%	2.940
89	1233	1100	30	0.965	8	0.008	16.276	15.911	0.365	2%	11.182	1.659	1.597	0.881	1.658	1.710	1.608	0.062	4%	47%	4.132
90	1233	1778	30	0.965	8	0.008	9.766	9.505	0.261	3%	10.707	1.014	0.990	0.641	1.040	0.991	1.012	0.024	3%	45%	2.205
91	1233	762	30	0.965	8	0.008	22.5	21.989	0.511	2%	11.308	2.253	2.090	1.223	2.187	2.260	2.311	0.163	8%	45%	6.102
92	1900	1100	30	0.965	8	0.008	20.939	18.767	2.172	10%	11.772	1.975	1.900	1.130	1.981	1.950	1.993	0.074	5%	55%	4.657
93	1900	1400	30	0.965	8	0.008	15.993	13.457	2.536	16%	11.886	1.465	1.406	0.798	1.397	1.479	1.385	0.059	5%	50%	3.861
94	1567	1100	30	0.965	8	0.008	18.867	17.901	0.966	5%	11.700	1.790	1.712	1.120	1.938	1.803	1.628	0.078	5%	53%	2.762
95	1567	762	30	0.965	8	0.008	26.293	25.313	0.98	4%	11.834	2.595	2.475	1.254	2.539	2.519	2.726	0.120	6%	51%	7.869
96	1567	1400	30	0.965	8	0.008	14.368	13.697	0.671	5%	11.307	1.354	1.296	0.943	1.420	1.451	1.343	0.058	5%	51%	1.402

APPENDIX I – Multilayer Geometry Depositions

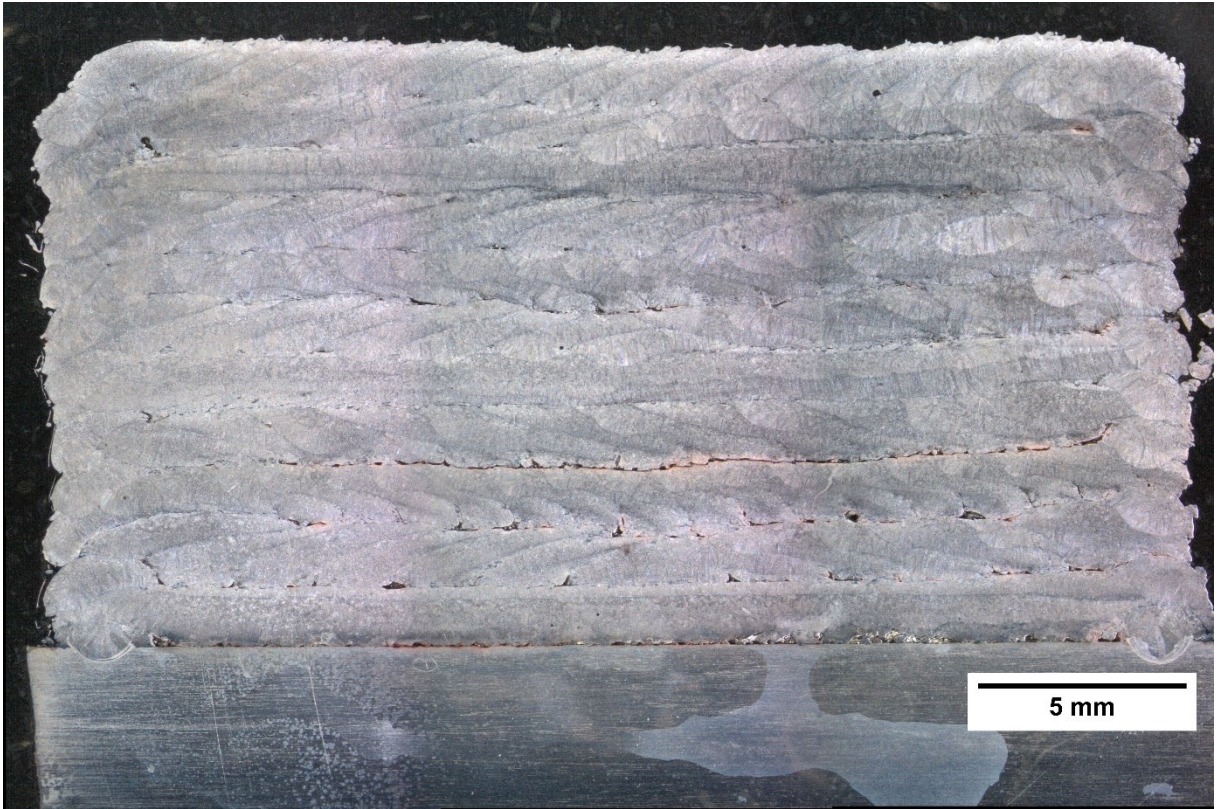
Single-layer:



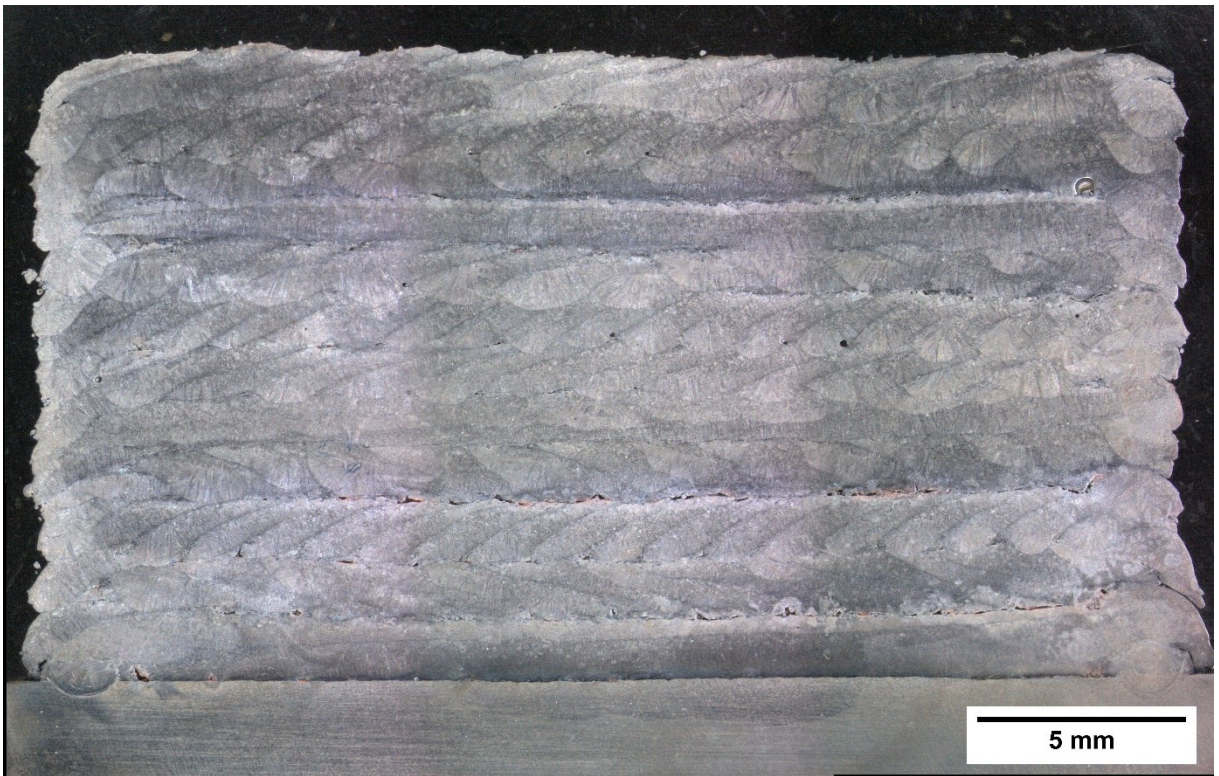
0% overlayer:



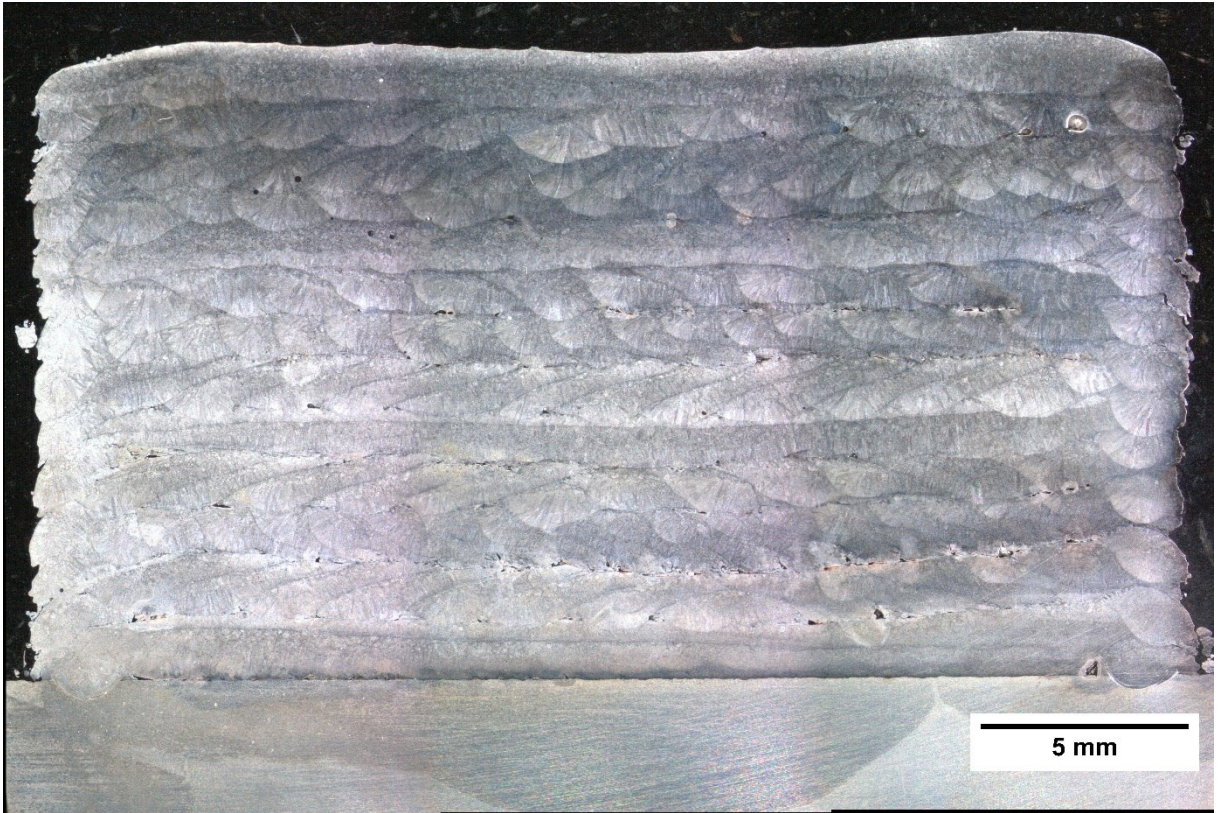
5% overlayer:



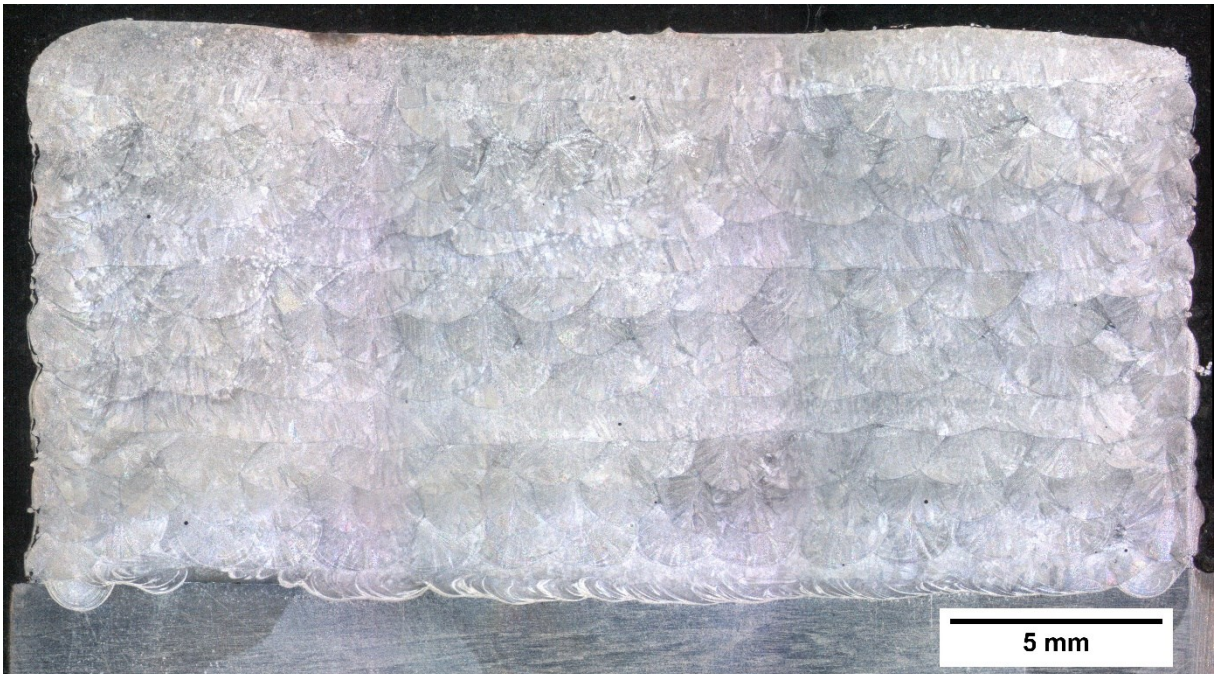
10% overlayer:



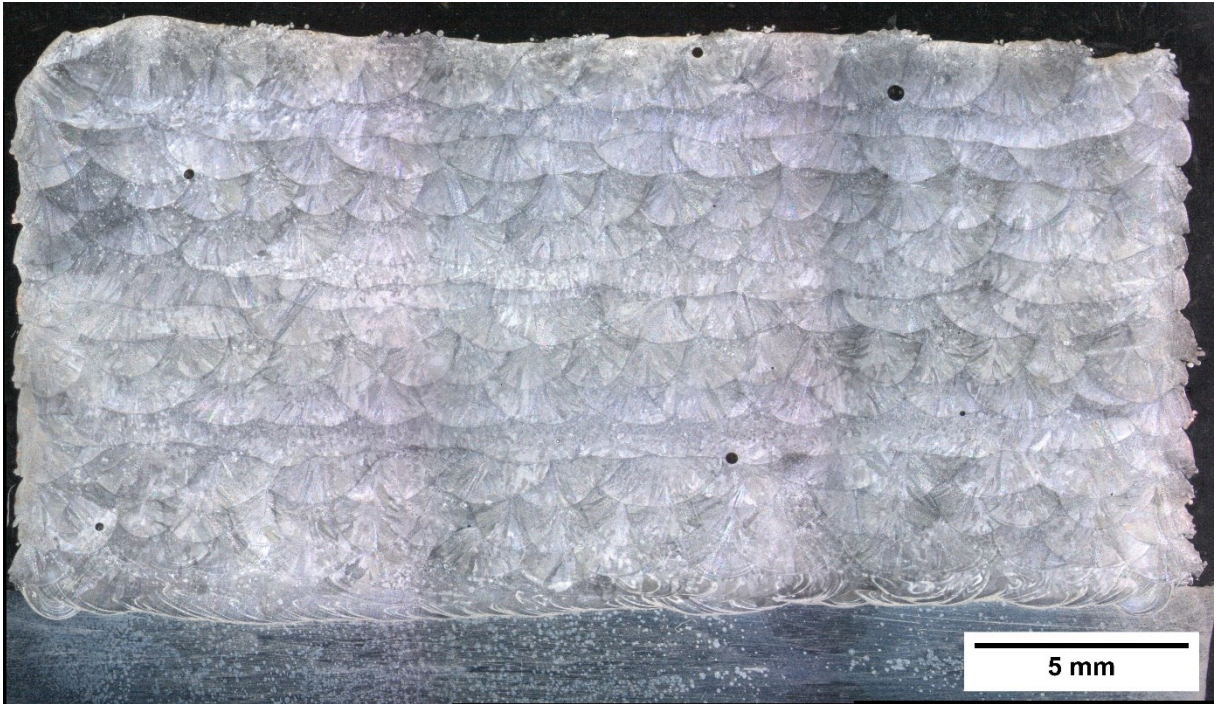
15% overlayer:



20% overlayer:



25% overlayer:



ATTACHMENT A – Reference material certificate



CERTIFICADO DE MATERIAL DE REFERÊNCIA Nº 1762-103

IPT 98

Aço Inoxidável (Cr-Ni-Mo-Ti)

Este material de referência foi certificado por meio do consenso de uma rede de laboratórios especialistas, utilizando diversas metodologias, e pode ser utilizado para calibração, verificação de precisão e exatidão e para demonstração de rastreabilidade de resultados em métodos de análise química por via clássica e instrumental.

O material apresenta granulometria entre 0,60 mm (peneira ABNT 30) e 2,00 mm (peneira ABNT 10).

Propriedades	Valores Certificados	Incertezas Expandidas	Unidade
Cr	16,75	0,06	%
Ni	11,01	0,04	
Mo	1,92	0,03	
Mn	1,88	0,01	
Ti	0,41	0,01	
Cu	0,292	0,004	
Si	0,26	0,01	
Co	0,125	0,003	
Al (total)	0,073	0,002	
W	0,053	0,003	
V	0,053	0,002	
C	0,050	0,001	
P	0,042	0,002	
Sn	0,019	0,003	
S	0,016	0,001	
N	0,0112	0,0005	
Al (solúvel)	0,070	0,002	%
Propriedades	Valores Informativos	Incertezas Expandidas	Unidade
Nb	0,007		%

Lote Nº 01

Prazo de validade: 5/11/2020

Os valores certificados e incertezas são garantidos pelo prazo de validade, considerando-se que o material seja utilizado e armazenado conforme as instruções apresentadas, desde que não tenha havido dano ou contaminação. O IPT mantém um sistema de monitoramento sistemático deste material de referência durante seu período de validade, e no caso de ser detectada alguma alteração significativa nos valores certificados, o usuário será informado e orientado adequadamente.

São Paulo, 18 de abril de 2011.

Centro de Metrologia em Química
Laboratório de Referências Metrológicas

Patrícia Hama
CRQ IV 04161340 - RE 103941
Pesquisador

Centro de Metrologia em Química
Laboratório de Referências Metrológicas

Ricardo Rezende Zucchini
CREA 195776 - CRQ IV 04362478 - RE 8272.7
Responsável pelo Laboratório

Incertezas

As incertezas expandidas dos valores certificados foram estimadas pela combinação, conforme ISO Guide 35:2006, das incertezas de caracterização obtidas experimentalmente no programa interlaboratorial de certificação, com as contribuições de homogeneidade e contribuições pertinentes de estabilidade, avaliadas em estudos realizados no IPT. O fator de abrangência utilizado é aproximadamente 2, proporcionando um nível de confiança de 95%.

Rastreabilidade

Os valores certificados das propriedades deste material foram obtidos por meio de determinações realizadas no IPT e em uma rede de laboratórios colaboradores, utilizando-se uma ou mais metodologias para cada propriedade estudada. As metodologias foram verificadas utilizando-se materiais de referência e padrões com valores certificados rastreáveis ao Sistema Internacional de Unidades (SI) por meio do NIST e outros produtores qualificados. Os instrumentos de medição foram calibrados com padrões rastreáveis ao SI através do Inmetro e da Rede Brasileira de Calibrações(RBC).

Massas mínimas de amostras

A massa de amostra necessária para a realização adequada das determinações depende das metodologias em particular, dos teores de analito, e de vários outros fatores. Recomenda-se que sejam respeitadas as massas estabelecidas nos métodos reconhecidos e normas técnicas mais atuais. Entretanto, para a garantia da validade de todos os valores certificados declarados neste documento e suas respectivas incertezas, não devem ser empregadas amostras com massas inferiores a 100 mg. Este limite foi estimado a partir das massas de amostra empregadas no estudo de homogeneidade deste material.

Instruções para utilização e armazenamento

Manuseio: A retirada de alíquotas deste material em limalhas deve ser realizada em ambiente apropriado e com acessórios limpos. Nunca retorne material ao frasco. Mantenha o material em seu frasco original, bem fechado. **Armazenamento:** Este material deve ser armazenado em local limpo, seco, em temperatura ambiente. A umidade relativa ideal para armazenamento é inferior a 60%. **Segurança:** As informações relevantes são apresentadas na FISPQ, disponível pela página: www.ipt.br/nmr.htm

Observações técnicas

Três laboratórios determinaram, também, o teor de nióbio (Nb), por espectrometria de emissão (plasma acoplado indutivamente) e espectrofotometria UV-Visível [4-(2-piridilazo)-resorcinol]. A informação obtida para este elemento foi insuficiente para o estabelecimento do valor certificado, sendo assim considerado valor informativo.

Informações complementares

A matéria-prima para a preparação deste material de referência foi doada por Aços Villares S.A. (Usina São Caetano do Sul). A certificação deste material foi coordenada por Maria Isabel Lima Craveiro e Tsai Soi Mui Lee. Este Certificado substitui o CMR IPT nº 0904

Laboratórios Colaboradores

AÇOS FINOS PIRATINI – São Jerônimo, RS
Neila Beatriz Bonatto, Wilson Rodrigues Cunha, Givaldo Rodrigues da Silva, Aldo M. Vianna, Pedro Erni Albert.

AÇOS VILLARES S.A. (Usina Anhangüera) – Mogi das Cruzes, SP
Irineu Alabarce de Paiva, Sérgio Luis Cotrim Martins, Mauro Antonio Cangioni.

AÇOS VILLARES S.A. (Usina São Caetano do Sul) – São Caetano do Sul, SP
Masanori Sato, Marcos A. Parise, Edson Estevam Castilho, Wellington R. Lentini, Wilson M. da Veiga, Nelson I. Filho.

COMPANHIA AÇOS ESPECIAIS ITABIRA – ACESITA – Acesita, MG
Antonio Carvalho Torres, Jorge Carvalho Raimundo, Paulo Roberto Drumond Guerra, Adailton Moreira Coelho, Andrea Marinho, Rogério Horta Marques.

COMPANHIA SIDERÚRGICA NACIONAL – CSN – Volta Redonda, RJ
Antonio Carlos Baliza, João Afonso Sampaio, José Angelo Pereira Filho, José Francisco Leal, José Maria da Silva, Valdeir Pereira dos Santos, José Francisco Chaves L. Silva.

ELETROMETAL S.A. METAIS ESPECIAIS – Sumaré, SP
Miguel Carlos Martins, Luiz Aparecido Panini, Antonio Rodrigues, José Carlos de Oliveira.

INSTITUTO DE PESQUISAS TECNOLÓGICAS DO ESTADO DE SÃO PAULO S. A. – IPT – São Paulo, SP
Vagner Tadeu Vallerde, Maria Salete L. F. Soares, Adelson Lopes da Silva, José de Alcântara.

Metodologias Utilizadas na Certificação do MRC IPT 98

Al (solúvel)	Espectrometria de Absorção Atômica
	Espectrometria de Emissão Óptica (plasma acoplado indutivamente)
Al (total)	Espectrometria de Emissão Óptica (plasma acoplado indutivamente)
	Espectrometria de Absorção Atômica
C	Combustão direta (infravermelho)
Co	Espectrofotometria de UV-Visível (sal nitroso R)
	Espectrometria de Emissão Óptica (plasma acoplado indutivamente)
	Espectrometria de Absorção Atômica
Cr	Espectrometria de Emissão Óptica (plasma acoplado indutivamente)
	Volumetria (sulfato de ferro II – potenciometria)
	Espectrofotometria de UV-Visível (ácido perclórico)
	Volumetria (ferro II amoniacal)
	Volumetria (ferro II amoniacal – permanganato)
Cu	Volumetria (iodometria – tiosulfato)
	Espectrometria de Absorção Atômica
	Espectrometria de Emissão Óptica (plasma acoplado indutivamente)
Mn	Espectrofotometria de UV-Visível (persulfato)
	Volumetria (persulfato-arsenito)
	Espectrometria de Emissão Óptica (plasma acoplado indutivamente)
	Espectrofotometria de UV-Visível (periodato)
Mo	Espectrofotometria de UV-Visível (tiocianato – cloreto de estanho II – acetato de butila)
	Gravimetria (alfa-benzoinoxima)
	Espectrometria de Emissão Óptica (plasma acoplado indutivamente)
N	Fusão sob gás inerte (condutividade térmica)
Nb	Espectrometria de Emissão Óptica (plasma acoplado indutivamente)
	Espectrofotometria de UV-Visível [4-(2-piridilazo)-resorcinol]
Ni	Eletogravimetria
	Espectrofotometria de UV-Visível (dimetilgloxima)
	Espectrometria de Emissão Óptica (plasma acoplado indutivamente)
	Gravimetria (dimetilgloxima)
P	Espectrofotometria de UV-Visível (azul de molibdênio)
	Espectrometria de Emissão Óptica (plasma acoplado indutivamente)
	Volumetria (hidróxido de sódio – acidimetria)
S	Combustão direta (infravermelho)
Si	Gravimetria (desidratação com ácido perclórico)
Sn	Espectrometria de Emissão Óptica (plasma acoplado indutivamente)
	Espectrometria de Absorção Atômica
Ti	Espectrometria de Emissão Óptica (plasma acoplado indutivamente)
	Espectrofotometria de UV-Visível (água oxigenada)
	Espectrometria de Absorção Atômica
	Espectrofotometria de UV-Visível (ácido cromotrópico)
V	Espectrometria de Emissão Óptica (plasma acoplado indutivamente)
	Espectrometria de Absorção Atômica
W	Espectrometria de Absorção Atômica
	Espectrometria de Emissão Óptica (plasma acoplado indutivamente)
	Espectrofotometria de UV-Visível (tiocianato)

A versão mais atual dos Certificados de Materiais de Referência do IPT está disponível para download na página: www.ipt.br/nmr.htm

Mod.060811

ATTACHMENT B – Particle Insight Report

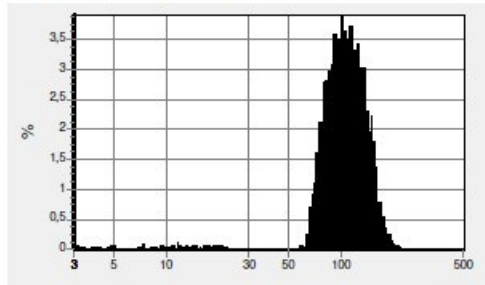


12 nov 2019 5:34:00 PM Page 1

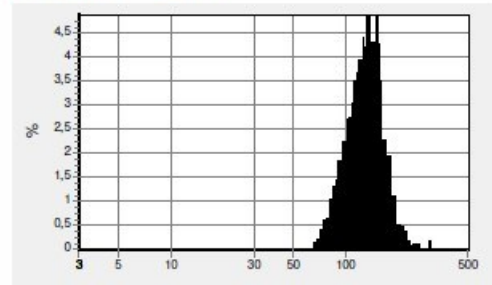
File name	316L_50-150_10000B-1
File location	C:\ProgramData\ParticleInsight\samples
Image file location	C:\ProgramData\ParticleInsight\images\316L_50-150_10000B-1
Saved images	20
Status	Entered
Particle database	Yes
Thumbnail database	Yes
Created by	
Data taken by	
Data taken in SW version	Particle Insight 2.55
Data taken on	12 nov 2019 5:34 PM
Last modified on	12 nov 2019 5:34 PM
Source:	Original data
Analysis conditions	PADRAO LMD
Run conditions	Padrão
Report options	Padrão

EQUIVALENT CIRCULAR AREA DIAMETER

ECA Diameter - number



ECA Diameter - volume

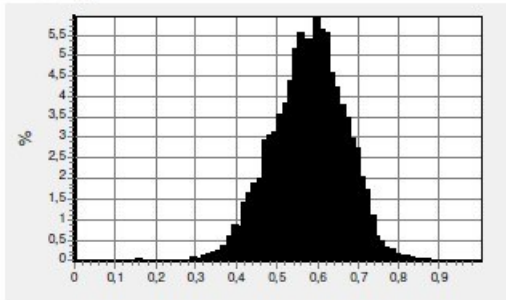


SAMPLE ANALYSIS SUMMARY (sizes in microns)

Count	8562	Number percentiles:	Area percentiles:	Volume percentiles:	Dp,q:	
Minimum	3.0	10,00 %	74.3	10,00 %	85.8	10,00 % 91.4 D1,0 105.6
Maximum	292.9	25,00 %	86.5	25,00 %	100.7	25,00 % 107.7 D2,0 110.3
Mean	105.6	50,00 %	104.3	50,00 %	120.6	50,00 % 127.8 D2,1 115.3
Std. dev.	31.9	75,00 %	125.4	75,00 %	141.6	75,00 % 148.4 D3,0 114.2
Mode	101.1	90,00 %	145.4	90,00 %	158.6	90,00 % 167.2 D3,2 122.4
						D4,3 129.5

CIRCULARITY

Circularity

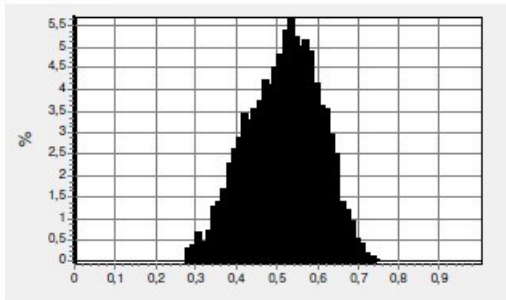


SAMPLE ANALYSIS SUMMARY

Count	8550	Number percentiles:	
Minimum	0.147	10,00 %	0.456
Maximum	0.931	25,00 %	0.517
Mean	0.575	50,00 %	0.579
Std. dev.	0.092	75,00 %	0.637
Mode	0.594	90,00 %	0.689

SMOOTHNESS

Smoothness



316L_50-150_10000B-1

12 nov 2019 5:34:00 PM Page 3

SMOOTHNESS

SAMPLE ANALYSIS SUMMARY

Count	8548	Number percentiles:	
Minimum	0.274	10,00 %	0.391
Maximum	1.000	25,00 %	0.449
Mean	0.514	50,00 %	0.520
Std. dev.	0.090	75,00 %	0.580
Mode	0.531	90,00 %	0.627

316L_50-150_10000B-1

12 nov 2019 5:34:00 PM Page 4

Hardware configuration

Camera	Manufacturer	PixeLINK
	Model	PixeLINK PL-B777U
	Serial number	777007945
	Horizontal resolution (pixels)	2592
	Vertical resolution (pixels)	1944
Maximum image resolution	horizontal (pixels)	2600
	Vertical (pixels)	3000
Calibration	Microns / pixel	0,000
	Magnification	0,0
	Image width (microns)	0,6
	Image height (microns)	767,8
	Source	Saved calibration
Software	Version	Particle Insight 2.55
	Image analysis version	6.12
	PI installation name	

ATTACHMENT C – Stress Relief Heat Treatment Report

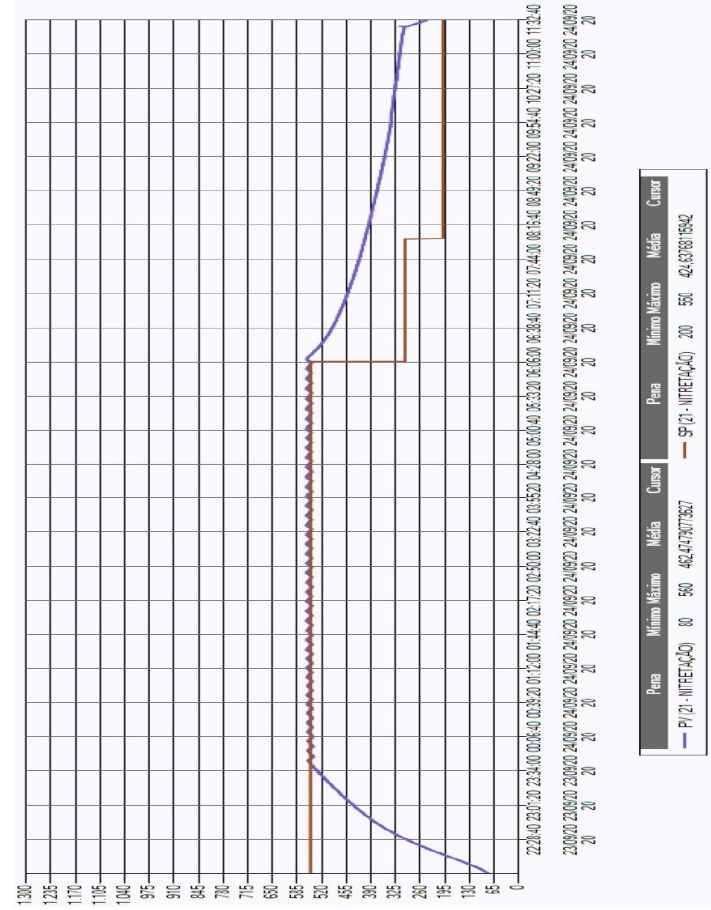
Título: ALÍVIO DE TENSÃO
 Cliente: SENAI

Data Início: 23/09/2020
 Hora Início: 21:56:01.707



N° O.S. PEDIDO 0921
 N° Série: AF 945
 N° Batelada:

Setor: forneiro
 Usuário: joel oliveira
 Arquivo:



ATTACHMENT D – Solubilization Heat Treatment Report

Título: SOLUBILIZAÇÃO
 Cliente: SENAI

Data Início: 25/09/2020
 Hora Início: 16:02:09.503

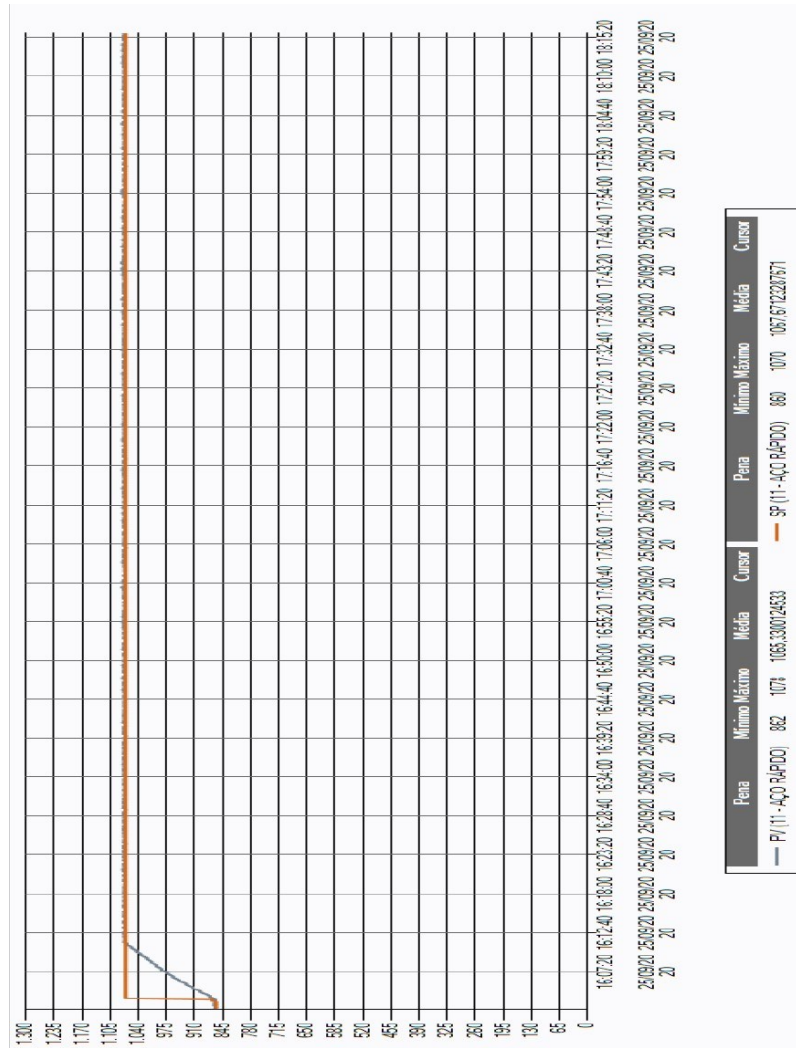


N° O.S: PEDIDO 0921
 N° Série: AF: 945

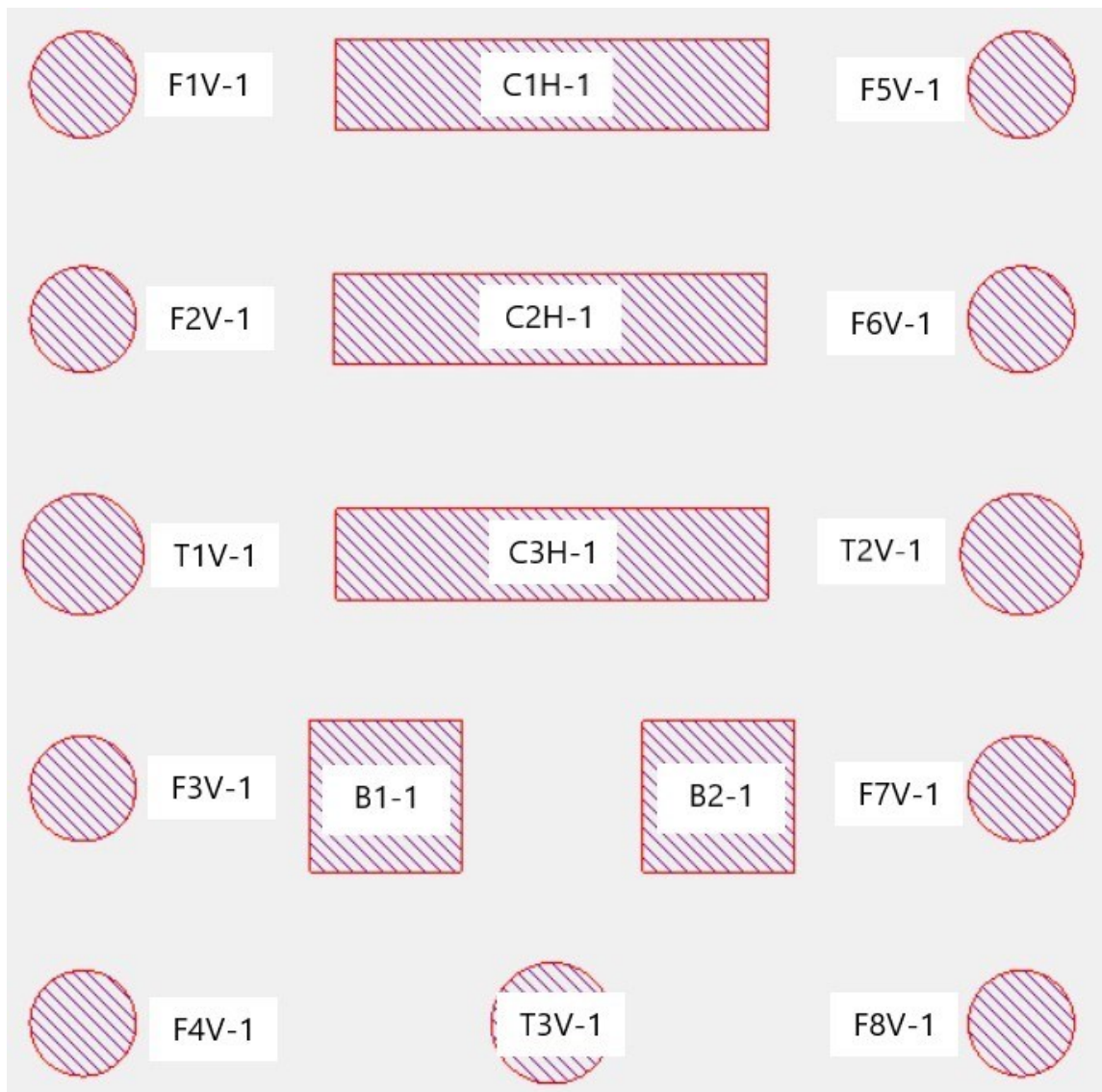
Setor: forneiro
 Usuário: joel oliveira

N° Batelada: CP's sem substrato

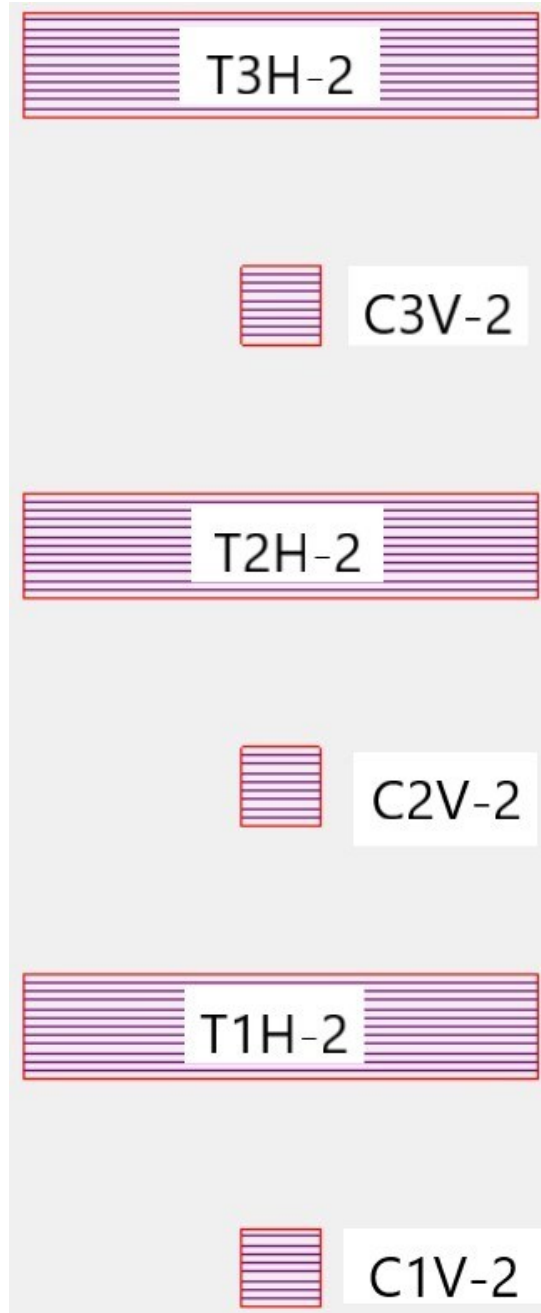
Arquivo:



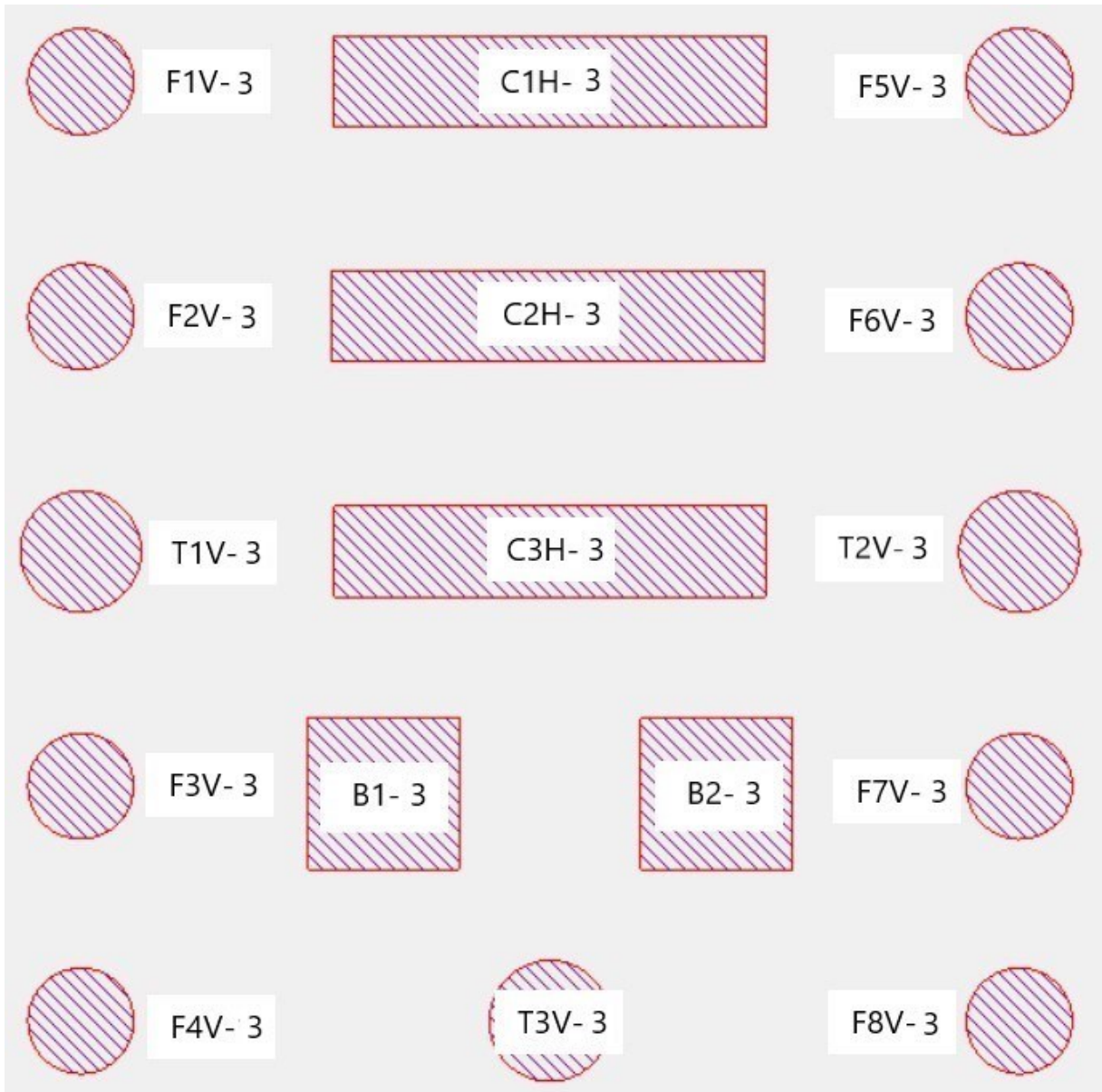
ATTACHMENT E – Sequence for the Deposition of Specimens



Build 1 sequence for the deposition: C3H-1 , C1H-1 , B1-1 , C2H-1 , B2-1 , T1V-1 , T3V-1 , T2V-1 , F4V-1 , F8V-1 , F3V-1 , F7V-1 , F2V-1 , F6V-1 , F1V-1 , F5V-1.



Build 2 sequence for the deposition: T1H-2 , T2H-2 , T3H-2 , C1V-2 , C2V-2 , C3V-2.



Build 3 sequence for the deposition: C3H-3 , C1H-3 , B1-3 , C2H-3 , B2-3 , T1V-3 , T3V-3 , T2V-3 , F4V-3 , F8V-3 , F3V-3 , F7V-3 , F2V-3 , F6V-3 , F1V-3 , F5V-3.

ATTACHMENT F – Porosity Report

Carl Zeiss Microscopy GmbH

Project P00008

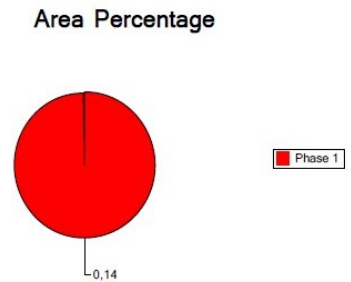
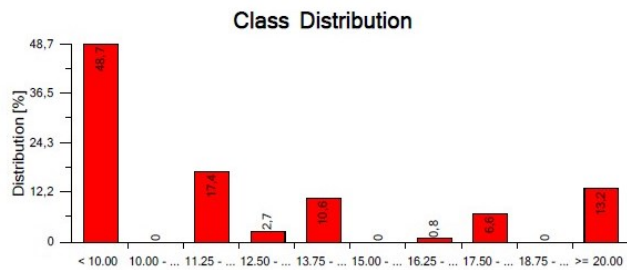
Date 26/10/2020

Project summary:

Project No: P00008
 Evaluation date: 26/10/2020
 Number of images: 1

Evaluated by:
 Material:
 Sample number:

Phase Name	< 10.00	10.00 - 11.25	11.25 - 12.50	12.50 - 13.75	13.75 - 15.00	15.00 - 16.25	16.25 - 17.50	17.50 - 18.75	18.75 - 20.00	>= 20.00	Object Count	Area Percentage [%]
Phase 1	48,67	0,00	17,42	2,66	10,64	0,00	0,80	6,65	0,00	13,16	752	0,14



Multiphase

Page 1 of 3

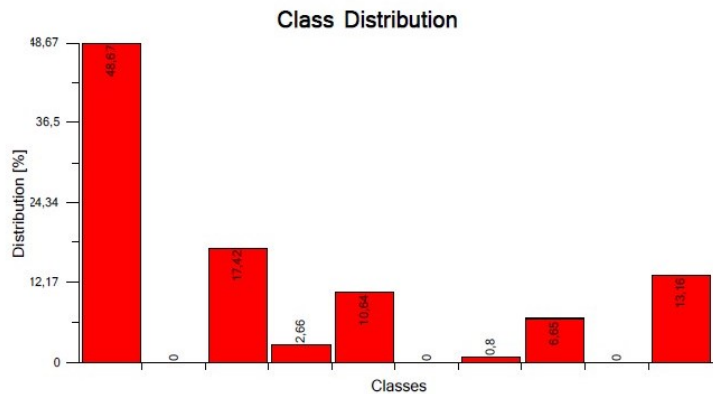
Carl Zeiss Microscopy GmbH

Project P00008

Date 26/10/2020

Results for image 1

Phase	< 10.00	10.00 - 11.25	11.25 - 12.50	12.50 - 13.75	13.75 - 15.00	15.00 - 16.25	16.25 - 17.50	17.50 - 18.75	18.75 - 20.00	>= 20.00	Object Count	Area Percentage [%]
Phase 1	48,67	0,00	17,42	2,66	10,64	0,00	0,80	6,65	0,00	13,16	752	0,14



Original image



Image with Annotations

Multiphase

Page 2 of 3

Classification settings:

Parameter for... Feret Maximum
 Unit for classification: μm

Key	Name	Lower Bound	Upper Bound
I	< 10.00	0	10
II	10.00 - 11.25	10	11,25
III	11.25 - 12.50	11,25	12,5
IV	12.50 - 13.75	12,5	13,75
V	13.75 - 15.00	13,75	15
VI	15.00 - 16.25	15	16,25
VII	16.25 - 17.50	16,25	17,5
VIII	17.50 - 18.75	17,5	18,75
IX	18.75 - 20.00	18,75	20
X	>= 20.00	20	-1

Acquisition settings:

Contrast method: Brightfield Refl.light
 Objective: EC Epiplan 5x/0.13 HD M27
 Camera: AxioCamMR3
 Scaling: 1,2853 Micrometer /Pixel

Order No:

Order No:
 Description:

Comment:

Checked by: